

# **Mechanical and contact guidance properties of live cortical neurons in vitro measured via atomic force and fluorescent microscopy**

A dissertation by

**Marc Simon**

in partial fulfillment of the requirements for the degree of

Doctor of Philosophy  
in  
Physics

**Tufts University**

[August 2016]

Adviser: Prof. Cristian Staii







## **Abstract**

Neurons are highly specialized cells that are the main building blocks of the nervous system. Neurons work together in complex networks to send, receive, store, and communicate information electrically and biochemically. In the developing vertebrate, neurons form connections with other neurons and cells to build the nervous system. They do this by extending processes called neurites. At the distal end of a neurite is a sensing structure called the growth cone, which has the ability to sense and respond to chemical, mechanical, and topographic cues, a process called neuron guidance. In this thesis we explore the mechanism of neuronal guidance by performing atomic force and fluorescence measurements. Specifically, we study the angular growth of neurites over time on three different types of polydimethylsiloxane surfaces imprinted with parallel ridges with  $\sim 0.8\mu\text{m}$ ,  $\sim 1.6\mu\text{m}$ , and  $\sim 3.3\mu\text{m}$  spaced parallel ridges and stud. We observe maximum parallel alignment with surface features with surface 1, followed by surface 2, and surface 3, and maximum perpendicular alignment with surface 1, followed by surface 2, and surface 3. Additionally, the stiffness of cells can be an indicator of cell health, function, and biopolymer arrangements. Most cells have a protective polymer brush layer that shields the cell from mechanical damage and allows other cells to adhere it. We perform the first mechanical measurements of the neuronal polymer brush layer using atomic force microscopy (AFM) indentation techniques, and delineate its properties from the underlying soma. Our measurements reveal the cell body is an elastic material, 3-4 times stiffer than

previously reported, and surrounded by a viscoelastic polymer brush layer. We show this brush layer is much softer than the cell body, and accounts for the previously reported viscoelastic properties of neurons. We also use AFM to measure mechanical and topographical properties of novel biomaterials that can be used as substrates for neuronal growth. Understanding the mechanical properties of neurons and their contact guidance properties is of great fundamental importance, and can also lead to better cellular modeling, new regenerative therapies and devices for nerve and brain regeneration, and safer and more effective surgeries and recoveries.

# Table of Contents

<b>ABSTRACT.....</b>	<b>I</b>
<b>TABLE OF CONTENTS .....</b>	<b>III</b>
<b>LIST OF FIGURES:.....</b>	<b>IX</b>
<b>CHAPTER 1: NEURON BIOMECHANICS .....</b>	<b>1</b>
1.1 OVERVIEW .....	1
1.2 NEURONS .....	5
1.3 NEURONAL MOLECULAR BIOLOGY .....	7
The Cytoskeleton .....	9
Adenosine and Guanosine Triphosphate Hydrolysis .....	10
1.4 CYTOSKELETAL COMPONENTS .....	13
Microtubules .....	15
Actin filaments.....	17
1.5 THE GROWTH CONE .....	19
Adhesion, Polarization, and Pathfinding .....	22
Signaling: The Rho GTPases .....	24
Actin Treadmilling.....	26
The Molecular Clutch .....	28
A stochastic model of neuronal growth .....	29
1.6 ELECTRIC SIGNALING .....	30
1.7 BIOMECHANICAL PROPERTIES OF NEURONS AND LAB BACKGROUND.....	34

Temperature response of the cytoskeleton.....	36
Growth and cell stiffness .....	41
Effects of surface assymetry on neuronal outgrowth.....	42
Conclusion .....	48
<b>CHAPTER 2: ATOMIC FORCE MICROSCOPY .....</b>	<b>49</b>
2.1 OVERVIEW .....	49
The Lennard Jones potential .....	51
2.2 PARTS OF THE AFM .....	55
The probe .....	57
The nano-positioning sytem.....	58
The deflection detection system.....	59
The feedback system.....	60
2.3 MODES OF OPERATION .....	61
Contact mode .....	62
Non-contact mode.....	63
Probe dynamics.....	63
2.4 CALIBRATION AND OPERATION .....	65
Tuning the cantilever .....	65
Force calibration .....	65
Terminology and scanning modes .....	70
Constant deflection mode .....	72
AC mode .....	74
2.5 SPECIAL MODES OF OPERATION .....	77



Friction force.....	77
Electrical methods.....	77
Force volume mapping .....	79
2.6 AFM ON BIOLOGICAL SAMPLES.....	81
Topography .....	82
Stiffness.....	83
Electrical .....	85
Conclusion .....	86
<b>CHAPTER 3: NEURONAL PATHFINDING .....</b>	<b>87</b>
3.1 OVERVIEW .....	87
3.2 LITERATURE REVIEW.....	88
Contact guidance of CNS neurites on grooved quartz.....	88
Topographically modified surfaces affect orientation and growth of hippocampal neurons .....	92
Geometric effect of cell adhesive polygonal micropatterns on neuritogenesis and axon guidance .....	94
Effect of surface asymmetry on neuronal growth.....	99
Neuronal growth as diffusion in an effective potential.....	105
Growth cone edge dynamics via Fokker-Planck .....	108
Neuronal alignment on asymmetric textured surfaces.....	111
Markov transitions and Fokker-Planck .....	113
Energy transduction .....	120
Flashing potentials .....	121

3.3 NEURONS ON MICROPATTERNED PDMS PARALLEL RIDGES .....	123
PDMS surface fabrication and characterization .....	124
Neuron culture .....	127
Fluorescent imaging and image processing.....	128
3.4 RESULTS .....	131
Time integrated growth.....	135
Time dependence of growth.....	141
Conclusions.....	145

**CHAPTER 4: LOAD RATE AND TEMPERATURE DEPENDENT  
MECHANICAL PROPERTIES OF THE CORTICAL NEURON AND ITS  
PERICELLULAR LAYER MEASURED BY ATOMIC FORCE  
MICROSCOPY..... 150**

4.1 OVERVIEW .....	150
4.2 INTRODUCTION.....	151
4.3 MATERIALS AND METHODS .....	156
Data analysis methods.....	157
4.4 RESULTS .....	165
Elastic behavior of the neuronal soma .....	167
Viscoelastic behavior of the neuronal pericellular brush.....	169
Effects of temperature variation on neuronal soma and pericellular brush.....	171
Reconstruction of the previously reported viscoelastic results via two- layer model.....	172

4.5 DISCUSSION AND CONCLUSIONS .....	175
4.6 SUPPLEMENTARY MATERIALS .....	182
 <b>CHAPTER 5: ELECTRICAL AFM IN FLUID ON BIOLOGICAL</b>	
<b>SAMPLES.....</b>	<b>189</b>
5.1 OVERVIEW .....	189
5.2 DIRECT MEASUREMENTS OF ACTION POTENTIALS WITH AFM .....	190
5.3 ELECTRICAL AFM IN POLAR FLUIDS .....	193
Fluid electric force microscopy .....	195
Electrochemical force microscopy.....	197
High bandwidth AFM .....	200
Band excitation piezo force microscopy .....	203
AFM on giant lobster neurons .....	204
5.4 DETECTION OF ACTION POTENTIALS VIA AFM.....	206
Methods.....	207
Scanning kelvin probe and mechanical detection of action potentials.	
.....	209
Fluorescent imaging.....	210
5.5 CONCLUSIONS .....	217
 <b>CHAPTER 6: AFM MEASUREMENTS OF SILK BASED</b>	
<b>BIOMATERIALS, POLYMER FILMS, AND HYDROGELS.....</b>	<b>220</b>
6.1 OVERVIEW .....	220
6.2 ELECTRICAL AFM ON BIOMATERIALS.....	221

6.3 FORCE SPECTROSCOPY ON SILK FILMS AND HYDROGELS .....	225
6.4 TOPOGRAPHIC AND MECHANICAL CHARACTERIZATION OF SILK BASED FIBERS .....	232
6.5 AFM ON POLYMER FILMS .....	244
6.6 NEURONS GROWN ON SOFT GELS AND FIBERS .....	248
Conclusions .....	253
<b>CHAPTER 7: FUTURE DIRECTIONS AND CONCLUSIONS .....</b>	<b>255</b>
7.1 OVERVIEW .....	255
7.2 FUTURE DIRECTIONS .....	256
Combined AFM and confocal microscopy on pericellular brush .....	256
ELB and CM for neuronal pathfinding .....	257
Develop a curvature sensing model .....	258
Branching mechanics .....	258
Electrical detection of action potentials .....	259
Conclusions .....	261
<b>REFERENCES .....</b>	<b>263</b>

## List of Figures:

<i>Figure 1.1. Fluorescent image of neuron .....</i>	<i>6</i>
<i>Figure 1.2. Neuron Internal Structure.....</i>	<i>8</i>
<i>Figure 1.3. The energy vs reaction coordinate for triphosphate hydrolysis. ....</i>	<i>12</i>
<i>Figure 1.4. Microtubule Structure.....</i>	<i>15</i>
<i>Figure 1.5. Actin Filament Structure.....</i>	<i>18</i>
<i>Figure 1.6. Growth Cone Diagram.....</i>	<i>20</i>
<i>Figure 1.7. Cell Adhesion Diagram.....</i>	<i>22</i>
<i>Figure 1.8. Mechanisms of Neuritogenesis.....</i>	<i>23</i>
<i>Figure 1.9. The Molecular Clutch Mechanism.....</i>	<i>28</i>
<i>Figure 1.10.Characteristic Action Potential .....</i>	<i>31</i>
<i>Figure 1.11. Action Potential Propagation .....</i>	<i>32</i>
<i>Figure 1.12.Temperature Response of Neurons. ....</i>	<i>37</i>
<i>Figure 1.13. Percent change of mean neuron elastic modulus from 37°C after drug treatments .....</i>	<i>38</i>
<i>Figure 1.14 Combined AFM/Fluorecent Cytoskeletal Mapping .....</i>	<i>40</i>
<i>Figure 1.15. Nano PPX AFM topography and Cross section .....</i>	<i>45</i>
<i>Figure 1.16. Fluorescent images of neurons on nano-PPX surfaces with angular Distributions .....</i>	<i>47</i>
<i>Figure 2.1 An Asylum MFP-3D and Topography Scan.....</i>	<i>50</i>
<i>Figure 2.2. Schematic of the Lennard-Jones potential .....</i>	<i>52</i>

<i>Figure 2.3. Two Hydrogen Atoms interacting via electrostatic forces and Pauli Exclusion.....</i>	<i>54</i>
<i>Figure 2.4. AFM Diagram.....</i>	<i>56</i>
<i>Figure 2.5. AFM Cantilever.....</i>	<i>58</i>
<i>Figure 2.6. Force Curve .....</i>	<i>67</i>
<i>Figure 2.7. Contact Mode Operation .....</i>	<i>73</i>
<i>Figure 2.8. AC Mode Operation.....</i>	<i>74</i>
<i>Figure 2.9. Example AFM Scans .....</i>	<i>76</i>
<i>Figure 2.10. Force map diagram of neuronal soma.....</i>	<i>84</i>
<i>Figure 3.1. Neurite Orientation vs Groove Width .....</i>	<i>90</i>
<i>Figure 3.2. Percent of neurites crossing grooves .....</i>	<i>91</i>
<i>Figure 3.3. Neurons on Micropillar Arrays.....</i>	<i>93</i>
<i>Figure 3.4. Neurons on Microprinted Geometric Shapes.....</i>	<i>95</i>
<i>Figure 3.5. Neurons on Microprinted Triangular Arrays .....</i>	<i>96</i>
<i>Figure 3.6. Neurite Polarization Schematic .....</i>	<i>97</i>
<i>Figure 3.7. SEM Image of Nano-PPX and Growth Cone Steering .....</i>	<i>100</i>
<i>Figure 3.8. Normalized angular distributions for different anisotropy parameters and fits centered around 0 and <math>\pi</math> directions. ....</i>	<i>103</i>
<i>Figure 3.9. Growth anisotropy vs anisotropy parameter .....</i>	<i>104</i>
<i>Figure 3.10. Normalized angular distributions vs normalized growth cone velocities .....</i>	<i>106</i>
<i>Figure 3.11. Growth cone edge potential vs advancement velocity .....</i>	<i>109</i>
<i>Figure 3.12. Frequency vs growth velocity with fit .....</i>	<i>110</i>

<i>Figure 3.13. Simulations of an ensemble of growth cones with different <math>\delta</math> and <math>\kappa</math> parameters .....</i>	<i>113</i>
<i>Figure 3.14. Markov Transition diagram between states A and B with transition rates <math>K</math>.....</i>	<i>114</i>
<i>Figure 3.15. Potential energy profile vs reaction coordinate .....</i>	<i>120</i>
<i>Figure 3.16. Flashing Potentials .....</i>	<i>122</i>
<i>Figure 3.17. AFM topography images of ridges with cross sections .....</i>	<i>125</i>
<i>Figure 3.18. Result of AFM elastic characterization .....</i>	<i>126</i>
<i>Figure 3.19. AFM topography and elastic modulus image .....</i>	<i>127</i>
<i>Figure 3.20. Example fluorescent images and normalized time integrated histograms of angular distributions.....</i>	<i>129</i>
<i>Figure 3.21. Neurite tracings of fluorescent images .....</i>	<i>130</i>
<i>Figure 3.22. Fluorescent image of neurons grown for 72 hours on surface 3...</i>	<i>131</i>
<i>Figure 3.23. Fluorescent image of neurons grown for 72 hours on surface 3 displaying abrupt direction change .....</i>	<i>132</i>
<i>Figure 3.24. Fluorescent image of neurons grown for 96 hours on surface 2. Ridges run vertically.....</i>	<i>133</i>
<i>Figure 3.25. Fluorescent image of neurons grown for 96 hours on surface 1. Ridges run vertically.....</i>	<i>135</i>
<i>Figure 3.26. Time integrated probability densities and potentials for surface 3.....</i>	<i>136</i>
<i>Figure 3.27. Time integrated probability densities and potentials for surface 2.....</i>	<i>137</i>

<i>Figure 3.28. Time integrated probability densities and potentials for surface 1</i>	138
<i>Figure 3.29. The percent of neurites growing in the rough parallel and perpendicular directions</i>	140
<i>Figure 3.30. Maximum angular distribution peaks vs time in hours for surface 3</i>	143
<i>Figure 3.31. Maximum angular distribution peaks vs time in hours for surface 2</i>	144
<i>Figure 3.32. Maximum angular distribution peaks vs time in hours for surface 1</i>	144
<i>Figure 4.1. Schematic of the AFM indentation experiment</i>	158
<i>Figure 4.2. An example of raw AFM approach curves and fit with the brush model</i>	160
<i>Figure 4.3. The results of alteration of pericellular brush with hyaluronidase</i>	166
<i>Figure 4.4. The elastic modulus of the neuronal soma as a function of indentation rate</i>	170
<i>Figure 4.5. Effective brush density (extracted from Eq. 4.4) vs. AFM indentation rate</i>	170
<i>Figure 4.6. Comparison between the elastic modulus obtained from the traditional single-layer Hertz model and the double-layer exponent model</i>	175
<i>Figure 4.S1. Two representative light microscopy images of neuronal cells used in this study</i>	183
<i>Figure 4.S2. Height image of a deformed neuron cell</i>	186



<i>Figure 4.S3. Effective amount of the pericellular brush vs. indentation rate.....</i>	<i>188</i>
<i>Figure 5.1. Deflection vs tip/sample separation with fits .....</i>	<i>196</i>
<i>Figure 5.2. EcFM scan of Au electrode on SiO<sub>2</sub>.....</i>	<i>198</i>
<i>Figure 5.3. First harmonic amplitude at 200nm separation .....</i>	<i>200</i>
<i>Figure 5.4. Mechanical spiking due to action potentials measure via AFM.....</i>	<i>202</i>
<i>Figure 5.5. ML and PF response comparisons.....</i>	<i>203</i>
<i>Figure 5.6. Voltage and Mechanical spikes vs time via AFM .....</i>	<i>206</i>
<i>Figure 5.7. Schematic of AFM measurement of action potential .....</i>	<i>208</i>
<i>Figure 5.8. SKPM potential cross section .....</i>	<i>213</i>
<i>Figure 5.9. Calcium ion imaging of neuronal cell culture .....</i>	<i>215</i>
<i>Figure 6.1. Roughness and surface potential comparison of silk chimeras .....</i>	<i>222</i>
<i>Figure 6.2. Surface potential SKPM scans and accompanying potential profile</i> <i>.....</i>	<i>224</i>
<i>Figure 6.3. Histograms of sample elastic modulus in MPa.....</i>	<i>226</i>
<i>Figure 6.4. Elastic modulus vs tropoelastin content.....</i>	<i>230</i>
<i>Figure 6.5. AFM images of silk nanofibril .....</i>	<i>234</i>
<i>Figure 6.6. AFM scans of micelleswith simulated results .....</i>	<i>236</i>
<i>Figure 6.7. SEM images of dried H(AB)<sub>12</sub> and H(AB)<sub>2</sub> .....</i>	<i>237</i>
<i>Figure 6.8. AFM amplitude scan of dried H(AB)<sub>12</sub> fibers .....</i>	<i>238</i>
<i>Figure 6.9. Graph of fiber elastic modulus vs treatment chemical .....</i>	<i>239</i>
<i>Figure 6.10. Images of H(AB)<sub>12</sub> silk fibers .....</i>	<i>242</i>
<i>Figure 6.11. Film thickness vs side chain type measured via AFM .....</i>	<i>245</i>

<i>Figure 6.12. 223nm absorbance dependence on number of deposited bilayers per stratum .....</i>	<i>247</i>
<i>Figure 6.13. Average Elastic Modulus vs individual cell grown on gels and glass .....</i>	<i>251</i>
<i>Figure 6.14. Fluorescent images of neurons on PLLA fibers with angular distributions .....</i>	<i>252</i>





# **CHAPTER I**

## **Neuron Biomechanics**

### **1.1 Overview**

This dissertation will explore three characteristic properties of neurons.

The first is a study of the pathfinding behavior of neurons on different topographic environments using fluorescent microscopy. The second is a study of the mechanical properties of neurons with atomic force microscopy. The third is a study of the behavior of electric signaling between neurons and other cells using atomic force and fluorescent microscopies. The mechanical properties of neurons can determine the macro mechanical properties of neuronal tissues [1].

Additionally, the mechanical properties of the neuronal growth substrate can affect cell differentiation and neurite extension [2]. In the brain, neurons work in complex and dense 3-dimensional networks, with the support of glial cells and various other cell types [1, 3]. Interestingly, the mechanical properties of the neuronal environment can have significant effects on cell mechanics and morphology [1, 4, 5]. For instance, cortical neurons (found in the frontal brain cortex) are very soft compared to dorsal root ganglia (DRG) neurons found in the peripheral nervous system [1, 5]. Brain tissue is generally protected from mechanical trauma by the cranium, thus the cells within the cranium do not need to be able to sustain impact and shock trauma [5]. Neurons in the peripheral nervous system, however, grow on stiffer, mechanically active, and unprotected

tissue, such as muscle tissue [4]. Thus neurons in this environment must be able to withstand trauma without failing, so they generally exert larger traction forces than neurons in the brain [4]. Knowledge of neuronal subtype mechanical properties allows for the development of better therapies and treatments for nervous system damage.

The most striking features of neurons are their cellular extensions. These extensions undergo a biased Brownian random walk during neuronal navigation [6, 7]. This stochastic searching behavior is variously called pathfinding, contact guidance, and guidance. Understanding the underlying principles of this pathfinding behavior is crucial to our understanding of nervous systems. In the developing nervous system, neurons must be able to navigate through a chemically and physically complex environment. Sensing and steering of the axon in this environment is performed by the highly sensitive growth cone. The growth cone detects a variety of cues, such as chemical, mechanical, and geometric [2, 8-17]. Neuronal growth cones are capable of precisely directing and steering the axon millimeters from its initial trajectory [8, 10, 11]. There have been important discoveries made describing the chemical pathways neurons use to modulate their cytoskeletons, such as ECM orientation and ECM presentation on the substrate [1, 5, 8, 12, 14, 16]. During pathfinding, cytoskeletal rearrangements induce growth direction changes [11, 19, 20] and respond to external stimuli [4, 2, 21, 30]. Pathfinding of axons and dendrites during nervous system development has been found to vary depend on the mechanical, chemical, and topographic

characteristics of the cell environment [4, 5, 7, 22-30]. Netrins, Ephrins, and other signaling molecules can have repulsive or attractive influences on extending neurites [5, 8, 16, 31], which, in turn control the forces generated by cytoskeletal filaments [32]. Small variations and defects in topography can influence a neurites growth direction and play an important role in neurite growth [21, 30, 70]. A detailed knowledge of how neurons sense their topographic environment is critical to understanding how the nervous system wires up and regenerates [7]. Surface features tend to profoundly bias neuron outgrowth directionality, speed, and even neurite branching [23-29]. Research has shown there are optimal configurations and frequencies of features that optimize outgrowth [33]. Although the mechanisms of outgrowth are not well understood, researchers are applying Fokker-Planck equations to describe neurite outgrowth [7, 34, 35]. Fokker Planck allows for a researcher to quantify neurite directionality and extract the intrinsic driving potentials of the neurons, and the driving potentials unique to micropatterned surfaces. Fokker-Planck framework can give substantial insight into the underlying mechanisms and rules that govern neuronal outgrowth and pathfinding. By being able to manipulate and engineer these surfaces, new novel substrates and materials could be developed to take full advantage of these neuronal pathfinding mechanisms.

Neurons from different areas of the nervous system have been shown to display different mechanical and pathfinding properties. Central nervous system (CNS) neurons grown in vitro on substrates of low stiffnesses do not grow much

differently than CNS neurons on stiff surfaces [5]. In contrast, peripheral nervous system (PNS) neurons show a higher degree of growth on stiff substrates, and a lesser degree of growth on soft substrates, which shows that the mechanical properties of the respective natural cellular environment for a given neuron type has a profound effect on a neuron's ability to navigate [4]. Cortical neurons grown on micropatterned grooved surfaces will show a feature frequency and geometry dependent growth pattern [7, 23- 29]. This shows that neurons are highly sensitive to surface topography. After the nervous system has organized and matured, neurons send electric and biochemical pulses to other neurons and cells. The electrical signals are called action potentials, and are characterized by a flow of ions along a neurite [36]. The action potentials are induced by neurite surface bound ion pumps that control the osmotic and electrical equilibrium of the cell [36]. During "firing" of an action potential, particular ion pumps open and allow a specific ion into the cell, while other ion pumps might let other ions escape [36]. The most common ions used in neurons are calcium and potassium ions, which are controlled by their respective calcium ion and potassium ion pumps [36].

The study of neuronal behavior is the study of the neuronal cytoskeleton, plasma membrane, its protrusions, and how they interact with molecular motors and signaling molecules [8, 11, 18]. In this chapter, I explain the underlying mechanisms of growth beginning neuronal anatomy, cytoskeletal components and their behaviors, the plasma membrane and its associated transmembrane molecules, and force transduction through the molecular clutch. In subsequent



chapters, we explore properties of the neuronal soma and the pericellular coat using Hertzian contact mechanics, pathfinding mechanics for neurons on micropatterned surfaces with the Fokker-Planck model, and finally, the electrical properties of neurons using electrical AFM.

## **1.2 Neurons**

Neurons are highly dynamic cells that are part of the central and peripheral nervous systems. They are the primary signaling cells that make up the brain, brain stem, spinal column, and nerves. Neurons work together in complex networks, with glial cells, to process, store, transmit and receive information. Neurons have three distinct features; the soma, dendrites, and axon (figure 1.1). To interact with their environment and other cells, neurons extend processes called axons and dendrites from the soma outward through a series of cytoskeletal rearrangements. The axon and dendrites, collectively called neurites, possess a highly sensitive structure at their distal ends called the growth cone [9]. The growth cone steers the neurites to or away from particular targets through a combination of topographic, chemical, and mechanical sensing with its surroundings [4, 5, 7, 8, 11, 18].

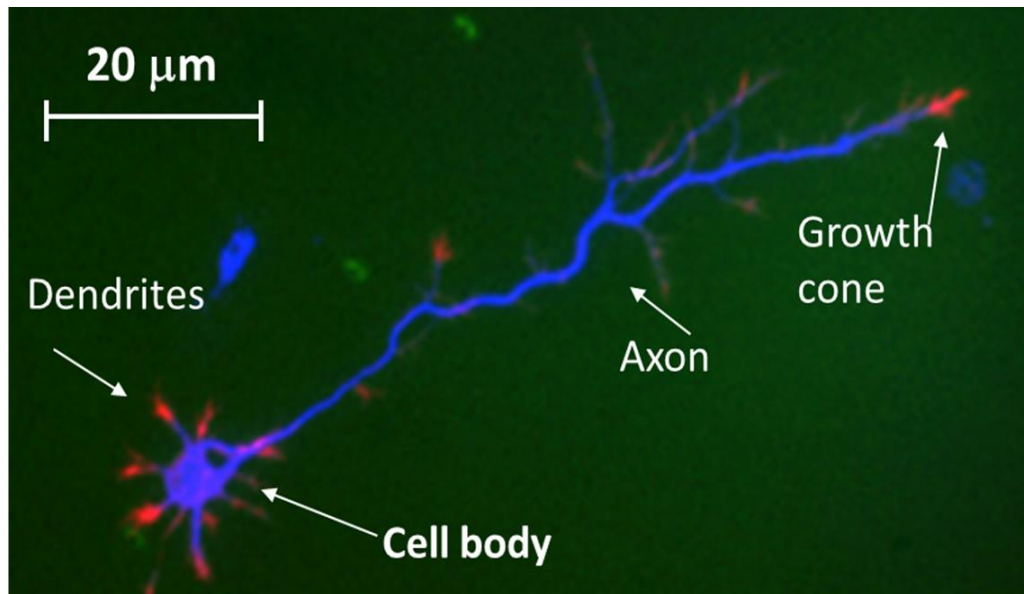


**Figure 1.1** *Fluorescent image of a neuron in culture on PDL coated glass. Red is phalloidin stained actin. Blue is tubulin stain. The longest process (blue) is the microtubule rich axon, and the shorter processes are the dendrites, which all extend from the cell body. The red areas at the distal ends of the neurites are the actin rich growth cones, responsible for neuronal pathfinding and relaying electric and biochemical signals to and from the cell body. (image from Cristian Staii's laboratory at Tufts University)*

The responsibility of the nervous system is to send, receive, process, and store information. These roles are performed through a feedback loop of chemical signals and cytoskeletal remodeling [8, 18]. Storing and processing information generally occurs in clusters of neurons that have complex connections between themselves. The nervous system can be broken into the Central Nervous System (CNS), which is protected within the cranium and spinal column, and the

Peripheral Nervous System (PNS), which is supported by surrounding tissues and links the CNS to the rest of the body. Neurons from the CNS and PNS will have different mechanical properties [37].

### **1.3 Neuronal Molecular Biology**

The cell body, or soma, of a neuron contains the majority of organelles and protein filaments which are contained by a phospholipid bilayer envelope (plasma membrane) (Figure 1.2) [18]. The plasma membrane is a lipid bilayer that envelops the cytoskeleton and organelles. The surface of the lipid bilayer has an abundance of transmembrane and surface bound molecules [8, 38, 39]. The molecules of significance are the transmembrane adhesion molecules (e.g. the integrins), and the conductive ion channels (ion pumps), and the surface bound hyaluronic acid based pericellular coat [36, 38, 39, 40]. The integrins are responsible for cellular adhesion and traction force transduction [18, 38, 39, 41]. The ion pumps are responsible for maintaining ionic equilibrium within the cell, and inducing action potentials [36]. Bound to the lipid bilayer exterior is the pericellular brush/coat, which is a viscoelastic entangled polymer tethered brush consisting of actin anchored hyaluronic acid and glycocalyx [40, 42].

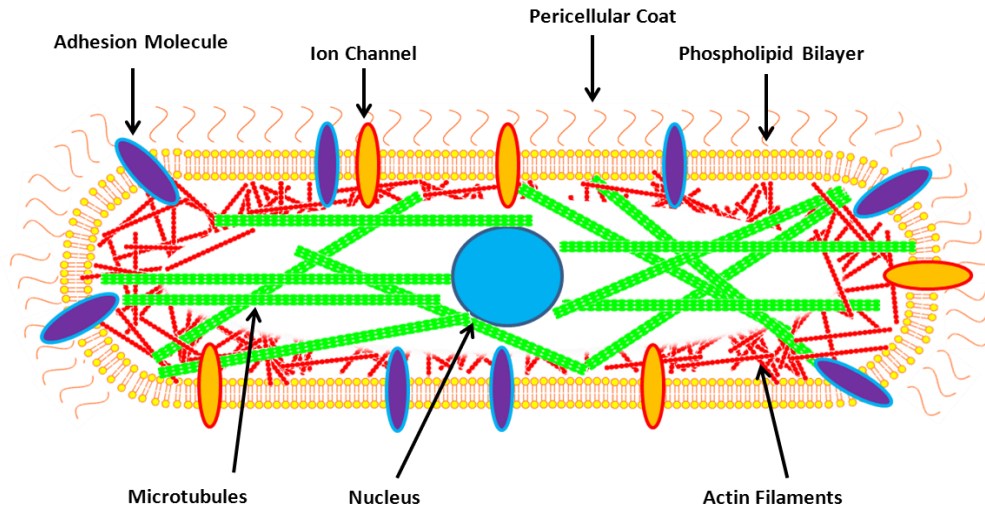


**Figure 1.2** *Neuron Internal Structure, showing the nucleus, cytoskeletal filaments, adhesion molecules (such as integrins), ion channels (such as potassium/sodium ion pumps), the phospholipid bilayer, and the pericellular coat.*

The cytoskeleton is composed of a delicate protein filament network extending throughout the cell [43]. Effectively, there are two dynamic force-producing cytoskeletons: the actin cytoskeleton and the microtubule cytoskeleton. However, intermediate filament cytoskeleton density within the cell affects overall cell elastic properties [44]. Microtubules are relatively rigid self-assembled “tubes” of tubulin dimers that extend from a centrosome or a plasma membrane and give the cell its rigidity [43]. Actin filaments are thin flexible chains of globular actin dimers that entangle with other actin filaments and branch out to form an intricate protein network/gel [43]. These cytoskeletal components are responsible for giving the soma its mechanical/elastic properties [45, 46].

## *The Cytoskeleton*

The cytoskeleton is the supportive structure for the cell and gives cells shape, structure, connects and positions organelles, and generates forces between the cell and its surroundings. Actin filaments (F-actin) are assembled from Globular actin (G-actin) monomers in filaments, networks, and bundles [43]. Microtubules are assembled from 10-15 protofilaments composed of tubulin dimers by hydrolyzing guanosine triphosphate (GTP) into guanosine diphosphate (GDP) and inorganic phosphate (Pi) for energy [18, 43]. Actin filaments and microtubules compose the "dynamic cytoskeleton" and are in a constant state of change. Actin dimers hydrolyze adenosine triphosphate (ATP) to adenosine diphosphate (ADP) and inorganic phosphate (Pi) to form filaments[43].

The cytoskeleton is generally modeled as a viscoelastic and semi-flexible network of loosely crosslinked filaments [47]. The elastic modulus of the cytoskeletal network is determined by the properties of the constituent filaments, such as persistent length, rigidity, binding properties, mesh density, and ambient temperature [47]. For a system with one type of biopolymer filament, the elastic modulus can be approximated as [47]:

$$E \approx \frac{1}{k_B T} \frac{k^2}{\xi^2 L} \quad (1.1)$$

Where persistent length  $l$  is related to chain length  $L$  and mesh size  $\xi$  by [47]

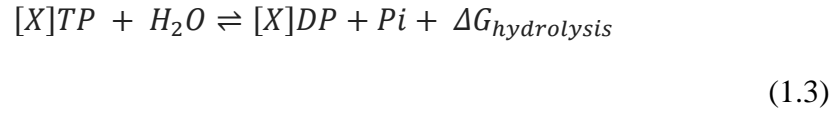
$$L \approx \xi < l \quad (1.2)$$

Here  $k_B$  is Boltzmann's constant,  $T$  is absolute temperature,  $k$  is the firmament bending modulus,  $\xi$  is mesh size, and  $L$  is the chain segment length [47]. However, this is not the entire picture. In cells, the cytoskeletal biopolymer filaments, such as Actin, interact with motor proteins, such as myosin II, which can contract actin filaments and bundles into tighter networks by reducing  $\xi$  [47]. Eq 1.1 shows that a decrease in  $\xi$  will cause an increase in  $E$ , thus a more dense meshwork result in stiffer networks.

#### *Adenosine and Guanosine Triphosphate Hydrolysis*

Dynamic nature of the cytoskeleton is due to the ability of both actin and tubulin to hydrolyze and bind to triphosphate molecules, and change its binding properties based on its hydrolyzed state. The process of hydrolysis changes the conformal and kinetic state of the protein allowing for a higher probability or

lower probability of binding to an associated protein [46]. This lowers the  $\Delta G_{activation}$  which allows for more probable liberation of  $\Delta G_{hydrolysis}$ . To bind, the protein gains energy from breaking a phosphate bond off the triphosphate molecule [X]TP plus water and producing diphosphate molecule [X]DP plus an inorganic phosphate, which in turn, changes binding affinity through the gaining of energy. In general, the liberation of usable energy  $\Delta G_{hydrolysis}$  of a triphosphate breaking into a diphosphate with inorganic phosphate can be written as the following [46]:



Hydrolysis results in a change of the energy state of the protein by reducing an activation energy barrier to cause a more probable transition to the [X]DP + Pi state.

Below shows the kinetics for ATP molecules to hydrolyze. For ATP and GTP, hydrolysis results in the liberation of  $\Delta G_{hydrolysis} = -12.3K_B T$  of energy [49]. This energy is used by a protein to do work.

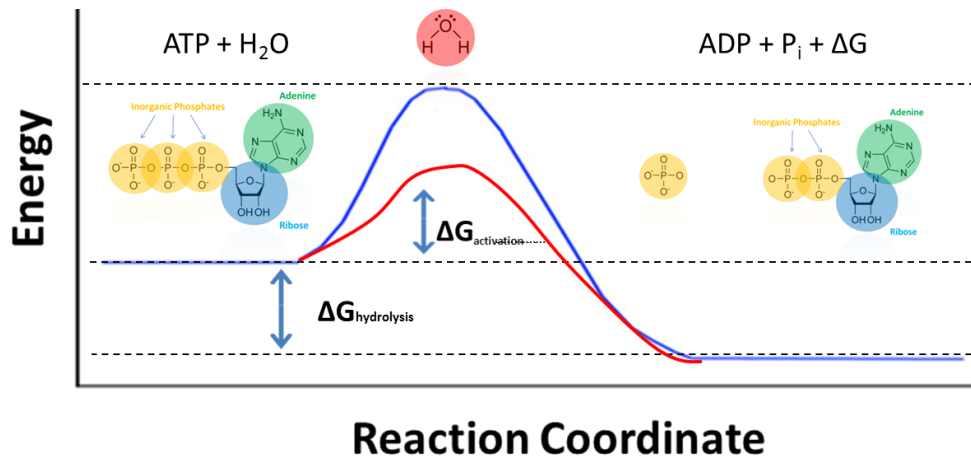


**Figure 1.3** The energy vs reaction coordinate for triphosphate hydrolysis. The reaction constituents are at higher energy to the left of the activation barrier. When a protein, such as a cytoskeletal filament binds to a triphosphate molecule, it lowers the activation energy cost, making hydrolysis more probable. The release of energy is used by the molecule to do work.

Tubulin hydrolyzes the molecule guanosine triphosphate (GTP) into guanosine diphosphate (GDP) and inorganic phosphate (Pi) [43]. Actin hydrolyzes adenosine triphosphate (ATP) into adenosine diphosphate (ADP) and inorganic phosphate (Pi) [46]. The process of one of these proteins binding to [X]TP increases that protein's affinity to bind to the same kind of proteins in the [X]TP state. After binding, the protein can stay in the [X]TP or be hydrolyzed by that protein into [X]DP and Pi.



## 1.4 Cytoskeletal Components

Cytoskeletal single filaments exert forces onto a substrate or other object by using the energy of triphosphate binding to rectify stochastic fluctuations in the motor or on the substrate. F-Actin and Microtubules are characterized by this process. A good example for this is a polymerizing F-Actin, which can exert forces in two ways. The first way is a pure Brownian ratchet [32], there the actin filament is stationary and does not bend, but a load object at the filament tip is allowed to thermally fluctuate along the filament axis. As the load thermally fluctuates in a thermal bath with ATP G-Actin at a concentration exceeding the critical concentration (so growth polymerization is favored). If the load object fluctuates and opens a space between itself and the filament's end, an ATP G-Actin chemically attaches to the filament, increasing its length by one G-Actin monomer. The load object is in contact with the filament leading edge, where thermal fluctuations vary the space between the actin tip and the load object. When a space that's large enough opens, one G-Actin monomer attaches to the tip and hydrolyzes, therefore rectifying the Brownian motion of the load along the polymerization vector [32]. The second type of Brownian ratchet operates where the filament is allowed to flex and thermally undulate. When the filament bends out of contact with the load object, and a space is large enough, an ATP G-Actin monomer binds to the filament tip and hydrolyzes, again increasing the filament length by one. Since the filament bent, energy was stored in the bend. Since the

contact angle is not zero, the filament exerts an elastic restoring force on the load object, pushing it forward. The load object and filament are in contact, then the filament bends away and gains a monomer. The filament then exerts a force on the load object and pushes it forward using energy stored in its deflection. Both of these processes are, again, required to be able to occur in reverse. Single cytoskeletal filament networks exert forces on other filaments through thermal fluctuation, pushing, bending, and branching due to new nucleation sites. For Actin, the dense filament meshwork grows and polymerizes new branched filaments at  $70^\circ$  relative to the filament axis from ARP2/3 (Actin Related Protein complex 2 and 3) actin binding sites [50]. As the network grows, given an ample supply of ARP2/3 and ATP regeneration, filaments bend, break, and reach a critical rigidity that is characteristic of the actin network [50]. Microtubules can also be considered a polymerization motor, since they exert forces by polymerization. Of the polymerization motors, microtubules have gained the most interest. They can be considered a very dynamic structural component of the cytoskeleton, and allow cells to interact with their environment by changing shape and extending processes. Microtubule polarity is determined by growth and GTP position on the tubulin dimer, with GTP bound to the  $\alpha$  tubulin section defining the depolymerizing minus end [43].

## Microtubules

The microtubule cytoskeleton is a fragile and ridged structure that gives cells their shape, positions organelles. Microtubules have many functions within the cell, for instance, during mitosis, microtubules adhere to and rip apart chromosomes in to halves and split the cell. More interestingly, they act as a molecular “highway” for transportation of cellular cargo via the dynein and kinesin families of motor proteins [49]. Microtubules are ~25nm diameter hollow tubes formed from protofilaments of GTPase  $\alpha\beta$ -tubulin dimers (Figure 1.4) [43].

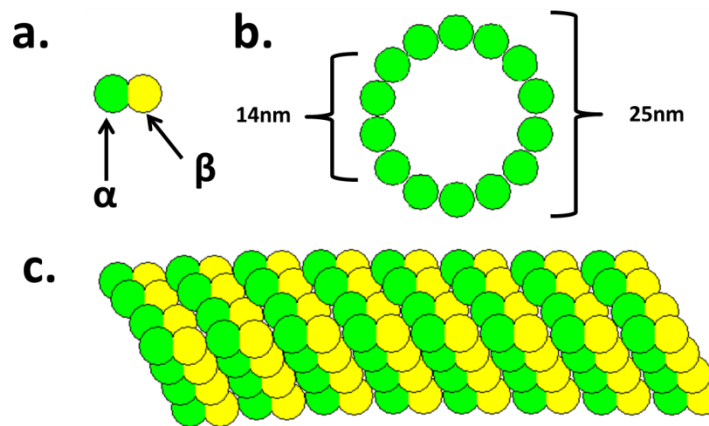


**Figure 1.4** Diagram of a microtubule. Microtubules are formed by  $\alpha\beta$ -tubulin dimers (a) arranged in a 12-15 protofilament tube (b and c), with ~25nm outer diameter and ~14nm inner diameter (b). Microtubules can measure hundreds of microns long. a. Yellow components are  $\beta$ -tubulin monomers, green components are  $\alpha$ -tubulin monomers. [43]

Generally, microtubule formation begins with a  $\gamma$ -tubulin nucleation site such as a centrosome. Dimer bound  $\beta$ -tubulin binds to and hydrolyzes GTP to

initiating the binding between dimer bound  $\alpha$ -tubulin and  $\gamma$ -tubulin, where GTP is then hydrolyzed into Guanosine diphosphate (GDP) and inorganic phosphate (Pi). After this stage,  $\alpha\beta$ -tubulin dimers bind and hydrolyze in the GDP state forming filaments. This gives the microtubule an unstable GTP Tubulin cap, with a stable GDP tubulin body. As the microtubule grows outward, it undergoes phases of slow growth and rapid depolymerization [43]. This property is called dynamic instability and is the source of constant microtubule cytoskeletal rearrangements. As microtubules are growing, they exert pico-newton forces that push on the cell's plasma membrane and organelles. Once a microtubule is formed, it is able to support the cell through dynamic instability, constantly modulating forces on a given microtubule's load. The microtubules act as a linear highway for the molecular motor families of kinesins and dyneins [49].

Microtubules found in vivo are generally composed of 13-15 protofilaments, which arrange in a staggered helical structure, with one protofilament leading tip [43]. Dynamic instability allows them to spontaneously grow and shrink. The GTP Tubulin concentration dependent growing and shrinking are known as rescue and catastrophe, respectively, and give cells their dynamic character. States of rescues and catastrophe are governed by hydrolysis of GTP. During rescue, GTP tubulin dimers form a cap at the microtubule end and promote polymerization. Behind this GTP tubulin cap, the majority of the microtubule is formed with GDP tubulin. If the GTP tubulin cap hydrolyzes to

GDP tubulin, catastrophe ensues, and the microtubule falls apart in chunks called oligomers.

### *Actin Filaments*

The Actin cytoskeleton is a highly dynamic meshwork of ~7-9nm diameter [43]. ATPase actin filaments and myosins that are the primary mechanism of force generator in a cell [51]. Like microtubules, F- actin filaments are polarized and have a + and – end, with a “barbed” morphology (Figure 1.5) [18, 43]. It is by far the most studied part of the overall cytoskeleton. Here, actin filament formation begins when globular actin (G-actin) forms dimers, then trimers, and by repeated monomer addition, become F-actin by rectification of Brownian motion by binding energy at a nucleation site. This binding is dependent on the nucleotide state of the G-actin (nucleotide free, ATP, ADP +Pi, or ADP). G-actin uses ATP binding to lower the binding barrier energy to make binding more probable. F-actin is most stable in the ATP nucleotide state [36]. Following ATP hydrolysis, the ADP state is less stable, and more likely to dissociate. The ATP-ADP change along F-actin makes one end (the + end) more likely to polymerize, where the minus-end is more likely to depolymerize, making actin very dynamic.

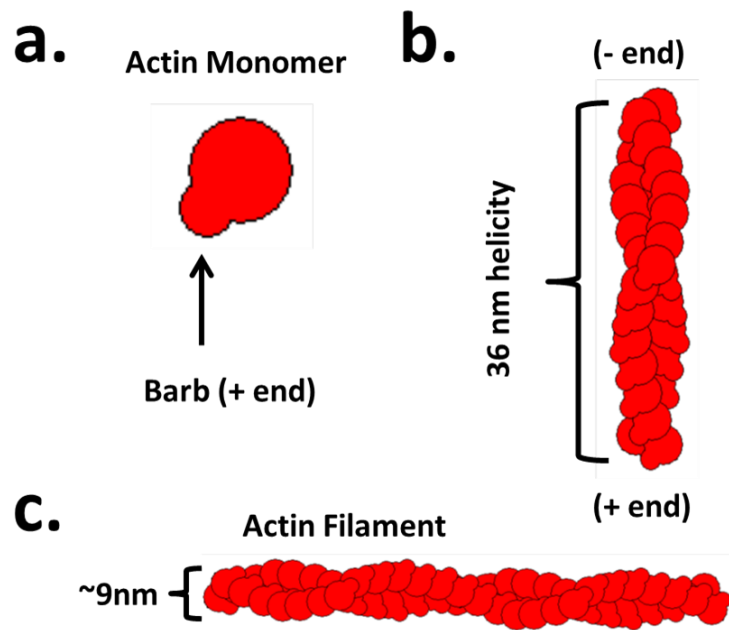
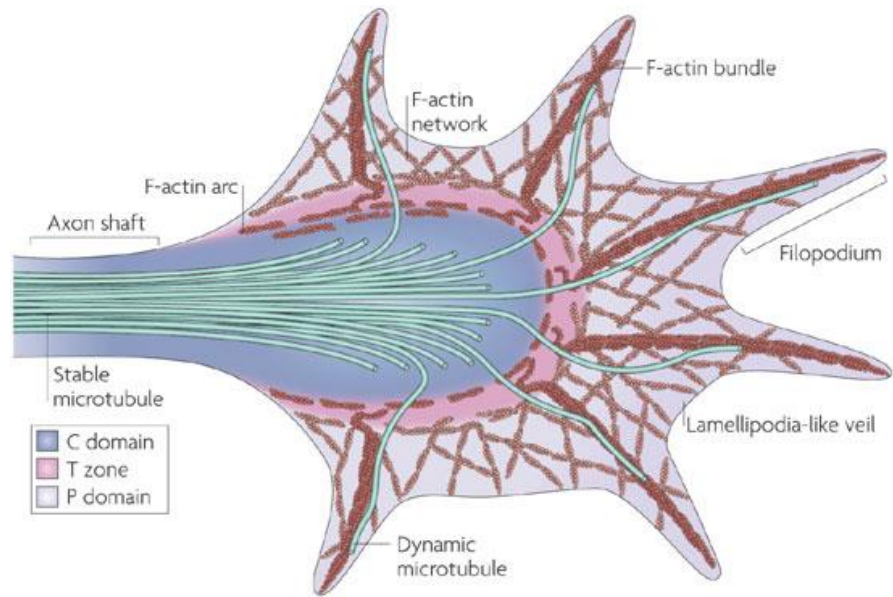


**Figure 1.5** Actin filament diagram. a. A cartoon of an Actin monomer showing barbed end (+ end). b. A cartoon of an Actin filament segment showing the intrinsic 36 nm helicity and + and – ends. c. A cartoon of an actin filament showing ~7-9nm diameter.

At the minus end, the protein cofilin increases the rate of dissociation of ADP actin and prevents the dissociation of ADP, and binding of ATP [43]. Another protein, profilin, catalyzes the exchange of ADP for ATP in G-actin, and prepares it for polymerization to the plus-end [43]. This cofilin/profilin mediated process of polymerization and depolymerization is known as actin treadmilling, and fuels force generation (See figure 1.9) [43].

## 1.5 The Growth Cone

Neurites are primarily composed of dense parallel bundles of microtubules [9, 18], enveloped by the plasma membrane, and act as structural support and transport pathways for intercellular cargo, such as mitochondria, to the distal ends of the neurites. A neuron of any type (such as cortical neurons, hippocampal neurons, Dorsal Root Ganglia (DRG), Purkinje cells, and hypothalamus neurons) will have multiple dendrites, yet the dendrite number, morphology, and branching behavior will vary for cell function. In cortical neurons, dendrites are relatively short and lack extensive branching. However, Purkinje cells have elaborate and heavily branched dendrite networks called the dendritic tree. Neurites that send information from the soma to other cells are called axons. Axons are generally the longest neurite, and can extend hundreds of microns from the soma [9]. During nervous system development, axons and dendrites extend from their soma and navigate to a potential synaptic target. Pathfinding is the process in which neurites undergo a directed Brownian walk by means of chemotactic, hypotactic, electric, and topographic cues. Processing of the guidance information is done by the growth cone, which is a highly sensitive sensing organ located at the distal end of neurites (Figure 1.6). The growth cone is responsible for steering the neurite to a target. Growth cones are incredibly sensitive, and can detect single molecules or tiny nanometer scale features and reacts to them.



Nature Reviews | Molecular Cell Biology

**Figure 1.6** Diagram of cytoskeletal arrangements of microtubules and actin in the neuronal growth cone [9], showing microtubules (green), actin (red), and the 3 domains of the growth cone: the Periphery (P) zone, Transition (T) zone, and Center (C) zone.

The ability to guide the neurite is intimately tied to substrate mechanics, topography, and the geometry and structure of the growth cone [4, 27, 33, 52]. The most notable morphological features of growth cones are the fingerlike protrusions called filopodia, and the web-like regions between filopodia called lamellipodia (Figure 1.6). Recently, Atomic Force Microscopy (AFM) revealed the 3D structure of the growth cone in detail [53]. The web-like lamellipodia, are a very flat, ~200nm [53], actin network bound to the plasma membrane through integrins. The lamellipodia exist between filopodia, which are believed to form



the main sensing mechanism of the growth cone and are precursors to focal adhesion formation [53]. Where lamellipodia acts as the main adhesion region between growth cone and substrate [9].

The growth cone cytoskeletal substructure has 3 distinct cytoskeletal regions, the Periphery (P) zone, Transition (T) zone, and Center (C) zone [9, 53] (Figure 1.6). The mechanical functions of these zones are best described by process of actin polymerization in the peripheral zone being driven, by expansion, into the transient zone, where in the actin filaments are compressed by an actomyosin arc, and recycled back to the p zone. From the polarized microtubule rich center zone, microtubules polymerize outwards and explore the T and P zones through polymerization [9], and rapid depolymerization, which is the property of dynamic instability [43]. The peripheral zone (P-zone) contains highly dynamic filopodia and lamellipodia. Filopodia are mainly comprised of dense fibrin bound actin bundles generated through polymerization at the filopodial tip [9, 43]. These actin bundles are driven back into the growth cone [9]. They act as sensory probes to explore the extracellular landscape. The lamellipodia are made of a dense actin network is generated at the periphery edge, and is pushed back into the growth cone much like the filopodia. The Transition zone (T-zone) occupies the region before the P-zone, and contains a myosin bound actin arc [9]. This arc pulls in, compresses, and depolymerizes filopodial actin bundles and lamellipodial actin networks. The depolymerized actin is recycled back to the growth cone periphery by actin treadmilling [9]. The central zone primarily

contains an array of polarized microtubules that explore into the T and P zones by dynamic instability. These microtubules serve multiple functions. They behave as highways for the motor proteins, kinesins and dyneins, to transport cellular cargo between the soma and growth cone [49]. They also help steer the growth cone, by binding to the actin cytoskeleton.

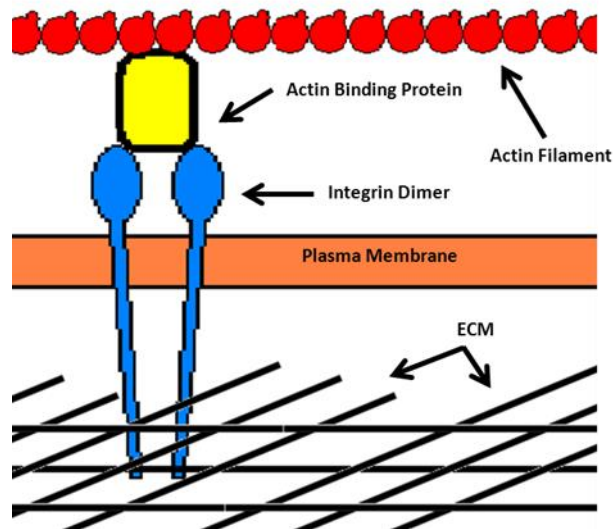


*Figure 1.7 Cell A simple diagram of actin (red)/ integrin (blue) coupling with actin binding proteins (yellow) to the extracellular matrix protein (black).*

### *Neuronal Adhesion, Polarization, and Pathfinding*

A predictable chain of events occurs after a neuron is formed within an animal nervous system or cultured in vitro. In a culture system, a set number of

neurons is seeded onto a biocompatible substrate (such as poly(D-Lysine)) coated glass or an Extracellular Matrix (ECM) loaded gel) and allowed to adhere. The process of neuron adhesion to a substrate begins with the lipid bilayer and its transmembrane adhesion molecules. The most notable transmembrane adhesion molecules are the integrins. These molecules are composed of a  $\alpha$  and  $\beta$  subunits that assemble into an  $\alpha\beta$ -dimer [18]. They behave like molecular clamps that attach to surface bound adhesion molecules and ECM. For the cell to remain structurally adhered to a surface, the integrins couple to the cytoskeleton, specifically the actin meshwork [18, 43]. Thus, the cytoskeleton-integrin couplings anchor the cell to specific adhesion areas of its substrate.

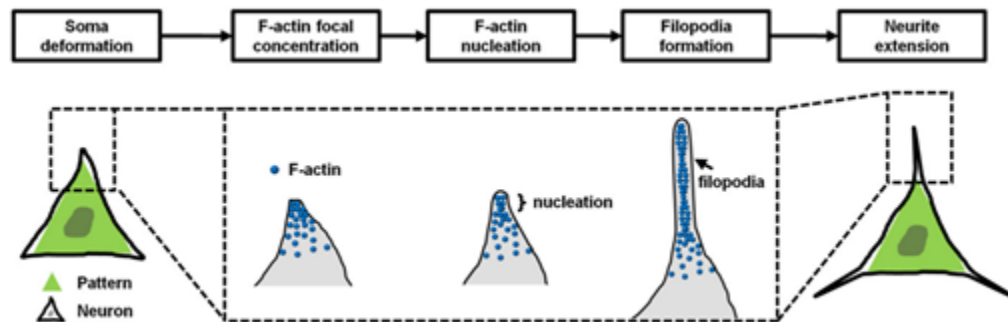


**Figure 1.8** Neuritogenesis of a neuron with micropatterned shape induced pyramidal morphology. Once a neuron adheres to a substrate, in this case a triangle pattern, induced actin polymerization from the related adaptor proteins bound to the integrins initiates neurite extension. F-actin nucleation results in membrane deformation and filopodia formation. From here, a series of signaling events takes place that allows the neurite to extend from the cell body [54].

Once the neuron has established F-actin-integrin adhesion sites and is well adhered to its substrate, internal signaling induces integrin rich focal adhesions [9, 18, 38, 39]. These sites act as polymerization sites for actin. A neurite then sprouts from a focal adhesion, however, this is not always the case [55]. Cytoskeletal dynamics are mediated with a variety of signaling and binding proteins and molecules [5, 8, 12, 16, 18, 31]. This process continues until the ridged microtubules reach a point where they jam against an object. At this point, polymerization continues, and begins to stretch the surrounding plasma membrane from the adhesion site [54]. This extends the neurite outward. The initial actinic protrusion is the first filopodia of the growth cone and initiates the neurite guidance/pathfinding process [54].

### *Signaling: The Rho GTPases*

Neurons respond to a variety of physical and chemical cues from their immediate surroundings. Biochemical cues, from the Rho GTPases, trigger cytoskeletal rearrangements through chemical signaling pathways that affect substrate coupling and actin network polymerization [18, 39, 56]. Additionally, Netrins, Semaphoring, Ephrins, Slit-ROBO, and Neurotopic molecules act as chemoattractants and chemorepulsants that regulate actin polymerization and neuron adhesion to ECM through the Rho-GTPases [5, 8, 12, 16, 31]. Adhesion

and cytoskeletal dynamics are regulated by Rho-GTPase expressing cell transmembrane adhesion molecules (CAMs) [38, 39]. In vitro neuron studies focus on the Integrins, which bind to substrate bound ECM [9, 18]. Integrin-actin interactions are linked with mechanosensitive talin, vinculin, and paxillin, and act as a molecular clutch for the actin motors to transduce force to the ECM (Figure 1.7) [18, 43, 57]. Integrins work in  $\alpha\beta$ -dimers and move along the plasma membrane and form clusters, called focal adhesions, and act as the main adhesive sites in GCs [9, 18, 39, 56]. Integrins bind to the actin cytoskeleton through talin, vinculin, and paxillin [9, 12, 18, 43]. This protein complex behaves as the clutch that transduces cytoskeletal forces to the ECM, and therefore controls cell motility. Signaling from extracellular molecules regulates neuritogenesis and GC motility through the molecular clutch [9, 18, 54].

Actin polymerization and depolymerization molecules are controlled by the family of small Rho-GTPases (CDC42, Rac, and Rho) [9, 12, 56]. These proteins signal actin and ABPs (Actin Binding Proteins) to modulate the actin cytoskeleton, and reinforce integrin connections. Rho GTPase mediates ROCK (rho associated protein kinase), which controls actomyosin contractibility, and is expressed in collapsing GCs [58-61]. Many chemical signaling pathways of Rho-GTPases have been identified, but the complexity of their interactions leaves much to be understood.

Arp2/3 (actin related protein 2 and 3) is an ABP that behaves as an F-actin branching protein [50]. Arp2/3 is used to form dense actin networks by adding actin nucleation sites to existing F-actin. Importantly, when Arp2/3 binds with an actin filament and forms a new nucleation site, the new branching daughter filament will grow  $70^\circ$  from the parent filament [50]. This  $70^\circ$  angle is believed to be important for the strength of the actin network [56]. Extracellular cues trigger the Rho-GTPase and Rho associated protein kinase (ROCK) [58-61]. Transporting proteins bind to Arp2/3 and transports it to an actin filament, where Arp2/3 binds. The subsequent binding releases the transport molecule, and allows for ATP-actin nucleation, and grows the network. The Binding of the Arp2/3 complex causes F-actin branches to grow at  $\sim 70^\circ$  from the filament axis.

### *Actin treadmilling*

In the growth cone, forces produced by the actin cytoskeleton are transferred to a substrate through transmembrane adhesion sites. This force is generated from actin polymerization from a nucleation site at the leading edges of the growth cone, and polymerizes forward by pushing on other cytoskeletal filaments. This causes the growth cone to advance. To control this advancement, the motor protein Myosin II pulls the newly formed actin filaments deeper into the growth cone, where the actin filament is ripped apart into G-actin, and cycled

back as raw materials for polymerization [9, 18, 43]. This process of polymerization, depolymerization, and recycling is called “actin treadmilling”.

### *The Molecular Clutch*

Traction forces are generated by the coupling of the polymerizing actin cytoskeleton and myosin II motors to Integrins (Figure 1.9) [18, 58-61]. Actin does not bind directly to integrin, but through actin binding proteins, such as of Talin, Arp 2/3, Paxillin, etc. Talin is linker of this complex and binds to actin by multiple binding sites, but has the ability to expose more under tension [57]. When tension is applied to Talin, it exposed vinculin binding sites[57]. These sites bind vinculin, which binds directly to actin. Stresses between the focal adhesion and the actin cytoskeleton pull on Talin, forcing it to unwind [57]. This, in turn, opens vinculin binding sites that allow for more actin binding, therefore strengthening the cytoskeletal coupling [57].

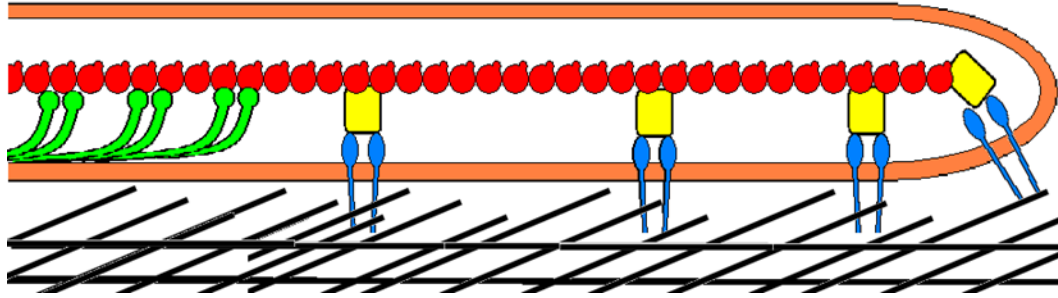


**Figure 1.9** Diagram of the molecular clutch. Actin polymerizes to the right, pushing the filaments to the left. Talin and the other actin binding proteins (yellow) form the actin clutching mechanism between integrin dimers (blue) and the actin cytoskeleton (red). Myosin II (green) pulls actin rearward.

The process of growth cone topography and bound chemical detection is not fully understood, however the effects of topography on neuronal pathfinding can be dramatic. Regardless of the cue (topographic or chemical), the growth cone will modulate its cytoskeleton in response to transmembrane adhesion molecules and signaling molecules [8, 5, 16, 31]. In the growth cone, integrins can group into focal adhesions [38]. As the name suggests, these are membrane organelles that are composed of spatially “focused” transmembrane adhesion molecules which create much stronger adhesion sites than single integrins [62]. This controls the neuronal steering, extension, and retraction [9].



Describing neuronal growth can be difficult considering the random nature of chemical diffusion and neuronal response to outside stimuli. Intracellular diffusion of growth factors [34, 57, 63-66], cytoskeletal reorganizing effects [67-70], adhesion organ formation [72] all play a key role in pathfinding. To describe and quantify neuronal growth one can use a phenomenological stochastic model to take into account these effects. We use Fokker-Planck formalism to phenomenologically describe the growth of neurites on a variety of surface topographies. The stochastic Fokker-Planck equation is:

$$\frac{\partial}{\partial t} P_i(t) = D \frac{\partial}{\partial x} \left[ \frac{-F_{ext} + \frac{d}{dx} \phi_i(x)}{K_B T} P_i(t) + \frac{\partial}{\partial x} P_i(t) \right] \quad (1.3)$$

Here,  $i$  denotes a growth mode,  $x$  is the variable of interest (this could be angle or velocity),  $P$  is the probability density of the event,  $D$  is the diffusive constant,  $F_{ext}$  is an externally applied force,  $\phi$  is the driving potential of growth, and  $K_B$  is Boltzmann's constant, and  $T$  is absolute temperature. For neurons on flat featureless surfaces  $\phi$  is the neurons intrinsic growth potential.

## 1.6 Electric Signaling

Neurons primarily send and receive single or periodic electrical pulses to other neurons. The electrical pulse, called an action potential, propagates from the axon hillock to the growth cone or synapse as a calcium ion cascade with a ~50mV to 120mV magnitude from the resting potential of ~-70mV [36, 73]. This cascade is triggered by the opening and closing of Potassium/Sodium transmembrane voltage gated ion pumps [36]. The structure of the neurite behaves as a coaxial cable. The opening or closing of ion pumps under certain conditions can cause electric polarization and depolarization of the plasma membrane. This electric disturbance propagates down the neurite as the action potential. Accompanying the electrical action potential is a mechanical disturbance that also propagates down the axon [74, 75]. Since ion channels open and close through conformational changes induced by voltage gating, the lipid membrane mechanically distorts. Both the action potential and the mechanical disturbance are measurable by atomic force microscopy [74, 75].

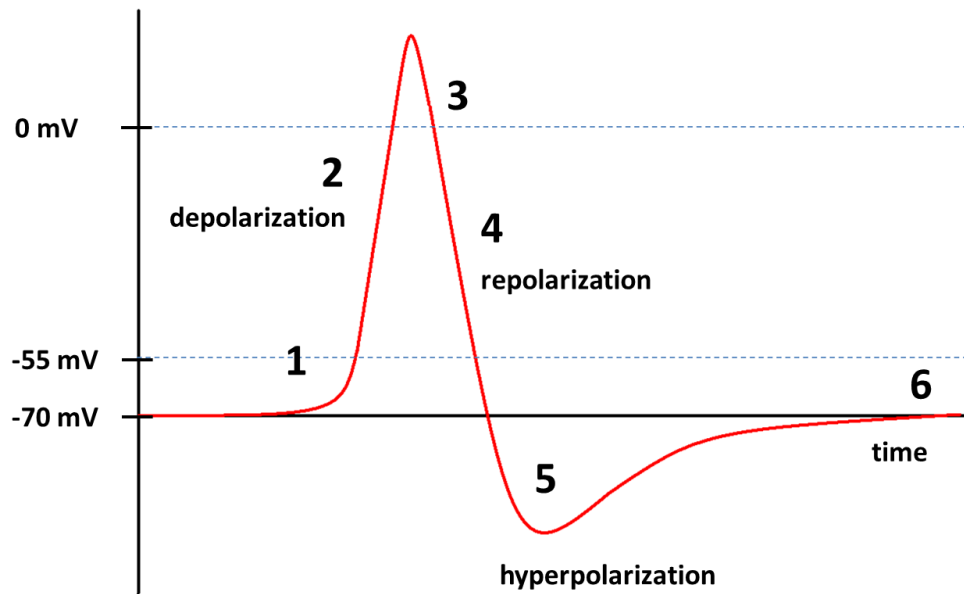


**Figure 1.10** A diagram of the characteristic action potential. Voltage is the vertical axis and time is the horizontal axis. Before the action potential begins, the cell membrane is at its resting potential of  $\sim -70\text{mV}$ . After a stimulus (1) with a  $\sim -55\text{mV}$  threshold, the sodium ion pumps open leading to rapid membrane depolarization, followed by the sodium ion gates closing (2) At peak potential, the potassium ion channels open and cause rapid repolarization (3) with the active K and Na pumps cycling. There is a “snap back” effect for the action potential due to Cl ion channel activity that causes hyperpolarization of the membrane (5), leading to the recovery of the  $\sim -70\text{mV}$  equilibrium state (6). [36, 73].

The action potential is caused by the precise opening and closing of transmembrane ion channels that are distributed on the lipid bilayer which propagates a membrane potential disturbance down the axon (figure 1.11) [36]. The ion channels are membrane pores that can behave as a switch to open or close

the cell interior to the cell exterior. They can open to the outer environment, bind to specific ions which trip the toggle, and induce a conformational change to close to the outside and open to the inside. Once this happens, the ion that was bound to the ion pump is released by the conformational change and released into the cell. This process can happen in reverse, evacuating ions from the cell. This switch is why water (an ionic molecule) kills cells, by causing disruption of ion pumps function, completely disrupting cell molecular kinetics inducing cell death.

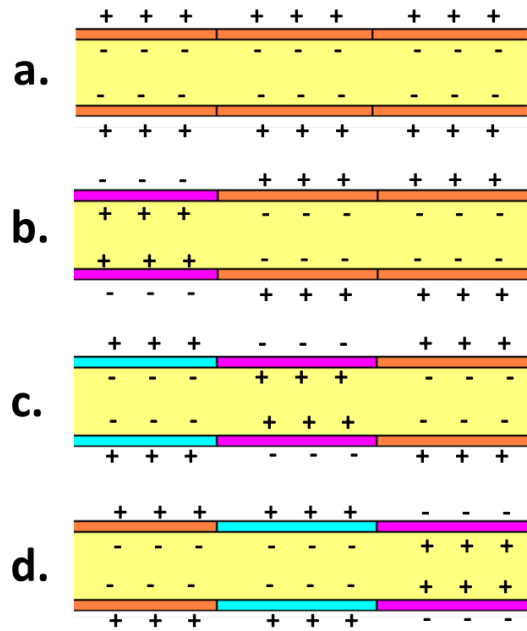


**Figure 1.11** Action potential propagation down an axon. *a.* Axon membrane at resting potential (orange) before stimulus with  $\sim -70\text{mV}$  resting potential. *b.* The action potential is stimulated and depolarizes the membrane (magenta) which causes sodium ion influx. *c.* Depolarization triggers depolarization of nearby ion pumps, while the previous ion pumps repolarize (blue) the membrane by potassium out-flux. *d.* The electrical disturbance propagates as an action potential down the neurite from left to right [36].

Ion channels can be classified as voltage gated, or not voltage gated [36]. Voltage gated ion channels open or close in response to membrane potential and are responsible for action potential propagation [36]. Action potential propagation in mammalian neurons primarily involves voltage gated sodium/potassium ion channels [36]. However, the opening and closing of these ion channels can mechanically or chemically induce other ion channels to open or close [36]. The sodium/potassium ion pumps regulate transmembrane polarity by pumping 3 sodium ions out of the cell for every 2 potassium ions to enter [36].

Most commonly, neurons have a membrane resting potential of  $\sim -70\text{mV}$  [73]. This potential is due to the potassium and sodium ion concentrations within the cell cytoplasm and outside in the cell media. Within the cell, there is a higher concentration of potassium ions than sodium ions. Outside the cell, there are higher concentrations of sodium ions. Although both ions are positive, sodium/potassium ion pumps are “leaky” [36], which allows some potassium ions to leave the cell. This biased leaky flow of ions creates a more ionically positive cell exterior compared to the cell interior, which results in the  $-70\text{mV}$  resting potential across the membrane.

If a stimulus triggers an action potential, this disrupts the membrane potential from  $-70\text{mV}$ . If the stimulus raised the membrane potential to or beyond the gating threshold voltage of  $\sim -55\text{mV}$ , the voltage gated sodium ion channels

open [36]. This introduces more positive ions to the cell interior, which raises the membrane potential above the threshold. The neighboring sodium ion pumps also open in response to the voltage change, and induce other sodium ion pumps to open down the axon. This is known as depolarization of the membrane since the potential across the membrane approaches 0mV. Also, depolarization overshoots equilibrium to around ~30mV [36]. Immediately following the sodium ion surge into the cell, the potassium ion pumps open in attempt to reestablish the -70mV resting potential by pumping the positive potassium ions out of the cell at a threshold voltage of ~30-40mV. This is the repolarization phase of the action potential, which as with the depolarization over shoot, the repolarization also overshoots the resting potential as hyperpolarization. After hyperpolarization, the sodium/potassium pumps pump sodium ions back out, and potassium ions back in to establish the -70mV resting potential.

## **1.7 Lab background literature review/ Biomechanical properties of neurons**

It is critical to our understanding of the biological world to treat cells as complex systems of protein based biopolymers so we can explore their properties with soft condensed matter physics. We know mechanical interactions between cells and their substrates play an integral role in the processes that control

neuronal growth and behavior. The properties of the cell's natural environment play a key role in their mechanics and behavior. CNS and PNS neurons grow from significantly different environments and this affects their physical properties. CNS tissue is relatively soft, and protected from impact by the glia, the cranium, and spine. PNS neurons, however, live in stiffer environments and are subject to more stresses. Due to environmental differences, CNS and PNS neurons behave very differently on soft and stiff substrates. CNS neurons, mainly cortical neurons, have low stiffness compared to other cell types in vivo [4, 46, 76, 77] and are highly sensitive to external stimuli [9, 21, 31, 76]. This is most likely due to their very soft natural environment. It is also important to note that stiffness measurements by AFM on single cells are load rate dependent, meaning indentation speed relates to elastic modulus through the viscoelastic time dependence of cytoskeletal rearrangements under load.

Additionally, a growing neuron must modulate its cytoskeleton and transport cytoskeletal components to facilitate growth. Growth is controlled through multiple chemical pathways by chemical ECM and topographic cues [8-16]. These cues activate signaling pathways within the cell and induce polymerization or depolymerization of regions of the cytoskeleton [8, 15, 16, 78, 79]. In particular, topographic cues such as micro ridges, plateaus, periodic geometric features, gradients, and nanopillars affect cell shape, outgrowth rate, and outgrowth directionality.

### *Temperature Response of the Cytoskeleton [45]*

Understanding the cytoskeletal temperature dependence of neurons can reveal valuable information on cytoskeletal structure, support mechanisms and their elastic moduli [37, 80, 81, 82]. Different cell types have had their stiffness measured at 25°C [45, 46, 83, 84, 85], however, physiological temperature effects cannot be ignored [45]. Atomic Force Microscopy combined with cytoskeletal fluorescent tagging showed there is an increase in elastic modulus at temperatures below 37°C [45]. Reviewed here, Spedden [45] shows the increased stiffness at 25°C is due to contractile actomyosin dynamics that are responsible for the temperature response, and normal physiological stiffnesses at 37°C are due to microtubule dynamics. Thus at temperatures lower than 37°C, contractile forces between myosin II and actin filaments reduce  $\xi$  and lead to the reported increased stiffness. Here, Spedden used the high spatial resolution of the AFM to map the temperature dependence stiffness of neurons to correlate cytoskeletal components with stiffness to reveal the underlying mechanisms that control the cytoskeletons mechanical response to temperature changes in vitro [45].

Reproducibility of temperature dependence is important to show that temperature effects are reversible and do not damage cell components. It is also important to determine the stability and structure of the cytoskeleton. To show



this, repeated AFM elastic measurements were acquired over the same cell at 37°C, reduced the temperature to 25°C, then raised it again to 37°C and repeated the measurement while simultaneously checking that the cell was not actively growing or retracting. The results show a variation in elastic modulus of under ~10%. An excellent example of elastic modulus and temperature are shown for 37°C, 31°C, 25°C, 31°C, 37°C, and 31°C (Figure 1.12), where the cell was held at a temperature for ~10 minutes to negate transient temperature effects. This is the first paper to show the natural temperature response of cortical neurons [45].

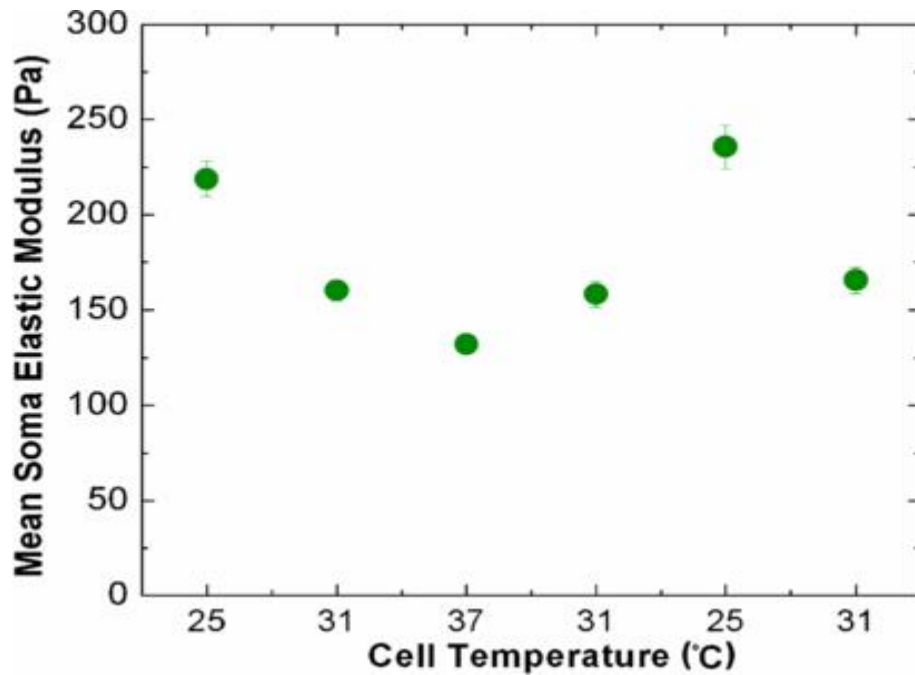


**Figure 1.12** Temperature recovery response of neurons shows neuronal cytoskeletal dynamics fully recover after heating and cooling [45].

To determine what biopolymers and molecular motors were responsible for these cytoskeletal changes, the neurons were treated with a variety of

cytoskeletal dynamic stabilizing or inhibiting drugs that target microtubule dynamics or actin dynamics. Cells were treated with three drugs at 25°C and 37°C to delineate microtubule and actomyosin dynamics. Blebbistatin is a Myosin II inhibitor and thus effects contraction of the actin cytoskeleton [56, 76, 86, 87]. Y-27632 is another Myosin II inhibitor, however it inhibits the downstream Rho A GTPase signaling molecule ROCK 1 [7, 58-61]. Taxol, a microtubule stabilizing drug, was used to inhibit microtubule dynamics by interfering with microtubule aggregation and temperature dependent flexural rigidity [61, 88-92].

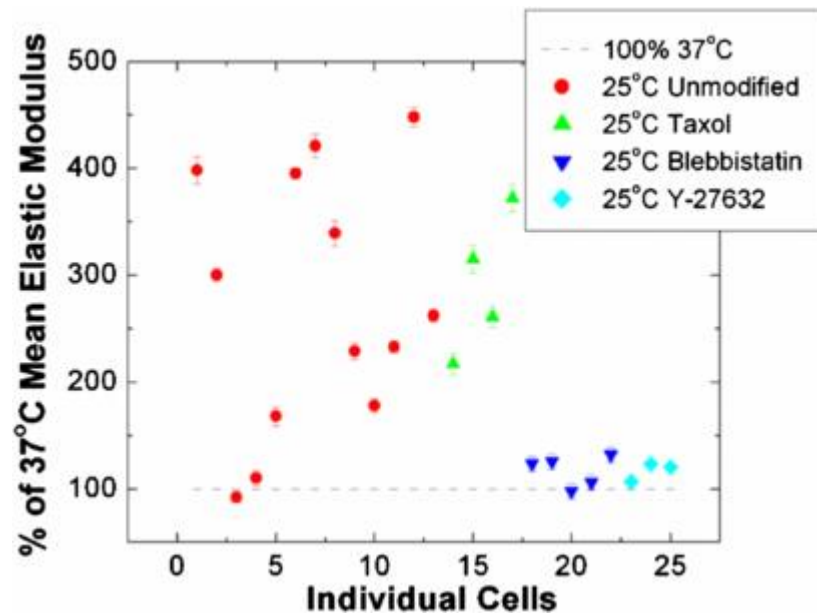


**Figure 1.13** Percent change of mean neuron elastic modulus from 37°C after drug treatments. Red circles indicate unmodified cells at 25°C, green triangles indicate taxol treatment at 25°C, blue triangles indicate Blebbistatin treatment at 25°C, and blue diamonds indicate treatment with Y-27632 at 25°C [45].

Figure 1.13 shows the percent difference in elastic modulus for cells at 25°C compared to 37°C for each drug. Untreated neurons at 25°C showed a large increase in stiffness up to 4 times higher than at 37°C. Taxol treated neurons at 25°C interestingly showed little difference compared to the untreated neurons. This indicated the microtubule cytoskeleton does not rearrange or change much at lower temperatures. However, both Blebbistatin and Y-27632 almost eliminate the temperature response in elasticity, and are nominally higher than untreated neurons at 37°C. This alludes to the fact that Actin dynamics dominate the cytoskeletal elasticity change at lower temperatures. Since Blebbistatin directly interferes with Myosin II, and Y-27632 interferes with the ROCK pathway that controls actomyosin contraction and actin depolymerization, it can be inferred that Myosin contraction at temperatures below 37°C causes the stiffening.

To directly show that elastic temperature dependence is intimately related to cytoskeletal arrangement combined AFM and fluorescent tagging of the Actin and Microtubule cytoskeletons were performed at both 25°C and 37°C for untreated neurons. The results (Figure 1.14) show a distinct correlation with cytoskeletal components and their density determined by fluorescent intensity. Untreated neurons stained for tubulin at 37°C show a distinct correlation with stiffness and tubulin density, where at 25°C, it is less apparent that it is only due to microtubules. Neurons stained for Actin show an obvious stiffness vs actin density correlation at 25°C. This correlation between actin density and stiffness reduces at 37°C. Actin and Tubulin staining of the same cell was compared to

AFM stiffness measurements at 25°C and 37°C. This showed a high correlation of stiffness to tubulin density at 37°C and a high correlation of actin density and stiffness at 25°C.

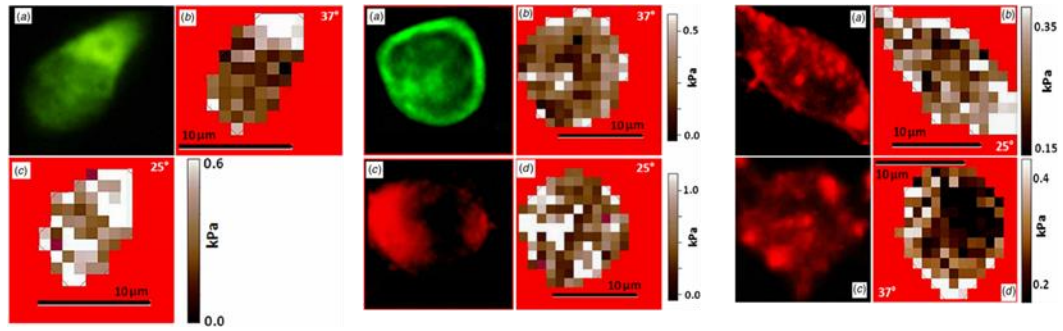


**Figure 1.14** Combined AFM/Fluorescent Imaging. Green is  $\beta$ -III Tubulin stain, Red is Actin stain. Left, tubulin stained neuron with corresponding elasticity maps at 25°C and 37°C. Middle, Taxol and Blebbistatin treated neurons at 25°C and 37°C. Right, Blebbistatin treated neurons at 25°C and 37°C with corresponding force maps. Dark points indicate softer areas than lighter points [45].

These results illustrate the cytoskeletal dependence of different biopolymers at different temperatures. At 37°C, the microtubule cytoskeleton contributes the most to cellular stiffness and support. However, at 25°C, contractile actin and myosin II interactions dominate the elastic properties of the cell. Importantly, this study also shows that temperature induced cytoskeletal changes are reversible and do not appear to affect cytoskeletal health.

### *Growth and Cell Stiffness [44]*

To grow and reach a synaptic target the neuronal growth cone must advance by a biased random walk and wander its environment in response to variations in its landscape. To do this, the microtubule cytoskeleton must rearrange and order itself in the soma, axon hillock, and axon to promote extension of the axon. These rearrangements are caused by substrate-cell coupling that allow the cell to exert traction forces on its surroundings to move [61, 76]. Multiple experimental methods, such as traction force, optical tweezers, magnetic tweezers, microneedle pulling, and AFM, have been used to apply forces on cells and explore how they affect outgrowth [4, 9, 41, 46, 62, 83, 85, 92, 93, 94]. Cell mechanical properties have been shown to have a significant impact on cell function and mechanosensitivity [4]. Studies have shown CNS neurons are less sensitive to substrate stiffness than PNS neurons [76, 92], most likely due to their environments). Combining AFM and fluorescent cytoskeletal tagging can correlate cytoskeleton density, in this case, tubulin density, with fluorescent intensity and AFM stiffness maps of cells. Reviewed here, Spedden [44] performed AFM elasticity measurements on three neuronal cell types, Dorsal Root Ganglia neurons (DRG), P19 embryonic carcinoma neurons (P19), and embryonic rat cortical neurons to compare their mechanical properties to their cytoskeletal arrangements. PNS neurons appear to be stiffer than CNS neurons (DRG>P19>cortical neuron stiffness) when comparing the stiffest 10% of force

curves over the cell. The middle 30% show the same trend within error, however the bottom 10% are virtually the same stiffness [44]. However, P19 neurons are similar to cortical neurons in the magnitude of their stiffness.

Since these three types of neurons exist in environments with different chemical and mechanical properties, it is important to check whether ECM has an effect on cell stiffness. Previous studies have shown that outgrowth of PNS neurons are more sensitive to substrate stiffness than CNS neurons, and that ECM can have a profound effect on the cytoskeleton [8, 46, 94] by altering adhesion dynamics. Spedden compares the three neuronal cell types used with the three most common ECM, Poly-D-Lysine (PDL), Laminin, and Fibronectin. Interestingly, ECM coating did not have a significant effect on cells stiffness, though it should be noted that the top 10% of stiffest points for a given cell could widely vary even on the same ECM coating. Since the variation is minimal, all cell types were measured on PDL coated glass surfaces.

Significantly, cell stiffness changes at 37°C depend on whether the neuron is “active” or “inactive”, or whether it is actively extending neurites or not, respectively [44]. To determine whether neurite growth activity affects cell stiffness and where, bright field optical microscopy images were taken before and after force maps. If the bright field image showed a significant change in shape or neurite extension, that neurite was deemed “active”. If the neuron appeared the same, it was considered “inactive”. Active neurites displayed an increase in

stiffness at and close to the axon hillock, indicating increased microtubule activity is critical to outgrowth. Also, after the growth phase ends, additional force maps of the cell show that the stiffness reduces back to the inactive state. This lends to support the idea that stiffness increases accompany neurite outgrowth.

Since neurite activity and stiffness are so intimately related, interfering with tubulin dynamics should inhibit this activity. The drugs Taxol and Nocodazole are used to treat the neurons. Cell stiffness is measured prior to treatment with Taxol or Nocodazole, and repeated after. Nocodazole appears to kill the cells, however the cells that survive showed no major difference from before treatment [44]. Taxol treatment showed the same tubulin activity near the axon hillock, but was not accompanied by neurite extension, showing that Taxol only disrupts microtubule growth.

Actomyosin plays a significant role in neuronal movement [9]. To determine whether the increase in stiffness is due to axonal tension from growth cone traction, Blebbistatin was used to treat the cells. Since Blebbistatin inhibits Myosin II activity and since Myosin II is responsible for actin dynamics, its disruption should show a clear increase of outgrowth since Myosin II activity counters actin retrograde flow. Interestingly, cells grown with Blebbistatin show a 20-55% increase in stiffness when active, which is the same as the median change of nontreated cells. This shows that Microtubule aggregation is responsible for the stiffening rather than axonal tension [44].

### *Effects of Surface Asymmetry on Neuronal Outgrowth [7]*

To study the influence of surface topography and texture on neurite outgrowth, particular growth cone sensing, Spedden [7] cultured neurons on novel PDL coated nanofabricated surfaces (reviewed here). The surfaces were composed of oblique angle deposition poly(chloro-p-xylene) (nano-PPX) [95]. This fabrication method results in nanorods that are tilted from the normal direction of the deposition substrate [95-98]. The nanorods clump into bunches that form a cross sectional ratchet structure. The ratchet structure is characterized by two angles (Figure 1.15) whose ratios denote ratchet asymmetry and orientation [7]. Different nanorod tilt angles resulted in different ratchet structures, with varying heights and frequencies that determine neuronal growth directionality [7]. The ratchet geometry has anisotropy defined by the anisotropy parameter,  $C_\alpha$ . The anisotropy direction was defined as:

$$C_\alpha = \frac{\alpha_\pi}{\alpha_0} \quad (1.5)$$



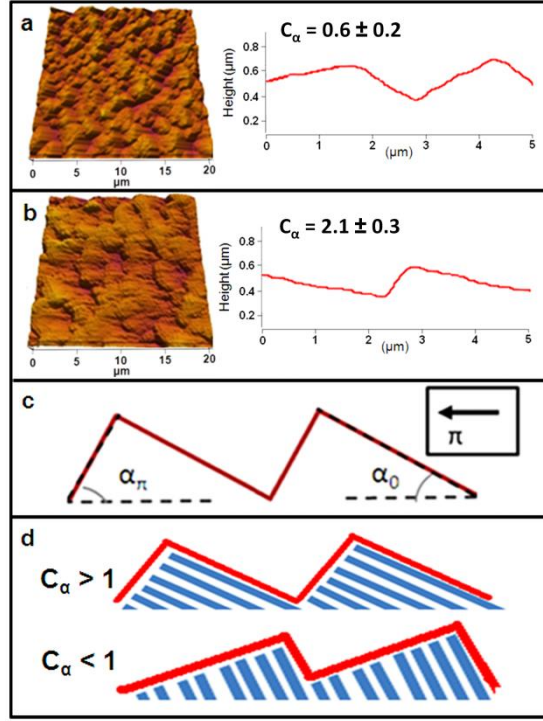


**Figure 1.15** AFM topography of Nano PPX and Nano PPX Cross Section.

Top a and b, AFM topography image with corresponding characteristic cross section of Nano-PPX. c and d define ratchet orientation to nanorod tilt [7].

Here,  $\alpha_\pi$  is the angle between nanorod tilt and the surface, and  $\alpha_0$  is angle between the opposite slope and the surface [7]. And denoted by the direction  $\pi$ .  $C_\alpha > 1$  corresponds to ratchets with the same orientation as the nanorods,  $C_\alpha < 1$  corresponds to ratchet orientations opposite to the nanorod tilt direction, and  $C_\alpha > 1$  corresponds to symmetric ratchets [7]. Neuronal growth cones navigating on these surfaces will feel an effective torque that promotes biased growth directions, such as in the  $\pi$  direction.

Neuronal directionality relative to this anisotropy direction was measured through fluorescent staining, to contrast the neurons from the opaque nano-PPX surface. The neurites were broken into  $\sim 20\mu\text{m}$  segments (31.25 pixels with a 10x objective) and their angular distributions were compiled into histograms. Neurons were grown on seven different PDL coated nano-PPX surfaces with different  $C_\alpha$  parameters between  $\sim 0.6$  and  $\sim 3.0$ . Interestingly, neurons displayed increasing direction growth bias when grown on surfaces with higher  $C_\alpha$  parameters. Generally, growth peaks at  $\pi$  and 0 radians for all surfaces. However, higher  $C_\alpha$  parameters begin to bias growth in the  $\pi$  direction due to the ratchet tilt direction (Figure 1.16). Distributions were fitted to extract the effective diffusion constants for each surface.

Taxol and Blebbistatin were used again to determine the role of microtubules and F-actin in navigation and outgrowth [7]. Taxol treated cells showed little substrate dependent directional growth [7]. Similarly, Blebbistatin treatment showed a decrease in surface dependent directional growth [7]. However, Blebbistatin treated cells showed a significant increase in outgrowth and neurite connections, most likely due to reduced Myosin II actin treadmilling that results in uninhibited growth from actin polymerization at the filopodia and lamellipodia fronts [7]. This shows that the microtubule and actin cytoskeletons play an important role in neuronal response to topographic cues.

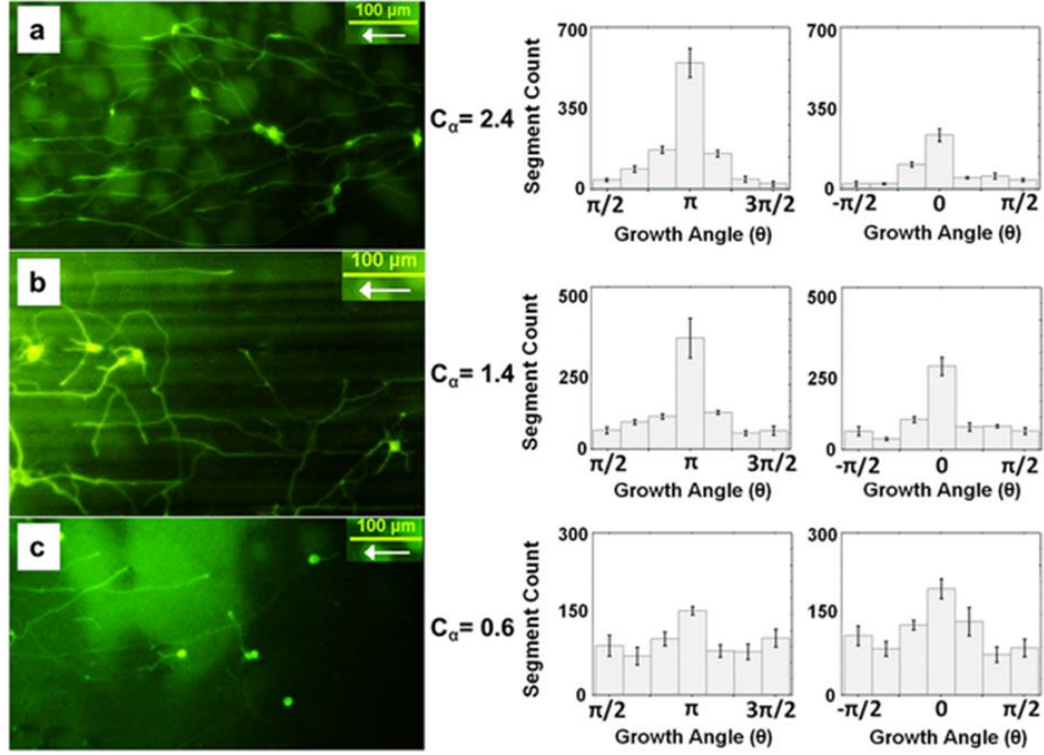


**Figure 1.16** Left, Fluorescent images of neurons on nano-PPX surfaces. Right. Corresponding non-normalized angular distributions (20 μm segments) [7].

Previous studies have shown neurons grown on nanopillar surfaces show increased neurite branching behavior, motility, cell-substrate adhesion, and growth speed [51, 99, 100]. Additionally, previous studies reported dependence between topographic feature size, cell size, and importantly, growth cone size [27, 33, 44, 52]. These results indicate curvature dependent effects of neuronal guidance that increase the grouping density of focal adhesions [6, 44]. Spedden suggests that the directional bias from the surface asymmetry is due to increased stresses within the growth cone as it encounters the steeper edge of a feature since

the growth cone must exert larger forces to accommodate the bending of filopodia invading microtubules. Higher traction forces also expose more actin binding sites in Talin [57], which reinforces focal adhesion connections.

### *Conclusion*

Neurons are highly dynamic cells that modulate their cytoskeletons to interact with their surroundings. The cytoskeleton is a biopolymer network that gives the cell its structural properties and is the generator of cell motility. Cytoskeletal properties can be deduced by AFM measurement and lend insight into the mechanisms that modulate the cytoskeleton. Cytoskeletal modulations are controlled by the Rho-GTPases and are the major influence on pathfinding behavior. Neuronal pathfinding can be characterized using a stochastic framework to uncover the underlying mechanisms of neuronal pathfinding.

## **CHAPTER II**

### **Atomic Force Microscopy**

#### **2.1 Overview**

Atomic Force Microscopy (AFM) is a form of scanning probe microscopy that utilizes a cantilever with a sharp tip, called a probe, anywhere from a few angstroms to tens of microns in radius. The AFM rasters the probe over a surface to physically probe and detect the nanoscale topography/surface features of a sample via atomic forces. The detection of atomic forces is done by monitoring cantilever deflections that result from the close range interaction forces between tip and sample. The cantilever can be deflected toward or away from the sample by electric forces and quantum effects or even twist as a result of frictional forces.

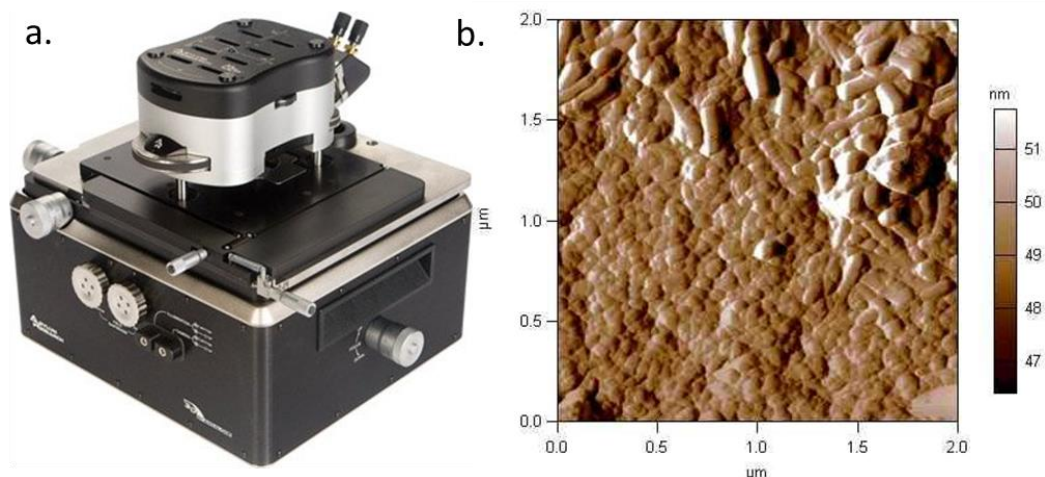


**Figure 2.1** *a. An Asylum MFP-3D atomic force microscope showing the scan head resting atop the XY scanner and controller [101]. b. An AFM topography scan of a silk nanofiber layer on glass. Brighter areas are taller than darker areas. The scale is 46-52nm.*

AFMs can operate in vacuum, gaseous, and liquid environments which makes them highly versatile. AFMs have the ability to measure sub-nanometer features in the vertical axis, and nanometer resolution in the x and y axes. Due to its mechanical nature, AFM is not bound by any diffraction limit and has much higher spatial resolution than traditional optical methods, which give it the ability to achieve atomic resolution. Not only can AFM be used to scan the topographic surface of an object, it can be used to detect surface charge and potentials, physically manipulate objects by pushing and pulling them, and perform nanolithography and nanomachining. These abilities make AFM an

extraordinarily versatile tool for biophysical research, allowing researchers to probe the 3D morphology and mechanical properties of biological samples.

When discussing AFM, it is good to be familiar with the output topography images. Figure 2.1b shows a typical AFM topography scan of a silk protein layer on glass, with the scan area being x and y coordinates, and the height as detected by AFM is the color scale. Scan sizes can vary from  $100 \times 100 \mu\text{m}^2$  to, realistically,  $\sim 100 \times 100 \text{nm}^2$ . Here, the color scale goes from dark to bright, or low to tall respectively.

#### *The Lennard-Jones Potential*

$$V_{LJ} = 4\varepsilon \left[ \left( \frac{\sigma}{r} \right)^{12} - \left( \frac{\sigma}{r} \right)^6 \right] \quad (2.1)$$

An AFM is able to detect sub nanometer features by detecting the deflections of the cantilever as it interacts with the surface at particular spatial coordinates. The interaction between the probe and surface is a combination of electrostatic attraction and repulsion and Pauli Exclusion. The resulting interaction potential is known as the

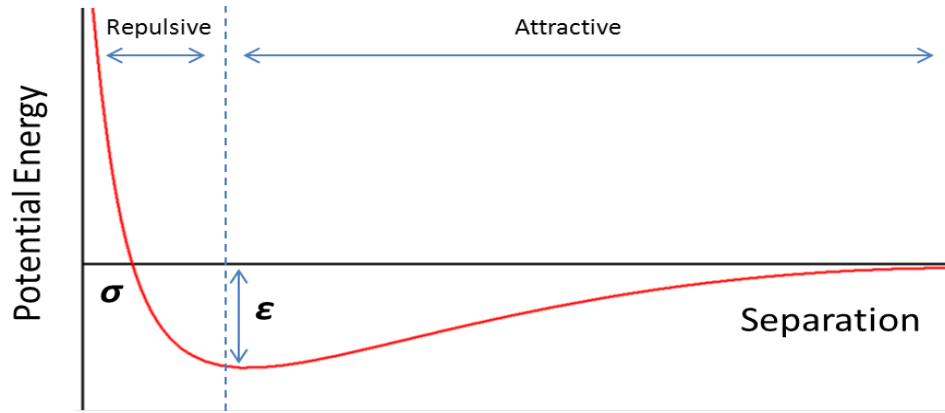


**Figure 2.2** Lennard-Jones Potential in arbitrary units. The horizontal axis is tip-object separation and the vertical axis is interaction potential. Separation is tip-sample separation (usually in angstroms),  $\sigma$  represents the position-potential energy intercept, and  $\epsilon$  represents the potential well minimum. The dotted line divides the attractive (right side) and repulsive (left side) regimes of the interaction potential at the potential well minimum. A separation of exactly zero is impossible due to Pauli Exclusion as it would require infinite energy.

Lennard-Jones Potential  $V_{LJ}$  (Eq 2.1 and Fig 2.2), where  $r$  is tip sample separation  $\sigma$  represents the position-potential energy intercept, and  $\epsilon$  represents the potential well minimum. As an electrically neutral probe tip and an electrically neutral surface are brought close together, a steadily increasing attractive force attracts the cantilever through instantaneously induced dipoles of the atoms in both the probe and sample. As they are brought very close together (a few angstroms), the probe and sample begin to repel, due to Pauli Exclusion affecting the electrons. The resulting force would follow  $F(r) = dV_{LJ}/dr$ .



Repulsion due to close proximity of the atoms results from the antisymmetric wave functions of fermions, as shown by Eq 2.2, where  $\Psi_1(A)$  and  $\Psi_2(B)$  are the wave functions of two indistinguishable particles, in spatial states A or B. The total wave function of two interacting fermions  $\Psi(A, B)$  must be zero when  $A=B$ , since  $\Psi_1(A)\Psi_2(A) = -\Psi_2(A)\Psi_1(A)$ . Additionally, two interacting fermions pushed into the same orbital must be paired with an electron of opposite spin, if the orbital allows the occupancy, similarly to equation 2.2.

$$\Psi(A, B) = \frac{1}{\sqrt{2}} [\Psi_1(A)\Psi_2(B) - \Psi_2(A)\Psi_1(B)] \quad (2.2)$$

The Lennard-Jones potential can be best visualized using two interacting hydrogen atoms and measuring interaction potential vs nuclear separation. Each hydrogen atom consists of one electron electrically bound to one proton. Since the proton is much more massive than the electron, the proton can be chosen to be the center of the atom. If two hydrogen atoms are held very far away from each other, there is no interaction. As they move closer and closer, the electron in one hydrogen is repelled by the other electron, one proton is repelled by the other proton. Since the protons are stationary relative to the electrons, and the electrons are free to move, and the hydrogen atoms form instantaneous dipoles whose magnitudes increase with decreasing nuclear distances. However, once the two hydrogens come too close together, the electrons are confined and forced into very similar quantum states, and begin to repel through Pauli Exclusion since the two electrons cannot occupy the same spatial and spin states, causing one

hydrogen dipole to switch polarity. This unshields the charge effects from the protons, and they electrostatically repel. By pushing the two hydrogens even closer together, the protons begin to repel each other through the same forces, electric repulsion, and spin interactions. This repulsive force increases very rapidly over 1 angstrom. This combination of electrostatic attraction, repulsion, and Pauli exclusion create the profile of the Lennard-Jones potential. The interaction between AFM tip and sample involves many atoms and atoms of higher atomic number than hydrogen. This is much more complicated to model than two interacting hydrogen atoms, but allows us to experimentally measure forces between the tip and sample by taking advantage of the different regions of the Lennard-Jones potential.

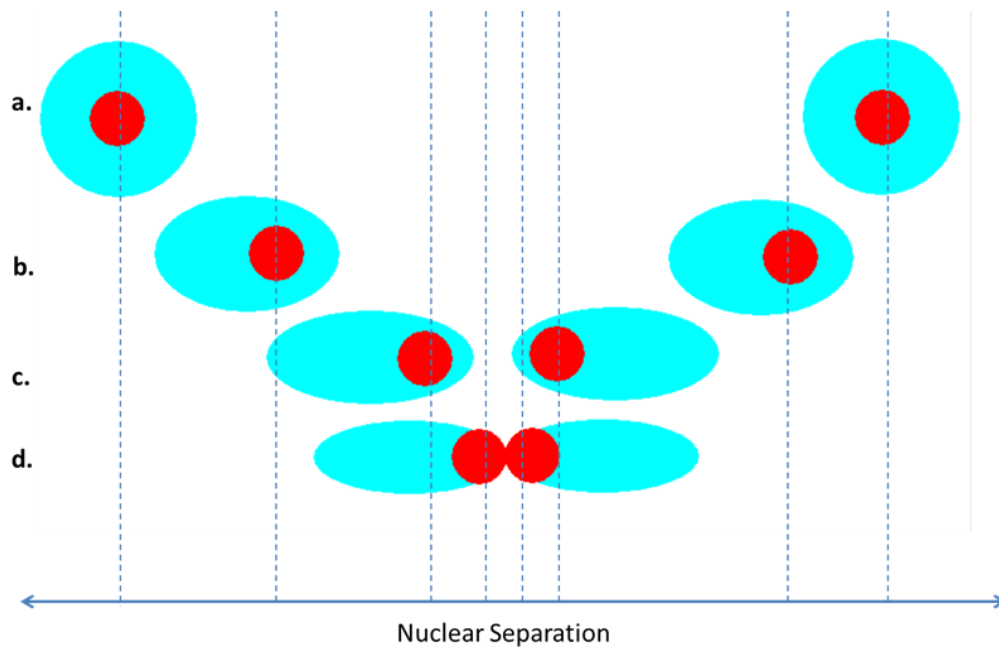


**Figure 2.3** *Two Hydrogen Atoms interacting via electrostatic forces and Pauli Exclusion. The red circles are protons, and the blue circles/ellipsoids are the electron clouds. a. At large nuclear separations, there is no interaction. b. As the protons are moved closer together, the electron clouds move and form attractive dipoles. c. At closer distances, the electron clouds repel due to electrostatic interactions and Pauli exclusion. d. At incredibly close distances between the protons, the electrons cannot exist between protons due to Pauli exclusion, and the protons seem unshielded to each other and repel electrostatically.*

## **2.2 Parts of an AFM**

A basic AFM system has two main physical units, the “head” and the “scanner”. These are made of four main operational parts: A flexible probe, and deflection detection system, a nanopositioning system, and a feedback system. On most AFMs, the scanner is the nanopositioning system (and could be located in the head) and the head which contains the probe and deflection detection system (figure 2.4). AFMs come in many configurations, so the head and scanner on one AFM could be one physical part, and the same parts on another AFM might be two separate parts. Therefore, it is better to think of the AFM as four operational parts rather than two physical units.

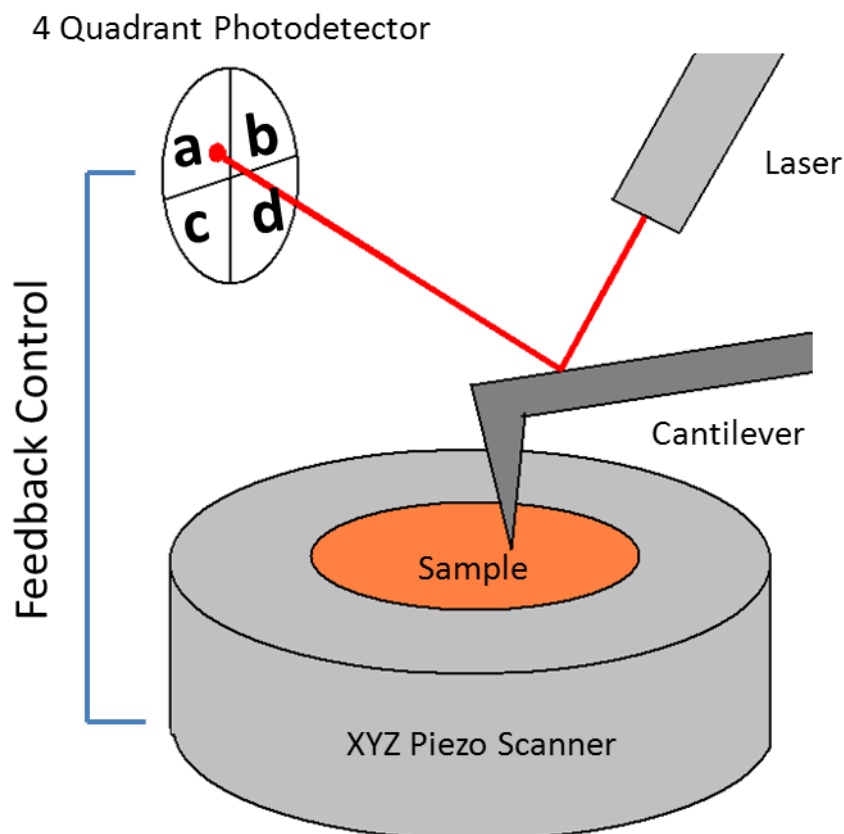


**Figure 2.4.** AFM diagram showing the probe (cantilever plus tip) the cantilever deflection system (photodetector plus laser), the feedback control, and the Nano positioning system (XYZ piezo scanner). Here, for example, the laser dot is in the a quadrant. However, in a real AFM system, the laser dot would be large and always be in all four quadrants to some degree. The laser dot may also not be symmetric.

## *The Probe*

The AFM probe is generally made of a silicon beam with known crystal plane orientation and reflective backside (aluminum) and a sharp silicon tip (figure 2.5). AFM probes can also have a variety of coatings that make them electrically conductive or insulating, more reflective, wear resistant, and even chemically functionalized. The beam can range from 50-400 $\mu\text{m}$  in length 30-50 $\mu\text{m}$  wide, and 0.5-10 $\mu\text{m}$  thick, and can vary widely in shape, from a “V” shape, to a simple rectangle. “V” shaped cantilevers are usually used in application that require measurement in fluid. Rectangle shaped cantilevers are better suited for dry measurements than wet due to hydrodynamic turbulence from fluid loading/dampening. The tip is usually made of the same material as the cantilever, though they can be different. Silicon probes can also be plain or come with special coatings such as silicon nitride, diamond, and aluminum. Tip geometries vary widely, depending on application, from blunt pillars, sharp cones, pyramids, and spheres/colloids. Cantilevers must be calibrated or tuned before certain applications, such as any oscillatory mode or a mode that requires quantitative force readings. The values of these are difficult to predict during manufacture because of small inconsistencies in cantilever geometry. In the case of a rectangular cantilever, small deviations in thickness, width, and length have the greatest effect on frequency and spring constant.

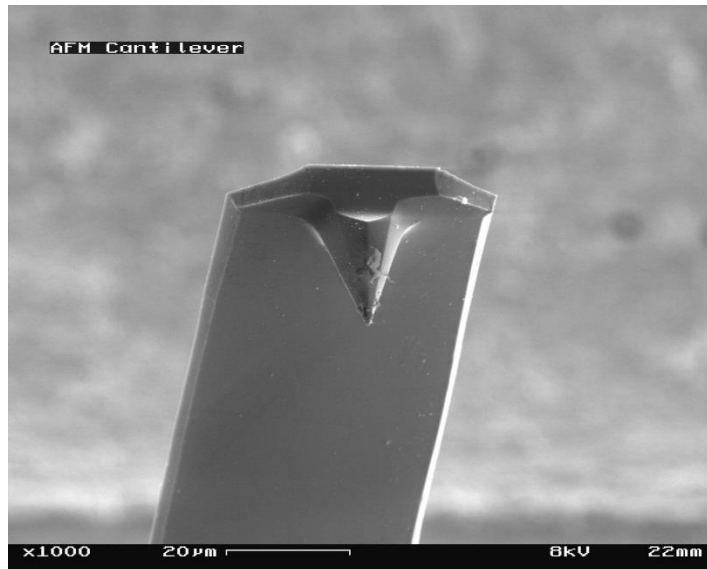


*Figure 2.5. A typical AFM cantilever and tip imaged by SEM. 20µm scale bar [102].*

### *The Nano-positioning system*

The nanopositioning system, or scanner, allows the relative XYZ motion between the probe tip and the sample being measured. The scanner configuration can utilize combined XYZ, or separate XY and Z scanners. To precisely move, the scanner uses materials that change shape with applied voltage, called piezoelectric materials. These materials change their interatomic spacing by the electrostatic force which polarizes the material under mechanical deformation, or mechanically deforms under induced polarization of the material. The scanner used high voltage low noise piezoelectric materials to accurately position the

sample and tip with piezo actuators, flexures, and tubes. The XY system moves the sample with relation to the tip in a rastering fashion. Due to tip geometry the XY, there is a maximum resolution of about 10-30nm on average that can be achieved in the XY. This uncertainty in XY position is acceptable considering scan dimensions are taken in the 1-90 $\mu$ m range. Unlike the XY scanner, the Z scanner needs much higher resolution of about 0.1nm to detect atomic features.

### *The Deflection Detection System*

During a scan, the deflection detection system detects cantilever position by reflecting a laser beam off the backside of the cantilever into a four-quadrant photo detector. The position and shape of the beam on the photodetector quadrants determine the cantilever position by comparing the voltage differences between the quadrants. A four quadrant photodetector is broken into the a,b,c, and d quadrants (Figure 2.4) which correspond to top left, top right, bottom left, and bottom right respectively, by convention. The voltage difference between a+b and c+d is the vertical error signal for the AFM. The deflection signal  $\delta'$  is as follows:

$$\delta' = \frac{(a + b) - (c + d)}{(a + b + c + d)} \quad (2.3)$$

This is the main signal used to compile an AFM image (a similar way is used for lateral AFM by substituting the numerator of Eq.3 with  $(a+c)-(b+d)$ ). The difference between  $a+c$  and  $b+d$  is the lateral error signal. This measures the lateral displacements of the cantilever, which arise from torsional flexing of the cantilever. The total  $a+b+c+d$  is the Sum, which is a measure of cantilever reflectiveness and photodetector positioning. Thus, Eq3 is the normalized signal.

*The Feedback system (with Constant Deflection Mode Example)*

The AFM feedback system ensured tip sample contact to be held at a constant force, height, or oscillation amplitude (discussed latter). During a simple contact mode scan, the tip is brought into contact with the sample with the Z scanner. As the Z scanner extends the tip into the sample, it is repelled by Pauli exclusion, and the cantilever bends. Since the cantilever deflections are very small, the force exerted by the cantilever on the sample can be accurately approximated to Hooke's Law. If the Z scanner was held at a constant position during the scan, the cantilever deflections would vary with the surface but also exert higher forces under larger deflection. This can result in poor image quality and high tip wear. Thus the cantilever is generally held at a low deflection (constant force) by the Z piezo to increase tip longevity and improve scan quality. This also has the benefit of allowing the Z scanner position to accurately reflect the true 3D topography of the sample. To accomplish this, cantilever deflection



must be compensated for with the Z scanner. To control the sensitivity of the feedback system, it is adjusted with a parameter called Integral gain, which adjusts the rate of correction between the deflection detection systems error signal and the Z piezo. A low integral gain could result in poor surface tracing during a scan, and an integral gain that is too high could result in amplification and distortion of ambient mechanical and electric noise, or even create it and amplify it.

## **2.3 Modes of Operation**

AFM can measure the topography of a sample in two basic ways, contact and noncontact. Since the notion of contact at the nanoscale level is difficult to define since it widely varies over a few angstroms, contact is defined by a parameter called the set point and is usually set within the repulsive regime of the Lennard-Jones potential. This is a user defined value of a photodetectors vertical error signal which commands the AFM to stop lowering the tip to the sample once a particular deflection or amplitude is achieved. Contact occurs within the repulsive regime of the Lennard-Jones potential, and non-contact occurs in the attractive regime (Figure 2.2).

### *Contact Mode*

Contact AFM operates within the electrostatic repulsive and Pauli regime of the Lennard-Jones Potential with an upward cantilever deflection. Forces between tip and sample follow Hooke's Law

$$F = -k\delta \quad (2.4)$$

for force  $F$ , spring constant  $k$ , and small deflections  $\delta$ . In this mode, the tip is physically stopped by the sample, sometimes to the point of deforming the sample or tip. Contact AFM can be achieved in constant deflection mode or in oscillation mode. In constant deflection mode, the cantilever is brought into contact with the surface and simply dragged across it in a raster pattern while the Z feedback control maintains the constant deflection. This method has the potential to damage the sample surface and quickly wear the cantilever. In the oscillation mode, the cantilever is shaken at its resonant frequency and the amplitude of oscillation is measured by the deflection detection system and the Z feedback loop maintains constant amplitude. This also has the added benefit of being more sensitive to small forces, thus raising resolution. When the cantilever makes contact, its amplitude is slightly lowered from its free amplitude. As the tip rasters over the

surface, it lightly taps it (intermittent contact) at the probes fundamental frequency and measures the surface.

### *Non-Contact AFM (attractive)*

Non-contact AFM operates within the long range electrostatic attractive regime of the Lennard-Jones potential with a downward deflection of the cantilever. This is considered the most “gentle” form of AFM since the tip and sample ideally never touch (enter the repulsive regime). As with contact AFM, the surface can be measured with a constant deflection mode and a constant amplitude mode, but unlike contact mode AC operation, the cantilever frequency is not constant, and changes based upon the tip/surface interaction potential. This method is highly sensitive and has the ability to resolve atomic arrangements in molecules bound to a substrate.

### *Probe Dynamics and Beam Theory*

As stated above, the AFM probe is a cantilever outfitted with a sharp (sometimes spherical) tip. The tip becomes trapped in a Lennard-Jones potential well when it is brought within ~1nm of the sample surface which causes it to

deflect. The deflection allows for the quantification of forces between the sample and probe. For a probe with a rectangular cantilever and small deflections the resulting force between sample and probe can be approximated using Hooke's Law. The cantilever spring constant  $k$  is related to the cantilever's elastic modulus  $E$ , the cantilever length  $l$  and moment of inertia  $I$ , by [103]

$$k = 3 \frac{EI}{l^3} \quad (2.5)$$

The cantilever fundamental frequency of oscillation is related to its spring constant [103]:

$$f_o \sim \sqrt{\frac{k}{m_{cantilever} + m_{tip}}} \quad (2.6)$$

Here,  $f_o$  represents the probe's fundamental frequency of oscillation,  $m$  represents mass (of the cantilever or tip defined by subscripts). This allows AFM to use the maximum sensitivity of the cantilever at resonance to topographically image the surface. Interestingly, it also allows for an AFM user to precisely measure the mass of objects picked up by the cantilever if one knows the position of the object on the cantilever by the change from the fundamental frequency.

## 2.4 Calibration and Operation

### *Tuning the cantilever*

Since the cantilever's spring constant varies wildly with very small geometric deviations for a given cantilever type, each cantilever must be tuned to its resonant frequency before use in oscillatory measurements. This is done experimentally by shaking the cantilever over a frequency range repeatedly, and identifying the largest peak in amplitude. This can be done by a variety of mechanisms, from shaking the cantilever with piezos to rapidly heating and cooling the cantilever with lasers. This can also be accomplished through two methods: the thermal method, and the Sader method (see Force Calibration).

### *Force Calibration*

To quantify the interaction forces between probe and sample, the cantilever must be calibrated. This is ideally done on a very hard surface to minimize tip-sample indentations (see below) which creates error in the calculation of the cantilever spring constant. The curve produced is commonly called a force curve. Although force curves are ultimately from the Lennard-Jones

interaction, AFM force curves look slightly different, and have four main parts constructed from an approach curve and a retraction curve. In Figure 2.6, The curve regions are produced during measurement as follows: a to b, b to c, c to d, d to e, then e to a. a to b is the zero force approach where the cantilever experiences no flexing. b is the region of “snap down”, where the cantilever is rapidly attracted to the surface through electrostatic attraction and sometimes capillary action due to a thin water layer that is present in atmospheric conditions (this can be eliminated by performing measurements in an appropriate fluid for the application. The region from b to c is in the repulsive contact region, where the cantilever follows Hooke’s Law for small deflections. c to d is the retraction curve (where the cantilever stays attached to the surface due to adhesion forces until a critical force is reached to break adhesion), where at e, the tip lifts from the surface and returns to its equilibrium position. From e to a, the cantilever still experiences no deflection until the curve acquisition process has ended. Ideally, the attraction and retraction curves should overlap between a and b and c and d. The area bound by the difference of the curves is the adhesion energy between the tip and sample surface (most likely due to atmospheric water). During a force map, one of these curves is performed over each point of an NxN force curve grid at a set scan size.

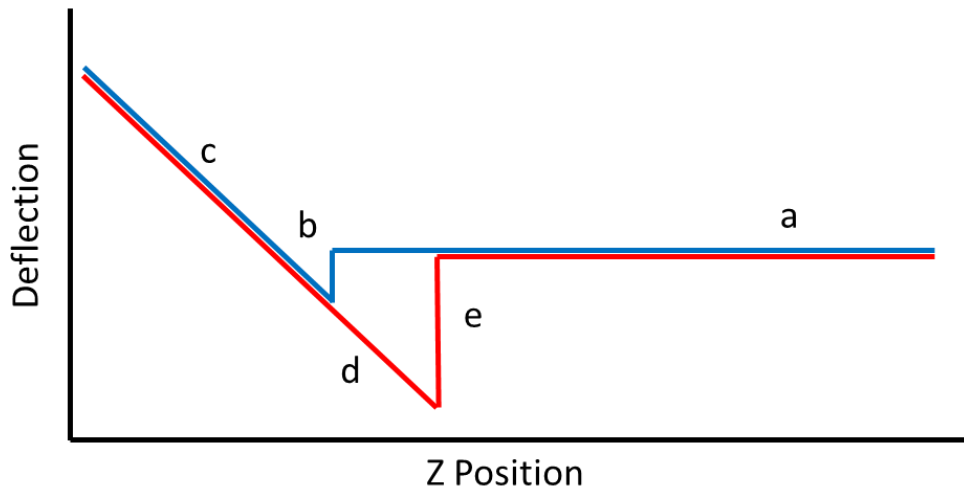


**Figure 2.6.** A representative AFM force curve. The blue curve is the approach curve, and the red curve is the retraction curve. The curve regions are produced during measurement as follows: a to b, b to c, c to d, d to e, then e to a. a to b is the zero force approach where the cantilever experiences no flexing. b is the region of “snap down”, where the cantilever is rapidly attracted to the surface through electrostatic attraction and sometimes capillary action due to a thin water layer that is present in atmospheric conditions (this can be eliminated by performing measurements in an appropriate fluid for the application). The region from b to c is in the repulsive contact region, where the cantilever follows Hooke’s Law for small deflections. c to d is the retraction curve within the repulsion region. During retraction, the cantilever is adhered to the surface and until a critical force is reached, where at e, the tip lifts from the surface and returns to its equilibrium position. From e to a, the cantilever experiences no deflection until the curve acquisition process has ended.

In some modes of AFM, the information of interest is the approach curve of the cantilever and sample plotted as deflection (related to force through Hooke's Law) vs tip/sample separation in  $Z$ . This plot is called the Force Curve, and can reveal adhesion forces and energies, elastic parameters of materials, and even yield stresses for materials or objects. The most common contact theory used in AFM is the Hertz Model. The AFM cantilever must be calibrated accurately, so it must be done on a surface much harder than the sample to be measured to minimize indentation  $i$ . The force exerted on a plane using a spherical indenter is shown by the Hertz Model of Indentation (Eq. 2.7). The Hertz model is derived under the assumptions of frictionless contact between two bodies, where the area of contact between the two bodies is small relative to indenter size, and the strains are small.

$$F_{applied} = \left( i \frac{4}{3} \Delta E R^{1/2} \right)^{3/2} \quad (2.7)$$

Here,  $F_{applied}$  is the force applied by the cantilever,  $i$  is the indentation of the tip in the sample,  $\Delta E$  is the effective elastic modulus between the sample and tip, and  $R$  is the probe tip radius. This shows a low force must be applied, or the measurement must be done on a sample with a very large difference in elastic modulus  $\Delta E$  between the indenter tip and surface, or a very large indenter radius  $R$  (it also happens that  $\Delta E$  is the quantity measured by AFM). The AFM measures the difference of the  $Z$  piezo position  $Z$  and the deflection  $\delta$  to yield the indentation.



$$i = Z - \delta \quad (2.8)$$

To be useful for calibration for a cantilever,  $i$  must be very small, so  $Z = \delta$ . A large indentation on a calibration surface with an elastic modulus close to that of the tip can yield a false elastic modulus value as seen by the following equation for effective elastic modulus  $E$ :

$$\frac{1}{\Delta E} = \frac{1 - \nu_{sample}^2}{E_{sample}} - \frac{1 - \nu_{tip}^2}{E_{tip}} \quad (2.9)$$

Here,  $\nu$  is Poisson's ratio (subscript denotes either the tip or sample surface), which is a measure of how a material behaves under deformation.

Under contact, the deflection measured is plotted against  $Z$  to yield the force curve. At this point, the deflection slope is measured from the point of contact to the end of the curve. This slope is called the deflection inverse optical lever sensitivity (Def invOLS, or just invOLS for short) and is used to find the spring constant  $k$  of the cantilever. After obtaining the invOLS, the cantilever's average thermal oscillations  $\langle \delta V^2 \rangle$  are measured as photodetector voltages to find its resonant frequency, with  $k_B$  as Boltzmann's constant and  $\chi$  as the invOLS correction factor.

$$k = \frac{k_B T}{\langle \delta V^2 \rangle \chi^2 \text{invOLS}^2} \quad (2.10)$$

Eq 2.10 [101] is derived from the equipartition theorem assuming the cantilever has 1 degree of freedom ( $\frac{1}{2}k\langle x^2 \rangle = \frac{1}{2}k_B T$ , where  $\langle x^2 \rangle = \langle \delta V^2 \rangle \chi^2 \text{invOLS}^2$ ). This is referred to as the Thermal Method of calibration. A cantilever can also be force calibrated similarly using the Sader method, which uses knowledge of cantilever's geometry and the cantilever's thermal oscillation profile to determine the spring constant and invOLS. The Sader method has an advantage over the Thermal Method since it does not require the tip to touch the sample for calibration, which in turn reduces the chance of damage to the tip before taking measurement [101].

### *Terminology and Common Scanning Modes*

Scanning Modes and parameters: As mentioned above, there are a few parameters important to AFM. Many scan types can be acquired simultaneously, such as amplitude, phase, Z, height, and oscillatory force scans (Figure 2.9).

These are listed below:

- *Deflection*: The amount in volts the cantilever bends from its initial deflection.
- *Amplitude*: The distance in volts of the cantilever's oscillation amplitude.

- *Phase*: The mechanical lag phase of an oscillating cantilever between the cantilever oscillation and feedback control.
- *Scan*: The image obtained by rastering the probe over a sample and generating a map of a measured quantity (from cantilever deflections) vs XY stage position.
- *Scan Angle*: The angle relative to the cantilever major axis at which the scanner rasters. Standard scans are done at  $0^\circ$ . Any other angle can be selected.
- *Deflection scan*: Image variable is constructed from the non-oscillating cantilever deflection.
- *Amplitude scan*: Image variable is constructed from the oscillating cantilever amplitude.
- *Phase scan*: Image variable is constructed from the oscillating cantilever phase.
- *Z scan*: Image variable is constructed from the Z piezo position.
- *Height scan*: Image variable is constructed from the difference of the Z scan voltage scaled to piezo sensitivity.
- *Potential scan*: Image variable is constructed from the deflections of a cantilever held at a set voltage difference with respect to the sample or ground.
- *Sum*: The total summation (all quadrants) of laser light reflected off the cantilever into the photodetector.

- Set Point: A predetermined limit of deflection or amplitude that determines when “contact” has occurred.
- Scan Area: The area of the image.
- Scan Rate: The frequency at which the AFM rasters over a given line during a scan.
- Scan Line: A single raster of a scan.
- Integral Gain: A gain associated with the sensitivity of the feedback system between the Z piezo and the measured cantilever deflection or amplitude.

### *Constant Deflection Mode*

The simplest form of AFM is constant deflection mode. The cantilever is bent by repulsive forces to a specified deflection by the set point. The cantilever is then rastered over the scan area. When the cantilever encounters a feature, it is deflected by that feature. To maintain constant deflection, the feedback loop controls the Z piezo to compensate for the change in deflection. During this type of scan, 3 images are generated. A Z scan, is a mapping of Z piezo position at particular points on the map. This gives an accurate 3D representation of topography. A Deflection scan, which is a map of the cantilever’s instantaneous deflections can reveal textures not seen in the Z scan. A Height image is generated by scaling the Z piezo voltage with Z piezo sensitivity.

Below are contact mode depiction of cantilever deflections without and with feedback (Figure 2.7b and c, respectively) feedback. The cantilever scans in contact mode over a square feature (Figure 2.7a). Without feedback (Figure 2.7b), the cantilever deflections show the surface feature. However, the force applied by the cantilever varies linearly with deflection. With feedback (Figure 2.7c), the deflection the cantilever deflects up when it encounters the square feature, and then deflects down when it comes off. The width of peaks corresponds to feedback lag. This mode offers constant force over the surface.

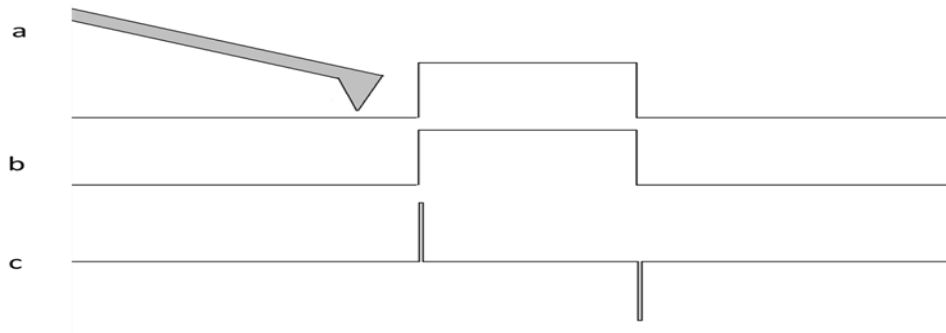


**Figure 2.7.** Contact mode depiction of cantilever deflections without and with feedback (b and c, respectively) feedback. a. The cantilever scans in contact mode over a square feature. b. Without feedback, the cantilever deflections show the surface feature. c. With feedback, the deflection the cantilever deflects up when it encounters the square feature, and then deflects down when it comes off.

### *AC Mode (Tapping Mode)*

This form of AFM is very similar to the constant deflection scans, but uses an oscillating cantilever driven at resonance to “tap” the surface. This has the advantage of being less invasive and more sensitive to topographic changes. However, instead of deflections, the cantilever’s amplitude is monitored and kept constant by the feedback system. Four images are obtained from these scans. A Z scan, much like the Z scan of constant deflection mode. An amplitude scan, which is a map of amplitude changes (like the deflection scan). A phase scan, which is a mapping of cantilever phase. Phase scan can prove very useful with electrical measurements (later). A Height image is generated by scaling the Z piezo voltage with Z piezo sensitivity.

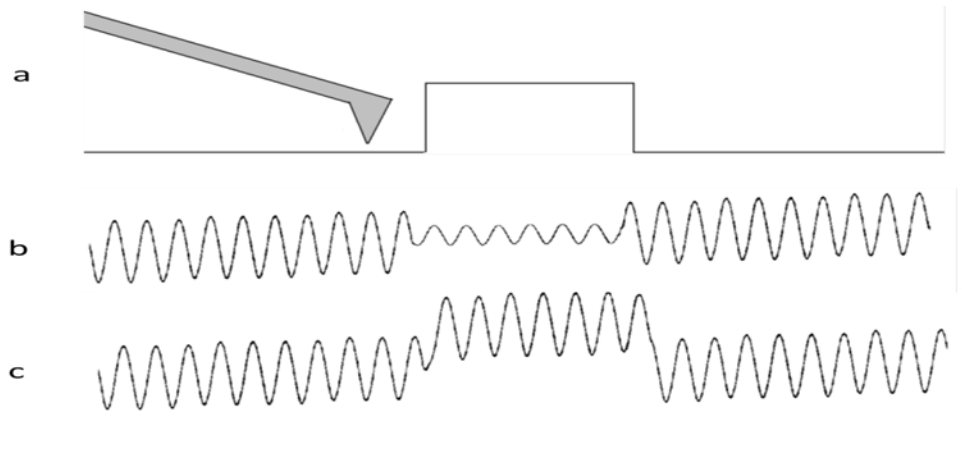


**Figure 2.8.** *AC tapping mode depiction of cantilever deflections without and with feedback (b and c, respectively) feedback. a. The cantilever scans in AC*

*tapping mode over a square feature. b. Without feedback, the cantilever amplitude change shows the surface feature. c. With feedback, the amplitude of the cantilever is dampened when it encounters the square feature, the Z piezo repositions to restore constant amplitude, and then amplitude increases when it comes off before the feedback control compensates.*

Figure 2.8 shows AC tapping mode depiction of cantilever deflections without and with feedback (Figure 2.8b and 7c, respectively). The cantilever scans in AC tapping mode over a square feature (Figure 2.8ba). Without feedback (Figure 2.8b), the cantilever amplitude change shows the surface feature. This mode exerts a higher force when the amplitude is dampened by the feature. With feedback (Figure 2.8c), the amplitude of the cantilever is dampened when it encounters the square feature before the feedback system needs time to respond to the amplitude change. The Z piezo repositions to restore constant amplitude, and then amplitude increases when it comes off before the feedback control compensates. This allows for constant intermittent force. The lag in the feedback controlled scan results in an apparent phase shift (Figure 2.9).

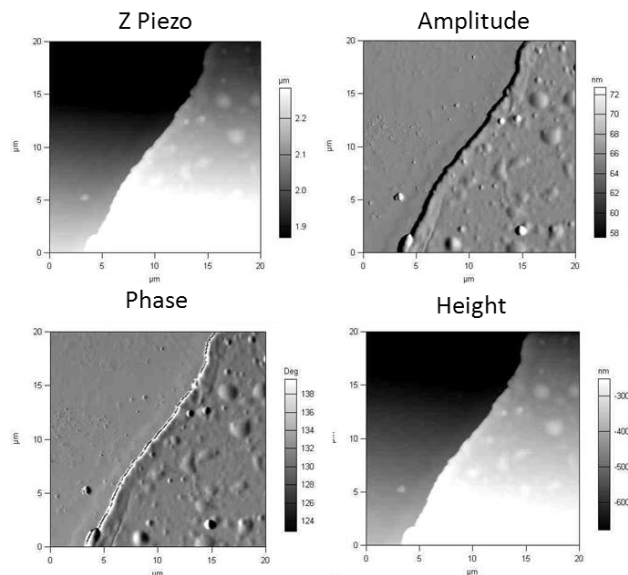


**Figure 2.9.** AFM AC mode images on a polymer layer showing Z piezo position, Cantilever amplitude, cantilever phase, and height. Z piezo and Height are almost identical and clearly show topographic differences between the higher right side and lower left side. The amplitude scan shows how the cantilever amplitude change before Z piezo compensation through feedback (the dark tracing of the layer boundary shows the phase changed caused by the height difference. The phase shows the lag difference between the cantilever and feedback control loop.



## 2.5 Special modes of operation

### *Friction Force*

Friction force scans, also known as lateral force scans, are constant lateral deflection scans taken with a  $90^\circ$  raster relative to cantilever direction. This causes the cantilever to twist based on tip/sample frictional forces. Three images are generated: Z, height, deflection, and lateral deflection. As with the other modes, feedback controls Z as a function of vertical cantilever displacements. Friction force AFM is unique in that it can detect chemical interaction between the sample and cantilever that would not be seen with a standard  $0^\circ$  scan angle.

### *Electrical Methods*

SKPM (Scanning Kelvin Probe Microscopy) and EFM (Electric Force Microscopy) are two common electrical AFM methods. SKPM measures surface potentials between an electrically conductive tip and a sample by treating the tip/sample system as a capacitor. The tip is held at a constant voltage. SKPM utilizes a “two pass” method, where an initial standard topography scan maps the surface geometry. A following scan over the same area occurs using this

information to maintain a constant noncontact tip sample separation, where the cantilever deflections/amplitudes are measured with the tip held at a constant pre-specified voltage. The resulting deflections or amplitudes are a result of the electric potential between the tip and sample. The deflections are caused by the capacitive Force  $F$ :

$$F = \frac{1}{2} \frac{dC}{dz} V^2 \quad (2.11)$$

Where  $V$  is the voltage between the tip and sample,  $C$  is the capacitance between tip and sample, and  $z$  is the tip-sample separation.  $V$  is expressed as a sum of voltages,

$$V = (V_{DC} - V_{CDC}) - V_{AC} \sin(\omega t) \quad (2.12)$$

With  $V_{DC}$  denoting the DC tip-sample voltage difference,  $V_{CDC}$  being the tip-sample contact voltage difference (the value of interest in SKPM),  $V_{AC}$  as the AC voltage applied to the tip,  $\omega$  as angular AC frequency, and  $t$  simply is time . The force resulting in deflection is:

$$\begin{aligned}
F = \frac{dC}{dz} & \left[ (V_{DC} - V_{CDC}) V_{AC} \sin(\omega t) \right. \\
& + \left[ \frac{1}{2} (V_{DC} - V_{CDC})^2 + \frac{1}{4} V_{AC}^2 \right] \\
& \left. - \frac{1}{4} V_{AC}^2 \cos(2\omega t) \right]
\end{aligned} \tag{2.13}$$

Equating this to Hooke's law allows for the calculation of the surface potential  $V_{CDC}$ .

### *Force Volume Mapping*

Since the cantilever behaves as a spring and follows Hooke's Law for small deflections, it is relatively simple to obtain an elastic modulus profile of a samples surface. Within the AFM community, "elastic modulus" refers to an elastic modulus that closely resembles Young's Modulus  $Y$  using the Hertz model (just called Elastic Modulus), but is calculated using Eq 11. This is done for a few reasons, most notably being that a very small area is compressed, which makes the AFM elastic modulus much closer to the Young's modulus.

$$Y = \frac{FL_0}{A\Delta L} \tag{2.14}$$

Here,  $F$  is the force applied to deform the sample,  $L_0$  is the initial sample length ( $i = 0$ ),  $\Delta L$  is the change in length (or indentation), and  $A$  is the tip crosssectional area of the tip. In this mode of measurement, the AFM pushes the non-oscillating tip into the sample and monitors cantilever deflections vs  $Z$  piezo position until the setpoint is reached repeatedly over a  $N \times N$  measurement grid (usually above  $10 \times 10$  points). Knowledge of the force exerted by the cantilever, cantilever material, and tip geometry are required to calculate the elastic modulus for the point measured. After force mapping is completed, the measurements can be graphed as histograms to choose the best representative elastic modulus for the sample. Generally, the elastic modulus histograms show a Gaussian bell curve that can be skewed. It is useful to compare the  $Z$  piezo position to the elastic modulus for each curve to see if surface topography affects the force measurement. This also helps to determine if a force measurement relates to surface features, which, in the case of proteins films, could indicate different conformal shapes or crystalline structure. A more advanced form of Force-Volume mapping, called Peak Force AFM, yields a scan of force over the surface in an oscillatory mode, eliminating the slow grid based force-volume mapping method.

## 2.7 AFM on Cells

AFM has filled a niche in biophysical and biomedical research since its invention and proven its versatility. Before AFM, researchers were only able to perform experiments with destructive methods and large scale data acquisition. AFM revolutionized the field by making noninvasive and nondestructive measurements possible in the samples natural environment (or close to it). AFM is commonly utilized in single molecule experiments such as forces and energies in unzipping DNA and unfolding proteins. It has also been widely applied to cells and biomaterials such as imaging cells and cellular structures in 3D, moving motor proteins and even the degradation of bacterial membranes by antibiotics in real time. Possibly, one of AFMs best features is its ability to integrate with other microscopes, such as RAMAN, confocal, fluorescent, optical, and SEMs. Using AFM with biological samples generally requires measurements to be taken in a biologically compatible electrolytic fluid environment so the samples aren't killed, damaged, dehydrated, or exposed to damaging UV light. Much of the time, AFM measurements on biological samples involves low spring constant (0.5pN/nm) specially shaped triangular cantilevers to minimize the effects of fluid loading and dampening, and still be able to resolve relevant information from the sample. When performing measurements on cells, using neurons as the example, the cells must be kept in an environment with the proper nutrients, pH, electrolytic concentration, temperature, atmosphere, and protected from damaging

light. Neurons, like most cells, are cultured and measured at 37°C in commercial medium (such as Neurobasal with proper nutrients and antibiotics for the cell type added). Luckily, AFM has no trouble measuring cells in fluid, aside from electrical measurements due to ion shielding (discussed later).

### *Topography*

AFM is the ideal tool to nondestructively measure the topography of live cells. This has been successful done on animal cells, bacteria, and viruses. Since cellular morphology is a result of cytoskeletal composition and arrangement, this can give insight into the physical function of a cell or cell features that is not measurable by other means. AFM has been used to measure the 3D shape of cells and their structures. AFM beautifully shows the 3D structure of the growth cone, and combined with cytoskeletal staining, reveals the cytoskeletal components and volumes of the growth cone regions. Of AFM topographic methods, High Speed AFM (HS AFM) could be the most interesting, and is the difference between a time integrated snap shot and a video.

## *Stiffness*

AFM has been used to characterize the mechanical properties of cells using force volume mapping in biologically relevant media on a variety of surfaces and coating. In essence, the study of cell stiffness is the study of the mechanical properties of the cytoskeleton, since the cytoskeleton provides mechanical and structural support for the cell membrane. Previous research sought to determine single cell stiffness for a cell type/line rather than the more common bulk measurements performed with Dynamic Mechanical Analysis. Further research is aimed at answering whether the substrate surface chemistry or elastic modulus affected cell stiffness. Force Volume mapping was also combined with fluorescent tagging of the cytoskeleton to reveal how the cytoskeleton changes and effects stiffness. AFM has also been applied to measure the velocity-force dependence on growth cones to determine the maximum force exerted on a substrate before it stops (stall force) and axon tension during growth. AFM is also used to study the physical properties of the viral capsid, such as capsid rupture forces and stress-strain curves.

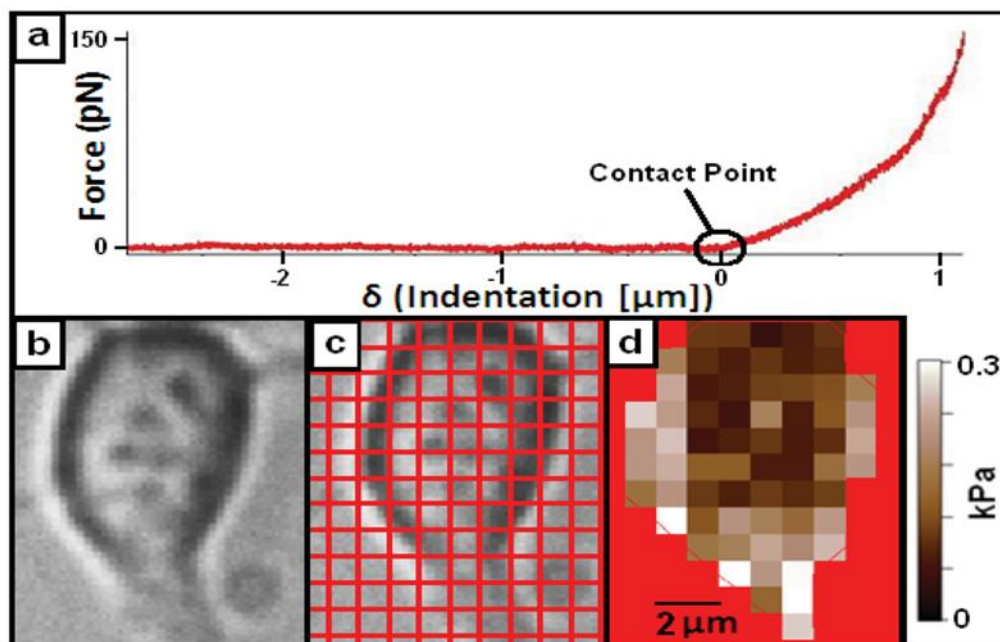


**Figure 2.10.** *a. An example of a force vs indentation curve for a neuronal soma showing the contact point. b. A brightfield image of a live cortical neuron. c. The same image as b, but with coarse force map grid overlaid. d. A map of cell stiffness in KPa generated from the force curves. Darker colors indicate areas less stiff than the lighter colors. Red is a “mask” over the substrate. Scale bar is 2  $\mu\text{m}$  [92].*

Figure 2.10b shows a neuron’s soma [92]. During the force map of the cell, the AFM performs force curves in the center of the grid squares in Figure 2.10c. The resulting stiffness information in kPa is shown in Figure 2.10d. Figure 2.10a shows the resulting force curve and contact point.



## *Electrical*

Electrical AFM measurements in air and non-polar fluids can provide valuable quantitative micro/nanoscale information on biological samples, and is readily performed in non-polar fluids. Air measurements are much easier to perform than fluid measurements, but it is worth noting that many fluid based electrical AFM modes have been developed. For biologically relevant polar fluids, freely moving ions make quantitative, and sometimes qualitative, measurements difficult to perform depending on the concentration of ions. The rearrangement of ions in solution create electric double layers at the sample/fluid interface, and screen most electrical surface properties of the sample outside of the Debye Radius if measured at timescales above the fluid's Debye Time. This makes electrical AFM measurements highly sensitive and requires accurate knowledge of cantilever geometry, tip/sample separation, exact cantilever deflection to a reference material, tip surface charge and chemistry, and ion concentrations. The importance of micro/nanoscale electrical properties is of great importance to understanding properties of biological materials and cellular processes. Of these double-layer-defeating techniques, oscillatory methods are much more sensitive to cantilever deflections than static cantilever ones. Simple AFM, Fluid Electric Force Microscopy (FEFM), Voltage Modulated Scanning Probe Microscopy (VMSPM) (such as Electrochemical Force Microscopy), High Bandwidth Atomic Force Microscopy (HBAFM), and Band Excitation Piezo Force Microscopies (BEPFM) have been used for these experiments. These

methods reveal important electrical, mechanical, and electromechanical information on biological samples.

### *Conclusion*

AFM is a highly versatile instrument that can be used to answer a wide range of questions in the biophysical and biochemical sciences. It can simultaneously measure a variety of parameters in one experiment that would normally require multiple instruments. Probably one of the biggest advantages of AFM over other microscopy methods is its ability to operate in a variety of gaseous and liquid environments to accommodate almost any type of sample. Also, this cantilever based technology gives a very large potential to develop new scanning and measurement methods. With new cantilever and tip materials it is possible to perform even more measurements. It is constantly showing us new information about cells we could not see with other forms of microscopy. From topography, force, and electrical experiments we can gather information and piece together the mechanisms that drive living things and the organic world.

## **CHAPTER III**

### **Neuronal Pathfinding**

#### **3.1 Overview**

Neurons grow by sending out long processes called axons and dendrites. For cortical neurons, axons are generally more active than dendrites and extend millimeters from their soma. At the end of the axon is a sensing structure called the growth cone. The growth cone senses its environment via chemical and physical cues, and extends/retracts and steers the axon. Of these physical cues, substrate topography is most easily controlled and seems to override chemical signaling. It has been previously shown that neuron neurite orientation can be greatly affected by topographic features [7, 23-27, 95, 52, 100]. The degree of growth perpendicular or parallel to these ridges appears to vary with ridge frequency and time. This can be modeled with a Fokker-Planck equation [7, 22, 67], whose solutions can be used to find the driving physical potential the neuron "feels" [67]. Using micropatterned PDMS surfaces with ~0.75 to 3  $\mu\text{m}$  spacing between ridges, we study how neurons steer on these surfaces with time by analyzing axonal angular distributions from fluorescent images.

Neuronal pathfinding and polarization mechanics are critical to our understanding of how the nervous system organizes during development and how to treat nervous system damage. Observing how neurons distribute neurites when grown on substrata with physical constraints, ordered geometric features, and protein microprinting [29, 30, 95] allows researchers to extract the underlying rules of neurons polarization and cytoskeletal dynamics. Combining these methods with cytoskeletal staining and chemical disruption of signaling mechanisms gives insight into the internal mechanisms of growth [45, 46, 92, 58-61, 104, 105]. Characterization of neuronal pathfinding can use neurite tracings after a suitable period of culture time, or video and time-lapse imaging. From these data, the frequency distribution of neurite segments can be normalized into probability distributions. At this point, Fokker Planck equations and Markov transition matrices can be applied to quantify the growth behavior. If the neurons are grown on specially micropatterned surfaces, the neurite extension could be biased to favor a particular direction, or rate of extension.

### **3.2 Literature Review**

*Contact Guidance of CNS Neurites on grooved Quartz [27]*

Neuron growth patterns are strongly influenced by substrate surface topography and this appears to override the other signaling mechanisms. To

investigate the mechanosensitivity of CNS neurons as influenced by ordered surface grooves, Rajnicek cultured rat hippocampal neurons and *Xenopus* spinal cord neurons on grooved quartz substrata. The grooved quartz substrata varied in groove width (1,2,4  $\mu\text{m}$ ) and groove depth (14, 36, 130, 140, 520, and 1100nm) to determine what groove characteristics affect neurite growth. *Xenopus* spinal cord neurons “exhibited classic contact guidance” [27] on the grooved surfaces and grew almost completely parallel to the grooved features regardless of groove width. Very little perpendicular growth occurred, but was more prevalent at the very shallow groove depths (14-140nm). In contrast, Rat hippocampal neuron guidance appeared to prefer to grow perpendicular to the grooves at 1-2 $\mu\text{m}$  groove widths. The 4 $\mu\text{m}$  width surfaces appeared to show a similar trend, however at groove depths above 520nm, the neurites preferred parallel growth. Overall, hippocampal neurons displayed a preference to grow more parallel to grooves as groove width and groove depth increased. (Figure 3.1)

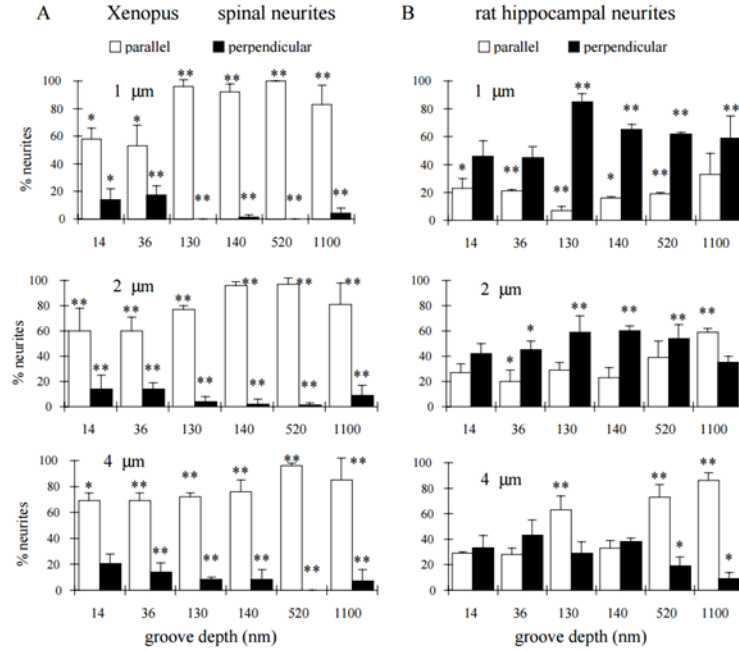


**Figure 3.1** Neurite orientation by groove width and groove depth and spacing. A. Alignment of *Xenopus* spinal neurites. B. Alignment of rat hippocampal neurites. White bars indicate parallel alignment, black bars indicate perpendicular alignment [27].

Additionally, groove orientation determined the emergence angle of sprouting neurites, showing the cytoskeletal arrangements within the soma and membrane surface proteins organize in a way that is affected by feature dependent membrane curvature. At groove depths above 36nm, *Xenopus* neurons showed a higher affinity to sprout parallel to the grooves, where rat hippocampal neurons showed a more complex growth behavior. For rat hippocampal neurons, emerging axons more frequently sprouted perpendicular to grooves, and dendrites tended to sprout parallel to grooves. This result depicts the different sensing in dendrite and

axon growth cones. After the *Xenopus* and rat neurites sprout, the majority of neurites actively steer themselves to extend in the preferred surface orientation direction. Interestingly, neurites also grew significantly faster in the preferred orientation direction. On flat quartz, neurites from both types grew outward with random emergence angles and very uniform neurite lengths. *Xenopus* neurites on 130nm deep and 1µm wide surfaces grew at ~26µm/hour in the preferred direction compared to neurons of the same type grown on flat quartz (~14µm/hour). Rat hippocampal neurons showed the same trend, but was shown by greater neurite length in the perpendicular direction.

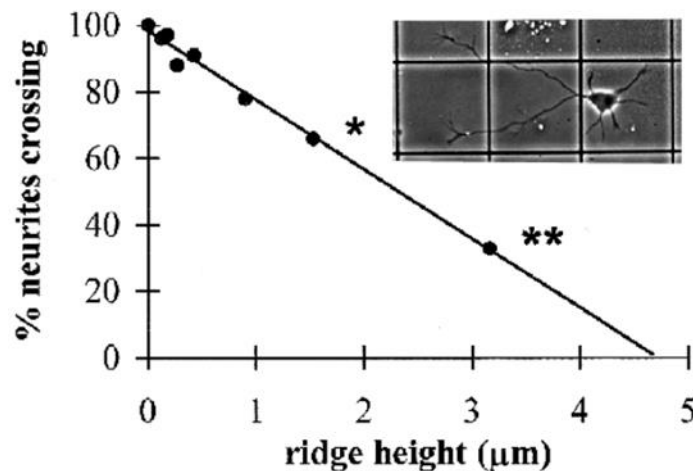


**Figure 3.2** Percent of neurites crossing grooves (perpendicular growth) vs ridge height with a linear fit of  $y = -21.3x + 100$  [27].

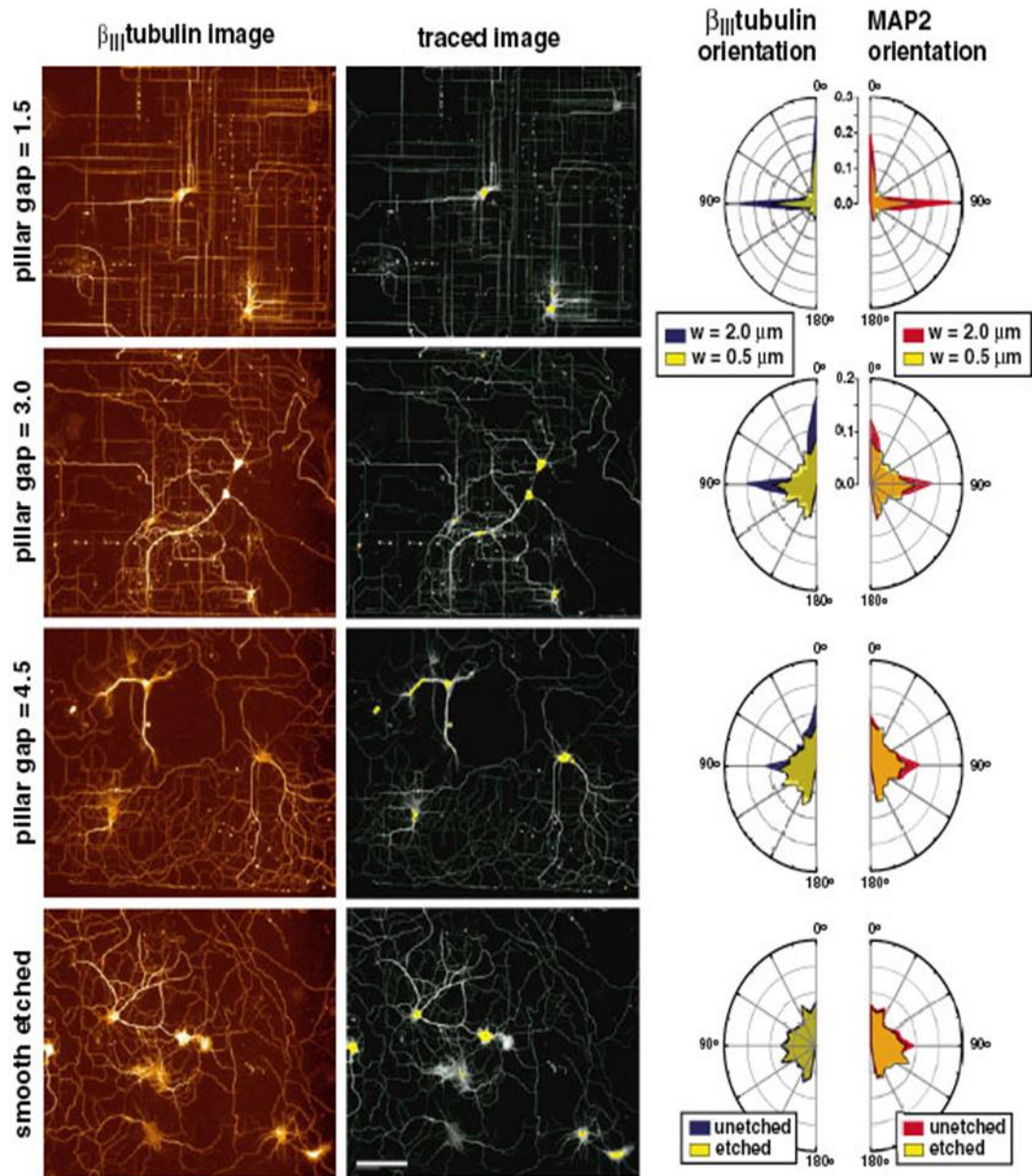
These results display how CNS neurons are highly sensitive to topographic cues and the grooves influence emergence angles and ultimate growth direction. *Xenopus* neurons grew primarily parallel to grooves, and rat

hippocampal neurons grew preferentially perpendicular to grooves, which shows rat hippocampal neurites behavior is subject to process identity (axon or dendrite). For rat neurons, increasing groove frequency increased the probability of perpendicular growth, and an increase in groove depth increased the probability of parallel growth. In conclusion, Rajincek suggests perpendicular alignment of rat hippocampal neurons is influenced by three factors: 1) Axons prefer to emerge perpendicular to grooves. 2) Neurites are more apt to turn from parallel to perpendicular and the turning occurs over greater angles. 3) Perpendicular growth across grooves is much faster than the average extension rate on flat quartz.

*Topographically Modified Surfaces Affect Orientation and Growth of Hippocampal Neurons [100]*

Neuronal growth is highly responsive to surface topography and chemistry. To study the effects of patterned square arrays via photolithography, Mesfin grew hippocampal neurons on square arrays of  $1\mu\text{m}$  heights and varying scales. The vary scale gives insight into the resolution of features a growth cone can resolve as it moves across a surface, from  $4.5\mu\text{m}$  gaps to  $1.5\mu\text{m}$  gaps. Figure 3.3 below shows the pathfinding behavior of neurons on these surfaces. As pillar gaps become smaller, the neurons begin to grow in a more ordered fashion, from a slightly biased growth pattern at  $90^\circ$  and  $0^\circ$ . As gaps decrease, the probability density peaks at those angles become more prominent and much sharper.

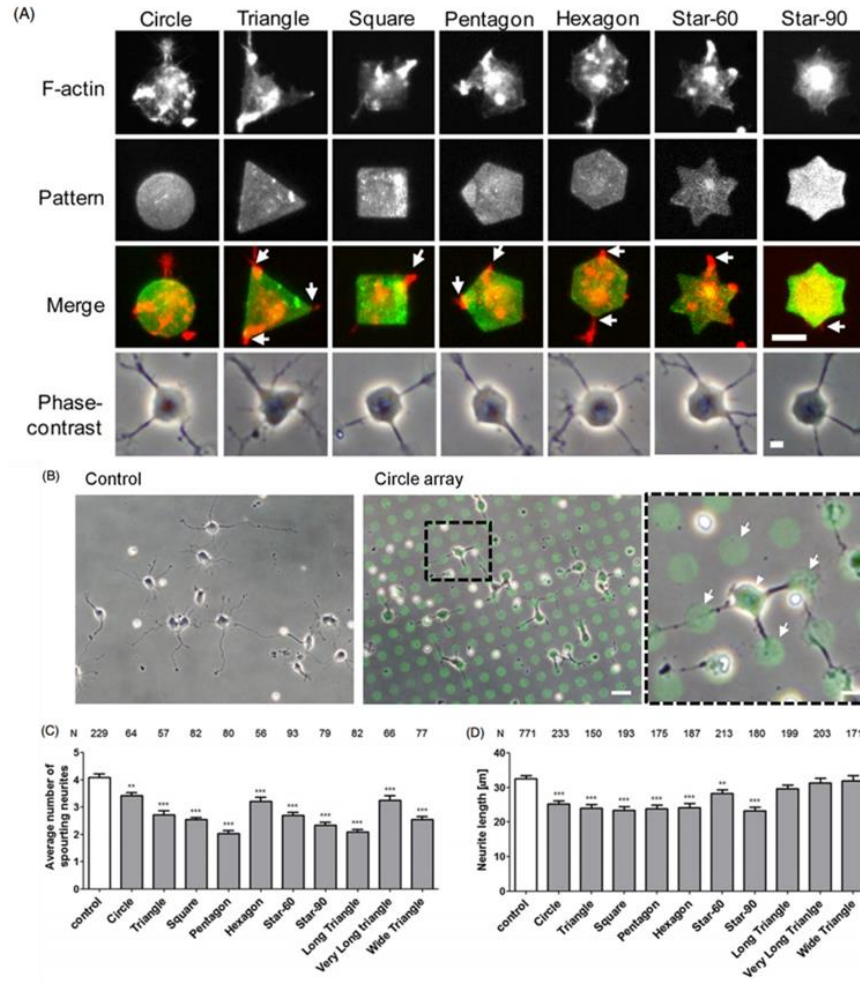




**Figure 3.3.** Immunostained fluorescent images of neurons on micropillar arrays (with pillar gaps of 1.5, 3.0, 4.5, and 0 microns) with corresponding angular distributions [100].

*Geometric Effect of Cell Adhesive Polygonal Micropatterns on Neuritogenesis  
and Axon guidance [54]*

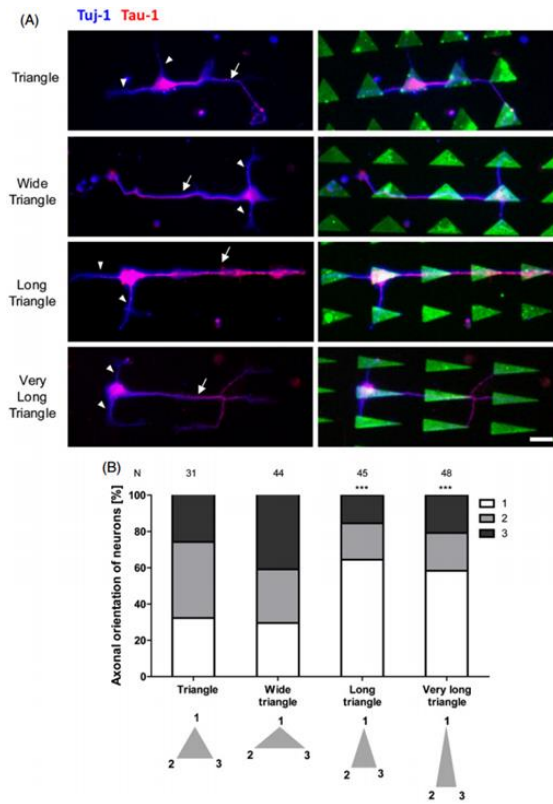
The cytoskeletal and membrane surface organelle rearrangements that take place during polarization of neurons in culture are profoundly affected by the geometry of the growth substrate. Jang studied the characteristic steps of neurite formation through



**Figure 3.4** FITC stained micropatterned geometries with F-Actin stained neurons and phase contrast images of the neurites for the varying geometries [54].

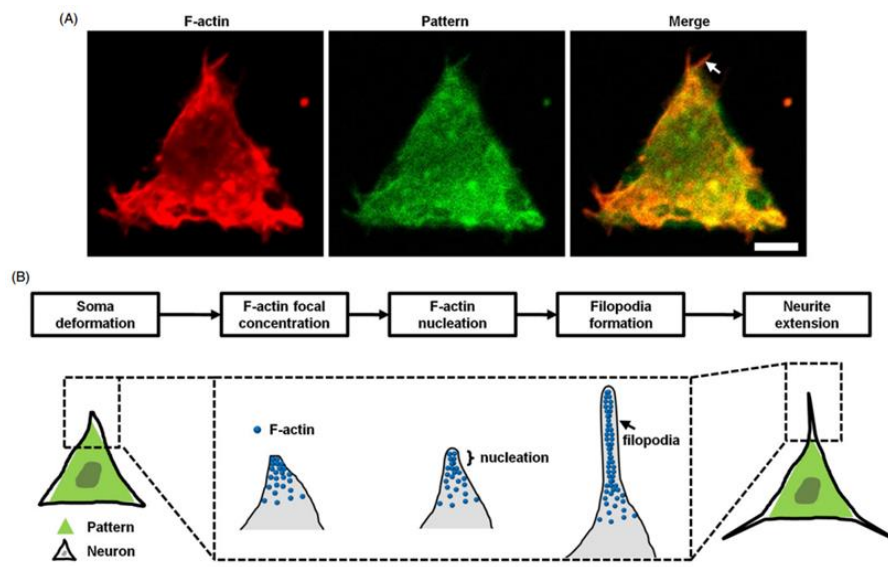
microprinting surface bound poly-L-lysine and laminin A chain synthetic peptides into flat substrates (with no adhesion molecules or ECM) to observe how cell adhesion contributes to neurite polarization and growth. Rat cortical neurons were grown on a variety of microprinted arrays of varying “micro polygons”

(feature sizes were all  $\sim 10\mu\text{m}$  across, which is very close to neuronal soma size) such as circles, triangles, squares, pentagons, hexagons, stars, and isosceles triangles since these features have varying vertex angles. All micropatterned arrays had the geometric features spaced  $10\mu\text{m}$  apart from feature centers in the array directions. The micropatterned geometries influenced neurite emergence angle, neurite number, neurite length, neurite orientation, and even soma shape.



**Figure 3.5.** A. Fluorescent images of neurons (purple) on micropatterned arrays (green). B. Percent of axons oriented along a vertex [54].

Soma preferentially attached to all microprinted features within the array and rearranged their cytoskeletons and membranes to fully adhere to the available ECM, which resulted in the soma mimicking the underlying patterned shapes. Outgrowth from the soma to neighboring features appeared to primarily occur in the left, right, top, and bottom directions (major directions). Neurite sprouting in the 4 major directions was 0.684, which is ~ twice as much as the random probability inferred from non-patterned substrates (0.316). Also, the average number of neurites per geometry appears to be independent of shape, at ~2.5 processes per neuron, where control samples had ~4 neurites each. Jang suggests that soma confinement due to the shapes restricts neurite sprouting. Also, the geometries have reduced neurite growth velocities compared to control. However, this is most likely due to the adhesive discontinuity between the features in the array (Figure 3.6).



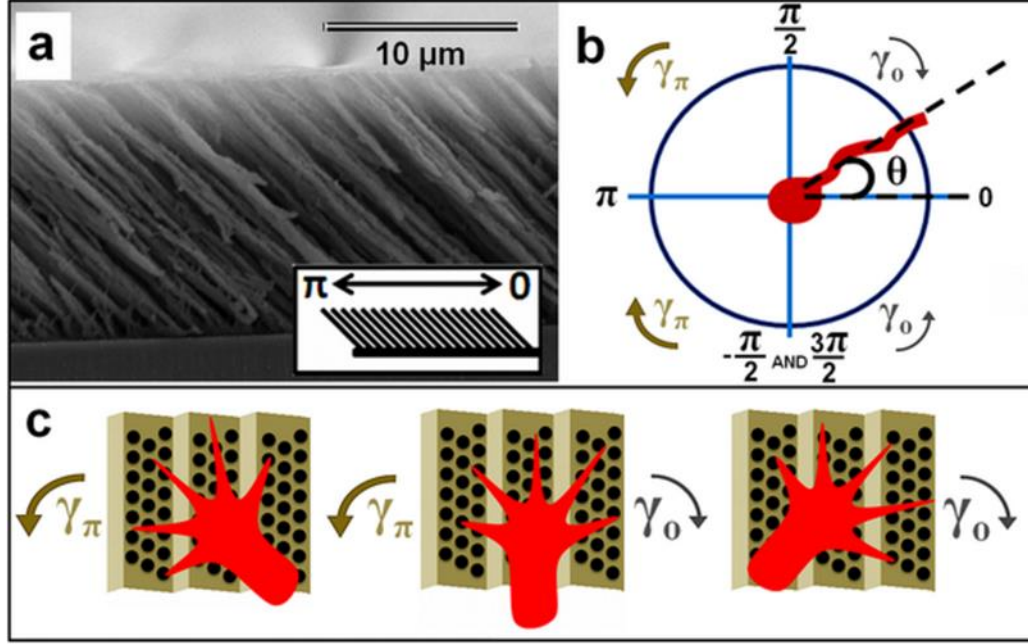
**Figure 3.6.** *A. Fluorescent images of cytoskeletal filaments (actin, red) and microprinted patterns (green),a and the combined image of neuronal soma adhered to the microprinted pattern. B. A diagram depicting neurite polarization through cytoskeletal rearrangement [54].*

Figure 3.6 A shows that there generally a higher concentration of F-Actin at feature vertices that correspond with neurite outgrowth for 12 hour post culture neurons. Since neurons tend to extend neurites in the major direction on the circle features, it appears that vertex sharpness is not the only factor controlling sprouting direction. For the circles, the neurites most likely preferentially grew to their nearest neighbor in the major directions only because this was the shortest distance to traverse before adhering. Comparing this to the polygonal features which show a similar outgrowth, there is a 0.171 higher chance for a particular neurite to extend in a major axis direction, compared to 0.0395 for the other directions. With this, Jang compared the other geometries to the circles and control groups showing that squares were less likely than predicted to form neurites at their vertices, and triangles seemed to have a significantly higher chance to grow along a vertex than predicted. Triangles with a 60° vertex showed the most biased outgrowth (Figure 3.6B), which is consistent with the theory that higher membrane curvature induces focal adhesion formation, which in turn focuses actin polymerization at those points of high curvature. The other geometries were not significantly different from the predicted values.

These results indicate that neurite initiation can be induced through membrane curvature. Figure 3.6 A and B shows the process of neurite sprouting/polarization, where the soma adheres to and mimics the underlying shape. Regions of high curvature induce focal adhesion formation or concentration. This, in turn, leads to actin polymerization at that point, filopodia formation, and ultimately neurite formation and extension.

*Effect of surface asymmetry on neuronal growth [7]*

As discussed in Chapter 1, Spedden applied a theoretical model for neuronal growth using Langevin derived Fokker-Planck equations to quantify the underlying mechanisms of E18 neuronal growth on asymmetric poly(chloro-P-zylene) tilted nanorod substrata (Figure 3.7). Asymmetry is quantified by  $C_{\alpha}$ .



**Figure 3.7.** *a. Nano PPX SEM image (scale bar 10μm). b. Neurite orientation angle and torque. c. Growth cone (red) engaging nano PPX structures and exerting an effective torque [7].*

Growth is described by a stochastic Langevin equation for an effective torque on the growth cone [7].

$$\frac{d\theta(t)}{dt} = -\gamma \sin(\theta(t)) + \Gamma(t) \quad (3.1)$$



$\theta$  is the angular position of the growth cone,  $\gamma$  is the magnitude of the effective force on the growth cone from the substrate, and  $\Gamma$  is the “stochastic torque” [7]. This parameter describes stochastic effects from chemotactic signaling.  $\Gamma$  is assumed to be Gaussian white noise, thus it has the property that  $\langle \Gamma(t) \rangle = 0$ . Spedden notes that if  $\Gamma$  was zero at all times, the system would be completely deterministic and predictable. Additionally,  $\Gamma$  is Markovian, with an average product of  $\Gamma$  at time  $t$  and some later time  $t'$  is described by a Dirac delta function,  $\langle \Gamma(t) \cdot \Gamma(t') \rangle = q\delta(t - t')$  [7, 22], where  $q$  is the strength of the stochastic noise. This property is required to enforce the noise has no memory of past states.

From this equation, the corresponding stochastic Langevin derived Fokker-Planck equation can be derived, where  $P(\theta, t)$  is the probability density function and  $D_\theta$  is the effective angular diffusion constant.

$$\frac{\partial P(\theta, t)}{\partial t} = \frac{\partial}{\partial \theta} [-\gamma \sin(\theta(t)) \cdot P(\theta, t)] + D_\theta \frac{\partial^2 P(\theta, t)}{\partial \theta^2} \quad (3.2)$$

Since the images were taken without time lapse, time independent solutions for growth in the asymmetric direction ( $\theta = \pi$  or  $0$ ) are desired, making the temporal term on the left zero. This reduces the differential equation to an easily solvable one, with solution [7]:

$$P(\theta) = A_{0,\pi} \exp \left[ \frac{\gamma_{0,\pi}}{D_\theta} \cos(\theta) \right] \quad (3.3)$$

The normalization constants  $A_0$  and  $A_\pi$  are found through integration over the respective intervals orientation;  $\pi/2$  to  $-\pi/2$ , or  $3\pi/2$  to  $\pi/2$ :

$$A_0 = \int_{-\pi/2}^{\pi/2} \exp \left[ -\frac{\gamma_0}{D_\theta} \cos \theta \right] \quad (3.4)$$

And

$$A_\pi = \int_{\pi/2}^{3\pi/2} \exp \left[ -\frac{\gamma_\pi}{D_\theta} \cos \theta \right] \quad (3.5)$$

Spedden found  $D_\theta = 92 \pm \frac{5}{2} \frac{\text{rad}^2}{\text{hour}}$ , which is similar to growth rates for neurons on glass.

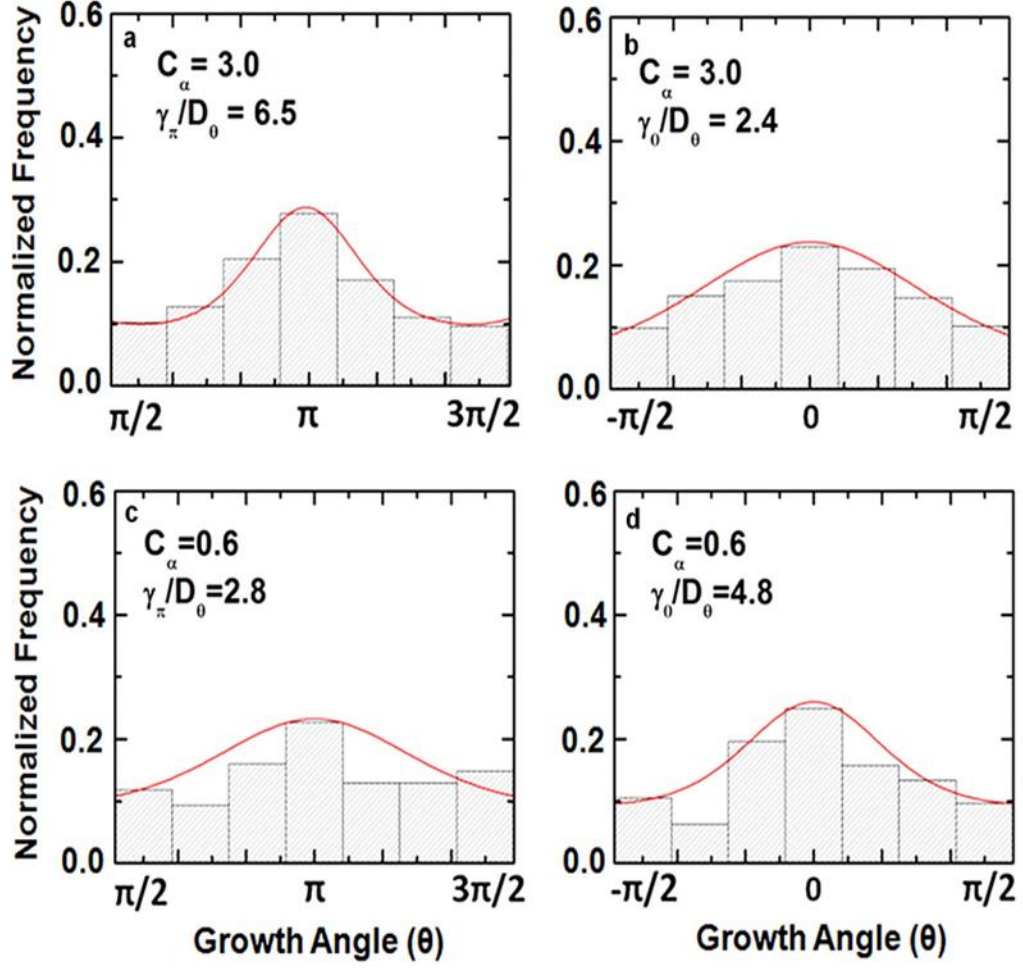


**Figure 3.8.** Normalized angular distributions for different anisotropy parameters and fits centered around 0 and  $\pi$  directions. Red Curve is best fit [7].

Fitting curves to the histograms (figure 3.8) for particular surface asymmetries yield good results (red curves are fits) in particular directions. This shows higher anisotropy biases growth in the  $\pi$  or 0 directions, and neurons advance over the surface significantly faster in the  $\pi$  direction ( $C_\alpha = 3.0$  is  $\gamma_\pi/D_\theta = 2.8$  and  $C_\alpha = 0.6$  is  $\gamma_\pi/D_\theta = 2.8$ ). At lower  $C_\alpha$ , growth in the 0 direction is higher ( $C_\alpha = 3.0$  is  $\gamma_0/D_\theta = 2.4$  and  $C_\alpha = 0.6$  is  $\gamma_0/D_\theta = 4.8$ ).

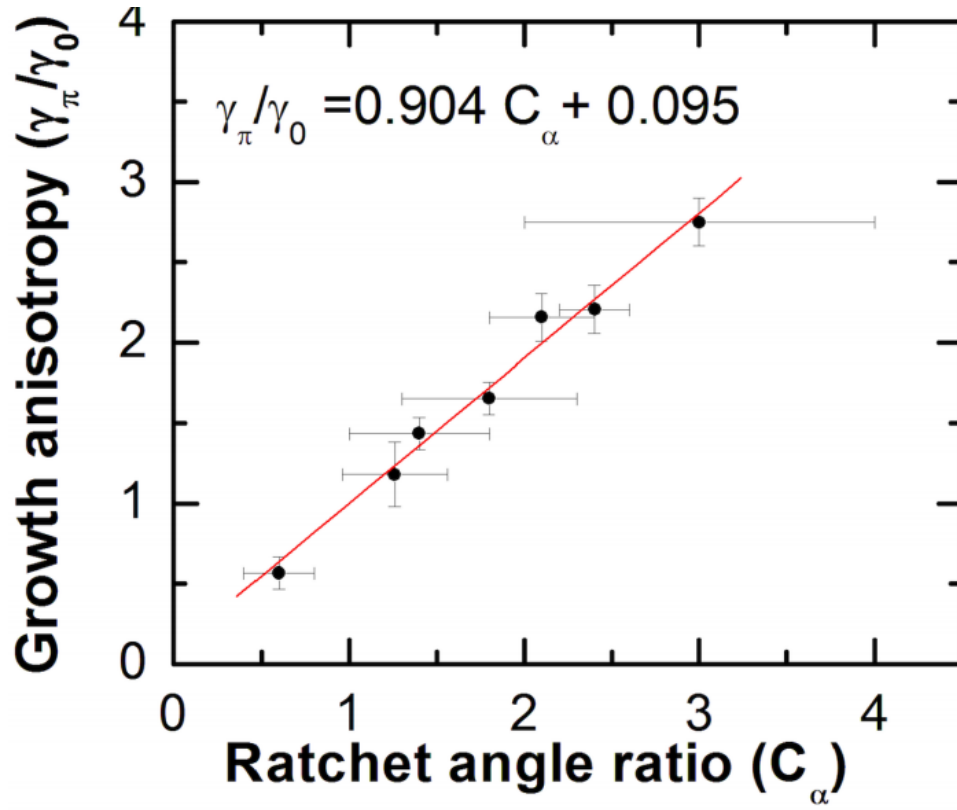


**Figure 3.9.** Growth anisotropy vs anisotropy parameter with fit of  $\gamma_\pi/\gamma_0 = 0.904C_\alpha + 0.095$  [7].

Plotting the ratio of torques  $\gamma_\pi/\gamma_0$  vs  $C_\alpha$  interestingly yields a linear relation of torque anisotropy and surface anisotropy (Figure 3.9). This is the first study to quantify asymmetric surface anisotropy with growth cone torques. This work shows that surfaces can be engineered to bias neuronal growth in a desired direction due to surface curvature inducing membrane curvature.

*Neuron growth as diffusion in an effective potential [67]*

As discussed in Chapter 1, Rizzo [67] analyzed E18 neuron growth velocities on flat PDL coated glass substrates to determine the effective potential that traps neuronal growth cones and biases their random walk search for a target. Using time-lapse imaging over a 8-46 hour interval and Fokker-Planck equation in velocity space, where  $v$  is growth cone velocity,  $V(v,t)$  is the effective biasing potential,  $D$  is the effective diffusion coefficient, and  $P(v,t)$  is the probability density function:

$$\frac{\partial P(v,t)}{\partial t} = \frac{\partial}{\partial v} \left[ \frac{\partial}{\partial v} [V(v,t)] \cdot P(v,t) \right] + D \frac{\partial^2 P(v,t)}{\partial v^2} \quad (3.6)$$

Solutions to this Fokker Planck equation yield effective stationary time integrated potential  $V(v)$  solutions:

$$\frac{V(v)}{D} = -\ln[P(v)] - \ln[N] \quad (3.7)$$

$N$  is the normalization constant for the non-normalized probability distributions. The  $P(v)$  solutions from Fokker Planck have exponential form, and  $\chi^2$  test yields the best fits as Laplace distributions.

$$P(v) \sim \exp(-\kappa|v - v_c|) \quad (3.8)$$

With  $v_c$  being the mean Laplace growth velocity ( $v_c=5.1\mu\text{m}/\text{hour}$ ) and  $\kappa$  is the scaling parameter for curve width ( $\kappa^{-1}=16.7\mu\text{m}/\text{hour}$ ). This gives stationary solutions of  $V(v)$  as

$$\frac{V(v)}{D} = \kappa|v - v_c| - \ln[N] \quad (3.9)$$

Which are “V” shaped potentials (shown below, Figure 3.10a).

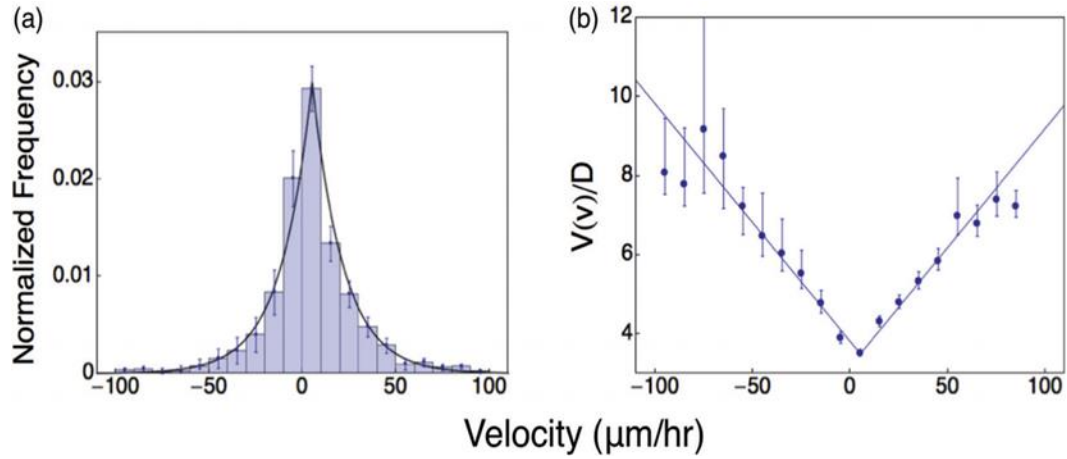


**Figure 3.10.** *a. Normalized angular distributions vs normalized growth cone velocities. b. The resulting effective “V shaped” potential [67].*

Time dependent solutions for  $P(v,t)$  can be found by “transforming the Fokker-Planck equation into a Schrodinger-like partial differential equation”

$q(v,t)$  and Schrodinger-like potential  $V_s$  and probability density  $P_s$ :

$$\frac{\partial q(v,t)}{\partial t} = V_s(v) \cdot q(v,t) + D \frac{\partial^2 q(v,t)}{\partial v^2} \quad (3.10)$$

With a corresponding  $P_s$  and  $V_s$  being

$$P_s(v,t) = \sqrt{P(v)} q(v,t) \quad (3.11)$$

And

$$V_s(v,t) = \frac{V'(v)}{4D} - \frac{V''(v)}{2} \quad (3.12)$$

Which yields two solutions; The symmetric (sym) and asymmetric (asym) eigenstates of integer  $k$

$$P_s(v)_k^{asym} = \frac{1}{\sqrt{\pi}} \sin[k(v - v_c)] \quad (3.13)$$

And

$$P_s(v)_k^{sym} = \frac{2k \cos[k(v - v_c)] - k \sin[k(v - v_c)]}{\sqrt{\pi(4k^2 + \kappa^2)}} \quad (3.14)$$

#### *Growth Cone Edge Dynamics via Fokker-Planck [6]*

Neurites navigate through their environment using the growth cone. In particular, the filopodia and lamellipodia are responsible for directing the growth cone through modulating actin and microtubule dynamics with membrane adhesion molecules and signaling molecules. Studying actively navigating growth cones and their morphology in detail with confocal microscopy gives new insight into how growth cone edge dynamics (filopodia and lamellipodia motion) effect growth. An important question to consider is if growth cones have multiple active filopodia extending and retracting around the growth cone periphery, how do these small growth fluctuations relate to the net motion of the growth cone. To explore this, Betz [6] observes active growth cone edge dynamics in time using a Fokker



Planck model in velocity space to describe growth cone advancement and retraction on a PDL coated glass substrate.

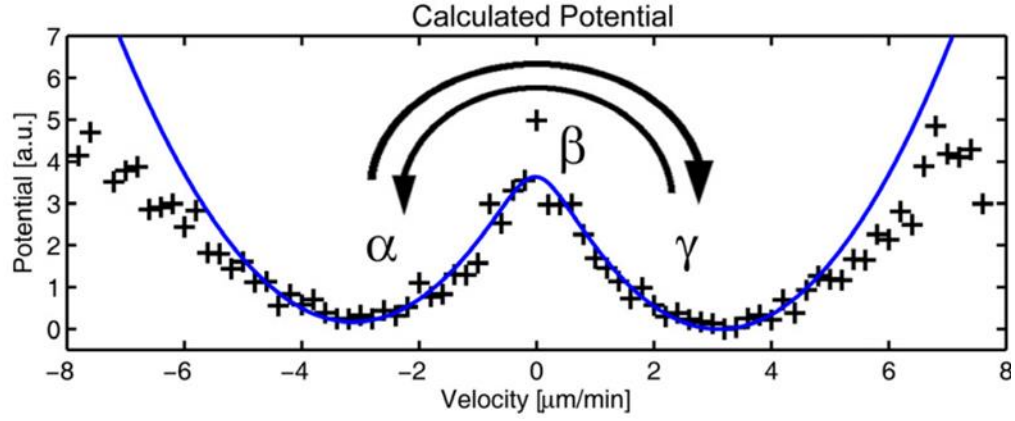


**Figure 3.11.** Growth cone edge potential vs advancement velocity.  $\alpha$  is the retraction state,  $\gamma$  is the extension state, and  $\beta$  is the potential barrier resisting transitions between the two states [6].

Betz [6] analyzed active growth cone behavior by identifying the “center of mass” (COM) of the growth cone, and drawing 500 lines from that COM to points on the periphery and monitored the length modulations of the edge and fitted the data points with a Fokker-Planck model. The wells were found by converting the kymograph-derived histograms to potentials through  $V(v)/D = -\ln(P(v))$ , where  $P(v,t)$  are Gaussian distributions. Figure 3.11 above shows the effective potential of the retraction and extension phases of an active growth cone as a function of outgrowth velocity (for a single growth cone). The bistable system is characterized by  $\alpha$  state (retraction state),  $\beta$  (barrier), and  $\gamma$  (extension state). To further investigate this extension/retraction potential, Betz applied a

focused laser to select points on the growth cone to bias growth. The resulting behavior shows a biased growth direction, indicated by breaking of the potential well in Figure 3.11, which causes a higher likelihood of retraction.

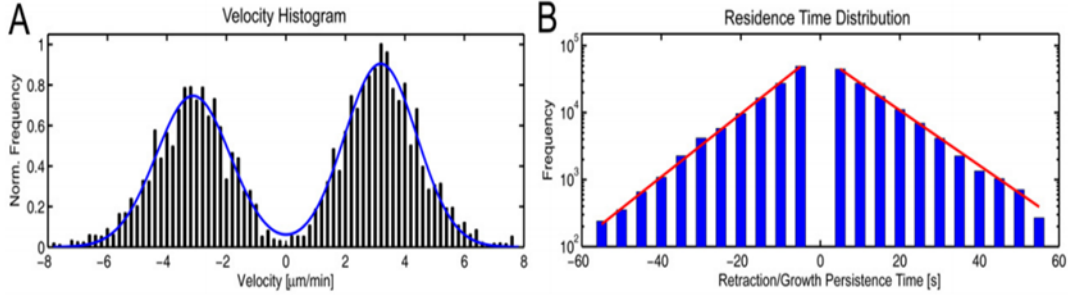


**Figure 3.12.** A. Frequency vs growth velocity with fit. B. Frequency vs Retraction Growth persistence [6].

Additionally, Betz used Kramer's rate to determine how  $\alpha$ ,  $\beta$ , and  $\gamma$  potentials effect the transition rates,  $r_K$ , between wells (For instance,  $\alpha \rightarrow \gamma$  by defeating the potential barrier  $\beta$ ).

$$r_{K(\alpha \rightarrow \gamma)} = \frac{\sqrt{V''(\alpha)|V''(\beta)|}}{2\pi} \exp \left[ -\frac{V(\beta) - V(\alpha)}{\eta} \right] \quad (3.15)$$

If  $\alpha$  and  $\gamma$  are sufficiently similar, and  $\beta$  has a magnitude that allows for transitions, it should be equally probable for the growth cone edge points to advance or retract. If  $\alpha$  and  $\gamma$  do not have similar depth, the deeper one will

become the more stable state, and transition rates to that state will be more common. If  $\beta$  is arbitrarily large, the probability of transition will be very low, and the growth cone will be trapped in in an outgrowth or retraction phase. Here, Betz shows that many important quantities can be extracted by applying stochastic Fokker-Planck theory to neuronal systems. Not only can a bistable potential be found when analyzing growth patterns, transition rates between the states can be calculated, thus yielding accurate characterization of living cellular systems.

*Neuronal alignment on asymmetric textured surfaces [22]*

Elaborating on work done by Spedden [7] with poly(chloro-P-xylylene) tilted nanorod substrates and Rizzo [67] on the diffusive behavior of growth cone navigation, Beighley [22] reanalyzes Spedden's work with both the velocity and angular Fokker-Planck model. He also simulates the growth cone navigate as a particle trapped within a potential well and shows how biased diffusion forces neuronal growth in a particular direction relative to surface feature orientation. The force that a growth cone experiences can be expressed as a Langevin equation.  $m$  is mass,  $v$  is velocity,  $\alpha$  is Stokes drag coefficient,  $F$  is a constant force, and  $\xi$  is a random force.

$$m\dot{v} = -\alpha v + F + \xi(t) \quad (3.16)$$

Beighley [22] described neuronal growth by simulating a 2 dimensional random walk of an ensemble of 100 growth cones in symmetric and asymmetric potential wells to simulate surface anisotropy and biased growth.

Eq 3.17 shows the Fokker-Planck equation for the system, where  $\delta$  is a coefficient that describes the anisotropy of  $\xi$  and  $\kappa$  quantifies the effective force exerted on the growth cone by the substrate.  $\delta$  follows the condition  $-1 \leq \delta \leq +1$ , where increasing magnitude of  $|\delta|$  indicated higher anisotropy. At  $\delta = 0$  and  $\kappa = 0$ , the distribution is symmetric with no bias.

$$\begin{aligned} \frac{\partial P(v, t)}{\partial t} = & \nabla[\gamma(v - v_c)]P(v, t) \\ & + \left[ (1 + \delta) \frac{\partial^2 P(v, t)}{\partial x^2} + (1 - \delta) \frac{\partial^2 P(v, t)}{\partial y^2} \right] P(v, t) \end{aligned} \quad (3.17)$$

Figure 3.13 shows altering these parameters influences the random walk of Brownian particles trapped in a potential well corresponding to surface anisotropy and surface-growth cone forces. Increasing the magnitude of  $\delta$  tends to cause a narrowing of the spread of the distributions. Increasing  $\kappa$  increases the affinity of the Brownian particles to travel in a particular direction.

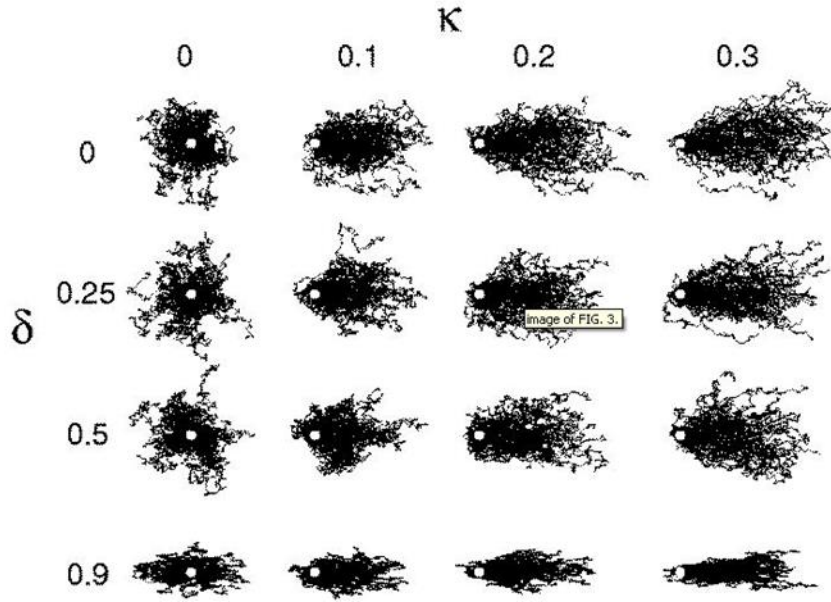


**Figure 3.13.** Simulations of an ensemble of growth cones with different  $\delta$  and  $\kappa$  parameters [22].

#### *Markov Transitions and Fokker-Planck*

Markov and Fokker-Planck theory provides a useful framework to describe probabilistic events without detailed knowledge of the underlying rules or mechanisms. It can be applied to almost any system affected by complicated or random events, most notably cell motility and molecular motor motion.

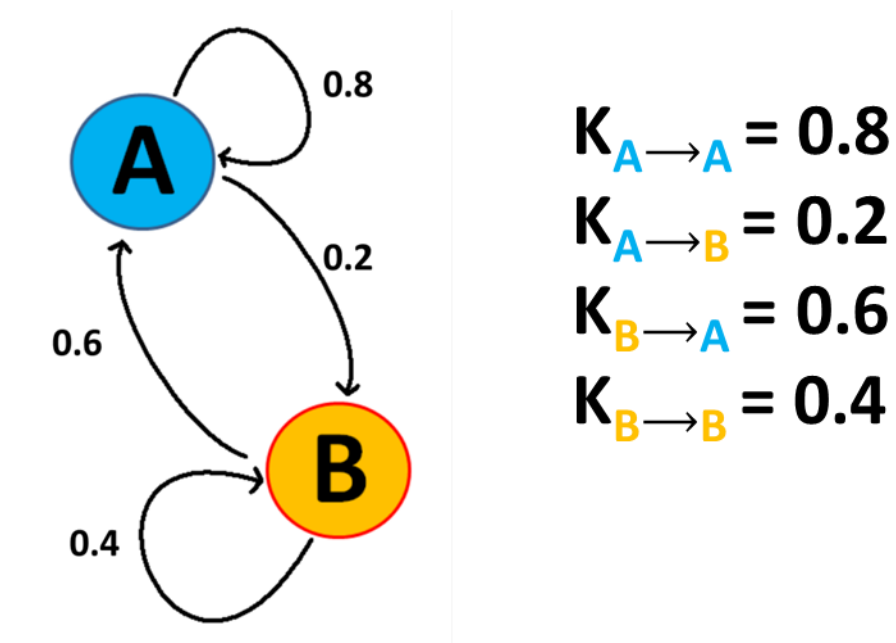


**Figure 3.14.** Markov Transition diagram between states A and B with transition rates  $K$ .

A Markov chain describes the probabilistic transition rates  $k_{i \rightarrow j}$  between states  $i$  and  $j$ . A two state (A and B) Markov chain describes the transition rates of states  $A \rightleftharpoons B$ , can be drawn as in Figure 3.14. These transitions are described by the probability transition matrix. The number of matrix elements is equal to the square of the number of states when a transition exists between all states. The  $k_{i \rightarrow j}$  transitions must satisfy conservation of probability, meaning that the net sum of transition probabilities for a given state must equal one. The transition matrix for the above Markov chain is as follows:

$$P = \begin{vmatrix} 0.8 & 0.2 \\ 0.6 & 0.4 \end{vmatrix} \quad (3.18)$$

For an arbitrarily large number of distinct states  $P$  is given as:

$$P = \begin{vmatrix} k_{i \rightarrow i} & \cdots & A k_{i \rightarrow N} \\ \vdots & \ddots & \vdots \\ k_{N \rightarrow i} & \cdots & k_{N \rightarrow N} \end{vmatrix} \quad (3.19)$$

The transition rates can be calculated given a probability density function (PDF) describing the event. In the case of neuronal pathfinding on micropatterned surfaces, the states and corresponding probabilistic transition rates can be shown with four active and one inactive states:  $k_{\text{state} \rightarrow \text{forward}}$ ,  $k_{\text{state} \rightarrow \text{reverse}}$ ,  $k_{\text{state} \rightarrow \text{left}}$ ,  $k_{\text{state} \rightarrow \text{right}}$ , and  $k_{\text{state} \rightarrow \text{inactive}}$  respectively. Here, the subscript denotes growth cone growth direction. For simplicity, combining Markov chain theory with Langevin derived Fokker-Planck, a more simple two state theory can be used, where the transition rates are between the four driving potentials (and probability densities) left/right growth and forward/reverse growth, or in the case of our ridged micropatterned surfaces,  $0$ ,  $\pi/2$ ,  $\pi$ , and  $3\pi/2$  directions and  $k_{\text{state} \rightarrow 0}$ ,  $k_{\text{state} \rightarrow \pi/2}$ ,  $k_{\text{state} \rightarrow \pi}$ , and  $k_{\text{state} \rightarrow 3\pi/2}$  transition rates.

Transition rates are also calculated by the statistical mechanics approach

that relates a probability density function to transition rates between minima,  $i$  and  $j$ .

$$\frac{k_{i \rightarrow j}}{k_{j \rightarrow i}} = \exp \frac{\Delta G}{k_B T} \quad (3.20)$$

$$\Delta G = \Delta H - T\Delta S + PV \quad (3.21)$$

$\Delta G$  is the free energy activation barrier between the minima in the PDF,  $\Delta H$  is the Helmholtz free energy, and  $\Delta S$  is the system entropy. Additionally, from the probability densities, one can calculate the entropy of the system to quantify randomness as follows:

$$S = - \sum_{i=1}^N P_i \ln P_i \quad (3.22)$$

One can also use Kramer's relation to determine the rate of transition between two wells with an energy barrier [6].



$$r_{K(\alpha \rightarrow \gamma)} = \frac{\sqrt{V''(\alpha)|V''(\beta)|}}{2\pi} \exp \left[ -\frac{V(\beta) - V(\alpha)}{\eta} \right] \quad (3.23)$$

The stochastic motion of a slowly moving object in a fluid can be described as an over damped Langevin (3.24) [105], with Boltzmann constant  $k_B$ , generalized coordinate  $q_i$ , drag coefficient  $\xi$ , mass  $m$ , bath temperature  $T$ , driving potential  $\phi(q_i)$ , stochastic noise  $\eta$ , and external force  $F_{ext}$  (such as fluid flow). The Weiner Process  $W(t)$  can be thought of as the temporal derivative of Gaussian white noise, where the time average  $\langle W(t) \rangle = 0$ , making the time averaged Brownian force  $\langle \sqrt{2K_B T \xi} \frac{d}{dt} W(t) \rangle = 0$ . Since growth cone advance is relatively slow, the objects state and subsequent motion is not affected by how it arrived, meaning the inertial term  $m \frac{d^2 q_i}{dt^2}$  is zero.

$$m \frac{d^2 q_i}{dt^2} = -\xi \frac{dq_i}{dt} + \frac{d}{dx} \phi(q_i) + \Sigma F_{ext} + \sqrt{2K_B T \xi} \frac{d}{dt} W(t) \quad (3.24)$$

Using conservation of probability in phase space, one can derive a corresponding Markov-Fokker-Planck equation (3.25) [105], with probability density  $P_i$  of state  $i$ , and diffusion constant  $D$ . The Markov transition rate  $k_{ij}(x)$  are the matrix elements of the transition matrix  $\mathbf{K}$  acting on probability vector  $\mathbf{P}$  in the probability equation  $\frac{d}{dt} \mathbf{P} = \mathbf{K} \cdot \mathbf{P}$ . These elements are defined as the transition rate between chemical state  $i \rightarrow j$  as a function of position, such as

transition rates  $\text{ATP} \rightleftharpoons \text{ADP} + \text{P}$ , with the properties  $k_{ij} = k_{i \rightarrow j}(x)$ , for  $j \neq$

$i$ ,  $k_{ii}(x) = -\sum_{i \neq j}^N k_{i \rightarrow j}(x)$  for diagonal elements, and  $\sum_{i=1}^N k_{ij}(x) = 0$  [105].

The transition rates can be thought of as an Arrhenius equation,  $k_{ij}(x) =$

$Ae^{\Delta\mu_{ij}/k_B T}$ , where  $\Delta\mu_{ij}$  is the chemical energy change of the transition and A is

the maximum rate [105]. In the case of ATP hydrolyzing to ADP+P,  $\Delta\mu =$

$\mu_{\text{ATP}} - \mu_{\text{ADP+P}}$ , with subscripts indicating reactants.

$$\frac{\partial}{\partial t} P_i(t) = D \frac{\partial}{\partial x} \left[ \frac{-F_{\text{ext}} + \frac{d}{dx} \phi_i(x)}{K_B T} P_i(t) + \frac{\partial}{\partial x} P_i(t) \right] + \sum_{j=1}^N k_{ij}(x) P_j(t) \quad (3.25)$$

The first term on the right is the probability flux (3.26),

$$J_i(x) = -D \left[ \frac{-F_{\text{ext}} + \frac{d}{dx} \phi_i(x)}{K_B T} P_i(t) + \frac{\partial}{\partial x} P_i(t) \right] \quad (3.26)$$

So the Markov-Fokker-Planck equation can be simply written as (3.27), with the Fokker-Planck terms to the right side, and the Markovian terms to the left.

$$\frac{\partial}{\partial t} P_i(t) - \frac{\partial}{\partial x} J_i(x) = \sum_{j=1}^N k_{ij}(x) P_j(t) \quad (3.27)$$

Velocities can be defined as (3.28)

$$V(F_{ext}, [fuel]) = \int dx \sum_{i=1}^N J_i \quad (3.28)$$

By knowing  $J_i$  and using the condition  $-F_{ext} + \frac{d}{dx} \phi_i(x) = 0$  at  $V(F_{ext}, [fuel]) = 0$ , the maximum force exerted by the growth cone can be found.

Solving the Fokker-Planck equation for  $\Phi$  yields solutions for driving potentials as a function of probability density:

$$\Phi_i = -\eta \ln P_i \quad (3.29)$$

The potentials can be used to calculate the transition rates between the potentials wells that indicate growth direction. For example, the following PDF represents a transition from state A to state B (left well and right well, respectively).

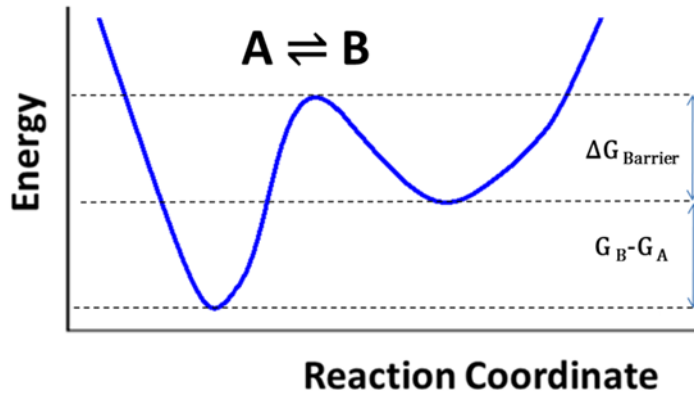


**Figure 3.15.** Potential energy profile vs reaction coordinate (entropy like coordinate), showing the well energy and barrier energy for a transition.

### Energy Transduction

It is instructive to discuss growth cone efficiency. In thermodynamics, the efficiency of a heat engine is defined as the ratio of power output to power input,  $\varepsilon = -F \cdot v / \dot{Q}$ , where  $F$  is the force the growth cone exerts,  $v$  is the velocity, and  $\dot{Q}$  is the transition rate of heat transfer from the cold reservoir to the hot reservoir. For a growth cone, heat transfer rate is not a good indicator of power input, since it operates at isothermal conditions, and thermal fluctuations vary widely. A better description defines the efficiency as the ratio of mechanical power output with chemical power input [105], where  $F$  is the force the growth cone exerts and  $v$  is its velocity,  $k$  as the Markovian transition rate for the process. Energy conservation is required such that total power dissipated  $P$  by the growth cone is:

$$P = F \cdot v + N * k \Delta \mu \quad (3.29)$$

$$(3.30)$$

$$P > 0$$

$$N * G = N * \Delta G^\circ - N * k_B T \ln \left[ \frac{G_A + G_{Barrier}}{G_B} \right] \quad (3.31)$$

Where  $k$  and  $v$  are functions of fuel concentration and external forces,  $N$  is the number of hydrolysis events fueling the growth cone. (Eq. 3.29) Complemented by (E. 3.20) (for ATP),

where  $N * \Delta G$  ( $-20k_B T$ ) is the system free energy change and  $N * \Delta G^\circ$  ( $-12.3k_B T$ ) for ATP hydrolysis) is the free energy liberated from fuel use [105]. (Eq. 3.31) Is true by virtue of maintaining equilibrium,  $\frac{k_{i \rightarrow j}}{k_{j \rightarrow i}} = \exp \frac{G_i - G_j}{k_B T}$ , at every state, where the  $G$ s are the free energies at the state [105].

### *Flashing Potentials [49]*

A good toy model for gaining insights into growth cone physics is the two state “Flashing Potential” model. Of course, a two state model would be an oversimplification for most systems.

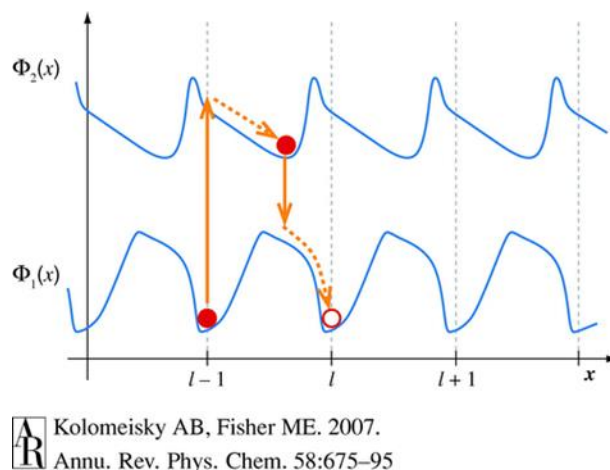


**Figure 3.16.** Two flashing potentials (blue), changing to move a Brownian particle one step further [49]. The particle (red) in potential  $\phi_1$  is trapped within a well at  $l-1$ . If  $\phi_1$  “flashes” to  $\phi_2$  the particle is moved into an unstable state and moves to a new stable state between  $l-$  and  $l$ . When  $\phi_2$  “flashes” to  $\phi_1$ , the particle moves to a new stable state at  $l$ . This process advances the particle in steps of  $l$ .

It is instructive to apply this framework to a general Brownian particle which quickly transitions between two periodic free energy potentials  $\phi_1(x)$  and  $\phi_2(x)$  with periodicity  $l$  (figure 3.16.), two transition rates,  $k_1$  and  $k_2$ , corresponding to fuel consumption and fuel synthesis, respectively. These states can be turning, extension, and retraction states for the growth cone. The two wells are shifted with respect to a constant energy and  $l$  period. In the first state in potential  $\phi_1$ , the particle is at “rest” at the bottom of the potential well at  $l-1$ , while fluctuating by Brownian motion within the well without escaping. Some

process occurs (possibly  $\text{ATP} \rightarrow \text{ADP} + \text{P}$  for a motor) that undergoes the transition  $\phi_1 \rightarrow \phi_2$ . During this transition, the particle is moved to the new potential, and as a result, falls to the bottom of the well of  $\phi_2$ . The potential transitions again, where  $\phi_2 \rightarrow \phi_1$ , and the particle rolls into the next well of  $\phi_1$ . The entire cycle of transitions,  $\phi_1 \rightarrow \phi_2$  to  $\phi_2 \rightarrow \phi_1$ , results in the particle advancing one well forward. The process can and must also run in reverse. The stability of the particle in each state  $\phi_i$ , depth of the wells, and a presence of an external force can cause the particle to hop between wells back or forth.

### 3.3 Neurons on Micropatterned PDMS Parallel Ridges

We culture neurons on micropatterned PDMS (poly(dimethyl siloxane)) to explore how surface topographic features, such as ridges with varying spacing) affect neuronal polarization and contact guidance. Three types of surface topographies were used, denoted as surface 1, surface 2, surface 3. Neurons were allowed to grow on the surfaces for 2-96 hours post culture, and imaged fluorescently at specific time-points, to observe their contact guidance behavior over time. Time integrated data (All times for a given surface) were used to characterize the time independent contact guidance behaviors for each surface. This thesis shows embryonic rat cortical neurons are sensitive to surface topography, and each surface has a unique time integrated angular distribution.

Additionally, this thesis shows that neurons grown on the large spaced surface shows time dependent growth behavior. The following are the most recent results of a continuing unpublished project.

### *PDMS Surface Fabrication and Characterization*

To produce micropatterned surfaces, 10ml of PDMS solution (Silgard) was poured over a 25x25mm<sup>2</sup> diffraction grating to produce micropatterned surfaces with three types of surface topographies, with elastic modulus of ~20MPa. Surface 1 =  $0.821 \pm 0.024\mu\text{m}$ , surface 2 =  $1.59 \pm 0.03\mu\text{m}$ , and surface 3 =  $3.27 \pm 0.05\mu\text{m}$  spaced parallel ridges with ratchet-like cross sections (Figure 17), with feature heights of  $0.115 \pm 0.002\mu\text{m}$ ,  $0.156 \pm 0.003\mu\text{m}$ , and  $0.723 \pm 0.011\mu\text{m}$ , respectively (Figure 3.17). The PDMS surfaces were left to polymerize for 48 hours at ambient laboratory conditions, before being carefully peeled away from the diffraction gratings before being cured at 60°C for 1-3 hours. To ensure the pattern was successfully transferred to the PDMS, AFM was used to characterize the surfaces (Figure 3.17 and 3.18). The cured PDMS was scanned in AC AFM mode with AC160TS-R3 cantilevers to determine surface profile and ridge orientation over a 10-20  $\mu\text{m}^2$  area. The same area was imaged in force spectroscopy AFM mode to determine elastic modulus, showing an elastic modulus of ~20MPa for all surfaces. The magnitude of the



substrate modulus will attenuate the efficiency of traction forces applied to the surface by energy loss to surface deformation.

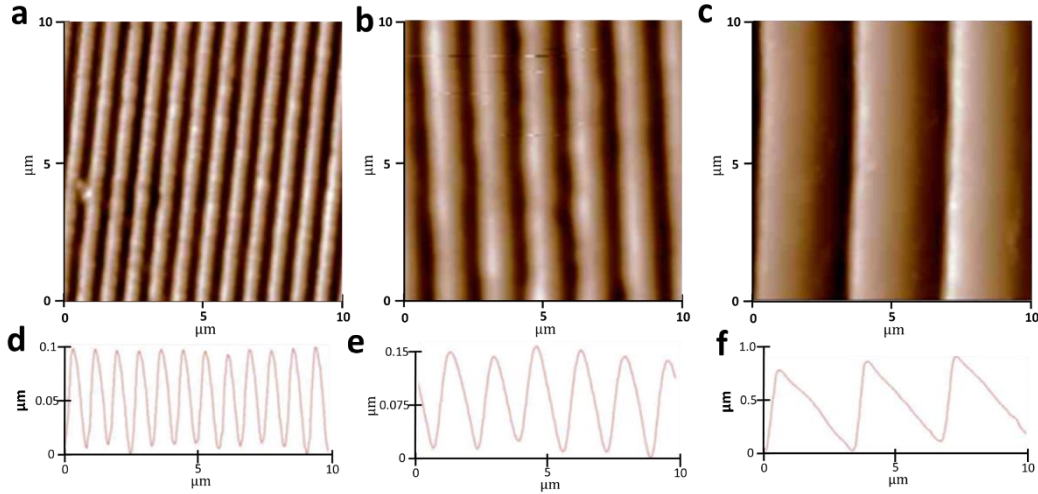


**Figure 3.17.** AFM topography images of ridges with cross sections. *a*, *b*, and *c* are  $10\mu\text{m} \times 10\mu\text{m}$  AFM topography images of the  $0.821 \pm 0.024\mu\text{m}$ ,  $1.59 \pm 0.03\mu\text{m}$ , and  $3.27 \pm 0.05\mu\text{m}$  spaced PDMS surfaces, respectively. With *d*, *e*, and *f* as the  $0.75\mu\text{m}$ ,  $1.5\mu\text{m}$ , and  $3.0\mu\text{m}$  cross sections, respectively. Here, the anisotropy direction faces left.

AFM force spectroscopy shows discrepancies between surface elastic moduli on different locations on the ridges (Figure 3.19). This is most likely not due to elastic modulus difference, but from perceived elastic modulus difference due to a change in contact area. If the tip is more like a punch geometry, there should be minimal geometry interference since only the apex can make contact. For pyramidal or cone type geometries, such as the AC240TS-R3 and AC160TS-

R3 series of cantilevers, the angle might cause secondary contact points that effect adhesive forces between tip and sample and miscalculated contact area.

Additional force maps (not shown) performed at different scan angles (~90 degrees) fixed this issue.

The surfaces were cut into  $\sim 4 \times 4 \text{ mm}^2$  surfaces pieces whose corners were carefully glued (silicone glue) to the bottoms of 35mm culture dishes and left to sit for greater than 72 hours. The grating orientation was etched on the culture dishes with an arrow indicating the  $\pi$  direction. Prior to culture, the surfaces were then coated with 5ml of 0.1mg/ml PDL for 2-3 hours, rinsed with distilled water three times, and UV irradiated for 45+ minutes.

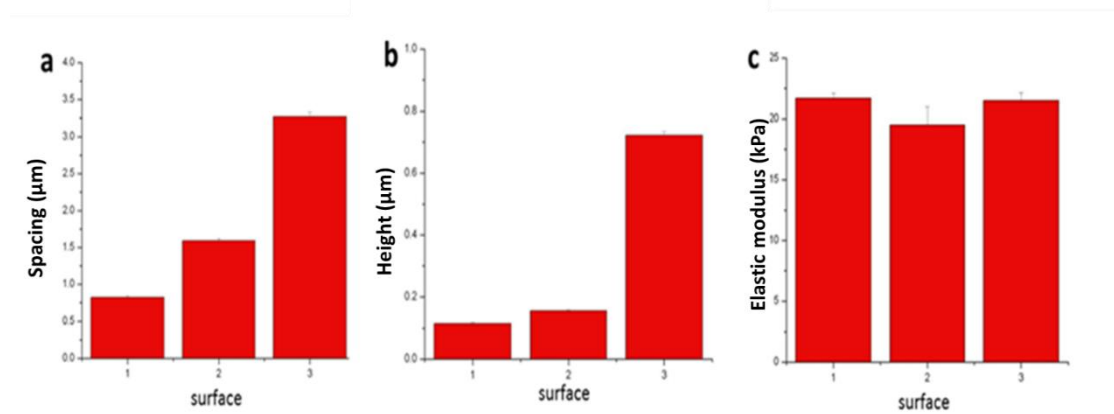


**Figure 3.18.** Result of AFM elastic characterization on the 3 surfaces. a. feature spacing in  $\mu\text{m}$ : surface 1 =  $0.821 \pm 0.024 \mu\text{m}$ , surface 2 =  $1.59 \pm 0.03 \mu\text{m}$ , and surface 3 =  $3.27 \pm 0.05 \mu\text{m}$  spaced parallel ridges with ratchet- like cross sections. b. Feature height in  $\mu\text{m}$ . surface 1 =  $0.115 \pm 0.002 \mu\text{m}$ , surface 2 =  $0.156 \pm 0.003 \mu\text{m}$ , and surface 3 =  $0.723 \pm 0.011 \mu\text{m}$ , respectively. c. Surface elastic modulus in MPa: nominal elastic modulus is  $\sim 20 \text{ MPa}$  for all surfaces.

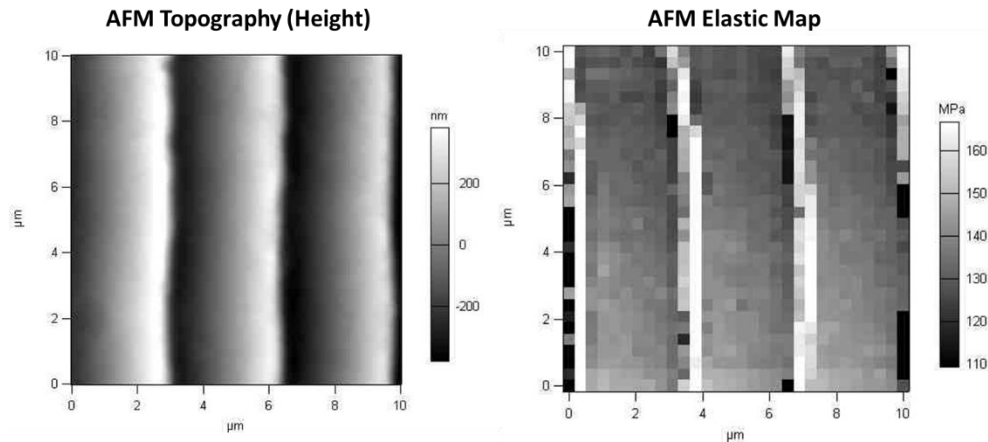


**Figure 3.19.** AFM topography (left) and elastic modulus map (right) of example PDMS surface showing that cantilever geometry effected elastic modulus of the ridges. Artificially high elastic moduli were measured on the steepest parts of the ridges since the cantilever would engage the surface with the probe face, rather than the probe apex.

### *Neuron Culture*

E18 fetal rat cortical neurons were obtained from Tufts University Department of Biomedical Engineering. Freshly isolated cortices were incubated for 20 minutes in Trypsin at 37°C. Trypsin was inhibited with soybean Trypsin inhibitor. Neurons were dissociated, separated by centrifuge, and suspended in Neurobasal Medium and supplemented with GlutaMAX, b27, and pen/strep. The cells were counted with a hematology analyzer and plated at 170 cells/mm<sup>2</sup> on the

micropatterned PDMS surfaces at 37°C and incubated between 2 and 96 hours in 2 or 8 hour increments before measurement.

### *Fluorescent Imaging and Image Processing*

Fluorescent imaging was performed on a Nikon Eclipse Ti Inverted fluorescent microscope using the FITC filter with excitation/emission of 495 nm/521 nm. Neurons were stained with 4ml of 0.5mg/ml fluorescein diacetate in 1xDPBS. Immediately after administering the stain, the neurons were imaged through the PDMS with a 10x Nikon Plan Fluor objective at ambient temperature ~25°C. Between 10 and 70 images were acquired for each time point. Example fluorescent images and time integrated angular distributions are shown for surface 1, 2, and 3.

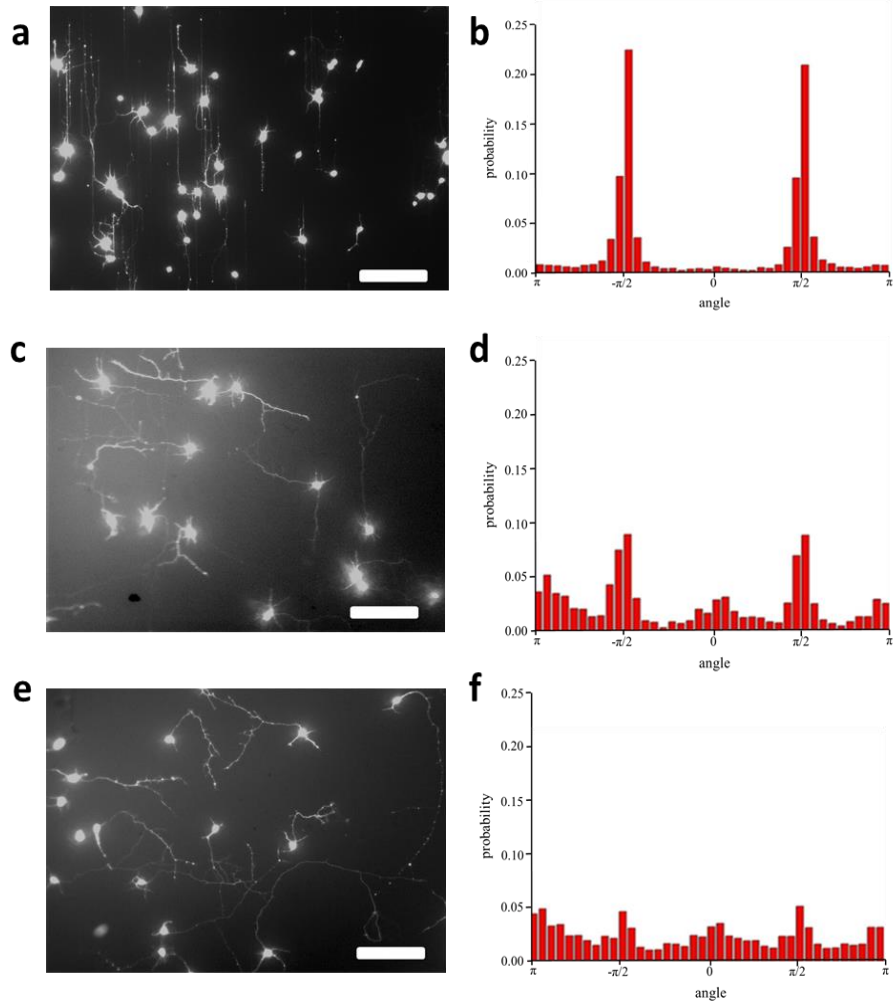


**Figure 3.20.** Example fluorescent images and normalized time integrated histograms of angular distributions. *a.* Surface 3 with *b.* probability distribution (bin width  $0.05\pi$ ). *c.* Surface 2 with *d.* probability distribution (bin width  $0.05\pi$ ). *e.* Surface 1 with *f.* probability distribution (bin width  $0.05\pi$ ). The two large peaks follow the ridges, with the right peak growing “up” in *a*, and the leftward peak growing “down”. Scale bar on *a*, *c*, and *e* is  $100\ \mu\text{m}$ .

Axons were traced using the NeuronJ add-on for ImageJ. Angular distributions were obtained from a custom Mathematica program, with the angles defined by Figure 3.7b. The axons were broken into  $\sim 20\mu\text{m}$  (31.25 pixels) segments in the Mathematica program, which were used to make the angular distributions as seen in Figure 3.20 b, d and f from the fluorescent images. The distributions were then normalized into probability densities. We analyzed distributions at time points, 2, 4, 6, 8, 8, 10, 12, 14, 16, 16, 24, 32, 40, 48, 72, and 96 hours for the surface 3, and 16, 24, 48, and 96 hours for surfaces 1 and 2. Figure 3.21 shows an example of neurite tracings in ImageJ, with purple lines as the traced neurites.

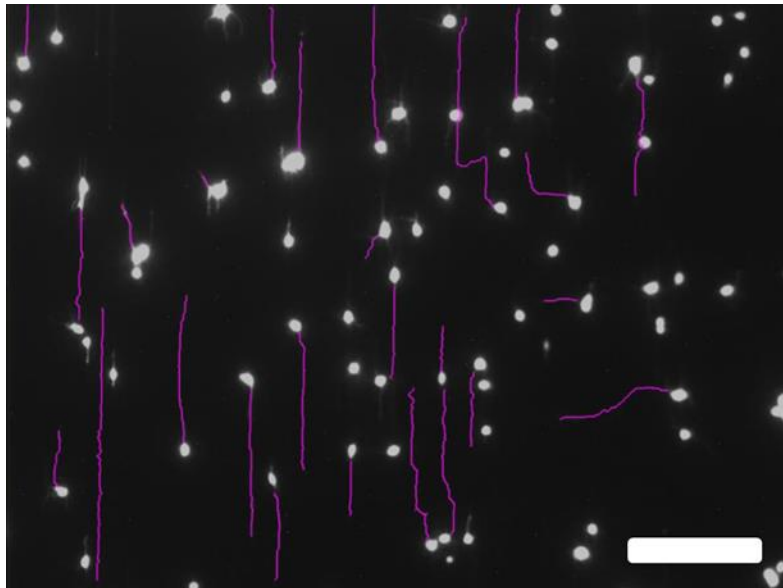


**Figure 3.21.** Example of neurite tracing of fluorescent images in ImageJ. Purple lines are traced neurites. Scale bar is  $100\mu\text{m}$ .

### 3.4 Results

E18 rat cortical neurons were seeded onto 7-16 samples of each surface. Neurons were observed with a Fluorescein Diacetate Live stain using a bottom up long range 10x objective at various times post culture (above). Neurons grown on our micropatterned PDMS surfaces displayed surface dependent contact guidance angular distributions. Surface 3 had the largest ridge spacing and the most dramatic effect on neurite outgrowth, with ~90% of the time integrated growth being parallel to the surface features, with very sharp peaks centered at  $\pm 0.5\pi$ . Approximately ~10% of time integrated growth being perpendicular to the surface features.

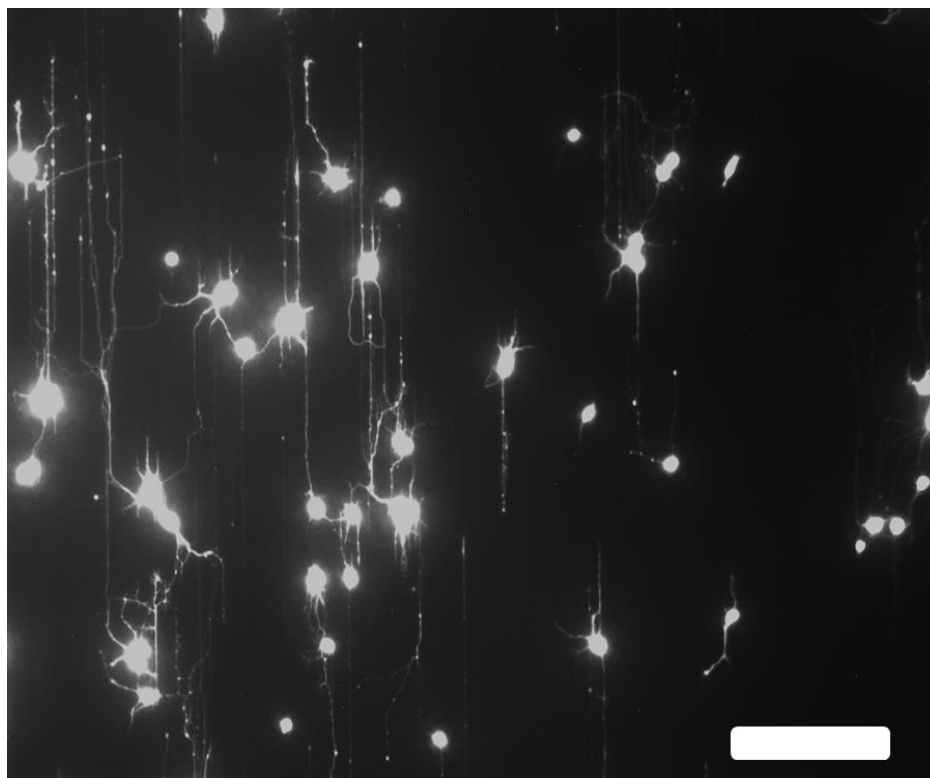


**Figure 3.22.** *Fluorescent image of neurons grown for 72 hours on surface 3. Ridges run vertically. Scale bar is 100 $\mu$ m.*

Figure 3.22 shows neurons at 72 hours post culture grown on surface 3, with the ridges in the image running vertically. It is clearly seen that the majority of neurites are very straight and grow parallel to the ridges. When a neurite does not sprout along a ridge, it will grow until it engages a ridge and turns. This can be seen in figure 3.22 when neurites sprout perpendicular to the ridge direction, and then make an abrupt turn in the  $\pm 0.5\pi$  directions. A good example of this can be seen in figure 3.23.

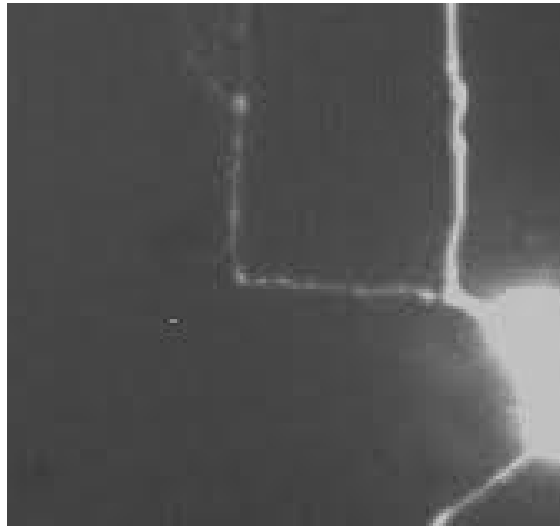


**Figure 3.23.** *Fluorescent image of neurons grown for 72 hours on surface 3 displaying abrupt direction change. Ridges run vertically.*



Surface 2 had about half the ridge spacing, and showed ~55% parallel time integrated growth, and ~45% perpendicular time integrated growth, with distinct peaks centered around the  $\pm 1\pi$  and  $\pm 0.5\pi$  directions. Figure 3.24 is a representative image of neurons grown on surface 2 at 96 hours post culture. In stark contrast to surface 3, neurite can be seen growing in both parallel and perpendicular directions. The neurites are also less straight since they are not always following a small amount of ridges. Instead, neurites are more free to deviate from the parallel and perpendicular direction, but still primarily grow along the  $\pm 1\pi$  and  $\pm 0.5\pi$  directions.

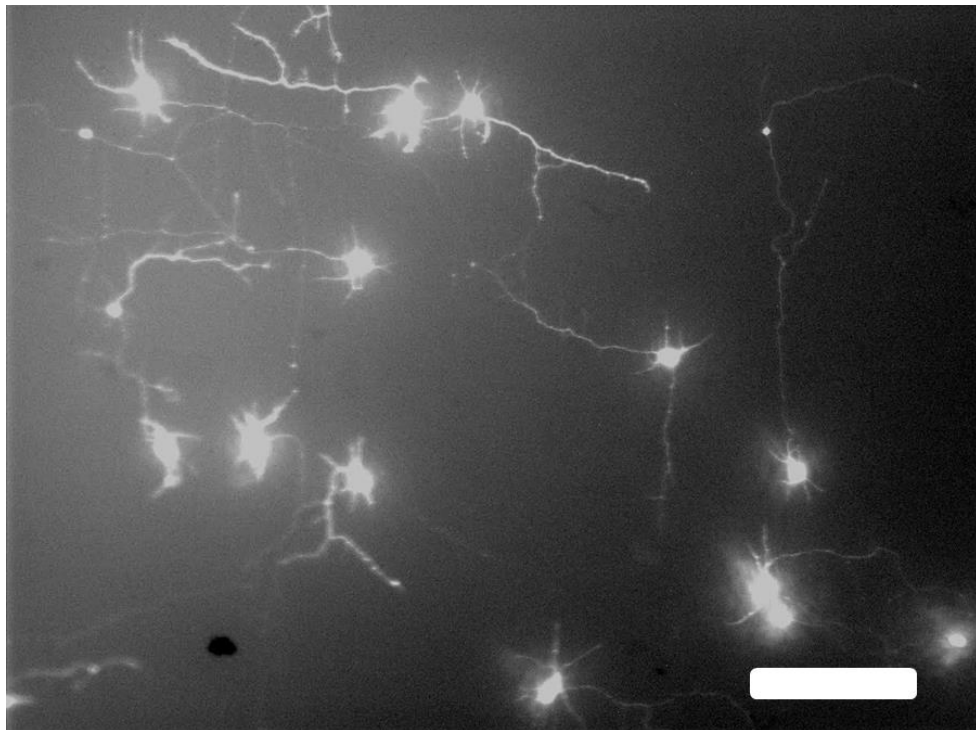


**Figure 3.24.** *Fluorescent image of neurons grown for 96 hours on surface 2. Ridges run vertically. Scale bar is 100 $\mu$ m.*

Surface 1 had about one quarter the spacing of surface 3, and showed weakest direct growth overall. However, surface 1 displayed distinct peaks centered around the  $\pm 1\pi$  and  $\pm 0.5\pi$ , with ~55% of time integrated growth being perpendicular, and ~45% of time integrated growth being parallel to the ridges. Figure 3.24 shows neurites grown on surface 1 at 96 hours post culture. The neurite in figure 3.25 look similarly distributed to neurites on surface 2, but show slightly less biased growth in the  $\pm 0.5\pi$ .

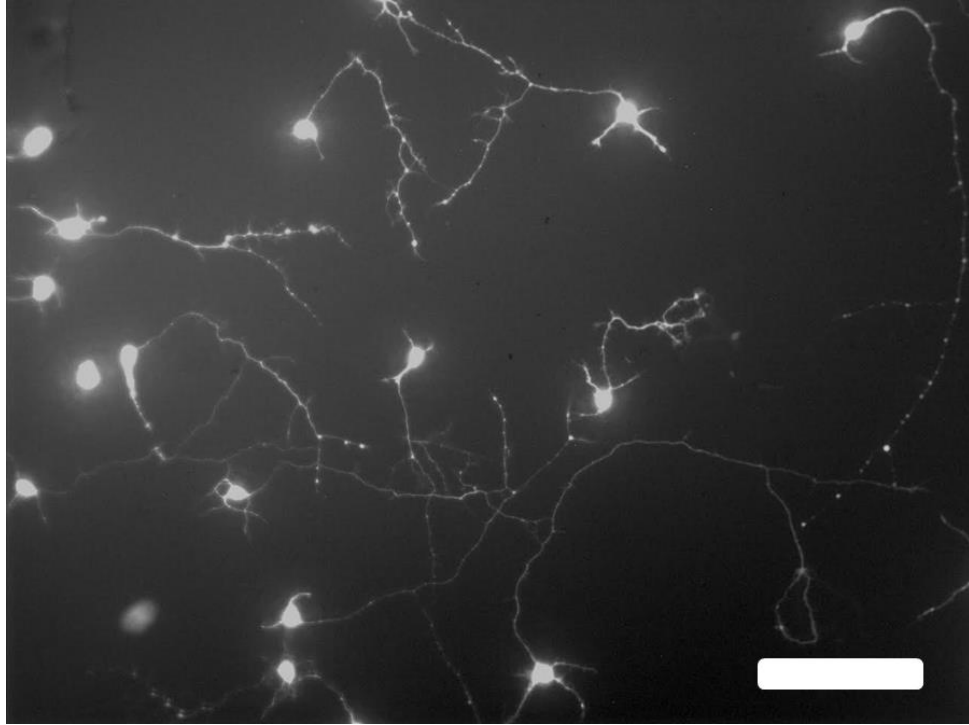


**Figure 3.25.** *Fluorescent image of neurons grown for 96 hours on surface 1. Ridges run vertically. Scale bar is 100 $\mu$ m.*

### *Time Integrated Growth*

We observed different growth effects for the various surfaces. To characterize the time independent contact guidance characteristics on the surfaces, we collapsed all time points measured into “time integrated” plots for probability density and growth potentials. We calculate the potentials with the Eq.  $\Phi = -\ln(P) + C$ , where C is a constant that “zeros” the tallest bin in the potentials to 0 potential. This allows us to analyze the effect the surface has on the neuron, and

have a better understanding of transition rates between growth states. Here, we show the probability densities and potentials with a bin size of  $0.05\pi$  to show the detailed growth profiles.

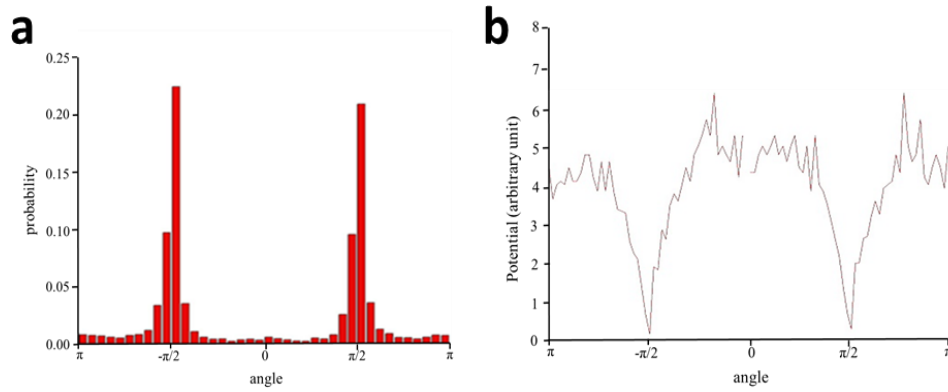


**Figure 3.26.** *a. Time integrated probability densities and b. potentials for surface 3.  $N=14,418$   $20\mu\text{m}$  segments were used.*

Neurons grown on surface 3 primarily display perpendicular growth. Figure 3.26 shows the normalized time integrated data from all experiments as angular distributions (Fig 3.26a) and potential (fig 3.26b). Axons are more likely to grow parallel to ridges, with a peak growth centered at  $\pm 0.5\pi$ . Once they begin growing in a direction, it is unlikely for them to significantly turn (e.g. from  $0.5\pi$  to  $-0.5\pi$  radians) due to the large potential barrier between  $-0.5\pi$  and  $0.5\pi$ . There are also small peaks around the perpendicular directions,  $0$  and  $\pi$ , with peaks of

about 0.01. The growth cone is most likely to become trapped in the wells at  $\pm 0.5\pi$ , and lightly trapped at 0, and  $\pi$ . Peaks at  $\pm 0.5\pi$  are very sharp, while peaks at 0 and  $\pi$  are much more widely distributed.

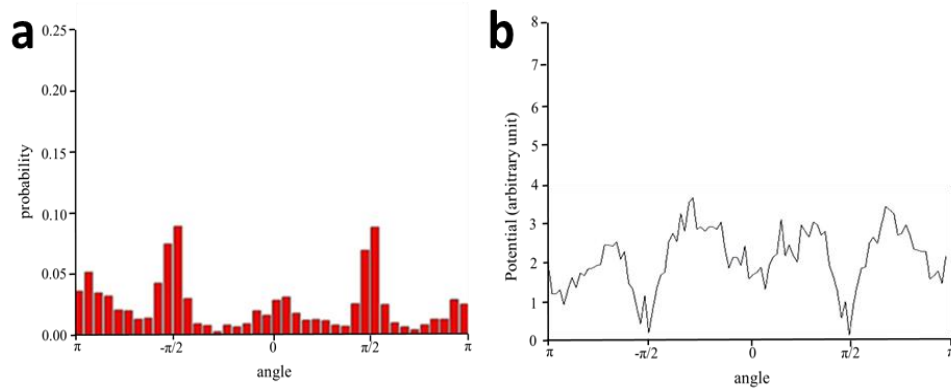


**Figure 3.27.** *a. Time integrated probability densities and b. potentials for surface 2.  $N=5,268$   $20\mu\text{m}$  segments were used.*

Neurons grown on surface 2 show much smaller peaks in both parallel and perpendicular directions compared to surface 3, but still with dominant peaks at  $\pm 0.5\pi$  with probabilities  $\sim 0.1$ . Neurons are half as likely to grow at 0 and  $\pi$  compared to  $\pm 0.5\pi$ . Interestingly, the peak shapes show the same trend as with surface 3, where the peaks at  $\pm 0.5\pi$  are sharper than the peaks at 0 and  $\pi$ . Figure 3.27b shows smaller potential barriers between wells, which allows for higher transition rates between the wells.

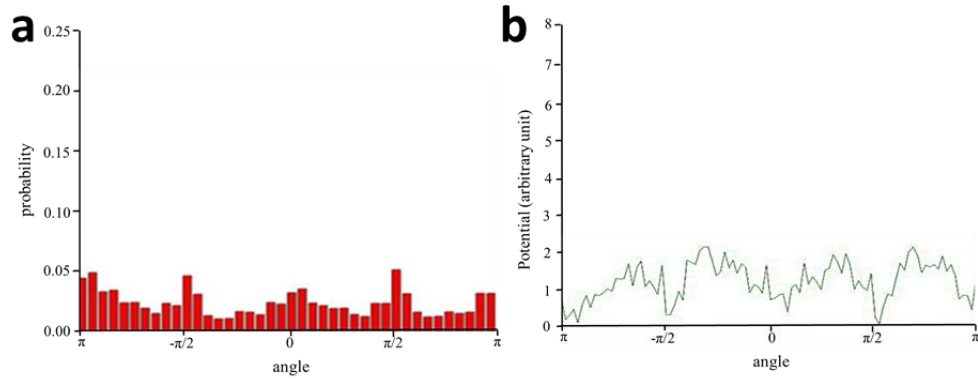


**Figure 3.28.** *a. Time integrated probability densities and b. potentials for surface 1.  $N=10,239$   $20\mu\text{m}$  segments were used.*

Neurons grown on surface 1 show much less preferential growth, however they appear to be affected by surface anisotropy similarly as surface 2. The peaks at  $\pm 0.5\pi$ ,  $0$ , and  $\pi$  are very similar, but still show sharper distributions at  $\pm 0.5\pi$ . Since the spacing is much smaller than the other surfaces, the contact sensing ability of the growth cone becomes muted. Figure 3.28 shows a lessening of the potential barriers between the wells, which shows transitions between the wells are more likely as feature spacing decreases.

These results show the growth cone is very sensitive to topographic features. A Kolmogorov-Smirnov test comparing each distribution shows a significant difference between surface 1, 2, and 3 ( $P < 0.001$ ). Features with wider spacing show highly directional growth in the  $\pm 0.5\pi$  directions, while lessening the spacing results in decreasing directionality. It could be inferred from these data that as feature spacing is decreased beyond the growth cone topographic

sensing resolution the results will begin to resemble totally random growth as with a flat surface. These results suggest that contact guidance is dependent on how many features the growth cone contact area encounters at a given time. Since the growth cone has an average width of  $\sim 5\mu\text{m}$ , as feature spacing is decreased, the growth cone encounters more features at a given time, which allows the growth cone to more evenly distribute its focal adhesions across regions of high curvature. For large spacing, the growth cone can only encounter a few features at once, which will result in a higher concentration of focal adhesions about a feature, increasing the growth cone feature coupling which aligns the growth cone to the features.

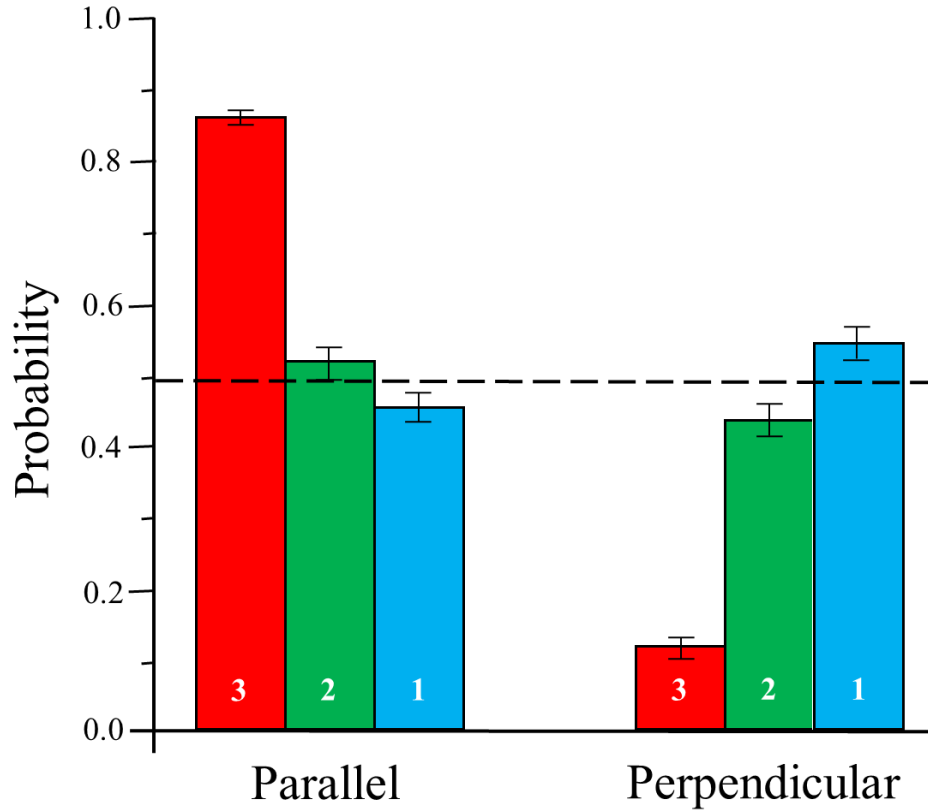


**Figure 3.29.** Average probability of growth in the parallel (left 3 bars) and perpendicular (right 3 bars) directions. Red is surface 3, Green is surface 2, blue is surface 1, and teal is control (C). Parallel direction percents for surface 3, 2 and 1 are  $0.86 \pm 0.02$ ,  $0.52 \pm 0.05$ ,  $0.44 \pm 0.04$ , respectively. The perpendicular directions for surfaces 3, 2, and 1 are  $0.14 \pm 0.03$ ,  $0.42 \pm 0.05$ ,  $0.53 \pm 0.05$ , respectively. The dotted line represents random growth. Surface 3 ( $N=16$  samples), Surface 2 ( $N = 4$  samples), Surface 1 ( $N= 4$  samples).

All surfaces show peaks in the 0 and  $\pi$  directions, with surface 3 showing the least amount of perpendicular growth, and surface 2 and surface 1 showing similar perpendicular growth. It has been suggested by Rajnicek [27] that feature



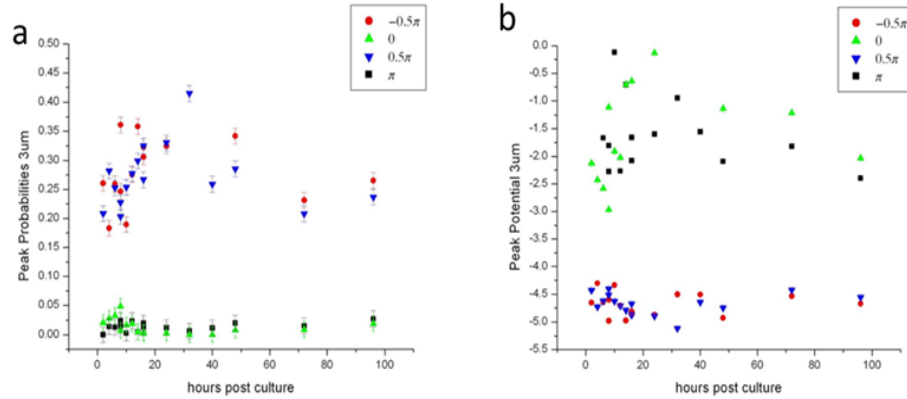
height affects cortical neurite feature crossing on micropatterned surfaces by <10% between 0 and 1  $\mu\text{m}$  feature heights. The range of heights on surface is ~110-730nm. This could have affected the peaks on surface 3 accounting for some of the much higher directionality in the  $\pm 0.5\pi$  directions (the peaks differences at  $\pm 0.5\pi$  between surface 2 and surface 3 are 0.15). This would not account for the increase in  $\pm 0.5\pi$  between surfaces 1 and 2, since they differed by <40nm. However, Rajnicek only characterized “neurite crossing”, which was any neurite that grew across multiple features. By collapsing the time integrated data for all 3 surfaces by defining “perpendicular growth” as any growth angles between  $0.25\pi > \theta > -0.25\pi$  and  $0.75\pi > \theta > -0.75\pi$ , and defining “parallel growth” as any growth angles between  $0.25\pi < \theta < 0.75\pi$  and  $-0.75\pi < \theta < -0.25\pi$ , we show the degree of perpendicular and parallel growth (figure 3.29). By loosely adjusting for height for surface 1, by taking 10% from parallel and adding it to perpendicular, we see that there is still a preference for growth in the parallel directions. We also see that when feature spacing is decreased, the preferred growth direction evolved from parallel to perpendicular.

### *Time Dependence of Growth*

Here, we combine the peak bin and it’s two adjacent bins to explore time dependence of growth by observing the total area of the peaks. This set of experiments should be further investigated to determine if there is a time

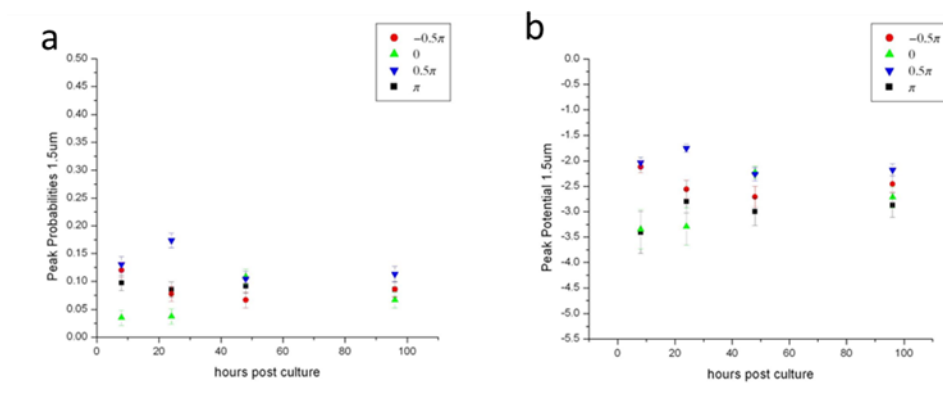
dependent trend, considering the differences in the  $0.5\pi$  peaks within a single time point should be identical if the sample size was sufficiently large, since there is no topographic bias to favor one direction over another. Variations in these peaks suggest more data is needed for all time points.

Figure 3.30a and b show the peak growth probabilities for the 4 peaks at  $\pm 0.5\pi$ , 0 and  $\pi$  for surface 3. The sharpest peaks are at  $\pm 0.5\pi$ , with very wide distributions at 0 and  $\pi$ . The potential for growth in the  $\pm 0.5\pi$  directions are large and relatively constant in time. The probabilities of growing in the 0 and  $\pi$  directions do not significantly vary, and are within error of each other. Since these data show the potential remains relatively constant in time, the variations of probability in time are most likely a random effect. Early time points show lower peak probabilities due to small sampling size ( $N \sim 100$ , for 2, 4 and 8 hours). Additionally, at early time point, very few observed neurons sprouted neurites long or fluorescently bright enough to identify or measure, due to weak fluorescents of the neurites compared to the soma. It cannot yet be ruled out that the apparent increase in parallel growth from 2-16 hours is due to a physical effect or neurite selection bias. Additionally, neurons measured at 12 hours and early only account for  $\sim 14\%$  of all measured segments on surface 3, so this should not affect the conclusions of the previous section. Time points at 72 and 96 hours post culture are within error of each other. Additionally, excluding pre 16 hour time points shows little significance between the remaining data.



**Figure 3.30.** Maximum angular distribution peaks vs time in hours for surface 3. Red indicates the  $0.5\pi$  peak, blue indicates the  $-0.5\pi$ , green indicates  $0\pi$ , and black indicates  $\pi$ .

Neurons grown on surface 2 show little time dependent contact guidance. Growth in the  $\pm 0.5\pi$  direction appear constant in time, and individual peaks from the same time point vary too much to show a trend. Neurons grown on surface 1 also show little time evolution between the peaks. As time increases, the peaks at  $\pm 0.5\pi$ ,  $0$ , and  $\pi$  appear to converge while still maintaining peaks at  $\pm 0.5\pi$  (Figure 3.31 a and b). Figure 3.29 shows this surface causes the neurites to favor perpendicular growth. Additionally, these results should be further investigated to determine these variations are real, or due to small sample size for early time points. 16 and 24 hours accounts for 10% and 20% of measured segments on surface 2, respectively. 16 and 24 hours accounts for 3% and 10% of measured segments on surface 1, respectively. No significant evolution is observed between the 48 hour and 96 hour time points for both surface 1 and 2.



**Figure 3.31.** Maximum angular distribution peaks vs time in hours for surface 2. Red indicates the  $0.5\pi$  peak, blue indicates the  $-0.5\pi$  peak, green indicates  $0\pi$ , and black indicates  $\pi$ .

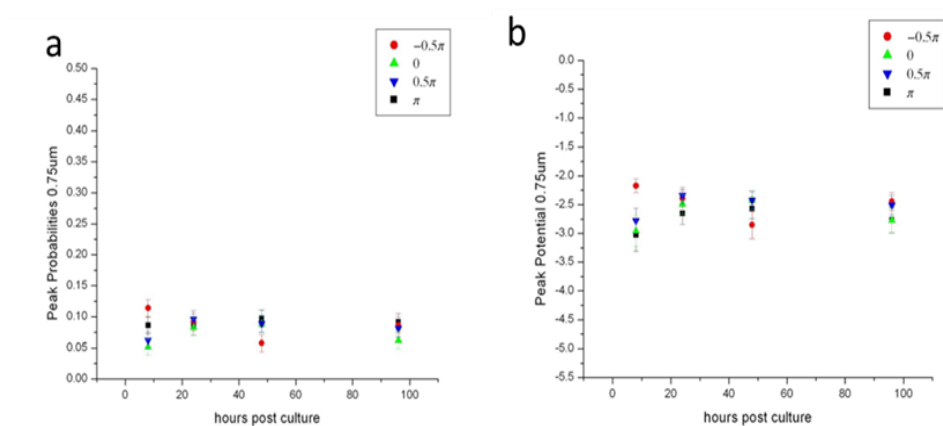


**Figure 3.32.** Maximum angular distribution peaks vs time in hours for surface 1. Red indicates the  $0.5\pi$  peak, blue indicates the  $-0.5\pi$  peak, green indicates  $0\pi$ , and black indicates  $\pi$ .

## *Conclusions*

As the neurites explore, they extend radially from the soma at a constant rate. As time elapses, the neurite has had more of a chance to encounter a feature and engage it, which results in stabilization of the distributions in time. However, the average outgrowth velocity for our neurons on average is  $\sim 11 \mu\text{m}/\text{hour}$ , which shows for all surfaces, the neurites should encounter a feature before our initial measurement window of 2-8 hours begins. Additionally, later time points are composed of much larger data sets which give a better indication of the true distributions, and better reflect the population ( $N \sim 100$  20 micron segments for  $< 4$  hours). Earlier data sets (e.g.  $< 20$  hours), are composed of smaller amounts of data with much wider  $\pm 0.5\pi$  distributions, and do not show smooth distributions.

Once the neurons are seeded onto the PDL coated PDMS, membrane deformations due to PDMS curvature induce focal adhesion sites to diffuse to areas of the highest membrane curvature, as suggested by Jang's work [54]. These somal deformations signal neurite initiations. As the first growth cones advance and mature, they grow over the surface in response to topographic cues that direct the growth [7, 10, 24, 25]. At the ridge peaks and valleys, the surface curvature induces localization of adhesion molecules [6, 27]. This anchors the growth cone to those areas, and reinforces actin connections to the adhesion molecules [18, 38, 39]. This increases traction at sites of high curvature, and directs growth parallel or perpendicular to the ridges. If the growth cone encounters multiple ridges, the

distribution of traction forces most likely influences the neurite to grow perpendicular to the ridges, as evidenced by the neurite distribution width in perpendicular and parallel directions (however, this must be further investigated using confocal microscopy and fluorescent tagging of integrins). We theorize, as ridge spacing is decreased, the neurite angular distributions should approach a random distribution since the adhesion sites would be evenly distributed instead of localized along a ridge.

Neuronal growth on our micropatterned surfaces affect growth cone steering through ridge frequency and possibly height. These are most likely dependent on the scale of the features compared to the soma or growth cone [27, 33, 52, 107]. If the soma adheres on top of multiple ridges, it might initiate many polarized neurites on top of different ridges. The number of ridges and their curvature and height will deform the membrane differently, and cause different distributions of focal adhesions. Less localized focal adhesions will lead to less geometry related coupling.

According to Rajnicek's study [27] on hippocampal neurons, there is a <10% variation in neurite feature crossing rates for square wave cross-sectional grooved surfaces. For our ratchet cross-sectional geometries, the effect of focal adhesion focusing on areas of high membrane curvature should be less, since apex geometry of the grooved surfaces have sharper edges, and the PDMS casted ridges are much smoother. This steep difference of high curvature of the grooved surfaces compared to the PDMS curvature leads to the crossover probability for

different height to be modified by surface adhesion by focal adhesions, thus the PDMS surfaces will have  $\ll 10\%$  crossover probability difference between the different patterns.

Jang's study [54] suggest that the soma and neurites rearrange their cytoskeletons based on feature curvature, influenced by adhesion of the cell to the areas of curvature. Jang showed neurites are more likely to be sprouted by areas where the soma plasma membrane was highly deformed, and that neurites are more likely to preferentially adhere to features with high curvature (Figure 3.6). Neurons grown on our surfaces appear to follow this trend, by having sharp probability distributions along the micropatterned ridges than against them. Neurites growing in the parallel directions showed much wider distributions, which indicates the neurites are still more likely to grow along areas of sharper curvature, by not fully growing along the pure  $0$  or  $\pi$  directions. Once a neurite begins to grow in one of the perpendicular directions, it has more angular freedom than it would if it was trapped in the sharp potentials at  $\pm 0.5\pi$ , and diffuses around the potential more. Here we show how neurons respond to different topographic cues with three PDMS surfaces. We see that decreasing feature spacing promotes perpendicular growth to the features. We have grown neurons on three types of PDMS surfaces, and analyzed neurite angular orientation and characteristics to our surface features over time. Our results show that surface topography can dramatically influence neuronal growth. We find that cortical neurons grown on surface 3 exhibited the most alignment with the PDMS ridges

in the  $\pm 0.5\pi$  direction, followed by surface 2, then 1. The extreme peak differences with surface 3 compared to surfaces 2 and 2 could be attributed to the much taller ridges of surface 3, such that if surface 1 had shorter ridges, there could be a greater likelihood for the neurites to grow in the perpendicular directions. Since the surface area of 1 tall ridge is greater than the surface area of 1 short ridge of similar spacing. Since the growth cone has a finite area, ridge height would affect how many ridges a single growth cone could encounter as it wraps around the ridge peak. However, surface 1 shows the most alignment in the  $\pm 1\pi$  and  $0\pi$  directions, followed by surface 2, then 3. This indicates growth cone sensitivity to ridge spacing due to the number of ridges encountered by a single growth cone. Additionally, neurites extending along the ridges have sharp probability distributions, while neurites extending perpendicular to ridges have very wide distributions. This effect is most likely due to the existence of a critical ridge/growth cone engagement angle, which should be researched further. At angles above this critical angle, the growth cone is most likely to engage the ridges and grow parallel to them, while if a growth cone engages ridges below this critical angle, it is more likely to grow perpendicular to the ridges. The width of the distributions in these directions results from this type of engagement. Since the growth cone is undergoing a biased random walk across the PDMS surface, and we see growth cones are more likely to stay growing parallel to a ridge once they begin, it makes sense to say a growth cone growing perpendicularly to a ridge will feel a strong potential to diffuse in the parallel directions without becoming trapped in the  $\pm 0.5\pi$  potential wells. Our data indicates a time



evolution of growth on surface 3, but not surface 1 or 2, however this must be further investigated due to the variations in parallel sample peaks, as evidenced by the repeats at 8 and 16 hours. However, the potential for growth in the  $\pm 0.5\pi$  directions for all surfaces appears to be constant or insignificant. After a short time of extension, they engage a ridge and continue growing along it. There should be little difference between neurites growing in  $+0.5\pi$  or  $-0.5\pi$  directions, and thus more data are needed for all surfaces.

## **CHAPTER 4**

### **Load Rate and Temperature Dependent Mechanical Properties of the Cortical Neuron and Its Pericellular Layer Measured by Atomic Force Microscopy**

The following was published in Langmuir, 2016: M. Simon, M. Dokukin, V. Kalaparthi, E. Spedden, I. Sokolov, and C. Staii, *Load Rate and Temperature Dependent Mechanical Properties of the Cortical Neuron and Its Pericellular Layer Measured by Atomic Force Microscopy*, Langmuir, 1111-1119 (2016) [40].

#### **4.1 Overview**

When studying temperature response of mechanical properties of cells by an indentation technique, it is important to take into account nontrivial pericellular interface (or pericellular “brush”) which includes a pericellular coating and corrugation of pericellular membrane (microvilli and microridges). Here we use atomic force microscopy (AFM) to study mechanics of cortical neurons taking into account the presence of the above pericellular brush surrounding cell soma. We perform a systematic study of the mechanical properties of both the brush layer and the underlying neuron soma, and demonstrate that the brush layer is likely responsible for the low elastic modulus ( $<1$  kPa) typically reported for

cortical neurons. When the contribution of the pericellular brush is excluded, the average elastic modulus of the cortical neuron soma is found to be 3-4 times larger than previously reported values measured under similar physiological conditions. We also demonstrate that the underlying soma behaves as a non-viscous elastic material over the indentation rates studied (1-10  $\mu\text{m}/\text{sec}$ ). As a result, it seems that the brush layer is responsible for the previously reported viscoelastic response measured for neuronal cell body as a whole, within these indentation rates. Because of the similarities between the macroscopic brain mechanics and the effective modulus of the pericellular brush, we speculate that the pericellular brush layer might play an important role in defining the macroscopic mechanical properties of the brain.

## **4.2. INTRODUCTION**

The mechanical properties of living cells are an integral part of their functional behavior, contributing to their ability to exert and resist forces with respect to the surrounding environment. Such mechanical interactions play an important role in many cellular processes in neurons including the generation of traction forces, cytoskeletal rearrangements, adhesion, and mechanosensing during growth [99, 27]. The elastic properties of cells, particularly in the brain, are known to be an important indicator of health at both the bulk tissue and at individual cell level. A significant change in cell stiffness has been observed in

Alzheimer's disease, multiple sclerosis, advancing age, inflammation, and cancer [27, 109 -113]. The components of the nervous tissue (neurons, glial cells, extracellular matrix proteins) form a nonlinear viscoelastic material, whose mechanical response depends on the magnitude and loading rates of the externally applied forces [31, 114]. Moreover, the mechanical properties of individual cells are dependent on a multitude of heterogeneous characteristics including the cell nucleus [3, 111], various cytoskeletal components and molecular motors (actin, tubulin, myosin II motors) [3, 4, 44, 111, 113, 115], as well as the properties of the pericellular interface [43, 116].

The pericellular interface was suggested to be called “pericellular brush” because of exponential force dependence measured by atomic force microscopy (AFM), which is typical for polymeric brushes. The pericellular brush consists of membrane protrusions, microridges, microvilli, and proteoglycans with linker proteins (the latter is generally referred as pericellular coat or glycocalyx), which surround most eukaryotic cells. A component, which typically serves as a backbone to the glycocalyx matrix, hyaluronan (HA), is anchored directly to the plasma membrane of the cell [42]. The length of this pericellular brush ranges from a few hundred nm to tens of  $\mu\text{m}$  depending on the cell type [42, 110]. Microridges and microvilli can reach several microns in size [117]. Recent studies have shown that pericellular coat is important for many cell processes including migration and differentiation [118], cell-substrate adhesion [119-122], mechanotransduction [123, 124], and may serve as a protective layer during

inflammation [125]. The pericellular coat is also known to affect cell motility. There is evidence that an increase in concentration of the HA component of the brush results in an increase in the motility and metastasis of dysfunctional cell types such as cancer cells [124]. The pericellular coat has been visualized on many cell types including fibroblasts [126], PC3 cells [127], several types of cancer cells [110, 124], chondrocytes [119], and epithelial cells [128].

However, these previous measurements of the pericellular brush were rather qualitative, by estimating only the size of this layer. Several methods, including environmental electron microscopy [128], exclusion assays [128], fluorescent labeling [129], optical tweezers [129], atomic force microscopy (AFM) [130] have been used to study pericellular coat and the membrane protrusions. AFM has the advantage of high spatial resolution as well as precise positioning and high degree of control over the magnitude and the orientation of the applied forces. A quantitative method to characterize the pericellular brush (is using so-called brush model) has recently been developed with the help of AFM [43, 116, 120, 131]. Using the Alexander-de Gennes brush model, one can quantitatively describe the pericellular brush layer with the length and effective brush density [43, 110 of the brush layer. Moreover, AFM is one of the most versatile tools for measuring the basic parameters of cell mechanics, such as deformations within a rather broad range of strains [132], and the cell elastic modulus [115, 133].

Determining the elastic modulus via AFM involves collecting force vs. indentation curves, i.e. loading and unloading the AFM probe while measuring the cellular response. Although cells are complex composite objects, it has recently been shown that the cell body can be treated as homogenous and isotropic material when the brush layer is taken into account and a relatively dull probe is used [134]. Nevertheless, the majority of works reported in literature consider cells in the homogenous material approximation without taking into account the pericellular brush interface. When measuring viscoelastic properties with AFM within this approximation, the viscoelastic modulus displays a loading-rate dependence [132, 135, 136]. The pericellular coat of cells has also been shown to be viscoelastic, with loading-rate dependent elastic modulus [127]. Values reported for the elastic modulus of pericellular matrix vary greatly depending on cell type, yielding values less than 10 Pa for prostate cancer cells [127], up to 10's of kPa for cartilage [137]. In addition, optical tweezers have been used to determine viscoelastic properties of the pericellular matrix on living cells [127, 129], and AFM indentation has been used to characterize isolated HA matrix on glass [138].

Neurons from the central nervous system have been characterized as mechanically compliant cells, with average values of the elastic modulus, for both brain tissue and isolated cortical and hippocampal neuron somas, in the range 0.2 - 1kPa [4, 44, 31, 115]. The general viscoelastic signature observed for other types of cells (elastic modulus depending on the loading-rate) was also observed

for individual neuron soma [31, 132, 139] as well as for glial cells and bulk brain tissue. These previous experiments have also demonstrated that the typical cytoskeletal components (actin, microtubules, and intermediate filaments) cannot be the only elements responsible for the measured viscoelastic behavior [31].

Here we report the first observation of a pericellular brush layer on neurons and perform the first mechanical characterization of both the brush layer and the underlying soma (hereinafter, soma is the cell body without the pericellular brush layer) of living cortical neurons. We show that the previously reported rate-dependent, viscous behavior of the elastic modulus of neurons [31, 50, 132] is due to the viscoelastic properties of the brush layer. The underlying neuron soma behaves purely elastically, with no loading-rate dependence in the range studied (1-10  $\mu\text{m/s}$  indentation speed). We also demonstrate that the compliant pericellular brush is mainly responsible for the relatively low ( $<1$  kPa) values of the Young's modulus typically measured on cortical neurons. When the brush layer is excluded, the elastic modulus of the soma is found to have values in the range 1-2 kPa.

We have previously reported that the cytoskeleton of cortical neurons, and thus their mechanical properties, is highly sensitive to changes in ambient temperature, with bulk elastic modulus values increasing by 100-300% with a drop in ambient temperature from 37°C to 25°C [115]. Additionally, many measurements of living cells, as well as measurements on the pericellular brush or

brush model systems were performed at room temperature (20-25° C) [110, 127], while others were done at physiological relevant temperatures (37°C) [129, 140]. Using the AFM measurements and the brush model [43, 120, 131] we determine how changes in temperature affect the measured properties of both the cellular brush layer and the underlying soma for living neurons. We demonstrate that a decrease in temperature results in an increase in apparent brush density, accompanied by a decrease in apparent brush length. We also show that the isolated neuron soma (cell body without the brush layer) undergoes an increase in the elastic modulus with decreasing temperature. This result is consistent with the previously reported dependence observed for the whole cell (i.e. cell body or soma and brush layer). This is the first study that analyzes the temperature dependence of both the pericellular brush and isolated soma for any type of living cell.

## **4.2. MATERIALS AND METHODS**

Rat cortices were obtained from Tufts Medical School isolated from embryonic day 18 rats and cultured according to pre-established protocols (see Supplementary Material). Force-volume maps were recorded on an Asylum Research MFP-3D-Bio AFM (Asylum Research/Oxford Instruments, Santa Barbara, CA) integrated with an inverted Nikon Eclipse Ti optical microscope (Nikon, Inc.). The AFM probe was optically positioned over each cell via 40x



bright field microscope. 10 cells were measured for each temperature. The same cells were measured for five indentation rates, 1, 2, 5, 7, and 10  $\mu\text{m}/\text{sec}$ , and then again at 1  $\mu\text{m}/\text{sec}$  to rule out potential cytoskeletal rearrangements or cell damage caused by the AFM indentations. Height data obtained from these force-volume maps was used to isolate the curves taken closest (*i.e.* within a disk of radius 2  $\mu\text{m}$ ) to the topmost point of the soma (force curves were taken at each indentation rate for every cell). These curves were analyzed to derive the elastic modulus and brush parameters. Details of sample preparation and the AFM measurement method are described in the Supplementary Materials.

#### *Data analysis methods*

The models described below were developed for a known geometry as a sphere over either a plane, a hemisphere or a sphere. Thus, we processed only the force curves from the top area of the cell. Specifically, we take the force curves in the surface points around the top when the incline of the surface is  $<10\text{-}15$  degrees. To identify such curves, the AFM image of cell heights was used (the height image was collected as a part of the force-volume data set; the effective radius of the cell was derived from these images after taking into account the cell deformation, see the Supplementary Information for detail).

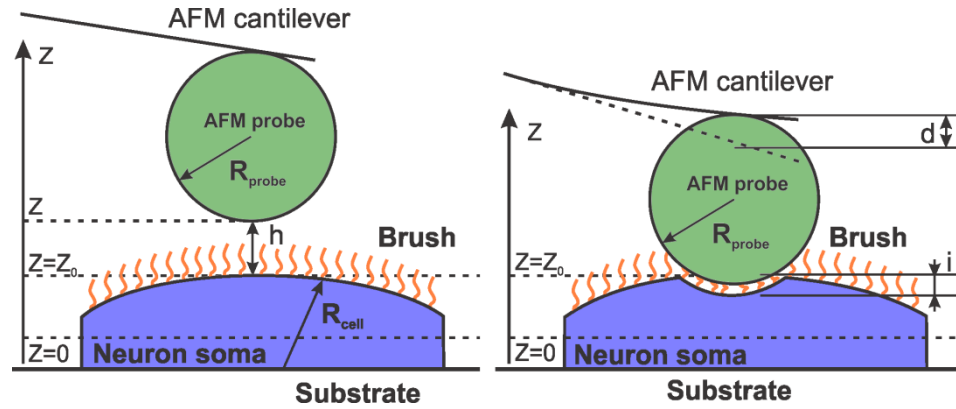


**Figure 4.1.** Schematic of the AFM indentation experiment. The cell body is represented as a two - layer structure (pericellular brush and cell body, or soma).  $Z$  represents the relative vertical scanner position of the cantilever,  $d$  is the cantilever deflection,  $Z_0$  is the nondeformed position of the soma,  $i$  is the deformation of the soma,  $Z = 0$  is the vertical scanner position corresponding to the maximum cantilever deflection,  $d$  is the cantilever deflection, and  $h$  is the separation between the soma and the AFM probe [40].

The Hertz model and its modifications [141-143] are typically used to extract the elastic modulus of cells when a spherical indenter is used. All these models require the cell to be a homogenous and isotropic material with a well-defined smooth surface. To take into account the pericellular brush, the brush model was developed [43, 110, 120, 131]. As it was shown in the previous works, after separating the contribution from the brush layer, the remaining cell body demonstrated behavior consistent with considering the cell body as a homogenous and isotropic medium, when the indentation was smaller than 10-20% of the cell body height [134]. The model allows for the derivation of the elastic modulus of

the cell body as well as the parameters of the pericellular brush. This model, previously described in detail [43, 110, 120, 131], is briefly outlined here.

As shown in the geometry of the indentation experiment (Figure 4.1), the distance  $h$  between neuron soma and the spherical indenter can be described by the following equation:

$$h = Z - Z_0 + i + d \quad (4.1)$$

The relative piezo position of the AFM scanner  $Z$  and the cantilever deflection  $d$  are directly measured with AFM when collecting the force-load curves. The other two parameters, deformation of the cell soma  $i$  and non-deformed position of the sample  $Z_0$  are determined by fitting the data, as described below. It should be noted that the pericellular brush layer is obviously deformed as well. However, molecules of the pericellular coat do not have a clear boundary. As a result, the deformation of the pericellular layer would be hard to define experimentally. From a theoretical point of view, we do not need to introduce such concept in our present model. The deformation of the soma  $i$  depends on the cell elastic modulus  $E$ . Since we are using a spherical indenter, the deformation of the soma is calculated using the Hertz model, which gives [43, 120]:

$$i = \left[ \frac{3k(1-\nu^2)}{4E} \left( \frac{R_{probe} + R_{cell}}{R_{probe} \cdot R_{cell}} \right)^{1/2} \right]^{2/3} d^{2/3} \quad (4.2)$$

Here,  $E$  is the elastic modulus of the soma,  $k$  is the spring constant of the cantilever,  $\nu$  is the Poisson ratio (following previous publications, hereafter  $\nu = 0.3$  is used in this work; specific choice of this value doesn't influence any particular conclusion of this work besides the value of the elastic modulus of soma),  $R_{probe}$  and  $R_{cell}$  are the radii of curvature of the AFM probe and cell, respectively.  $R_{probe}$  was found before performing the indentation experiments ( $R_{probe} = 6.5 \mu\text{m}$ ).  $R_{cell}$  has been measured from the AFM topographical image of the cell obtained in the force-volume mode, and corrected by the soma deformation  $i$ . Typical values of the cell radius were in the range of 10-20  $\mu\text{m}$ .

Combining Eq. 4.1 and Eq. 4.2 yields:

$$h = Z - Z_0 + \left[ \frac{3k(1-\nu^2)}{4E} \left( \frac{R_{probe} + R_{cell}}{R_{probe} \cdot R_{cell}} \right)^{1/2} \right]^{2/3} d^{2/3} + d$$

(4.3)

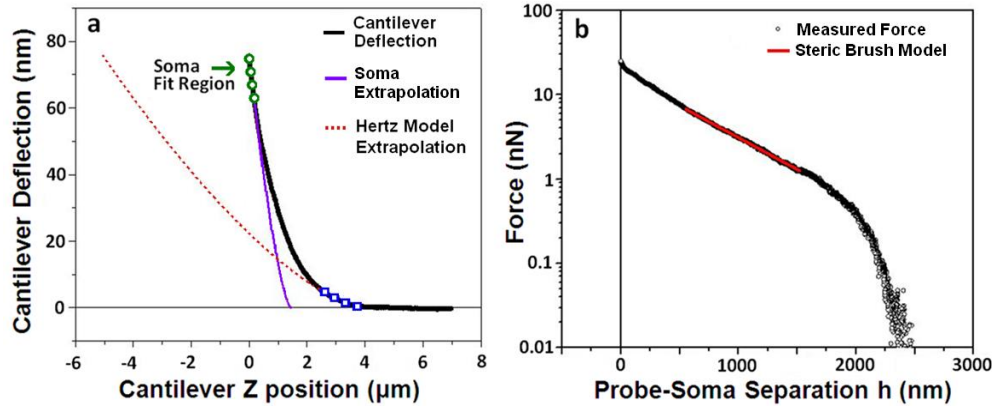


Figure 4.2: An example of raw AFM approach curves and fit with the brush model. (a) Black line: measured deflection of the cantilever vs. vertical position of the AFM scanner ( $d$  vs  $Z$ ). The green circles show the region of the experimental curve which is fitted with the brush model (Eq. 4.3) to extract  $E$  and

*Z0. The extrapolated curve from the brush model with  $h=0$  is shown as a purple solid line. The blue circles show the region of the experimental curve which is fitted with the Hertz model. The extrapolation of the traditional Hertz model (which does not take into account the brush layer) is shown as dotted red line. (b) Measured indentation force vs. calculated soma-AFM probe separation distance. The solid red line shows the fit with the steric force formula (Eq. (4.4)) [40].*

Assuming that the brush is softer than the cell body, the cantilever reaches an indentation force where the brush is considered to be completely squeezed (i.e.  $h=0$ ) before reaching the maximum load (Fig. 4.2 a, green circles). This assumption depends on the value of the maximum load, which should be sufficiently large (i.e. order of 10 nN in our experiments).

It has to be noted that  $h=0$  is definitely an approximation (it is impossible to squeeze a physical object to zero size). Moreover, it is impossible to define the force needed to completely squeeze the brush layer (i.e., to reach  $h=0$ ) in advance. It has to be done retrospectively. Specifically, one should find the elastic modulus of the soma assuming  $h=0$  starting from some “threshold” force, and then to derive parameters of the brush (as described in detail later). After that one can check at which force the brush layer is sufficiently squeezed (say, up to 90% of its initial size). As was shown in [43, 134], the model is self-consistent if we treat the brush as “completely squeezed” when the AFM probe-surface distance ( $h$ ) is 10% of the brush length. For the cells considered in this work, this threshold force is

equal to 3-4nN (when the brush is squeezed more than 90%). Another part to check self-consistency of the model is to verify that the elastic modulus and the brush parameters do not change if one considers the load forces higher than the threshold value (3-4nN), see [134] for more detail. As a rule of thumb, it is reasonable to consider the load force at least twice higher than the threshold value. That is why we use the maximum load force of 10nN in this work.

The soma elastic modulus  $E$  is calculated by fitting the deflection vs. cantilever position data for this region (“Soma Fit Region” in Fig. 4.2 *a*) with Eq. 4.3, with the condition  $h=0$ , which is satisfied in this region. The purple curve in Fig. 4.2 *a* shows the extrapolation of Eq. 4.3 from the “Soma Fit Region” to larger values of the relative vertical scanner position  $Z$ , while still imposing the condition  $h=0$ . The soma extrapolation curve departs from the actual  $d$  vs.  $Z$  data (black curve) as expected, since the brush is not completely squeezed in this region. The intersection of the purple curve with the horizontal line  $d=0$  (zero deflection) gives the parameter  $Z_0$ . With the parameters  $E$  and  $Z_0$  known from the “Soma Fit Region” we can now calculate the soma-AFM probe separation  $h$  for any value of the relative vertical scanner position  $Z$  (Eq. 4.3). The force due to brush is then found by inverting  $h(d)$  in Eq. 4.3 and using  $F(h) = kd$ . The dependence of this force on the probe-soma separation  $h$  is shown in Fig. 4.2 *b*. We note that the traditional Hertz model [141] can be used to describe the force vs. indentation curves, without taking into account the brush layer (as discussed below, see Eq. 4.5). However, the extrapolation of this model to low values of  $Z$

(dotted red curve in Fig. 4.2 *a*) would yield values for the elastic modulus, which are clearly inconsistent with the experimental data.

Because of the specific force dependence, the behavior of the brush layer cannot be described by an elastic modulus in a self-consistent way within simple models. In terms of stiffness, the brush layer increases its stiffness from smaller than the cell body (for small deformation by the AFM probe) to values equal to the cell body stiffness when the deformation is sufficiently large. Among others, the consistency of the model was verified by observing independence of the elastic modulus of the cell body of the indentation depth. Coincidental compensation of possible non-elastic response of the cell body and brush are highly unlikely because the above said consistency has been observed on a large number of various cells of different phenotypes.

To describe the brush parameters quantitatively, we use the Alexander - de Gennes model combined with Derjaguin approximation describing steric interaction between a spherical probe of radius  $R_{probe}$  and a semi-spherical cell of radius  $R_{cell}$  due to the existence of an entropic brush [43, 144]:

$$F(h) \approx 50k_B T R^* N^{3/2} \exp\left(-2\pi \frac{h}{L}\right) L$$

(4.4)

where  $k_B$  is the Boltzmann constant,  $T$  is the temperature,

$R^* = (R_{probe} \cdot R_{cell}) / (R_{probe} + R_{cell})$ ,  $N$  is the surface density of the brush constituents (effective molecular grafting density), and  $L$  is the “thickness” of the brush layer. The fitting of data with this formula is done within the limits of its

applicability  $0.1 < h/L < 0.8$ . It is worth noting that the necessity of fitting two parameters ( $N$  and  $L$ ) in equation (4.4) does not bring an additional uncertainty because these parameters are uncorrelated. This can, for example, be seen from the fact that parameter  $L$  is unambiguously defined by the tilt of  $\text{Log } F(h)$ . Despite the complex structure of the brush layer, the use of eq. (4.4) is justified by good fitting of the experimental data (see, Fig. 4.2 example, which shows a clear straight line in log scale (exponential dependence of eq. (4.4))).

It should be noted that the use of this brush model to describe the observed pericellular brush layer is obviously an approximation. We use it here because of two reasons: a) it seems to be plausible to expect the motion of soft glycocalyx molecules is balanced by entropy, this assumption used by Alexander and de Gennes in derivation of their model; b) it helps to reduce the entire force curve observed in the experiment to only two parameters, the effective grafting density and thickness of the brush layer (the Flory radius in the Alexander - de Gennes model). It is worth noting that the same exponential behavior can be described by other models, for example, by the correlation length of the polymer network of glycocalyx [129]. Conclusions of this work do not change if we choose another model to describe the brush layer because it was used just for convenience of the description of the observed results.



### 4.3 RESULTS

First, we demonstrate that the brush layer, which is approximated by equation (4.4), can indeed be associated with pericellular brush. As was noticed in the previous studies of human cervical and breast epithelial cells [43, 116, 120, 134], the pericellular brush is a complex mix of glycocalyx and membrane protrusions. Here we used the enzyme hyaluronidase to degrade the part of glycocalyx, hyaluronic acid, which is abundant in the brush but not in the cell body. Figure 4.3 shows the results of the treatment of neurons with hyaluronidase at different concentrations and for different durations in comparison with the untreated (control) cells. It demonstrates a statistically significant correlation between the treatment and the brush parameters, whereas there was no significant correlation with the modulus found for the cell body. To demonstrate it, we combined both the effective grafting density  $N$  and length  $L$  in one parameter,  $N*L$ . Furthermore, if all molecules of the brush are real (not “effective”) and fully stretched, this multiplication  $N*L$  would be equal to the total length of all molecules of the brush per unit area.

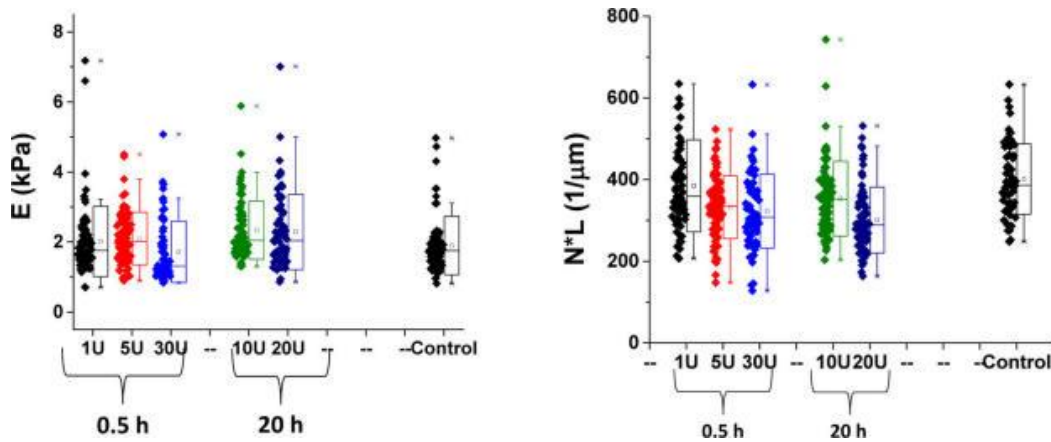


**Figure 4.3.** The results of alteration of pericellular brush with hyaluronidase. Different colors I used for clear separation between various hyaluronidase concentrations ( black is 1U and control, red for 5U, Navy blue for 30U, green is 10U, and dark blue is 20U; U is the unit of activity of hyaluronidase, 1U is defined as the concentration that causes a change in absorbance/scattering of hyaluronidase at 600nm of 0.330 per minute at pH 5.7 at 37 °C in a 2.0 ml reaction mixture). The elastic modulus of the neuronal soma (left figure), and the effective amount of the pericellular brush on treated and nontreated (control) neuronal cells (right figure). The bar height is the average value, and the error bar is the standard deviation. For these measurements 10 cells of each type were studied; 9-10 force curves around the cell top were analyzed for each cell. All cells were measured with the indentation rate of 5  $\mu\text{m/s}$  at 37°C, with a maximum applied force with respect to contact area of 10nN (the elastic modulus was measured for the forces 4-7nN when the modulus was indentation independent and the pericellular brush was squeezed) [40].

There is no statistically significant change in the elastic modulus of treated cells in comparison to the control sample of untreated cells (*left figure*). In the same time, the total amount of the brush ( $N \cdot L$ , which approximates the total length of all molecules of the brush per unit area if the molecules were fully stretched) derived in our model does change statistically significantly starting from the enzyme concentrations above 5U. (The statistical significance was tested by using ANOVA test with the confidence level  $p$  of 0.05). These results present strong evidence that the parameters derived from the brush model do describe the pericellular brush.

#### *Elastic behavior of neuronal soma*

The elastic modulus for neuronal soma was extracted by fitting each AFM indentation curve as described in the data analysis methods section (Fig. 4.2 *a*). The elastic modulus was derived for a typical indentation range of 500-900nm (within this range we observed more than 90% squeezed brush and a weak dependence of the modulus on the indentation depth). The radius of contact is 2.5-3.3  $\mu\text{m}$ , which is smaller than the probe radius (6.5  $\mu\text{m}$ ) and is a condition needed for the validity of the Hertz model. Higher indentations may also result in stronger depth dependence of the modulus [134], which would make our model self-inconsistent. The elastic modulus is measured for each cell at five separate

indentation rates (loading speed): 1, 2, 5, 7, and 10  $\mu\text{m}/\text{sec}$ , and at 37°C. The values of the elastic modulus show no dependence on the indentation rate within the statistical variation (Fig. 4.4).

These results are in sharp contrast with the rate-dependent measurements performed on neurons, which were obtained using the traditional Hertz model for AFM indentation experiments but did not take into account the brush [115]. As we show below, when the contribution from the brush is taken into account, the effective elastic modulus of the entire cell displays the typical loading-rate dependence (see Fig. 4.6 in the text) as previously reported in literature.

It should be noted that the brush model applied here was developed for the case of static deformation. When applying this model to viscoelastic measurements, we assume the same load rate for both brush and soma. While a more detailed model could be used in this case, it should be stressed that the results will qualitatively remain unchanged (mostly the loading rate will be redefined).

### *Viscoelastic behavior of neuronal pericellular brush*

The two-layer model described above allows separation of the force dependence due to the pericellular brush layer from the deformation of the soma. As was previously shown [116], the brush layer can be reasonably characterized by the steric repulsion typical for a polymeric brush (Eq. 4.4). By fitting the force vs. probe-soma separation data (Fig. 4.2 *b*) with Eq. 4.4, we obtain both an effective brush density  $N$ , and an effective brush length  $L$ .

Figures 4.4 and 4.5 show the dependence of the soma elastic modulus and brush parameters on the indentation rate, respectively. While the neuron soma behaves elastically (no indentation rate dependence for the elastic modulus, as shown in Fig. 4.4), one can see that the brush clearly demonstrates viscoelastic properties, that is both the effective brush density  $N$  and the effective brush length  $L$  depend on the indentation rate (Fig. 4.5). The dependence of  $N*L$  on the loading speed is shown in figure 4.S3 (found in 4.6 Supplementary Materials at the end of this chapter).

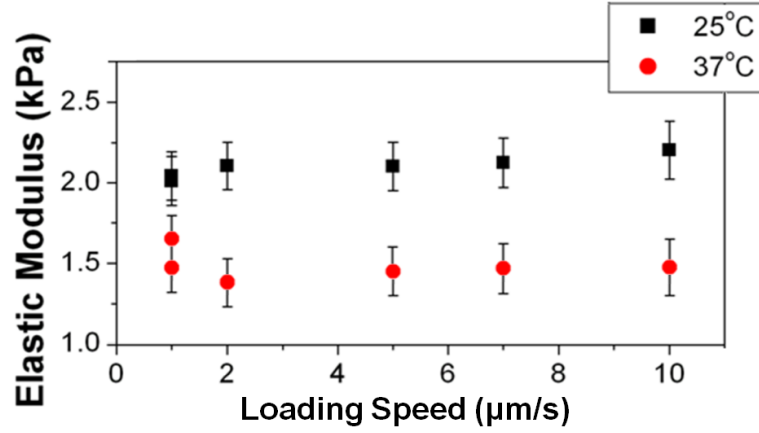


**Figure 4.4.** The elastic modulus of the neuronal soma as a function of indentation rate at 37°C (bottom values, circles), and 25°C (top values, squares). Each value represents the average modulus over 10 cells. The error bars represent the standard error of the mean [40].

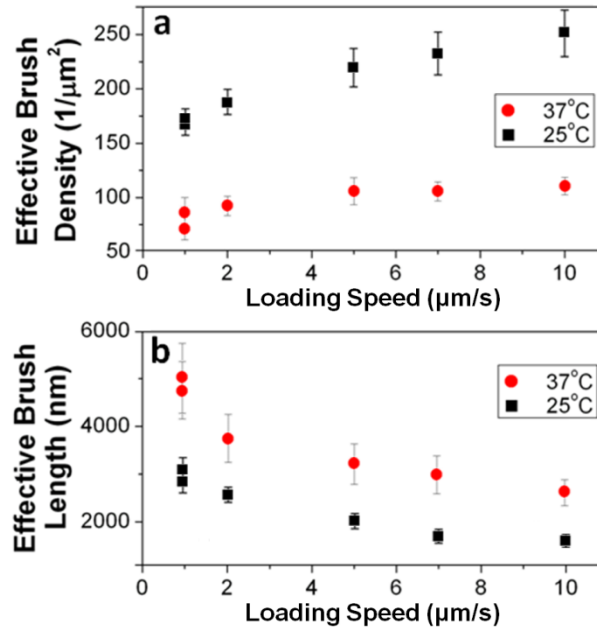


**Figure 4.5.** (a) Effective brush density (extracted from Eq. 4.4) vs. AFM indentation rate, indicating an increase in effective brush density with decreasing temperature from 37°C (dots) to 25°C (squares). (b) Effective brush length

*(extracted from Eq. 4.4) vs. AFM indentation rate, indicating a decrease in effective length with decreasing temperature from 37°C (dots) to 25°C (squares). Each value represents the average modulus over 10 cells. The error bars represent the standard error of the mean [40]. Note that these loading speed dependent data are “effective”, and reflect a viscoelastic response of the brush, and not necessarily a change in brush length or grafting density since the brush equation was derived for adiabatic compression.*

*The effects of temperature variations on neuronal soma and pericellular brush*

The same measurements as reported above were also performed at room temperature (25°C), which is often the default condition used when measuring mechanical properties of cells. Fig. 4.4 shows the values of the elastic modulus for the isolated neuron soma at 25°C. The previous results obtained at 37°C are also shown (red dots) for the ease of comparison. The data show that the elastic modulus of the soma increases with the drop in temperature. This result is qualitatively in agreement with results reported previously for the entire cell [115]. We emphasize that the values of the elastic modulus of the soma are rate independent within statistical variations within the measured indentation rates (1-10  $\mu\text{m}/\text{sec}$ ) for a given temperature.

Fig. 4.5 shows the dependence of the brush parameters  $L$  and  $N$  on the indentation rate measured at both 37°C and 25°C. The data shows that the effective brush length  $L$  decreases, and the brush density  $N$  increases with decreasing temperature. These data also demonstrate that the general viscoelastic trends measured at 37°C persist for the neuronal brush measured at 25°C.

It should be stressed that the derived parameters of the brush layer (the thickness and grafting density) should always be treated as effective. The formula describing the entropic brush was derived based on an adiabatic compression approximation. Therefore, the observed dependence of the brush parameters on the loading rate should be considered as an indication of rate dependent properties of the brush, rather than literal change of the grafting density and brush length. The development of viscoelastic models of the brush layer is beyond the scope of this work, and will be done in the future.

*Reconstruction of the previously reported viscoelastic results via a two-layer model*

It is instructive to test self-consistency of the results obtained with the brush model. Since the brush model provides the data for two effective layers (brush layer and soma), one can use a two-layer model to recover the value of the



elastic modulus that should be obtained by using the standard Hertz model [29, 111, 141, 145]. In this way, we can clearly see the contribution of each layer to the Hertz model results previously reported in the literature. Within the Hertz model, the cell is treated as a homogenous smooth (well-defined boundary) medium of radius  $R_{cell}$ . To derive the elastic modulus of the cell, the experimental force-indentation curves are fitted with the following formula [141] :

$$F(i_c) = \frac{4}{3} \frac{E}{(1-\nu^2)} \left( \frac{R_{probe} \cdot R_{cell}}{R_{probe} + R_{cell}} \right)^{1/2} i_c^{3/2} \quad (4.5)$$

where  $F$  is the load force,  $E$  is the elastic modulus,  $i_c$  is the indentation depth, and the other parameters have been defined in Eq. 4.2 and Eq. 4.3.

A representative example of fitting the experimental data with equations 4.5 was shown in figure 4.2a (dot line). One can see that this fit deviates substantially for large indentations. For direct comparison of the Hertz and brush models for all indentations, we convert the elastic modulus of the cell body and brush parameters (derived with the brush model, Eq. 4.1-4.4) into a single effective elastic modulus  $M_{eff}$  using the double-layered medium model for a system composed of two distinct layers [146, 147]:

$$\frac{1}{M_{eff}} = \frac{1-\nu_{brush}^{*2}}{E_{brush}^*} \left( 1 - e^{-\Psi \frac{L}{a}} \right) + \frac{1-\nu_{cell}^2}{E_{cell}} \left( e^{-\Psi \frac{L}{a}} \right) \quad (4.6)$$

where  $E_{cell}$  and  $\nu_{cell}$  are the elastic modulus and the Poisson ratio of the cell soma, and  $E_{brush}^*$  and  $\nu_{brush}^*$  are the effective modulus and Poisson ratio of the

brush layer, respectively. In Eq. 4.6,  $L$  represents the brush length,  $\Psi$  is an empirical constant,  $a = (\pi\delta R_{probe})^{1/2}$ , and  $\delta=L-h$  is the indentation depth for the brush layer. The effective modulus for the brush layer  $E^*_{brush}$  can be derived by determining the force needed to have the same deformation in the brush layer and the elastic material (soma, via the Hertz model) [148]:

$$F(h) \approx 50k_B T R^* N^{3/2} \exp\left(-2\pi \frac{h}{L}\right) L \approx \frac{4}{3} \frac{E^*_{brush}}{(1-\nu^2)} (R^*)^{1/2} (L-h)^{3/2} \quad (4.7)$$

From this condition, the effective brush modulus can be found as follows:

$$E^*_{brush} = \frac{75}{2} k_B T (R^*)^{1/2} (1-\nu^2) \left(\frac{N}{L-h}\right)^{3/2} \exp\left(-2\pi \frac{h}{L}\right) L. \quad (4.8)$$

When the effective elastic modulus at a fixed maximum force (0.5 nN) obtained from Eq. 4.6-4.8 (“Exponent Model”) is compared with the elastic modulus obtained from the data via the traditional Hertz model, we find that both models yield consistent results indicating a viscoelastic system with loading speed dependent elastic modulus (Fig. 4.6).

Fig. 4.6 shows that by combining the contributions of the viscoelastic brush layer with those of the elastic soma, we are able to recover the typical viscoelastic results (at both 25°C and 37°C), observed when the system is evaluated via the traditional single-layer Hertz model. This demonstrates the self-consistency of the brush model and explains the discrepancy in viscoelastic behavior previously obtained in the literature.

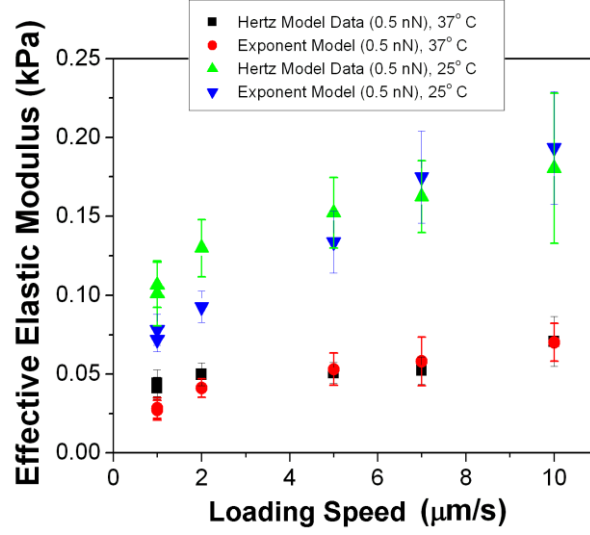


**Figure 4.6.** Comparison between the elastic modulus obtained from the traditional single-layer Hertz model and the double-layer exponent model that combines the viscoelastic brush and elastic soma (Eq. 4.6). The elastic moduli are shown as a function of the loading rate at two different temperatures. Black squares: single-layer Hertz model data at 37°C. Green triangles: single-layer Hertz model data 25°C. Red circles: exponent 2-layer model data at 37°C. Blue inverted triangles: exponent 2-layer model data at 25°C [40].

## 4.4 DISCUSSION AND CONCLUSIONS

All previous studies of the viscoelastic properties of cells, including neurons, have demonstrated that their elastic modulus depends on the loading-rate [31, 132]. We have confirmed that when cortical neurons are treated as a homogeneous medium and analyzed via the Hertz model, they appear

viscoelastic, similar to the previous reports. However, by separating the relative contributions of the pericellular brush layer and the underlying soma, we demonstrate that the viscous behavior (the loading rate dependence of the elastic modulus or brush parameters) comes entirely from the brush layer, while the soma itself shows purely elastic (rate-independent) behavior within the loading rate range of 1-10  $\mu\text{m}/\text{sec}$ . This is a rather unexpected result, particularly when taking into account that the cytoskeleton itself has components that display viscoelastic behavior. For example, actin has been shown to have a scan-rate dependent elastic modulus when cross-linked [149-151].

We have used a semi-empirical model that treats the neuron as consisting of two layers with different mechanical properties. This model allowed us to obtain an effective elastic modulus that is scan-rate dependent, and in quantitative agreement with the values obtained via the standard Hertz model, which considers the cell as one single homogeneous and isotropic material. Furthermore, the model has proved both self-consistency of the brush model and explained the discrepancy between our results (independence of the soma elastic modulus of the indentation rate) and the observed rate dependence previously reported in the literature.

Previous studies have underscored the importance of distinguishing between the elastic modulus of soma vs. pericellular brush for other cell types. While cancer cells are regarded as being softer than healthy cells [152], evidence

suggests that some, if not all, of this difference comes from variations in the brush layer, rather than the underlying cell body [110]. The contribution of the brush layer to the average soma elastic modulus in neurons is also of particular interest. Single cortical neurons are particularly compliant cells, typically regarded as having an average soma elastic modulus in the range of around 50-500 Pa [114, 132]. These values for single-cell elastic modulus are similar to those obtained on glial cells [31], as well as bulk measurements on brain tissue or explants [31, 153], all of which typically lie below 1 kPa. We have determined that the soma of cortical neurons possesses an average elastic modulus value around 1.5 kPa, several times higher than typically measured for individual neurons, or bulk brain tissue. Local mechanical properties are known to affect directed neurite outgrowth, as well as glial proliferation [1, 154], with neuronal outgrowth being optimized for weaker substrates, similar to that of bulk brain tissue. These processes are important both in the initial wiring up of the nervous system, and in recovery after injury. The brush layer on neurons decreases the whole-cell elastic modulus down to values consistent with an optimal growth environment. Thus, we conclude that the mechanics of the pericellular brush layer plays an important role in defining the mechanical properties of individual neurons and of the macroscopic brain.

As the brush layer is a substantial contributor to the whole-cell elastic properties, changes in brush or degradation of the brush layer would have substantial effects on local elastic modulus and thus neuronal outgrowth or

recovery. Additionally, modeling for traumatic brain injury at the cellular or sub-cellular level requires information on the mechanical properties of individual neurons [44]. Such modeling has previously considered all components of neurons to behave as viscoelastic materials, and typically does not account for the brush layer. Our results indicate that the brush layer is an important component that affects the mechanical properties of individual neurons, and should be considered when modeling the effects of mechanical trauma of brain. Obviously the importance of mechanical properties of other components of brain, and possible difference between mechanics of 2-D versus 3-D cultures have to be further investigated to make accurate conclusions about mechanics of brain.

Another significant result of this work is the study of the influences of temperature on the mechanical properties of neurons and the brush layer. Temperature response of the cytoskeleton of cortical neurons has been studied previously. It was shown that the typical effective elastic modulus of neurons underwent a significant increase with a drop in temperature from 37°C to 25°C [115]. Here we demonstrate that when the contribution of the soma is isolated from the brush layer, a substantial increase in the soma elastic modulus is still observed. However, the properties of the brush layer also change. By assigning an effective elastic modulus to the brush layer, we show that this elastic modulus also increases with a drop in temperature. For example, the effective elastic modulus of the “isolated” brush increases by ~200% with a drop from 37°C to 25°C when measured, for example, at a scan rate of 2  $\mu\text{m}/\text{sec}$ . We have

previously shown that the temperature change affects the neuron cytoskeleton, and that disruption of actin dynamics in the cytoskeleton drastically inhibits temperature-induced stiffening. However, some stiffening (an increase between 2% and 30%) is still observed even when the actin dynamics are inhibited [115]. Thus we can speculate that some of this stiffening may be attributed to the changes in the elastic modulus of the brush layer. It also relevant to mechanics of brain study, see for example, refs.[155] in which the effect of temperature on brain mechanics was studied.

When characterizing the neuronal pericellular brush, we have demonstrated that it increases its effective density, and decreases the effective length, with a drop in surrounding temperature. The brush layer of cells measured with AFM consists of three major components, glycocalyx (glycoproteins and polysaccharide), microridges (membrane ridges) and microvilli (F-actin fibers) enveloped by the pericellular membrane. Semi-quantitative measurements demonstrated that reorganization or disruption of the actin cytoskeleton is correlated with changes in pericellular thickness [119]. The cytoskeleton, particularly the actin component, of cortical neurons has been shown to change substantially with a drop in temperature from 37°C to 25°C [115]. This may explain the observed decrease of the brush length with temperature and the increase of effective grafting density (Fig. 4.5). This also results in the increase of the elastic modulus of the brush layer (Fig. 4.6). The fast increase of the effective elastic modulus with the loading speed at the lower temperature is consistent with

the behavior of polymers with temperature above glass transition [156]. The interplay between cytoskeletal dynamics and the brush layer may be a factor in the temperature response of neuronal brush. The cytoskeleton of cortical neurons, however, appears to be fairly unique, with an elastic modulus dependence on tubulin at 37°C and on actin at 25°C [115]. The opposite temperature dependence was observed for human alveolar epithelial cells [157]. Future studies should establish if the brush temperature response is similar on cells which do not undergo the tubulin/actin switch. In addition, the glyco-content of the pericellular coat will have to be identified. Our results demonstrating the alteration of the pericellular brush with hyaluronidase show that it contains some percent of hyaluronic acid. However, other glycoproteins and polysaccharides are present in the pericellular coat.

Our results demonstrate that the viscoelastic nature and the values of the elastic modulus for individual neuron soma should be reevaluated in light of the contributions of the pericellular brush layer. The AFM is a precise tool for quantifying the contribution of pericellular brush as well as characterizing the properties of the underlying soma. We additionally have demonstrated that variations in temperature affect not only the underlying soma and the cytoskeleton of living cells, but also the pericellular brush.

Here we demonstrated that pericellular brush layer surrounding cell soma is important when measuring mechanical properties of cortical neurons. To measure



it, we used the AFM indentation method, specifically, the AFM force volume mode which allows simultaneous measurement of force indentation curves and geometry of the cell surface. The physical response of the pericellular brush layer and the underlying neuron soma were separated with the help of the brush model. The study of the properties of both the pericellular brush layer and the neuron soma were performed at two different temperatures (25 and 37C) at different indentation rates (ranging between 1-10  $\mu\text{m}/\text{sec}$ ). We found that the elastic modulus of cell soma 3-4x larger compared to the previously reported values measured for neurons under similar physiological conditions. We demonstrated that this discrepancy came from consideration of the pericellular layer as the elastic part of the cell body. However, as was demonstrated in [134], the pericellular cell brush cannot be described with such parameters as the elastic modulus in a self-consistent way, and the only way to describe cell mechanics is to measure the elastic modulus of the cell body and parameters of the pericellular layer as the entropic brush separately.

Analyzing viscoelastic response of the cell soma and pericellular brush layer, we found that surprisingly the soma behaves as a non-viscous elastic material over the indentation rates studied (1-10  $\mu\text{m}/\text{sec}$ ), whereas the brush parameters do depend on the indentation rates. To verify that this interesting observation does not contradict the previously observed viscoelastic behavior, we combined the mechanical properties of the cell soma and the brush layer with the help of a two layer model. We demonstrated that this recovers the viscoelastic

cellular response observed previously. It is also worth noting that because of the similarities between the macroscopic brain mechanics and the elastic moduli which could be effectively assigned to the pericellular brush, we can speculate that the macroscopic mechanical properties of the brain might be mostly defined by pericellular brush layer rather than the cell soma.

## **4.6 Supplementary Materials**

### *Sample preparation*

The isolated cortices were incubated at 37°C in 5 mL of trypsin for 20 minutes. Trypsin was inhibited with 10 mL of neurobasal medium (Life Technologies, Frederick, MD) which was supplemented with GlutaMAX, b27 (Life Technologies), pen/strep (Life Technologies) 1%, and 10 mg of soybean trypsin inhibitor (Life Technologies). The cortices were mechanically dissociated, the cells were centrifuged, the supernatant removed, and the cells were re-suspended in 20 mL of neurobasal medium with L-glutamate (Sigma-Aldrich, St. Louis, MO). Cortices were incubated in serum-free media, which reduces glia proliferation. We have previously demonstrated that this treatment produces high neuron purity for our cultures [19, 20]. The cells were mechanically re-dispersed,

counted, and plated at a density of 250,000 cells per 3.5 cm culture disk. Each sample of cells was grown in 5% CO<sub>2</sub> at 37°C for a minimum of 2 days before measurements. Neuronal cells were optically identified based on morphology (see Figure 4.S1).

Cell samples were cultured on 3.5 cm glass disks manufactured to fit in the Asylum Research Bioheater fluid cell (Asylum Research, Santa Barbara, CA). Poly-D-lysine (PDL) (Sigma-Aldrich, St. Louis, MO) coating was added to the glass disks by immersing them in a PDL solution (0.1 mg/ml) for 2 hours at room temperature. The disks were rinsed twice with sterile water, and sterilized using 254nm, 13.4W ultraviolet light for 30 minutes (the ultraviolet light source was placed at a distance of ~0.5m from the sample).



**Figure 4.S1.** Two representative light microscopy images of neuronal cells used in this study. Length of the scale bar is 20  $\mu\text{m}$  in both images [40].

*Atomic force microscopy (AFM) and AFM force-volume map acquisition*

Neurons were kept on the AFM stage in neurobasal medium, at a fixed temperature (either 37°C or 25°C) for a minimum of 15 minutes before starting each measurement, and no longer than 2.5 hours in total. In previous work [46] we have demonstrated that the elastic moduli of cortical neurons measured on PDL coated glass, within 24-72 hours after culture are close to the values expected in vivo. Force-volume maps were taken with NP-O10 SiN probes with spherical tips, purchased from Bruker Corporation (Billerica, MA). Force curves were collected by using the AFM force-volume mode on the somas of live cortical neurons at a mapping distance of 2  $\mu\text{m}$  between points using a spherical AFM probe with a radius  $R = 6.5 \mu\text{m}$  (measured optically via a microscope with a 40x objective, NA 0.6), a RMS roughness ( $R_q$ ) of  $16.93 \pm 1.13 \text{ nm}$  (measured using tapping mode AFM), and a calibrated spring constant  $k = 0.12 \text{ N/m}$  (measured by using the thermal calibration built in to the MFP3D software of the AFM). The tallest points of the soma (nuclear region) were selected, see the Data Analysis section of the main text for more detail.

*An example of how the force-volume data was processed to extract the radius of the cell, and identify the exact location of the force curves on the cell surface.*

Figure 4.S2a shows a representative height image collected in the force volume mode. Because we don't want to disturb cells for excessively long time, only 16 x 16 pixels maps are collected. However, as one can see it is quite enough to obtain the radius of the object (cell) of study and identify the force curves which can be used for the data analysis. It should be noted that because we use the Hertz model, we can only use the pixels around the top (see the main text for more details). To calculate the radius of the cell, we have to correct the height data for their deformation. This is important because the cell is soft and deformation can be substantial. This can easily be done by increasing the height at each pixel by the amount of deformation calculated with the help of equation 4.2 of the main text. The result of such correction is shown in figure 4.S2b. Figure 4.S2c shows the cross-section of the unreformed cell shown in figure 4.S2b. The radius of the cell was calculated by parabolic fitting (done with the help of SPIP software by Image Metrology Inc.). It is 6.9  $\mu\text{m}$  in this specific example.

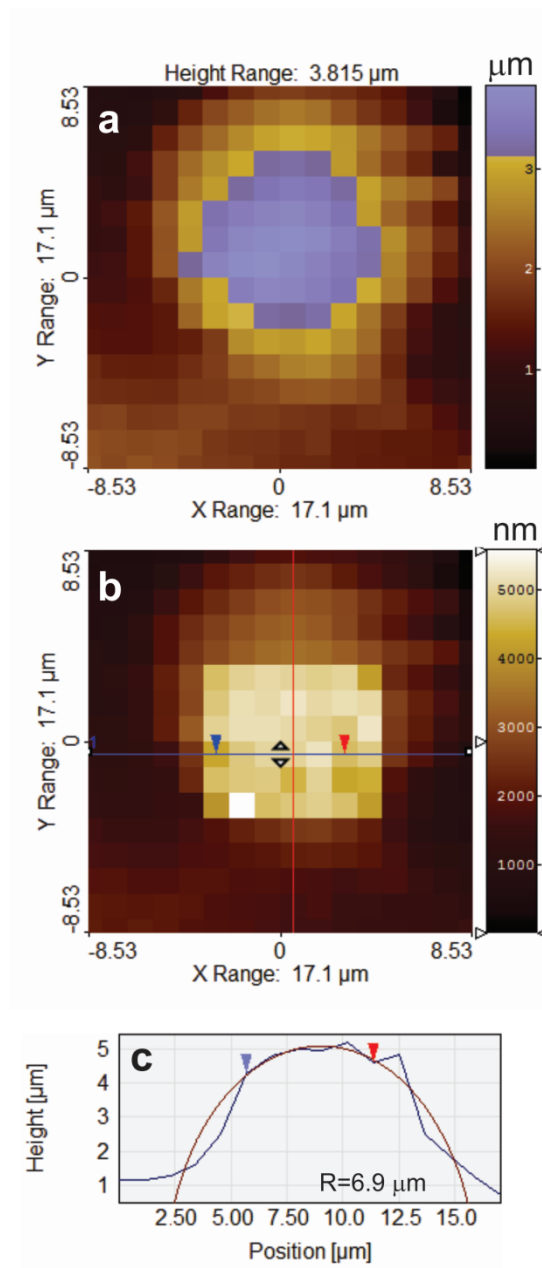


**Figure 4.S2.** A representative (a) Height image of a deformed neuron cell. Area in the center of the cell where force curves were extracted is highlighted by blue color. (b) Underformed cell topography restored near the cell center. (c) Radius of an underformed cell calculated from the cross-section. Radius used for

*the final calculation was derived as a geometrical average from radii taken from vertical and horizontal cross-sections [40].*

*Dependence of the effective amount of the pericellular brush on the load speed*

Since one can speculate that  $N * L$  values are indicative of the total amount of pericellular brush, we demonstrated it in figure 4.3, in which the effect of enzymatic treatment was seen because the enzyme physically removed a part of the brush. Although we do not expect to have a physical change of the brush at different indentation speeds, it is of methodological interest to see the dependence of  $N * L$  on the indentation speed. Using the data shown in figure 4.5, we plot the change of  $N*L$  in Fig. 4.S3.

One can see the most noticeable dependence in brush parameters, in particular, in the low temperature of 25°C. This is not a surprise. It is a result of viscoelastic response of the force due to brush because the formula for brush was derived in adiabatic/equilibrium approximation. The increase of the resistance to squeezing for higher load speed is translated through the formula into the changing parameters of the brush. A strong dependence on the load speed in the low temperature is also expected because of stronger viscoelastic response (high

effective viscosity of the brush at low temperatures; this is typical for virtually all materials).

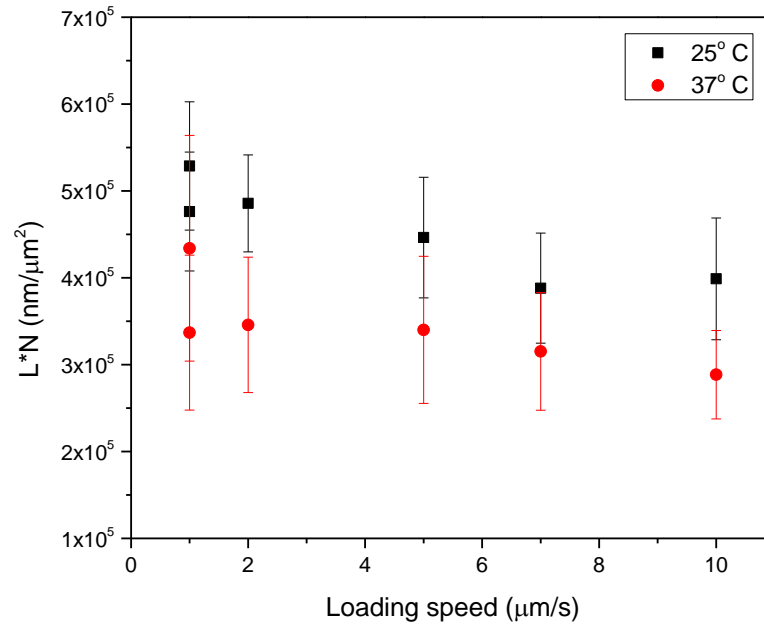


**Figure 4.S3.** Effective amount of the pericellular brush ( $L*N$ ) as a function of AFM indentation rate calculated for 37°C (dots) and 25°C (squares). Each point represents the average value over 10 cells. The error bars represent the standard error of the mean [40].



## **CHAPTER 5**

### **Electrical AFM in Fluid on Biological Samples**

#### **5.1 Overview**

A defining characteristic of neurons is their ability to communicate electrically and biochemically with other neurons using action potentials. Simultaneous measurements of many neurons in the same network would be ideal, however, existing techniques limit the feasibility of these types of experiments. It is fundamental to our understanding of neurons to develop detailed physical models of neuron firing. Here we attempted to measure the electrical signal of action potentials of cortical neurons using combined AFM and fluorescent microscopy. We stain the neurons using a calcium indicator to fluorescently detect action potentials and use AFM to attempt to detect the electrical and mechanical signals due to the action potential. We use Scanning Kelvin Probe Microscopy (SKPM) to attempt to detect depolarization of the plasma membrane during action potential firing. We also attempt to artificially induce action potential firing using SKPM. Additionally, we use contact AFM to attempt to detect mechanical movements of the neuronal membrane under action potentials. Unfortunately, the following experiments were unsuccessful due to

difficulties in action potential detection and moving the AFM tip into position over a neurite after action potential detection.

## **5.2 Direct Measurement of Action Potentials with AFM**

Various techniques exist to directly and indirectly measure cellular electrochemical activity. Perhaps the simplest indirect method is calcium ion and voltage sensitive dye fluorescent imaging [158]. These techniques are used to indirectly measure electrical activity of a cell [159] by using measured fluorescent intensity and referencing it to known values at certain ion concentration vs voltage tests. This method is simple, and only requires the introduction of a voltage sensitive dye or membrane permeable stain into the cell media. This provides limited spatial and temporal resolution and more qualitative measurements [160], but can show whole network activity and action potential propagation down a single neurite.

Patch clamp is possibly the most widely used and established electrical method for cells. Patch clamp involves micropipettes or micropore arrays to “clamp” to the cell or cell membrane fragment using suction [160, 161]. However, patch clamp limits measurement to a membrane “patch”, and has the potential to damage or destroy the cell. This is difficult to perform on multiple neurons in a network [161].

Extracellular planar microelectrode arrays (MEAs) utilize micropatterned arrays of stationary electrodes/transistors to measure electrical activity. Neurons are grown or patterned onto the MEAs, and action potentials are detected by voltage changes in the electrodes [161]. This method can be used to detect an action potential from 10-20 microns away [162] from the cell. Measurements can be difficult since the neurite must grow within 20 microns of an electrode to have its potential measured, however they can be improved using micropatterning and microprinting to spatially guide neurites.

All of these techniques lack the precision, and spatial and temporal resolution of AFM. Additionally, AFM is minimally invasive compared to other techniques. AFM also does not require specially made MEA substrates, which can be damaged or corroded, or otherwise fouled by cell media or polar fluids. Since the AFM cantilever is the electrode, it can be positioned at any point along a neurite or cell body, and can be used on neurons grown on biomaterials, hydrogels, glass, plastic, etc., unlike MEAs. Additionally, AFM has the ability to measure individual ion channel activity on the cell membrane, and relatively quickly move between cells. Development of AFM techniques to measure neuron electric activity would be a significant step forward in our experimental abilities. Additionally, AFM is a proven technique for measuring the electrical properties of nanoscale circuits and biological materials [163-166].

Direct measurement of action potentials with AFM can provide spatially resolved information of ion channel location and action potential behavior. The majority of measurements on action potentials has been through calcium

fluorescent imaging and patch clamp techniques. Fluorescent imaging techniques measure action potential intensity by fluorescent intensity of a calcium indicator that fluoresces upon chelation of  $\text{Ca}^{2+}$  ions within the cell. Comparing and normalizing fluorescent intensities to known intensities of a particular dye allows for quantification of the action potential voltages. Patch clamp techniques are direct measurements, where a whole cell or cell membrane portion is bound by suction to a needle or pipette. To measure the membrane potential or ion channel voltage states, one electrode is placed into the cell's media bath, while another is within the pipette or needle. The ion channels on the attached cell membrane are contained by the pipette, so all ions flowing in or out must go through the pipette. The voltage in the pipette is measured with amplification circuits. Interestingly, the pipette can be used to tear off part of the membrane and test its properties independently of the cell's internal properties. Unfortunately, both of these techniques have significant measurement errors involved, however both are very well suited for detecting the action potential and its shape. Electrical AFM is a great tool for measuring membrane electrical properties since it has the capability of measuring the action potential directly, and can be combined with fluorescent calcium imaging. AFM's high spatial resolution and sensitive probe are well suited for measuring the electrical activity of the cell, as well as any accompanying mechanical disturbance of the membrane through potentials. However, applying AFM to measure action potentials can be difficult due to the cell's environment of polar ionic fluid. Mainly, AFM performs electrical measurements through noncontact methods such as EFM and SKPM, whose

signals are perturbed by ionic screening. To defeat the ionic screening, the AFM must either be able to perform measurements faster than the Debye time of the media, or measure action potentials that change their voltage faster than the characteristic time of media ion rearrangement.

### **5.3 Electrical AFM in Polar Fluids**

Electrical AFM measurements in fluid can provide valuable quantitative micro/nanoscope information on biological samples [169] and is readily performed in non-polar fluids [167]. However, for biologically relevant polar fluids, freely moving ions make quantitative, and sometimes qualitative, measurements difficult to perform [163] depending on the concentration of ions. The rearrangement of ions in solution create electric double layers [74, 167, 168, 170] at the sample/fluid interface, and screen most electrical surface properties of the sample outside of the Debye radius [74, 167, 168] if measured at timescales above the fluid's Debye Time [167]. The Debye radius is typically around 1-10nm [163], and the Debye time is typically in the nanosecond to microsecond range [167]. This requires electrical AFM measurements to be highly sensitive and require accurate knowledge of cantilever geometry [163, 164, 169], tip/sample separation [74, 167-169], exact cantilever deflection to a reference material [163, 169, 170], tip surface charge and chemistry [163, 164, 167], and

ion concentrations [74, 167-170]. The importance of micro/nanoscale electrical properties is of great importance to understanding properties of biological materials and cellular processes. Electromechanical AFM has been performed measuring electrical and mechanical spikes from firing lobster giant neuron axons [75] (a theoretical mechanism for mechanical spikes following action potentials [172] has been explored), mammalian neurohypophysis [74], cell ion channel distribution [171], characterization of bacteria membrane potentials [168, 170], and biomineralized material electrical nanoscale structure [169]. Much effort is being put into developing quantitative electromechanical methods for polar fluids. Of these double-layer-defeating techniques, oscillatory methods are much more sensitive to cantilever deflections than static cantilever ones. Simple AFM, Fluid Electric Force Microscopy (FEFM) [163, 164], Voltage Modulated Scanning Probe Microscopy (VMSPM) (such as Electrochemical Force Microscopy) [167], High Bandwidth Atomic Force Microscopy (HBAFM) [74], and Band Excitation Piezo Force Microscopies (BEPFM) [168-170] have been used for these experiments. These methods reveal important electrical, mechanical, and electromechanical information on biological samples.

*Fluid Electric Force Microscopy (FEFM) of Lipid Bilayers in Polar Fluid*  
[163]

At the fluid/sample interface, free ions screen surface charges and potentials by forming electric double layers, and render standard EFM measurements useless. To defeat this double layer, one must measure electric forces under the Debye radius, which is typically  $<10\text{nm}$  [163, 164]. At this tip/sample separation, it can be difficult to distinguish topography from electrical interactions, so traditionally researchers would take repeated scans of a sample at different ion concentrations and subtract them from topography images to be left with the electrical maps [163]. Fortunately, charge screening outside of the Debye radius is not complete, so an approximation for cantilever deflection outside of the Debye radius can be used to quantitatively measure surface charges [163, 164] with FEFM (with knowledge of tip surface charge and chemistry) via the double layer interactions with the sample and tip.

Using FEFM, Hafner [163] was able to obtain high resolution maps of supported lipid bilayers on mica in 1mM and 3mM NaCl. By scanning over the sample (with  $k=0.12\text{-}0.06\text{ N/m}$  cantilevers), he was also able to show cantilever deflection as a function of tip/surface separation (0.2-20nm) for different lipid bilayer types (DOTAP/DOPC and DOPS). Other than scans, force maps were used to find membrane charge distributions. By fitting the deflection ( $d=F(L)/k$ )

to equation 1 (Force  $F$ , tip/sample separation  $L$ , tip radius  $r$ , Debye Length  $\lambda$ , medium dielectric constant  $\epsilon$ , vacuum permittivity  $\epsilon_0$ , tip and sample charges  $\sigma_s$  and  $\sigma_t$ , respectively)

$$F(L) = \frac{4\pi\lambda r\sigma_s\sigma_t}{\epsilon\epsilon_0} e^{-L/\lambda} \quad (5.1)$$

vs lift height curves for a given bilayer in its polar fluid, one can measure the Debye length and compare it to calculated lengths and show they are in agreement [163] (Figure 5.1); which indicates a good model for FEFM.

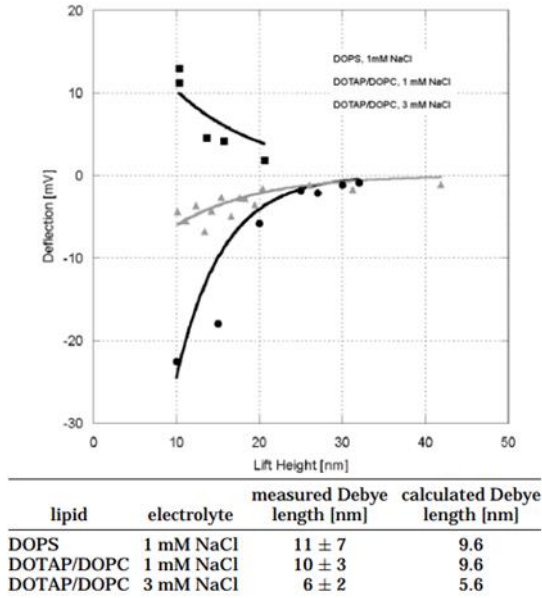


**Figure 5.1.** (top) Deflection vs tip/sample separation with fits from Eq. 1.

(bottom) Table of fitted Debye lengths [163].



A few years later Hafner performed a more complete study of FEFM over supported lipid bilayers at over 4 Debye lengths above the samples, which yielded 1-3mV changes measured with the cantilever [164]. Scans show variations with 50nm resolution. Analyzing deflections from force curves show high cantilever sensitivity at even >60nm separation [164]. It was shown that using a numerically solved Poisson-Boltzman equation and Gouy-Chapman theory [164] yields quantitative information, and doesn't significantly underestimate the values like the approximate analytical formula [164].

*Electrochemical Force Microscopy (EcFM) of Au/SiO<sub>2</sub> substrate in polar Fluid*  
[167]

Open Loop Kelvin Probe Microscopy is a powerful tool in vacuum, ambient air, and non-polar liquids [167]. It fails to work in polar fluids since fundamental operation conditions of second harmonic contact potential difference and first harmonic electrostatic force response are violated due to mobile ion screening, Debye time, ion relaxation time, and ion diffusion time [167]. To overcome this, EcFM measures electric potentials using amplitude modulated bipolar pulses at single frequency AC excitations at some tip/sample separations

with sampling rates under the Debye time, ion relaxation time, and ion diffusion time. As tip/sample separation increases, all timescales increase (and some become more dominant than others), which gives a frequency space AFM can operate within. As tip/sample bias increases ( $>500\text{mV}$  at  $200\text{nm}$  separation over gold in milliQ water), other transient processes and chemical reactions occur [167], making high biases less useful. At lower biases, and lower timescales, one can deconvolute the competing surface electrical signals from the polar fluid rearrangements thus making EcFM very useful for measuring electrical potentials in biologically relevant media. Figure 5.2 shows cantilever response over an Au electrode, demonstrating EcFM's high degree of spatial resolution.

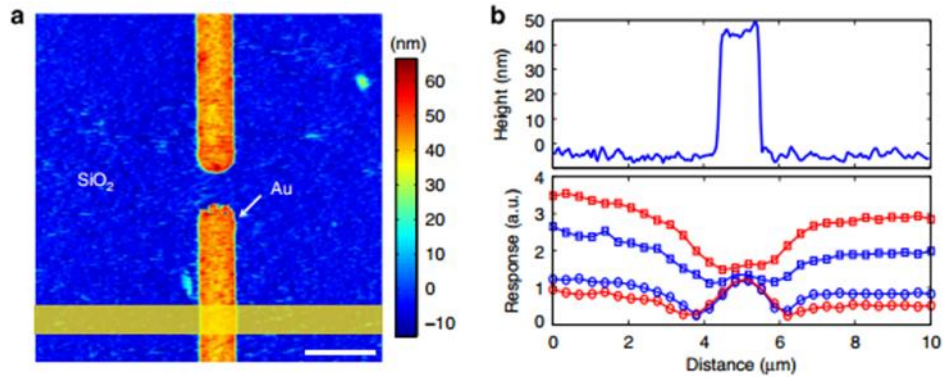


**Figure 5.2.** (a) EcFM scan of Au electrode on SiO<sub>2</sub>. (b) electrode height scan (top) and cantilever response at 4 tip/sample separations in arbitrary units. Squares are first harmonic and circles are second harmonic during red 1.5V and blue -1.5V biases. All data points were recorded 5ms after onset of bias [167].

Time-Dependent Force Mapping Au electrodes on SiO<sub>2</sub> substrate (in MilliQ water, 1nM, 10mM, and 100mM K<sub>2</sub>SO<sub>4</sub> aqueous solution at 0-200nm tip/surface separations, 30mV DC bias), reveals electrolyte relaxation times (< 1 ms) using EcFM [167]. The study carefully examines first responses (from  $\pm 1.5$ V biases), and shows the response and relaxation 0-200nm above the surface for different electrolyte solutions. As expected, response is low between all biases around 0V, and quickly increases in magnitude with increasing bias (Fig. 5.3). Different ion concentrations cause varying degrees of cantilever sensitivity. Figure 5.3 shows how ion concentration affects measurement. Low ion concentrations have slower ion rearrangement times compared to larger concentrations which show faster relaxation times. The sampling rate must be faster for larger ion concentrations. Unfortunately, Figure 5.3 a,b,c and d all have relaxation times smaller than detectable by the experiment (10s to 100s  $\mu$ s), but show a higher degree of screening at higher ion concentrations.

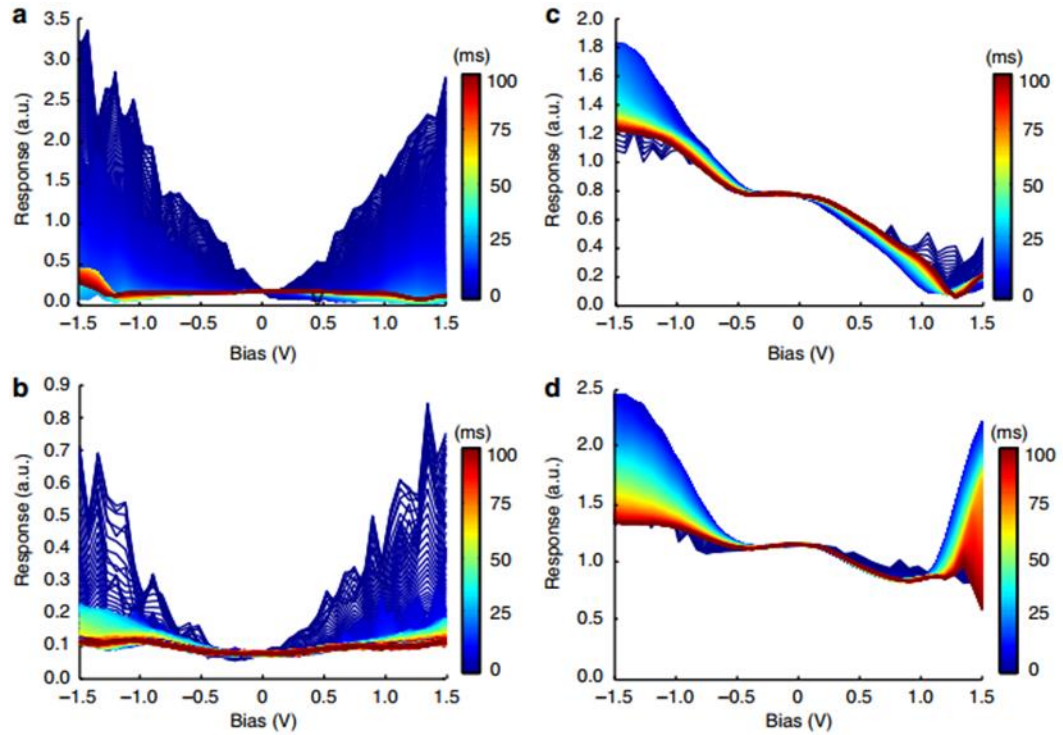


**Figure 5.3.** First harmonic amplitude at 200nm separation. MilliQ water (a), 1mM K<sub>2</sub>SO<sub>4</sub> (b), 10mM K<sub>2</sub>SO<sub>4</sub> (c), 100mM K<sub>2</sub>SO<sub>4</sub> (d). blue to red indicates increasing ion relaxation times [167].

*High Bandwidth Atomic Force Microscopy (HBAFM) on CD-1 Mouse Neurohypophysis Action Potential Induced Mechanical Waves [74]*

Standard AC AFM is very sensitive to small cantilever deflections; however, the Z feedback loop can filter out small and rapid deflections. To better

detect mechanical signals from a sample, the Z-Feedback Loop is turned off to provide a higher bandwidth of Z axis measurements [74]. This allows for the detection of very fast and small deflections [74], that might be filtered out otherwise. In particular, this is useful for the detection of the Angstrom [74, 75] mechanical spikes that accompany action potentials and nerve terminal electrical excitation.

The mammalian neurohypophysis is an endocrine organ consisting of “granules” of hypothalamic magnocellular neuron neurosecretory terminals. Kim [74] showed that HBAFM in conjunction with fluorescent scattering measurements, some of these granules undergo mechanical swelling resulting from action potential polarization. While fluorescently observing the firing of the neurohypophysis, a tipless non-conductive MikroMasch CSC12 silicon cantilever ( $k = 0.03 \text{ N/m}$ ) is AC mode engaged atop a column of neurohypophysis, over a granule. The mechanical signal is recorded with a 0-20kHz bandwidth and sub millisecond resolution. As a characteristic ~5ms positive electrical spike of the neurohypophysis occurs, a ~0.5 Angstrom ~5ms upward deflection is measured. This indicates electrically induced mechanical swelling of the granules. Unfortunately, this is the total Z axis swelling from the nerve terminals, and not single neurons. It can be seen that the mechanical spikes are a result of the mechanical perturbations due to electrical firing, by observing the spike shapes, durations, and times (Fig. 5.4). Since the AFM cantilever is in contact with the granules and the cantilever is non-conductive, the AFM deflection signal is mechanical and not due to electric fields.

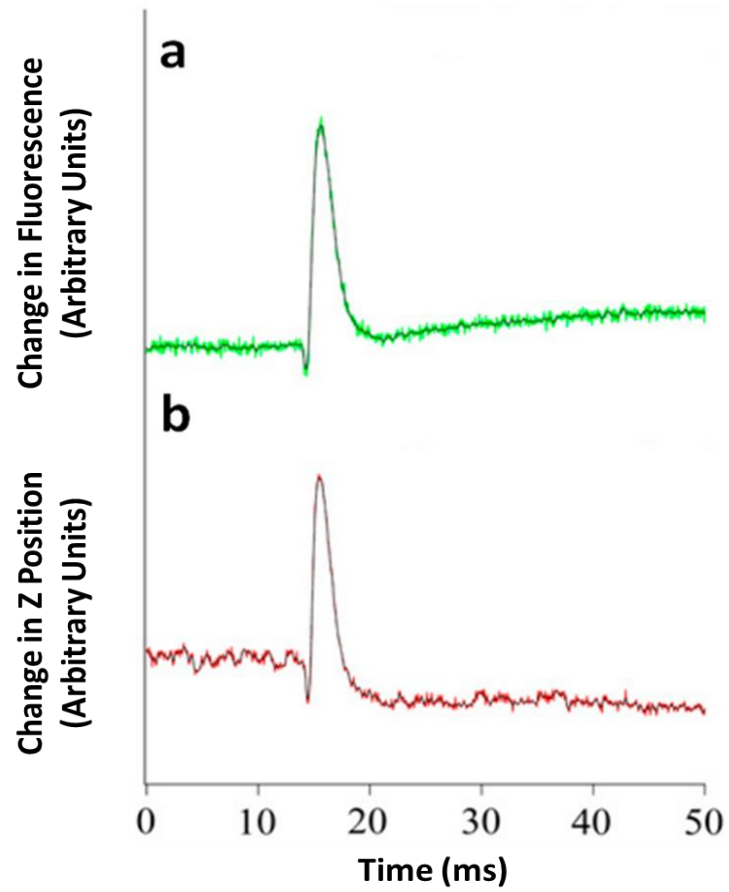


**Figure 5.4.** Mechanical spiking due to action potentials measured via AFM. (a) Electrical impulse from granule detected via change in fluorescence. (b) AFM Z position change measured at 20kHz. Note very similar curve shapes [74].

*Band Excitation Piezo Force Microscopy (BEPFM) of Bacteria Membrane  
Charge Distributions in Polar Fluid [169]*

Band Excitation Piezo Force Microscopies have been gaining popularity in Piezo Force Microscopy studies of biomaterials [169] and cell membrane properties [168, 170]. In Band Excitation Piezo Force Microscopy, the cantilever electrical signal is frequency modulated over a piezo electric sample and mechanical deformations due to the electric stimulus are recorded. BEPFM has the advantage of PFM since it can generate peak sample resonance maps since it rasters over many electrical frequencies, revealing more detail than single frequency PFM. This method details the electromechanical response of cells.

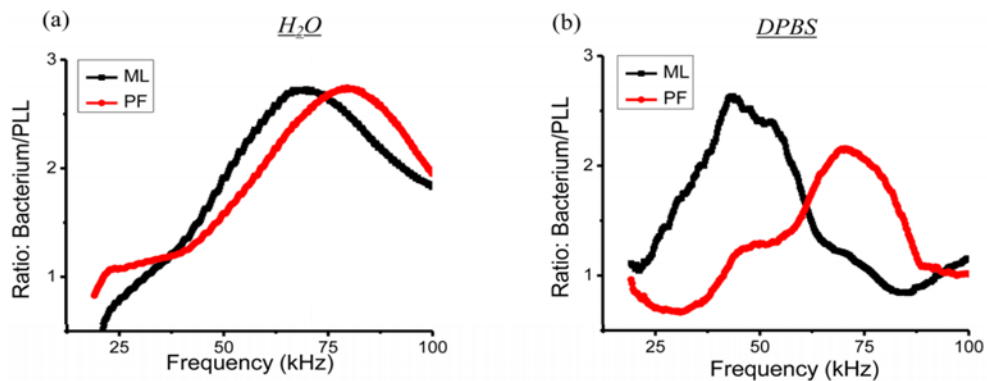


**Figure 5.5.** ML and PF response comparisons. (a) comparative electromechanical response vs frequency in Millipore water. (b) Comparative electromechanical response vs frequency in 1x DPBS [169].

BEPFM was demonstrated in electrolytic solution for the first time (Millipore water, 1x DPBS, and DMEM) [170]. Gram positive ML and Gram-negative PF bacteria on PLL coated glass were probed at ~1nm Debye lengths (for all electrolytic solutions) and cantilever amplitude, resonance, Q factor, and phase were recorded to completely characterize their membranes, though peak resonance amplitude and resonant frequency reveal differences between ML and PF bacteria. Bias only affects image contrast; water>DMDM>DPBS). Both bacteria could be distinguished readily in Millipore water and DPBS (Fig. 5.5), but not in DMEM. DMEM and DPBS have similar ion concentrations, but DMEM has organic components that affect cell biological activity and image formation. Differences between the bacteria were observed as electromechanical response vs resonance (Fig. 5.5). DPBS resonance curves differ the most. Differences in bacterium membranes are attributed to different membrane proteins and structures.

#### *Mechanical Atomic Force Microscopy on Lobster Giant Axons [75]*

Lobster Giant Neurons present the opportunity to use AFM to study the mechanical spikes that follow action potential firing in the axon, without the difficulty of working with the comparatively small mammalian axons. This



eliminates the need for precise positioning of the cantilever tip over a  $<\mu\text{m}^2$  region, and makes the use of electrodes to measure action potential signals without damaging the cell much easier.

Here, the MG and LG axons of the lobster connectives are exposed, and electromechanical signals are recorded via AFM and electrodes in electrolytic solution [75]. A tipless cantilever is engaged upon either the exposed MG or LG axons in solution, and the vertical deflection is recorded over 100 action potentials (Fig 5.6d.) at 40kHz and 1ms sampling rate at 0.2 second stimulated intervals. Comparison between AFM action potential averaged data and electrode data for both axons shows mechanical and electrical spikes with very similar morphologies that occur simultaneously, and lasts ~2-4 ms with a 0.2-1.2nm peak (Fig. 5.6), which is expected for an action potential [75]. The action potentials always occurred with a mechanical spike, showing the membrane polarization is piezo electric in nature.

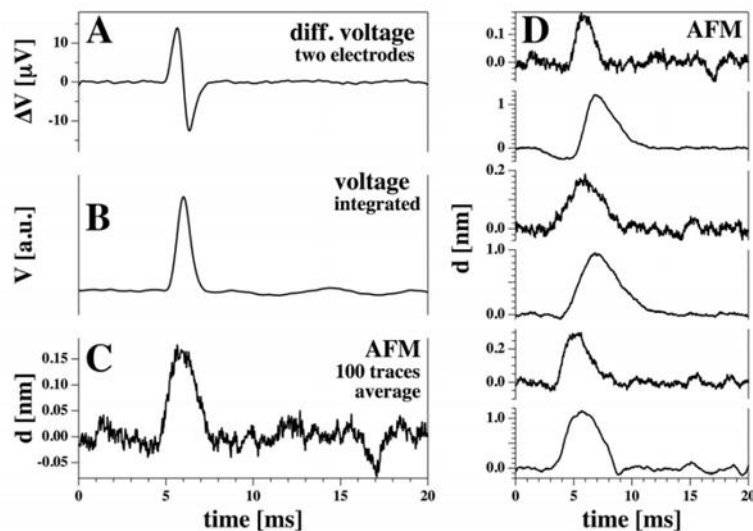


**Figure 5.6.** Voltage and Mechanical spikes vs time via AFM. (a) voltage change detected via electrodes. (b) Integrated signal. (c) Average of 100 AFM traces of single axon action potential detected via AFM. (d) Cantilever mechanical deflection on 6 different lobster LG axons [75].

## 5.4 Detection of Action Potentials via AFM

AFM proves to be a useful tool for measuring electrical, mechanical, and electromechanical responses of biological materials. It has been shown to be able to use the electric double layer to extract important quantitative electromechanical information from samples in electrolytic solutions, such as piezo response [168-170], membrane electrical characteristics [168, 170, 171], cell electrical activity

[171], and charge distributions [163, 168], with high sensitivity (angstrom and mV resolution).

As suggested by previous research, AFM can be used to detect electrical signals in polar fluids, and by extension might be used to electrically and mechanically detect neuron action potentials. Measurement of action potentials with AFM would allow for their characterization in live whole cells with high spatial resolution. However, there are technical obstacles to overcome before measurements of this type can be made; mainly quantification of electrical noise in the AFM and overcoming ion screening effects in polar fluids like DPBS and cell media, such as Debye time and length.

### *Methods*

In this experiment, we use combined AFM and FM to measure the electrical and mechanical properties of action potentials, and attempt to induce action potentials electrically and mechanically. We use E18 rat cortical neurons plated at 170, 340, and 680 cells/mm<sup>2</sup> cultured between 2-21 days. We fluorescently observe neurons within a 5-10 minute window to optically detect firing to identify electrically “active” neurons. After a neuron is seen to be active, the AFM probe is optically positioned over the neurite, hillock, or soma, and the

cantilever voltage is changed to lessen the transmembrane potential to induce firing (Figure 5.7). AFM scans with AC240-TM-R3 Electrilevers dislodge neurites and soma during a topography scan. We also attempt to induce neurite firing by electrically stimulating voltage gated ion channels close to their reported threshold voltages, or by mechanically perturbing voltage gated ion channels or mechanosensitive ion channels.

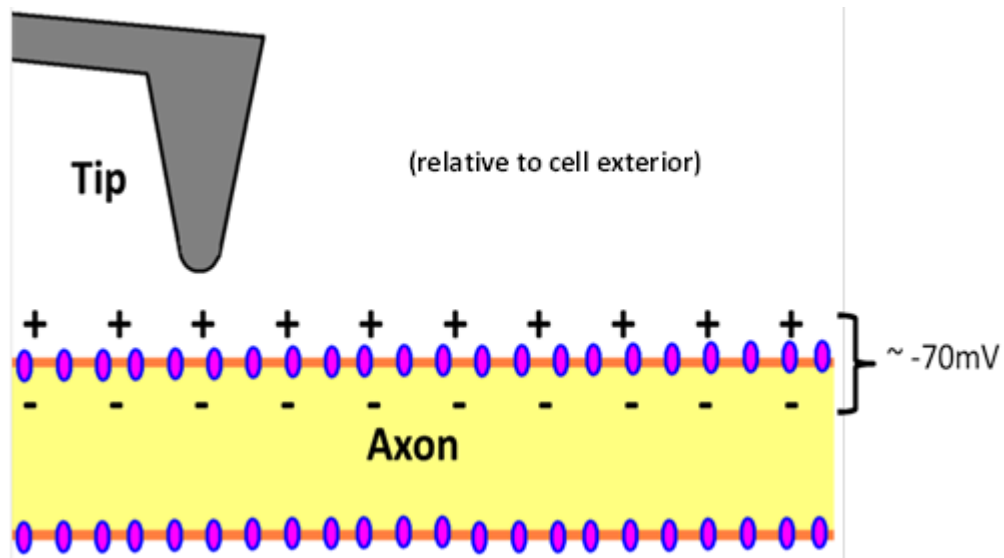


**Figure 5.7.** Schematic of AFM measurement of action potential. The AFM tip is aligned with an axon to induce an action potential by either scanning over a firing neuron or changing the transmembrane potential ( $\geq -55\text{mV}$ ) by changing the tip voltage relative to the outside media and making contact with the axon. The axon exterior (white) is more positive than the axon interior (yellow). Action potentials are propagated to K/Na voltage gated ion channels (purple).

E18 fetal rat cortical neurons were obtained from Tufts University Department of Biomedical Engineering. Freshly isolated cortices were incubated for 20 minutes in trypsin at 37°C. trypsin was inhibited with soybean trypsin inhibitor. Neurons were dissociated, separated by centrifuge, and suspended in Neurobasal Medium and supplemented with GlutaMAX, b27, and pen/strep. The cells were counted with a hemotometer and plated at 170cells/mm<sup>2</sup>, 340cells/mm<sup>2</sup>, and 680cells/mm<sup>2</sup> (Figure 5.9) to see if density affected firing rates and behavior.

#### *Scanning Kelvin Probe Microscopy (SKPM)/AFM*

The electrical AFM methods described previously show sensitivity and versatility of AFM for measuring electrical and mechanical signals in live tissues and cells. Here, SKPM was used to detect and induce action potentials in cortical neurons using AC240TM-R3 Electrilevers with a spring constant of 0.3-4.8N/m and a resonant frequency of 45-95kHz. SKPM was chosen since it is highly sensitive to electric potentials, and can simplify the measurement process since it can be used with minimal set up and is a built in method on our AFM.

Additionally, neuron action potentials have large enough potential changes to measure via SKPM (~70mV) while within one Debye length. The electrilevers were also used to mechanically probe the neurons to induce firing. All measurements were performed on an Asylum Research MFP3D-BIO Atomic

Force Microscope with an integrated inverted fluorescent microscope. Action Potential detection used the AFM as a deflection kymograph, over 5-10 minutes to observe changes in potential over time over a point.

*AFM for mechanical detection of Action Potentials*

Tipless NPO cantilevers, with very low spring constants (0.06N/m), from Bruker were used to mechanically detect axon action potentials in both standard contact mode and AC mode. Mechanical AFM was used over an axon, axon hillock, or soma, for 5-10 minutes for each neurons. Since AFM measures deflections by rastering over a surface and we are concerned with observing deflections over time, we perform AFM scans with an arbitrarily small scan size (0nm) with a scan rate of 0.5-2 hz and 512-1024 scan lines. This yields deflection vs time kymographs, since the probe is stationary, and the image produced shows deflection vs time at a resolution. No results were obtained because firing axons could not be found.

### *Fluorescent Time Lapse Imaging*

Fluorescent imaging was performed on a Nikon Eclipse Ti Inverted fluorescent microscope using the FITC filter with excitation/emission of 495 nm/521 nm. Neurons were stained with 1ml of stock Fluo 4 No Wash (NW) calcium indicator and imaged with the 485nm excitation and 525nm emission FITC filter for up to two hours at 37°C with the 10x Plan Fluor long range objective. Timelapse imaging was performed with a 500ms exposure time at half intensity, in 0.2 -1 second intervals over a course of 5 to 10 minutes before moving to a new location.

### *Calcium Ion Imaging*

During firing, voltage gated K and Na ion channels are the primary contributors to action potential shape and intensity. Calcium imaging takes advantage of voltage gated calcium ion channel that is triggered upon a threshold voltage between -40mV and -60mV, which is achieved during the depolarization phase. This causes an influx of  $\text{Ca}^{2+}$  ions into the cell. These ions are bound by fluorescent calcium indicators that permeated the membrane, and cause the cell to

fluoresce. Fluorescent intensity is determined by  $\text{Ca}^{2+}$  ion concentration and indicator concentration.

Calcium imaging is used to ensure any AFM measurement of an action potential occurred, or to target firing neurons. Neurons were stained with Fluo 4 NW or Fluo 4 AM. Fluo 4 NW was used to reduce the time needed for imaging. Fluo 4 AM worked much better, but took too long to stain the neurons, resulting in cell death. Here, we do not quantify intensity, and only use fluorescent measurement as a way to optically refer the AFM signal to the intensity function, and to locate firing neurons.

#### *Chemical Excitement of Neurons (L-Glutamate and KCl)*

Neurons were excited by either 100 $\mu\text{M}$ -500mM L-Glutamate, which activates the NMDA (N-methyl-d-aspartate) receptors, or 1 $\mu\text{M}$  to 100mM KCl, which induces excitotoxicity in the neuron. Unfortunately, no excitation was fluorescently observed before cell death at any concentration between 2 and 21DIV.



### *Quantification of Electrical Noise with SKPM*

Noise is the largest concern with detecting an action potential. Fortunately, noise detected by the AFM is Gaussian, and has a mean of zero, so the underlying signal can be determined as a constant or function added to the noise. In the case of the noise calibration, the signal should be a constant determined by the potential difference between AFM tip and ground. Two tests were performed to determine the AFM sensitivity to voltage changes in air (Figure 5.8) and in 1xDPBS over a grounded gold surface.

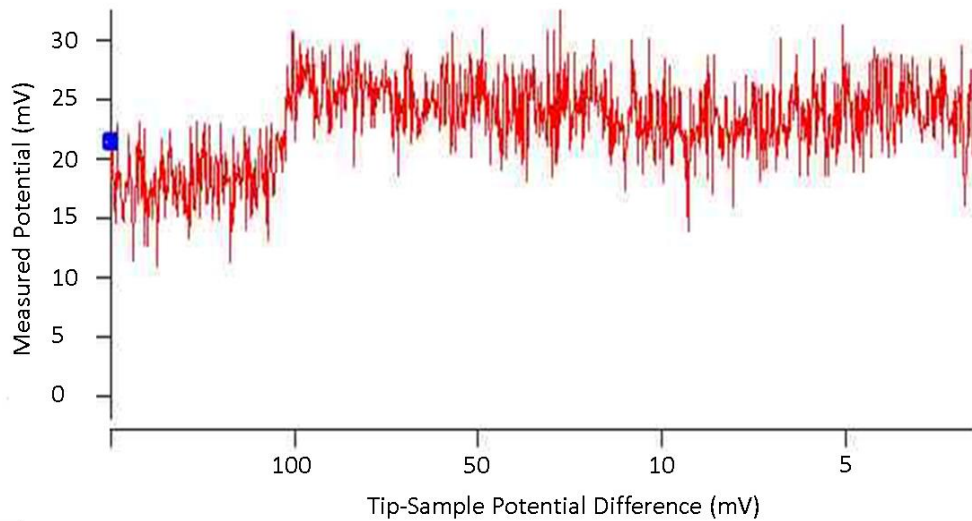


**Figure 5.8.** SKPM kymograph cross section, showing a dip in potential when the tip/sample potential difference was changed by 100mV and electrical noise. Horizontal axis shows potential-difference steps, the vertical axis is measured potential.

We first tested AFM noise by SKPM over a gold electrode in air and only detected a  $6 \pm 2.660$  mV difference in potential from a 50 mV potential change. The below image shows the results of the SKPM kymograph. In the image, the potential difference started at 1 mV then changed by 5 mV, 10 mV, 50 mV, and 100 mV.

The second test measured the signal in 1xDPBS, showed no signal change due to potential difference change, which is most likely due to ions screening. The scan was also much less “noisy” with significantly smaller deviation of 0.64 mV. Since null results were obtained from the AFM SKPM test in 1xDPBS, they were not continued in Neurobasal. Additionally, the AFM would cause hydrolysis of the 1xDPBS to occur at tip-sample voltages  $>1$  V and give deviations of  $\sim 40$  mV, so measurements were stopped.

#### *Fluorescent detection of Action Potentials*

Action potentials were detected fluorescently with Fluo 4 AM and Fluo 4 NW, but not with Atomic Force Microscopy. Fluorescent imaging reveals the most firing at neuron culture densities of 680 Cells/mm<sup>2</sup> after 3-5 DIV ( $<4\%$  active cells over a 10 minute imaging period). The 680 Cells/mm<sup>2</sup> cultures showed a significant amount of neurite fasciation which could contribute to higher firing rates, At lower densities, very little firing and no fasciation was observed and the cultures were not as healthy. Figure 5.9 shows a neuronal network at 680 Cells/mm<sup>2</sup>.

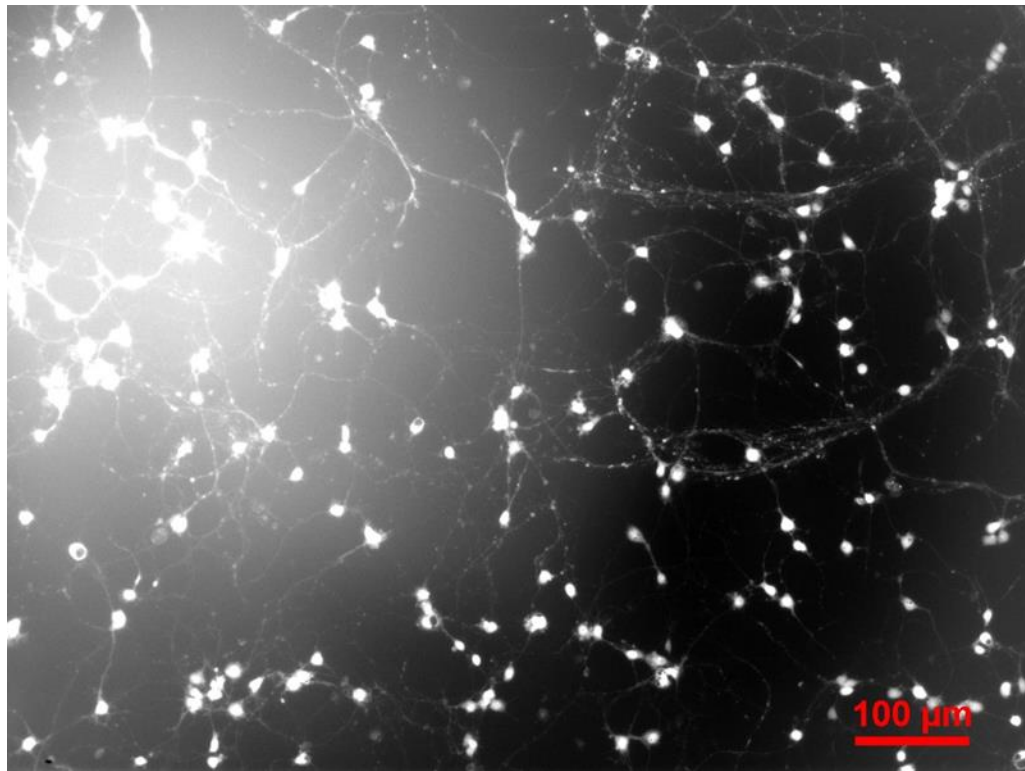


**Figure 5.9.** 5 Calcium ion imaging of neuronal cell culture. DIV 680 cells/mm<sup>2</sup> neuron culture imaged with Fluo 4NW showing neuronal fasciation. Less than 4% of neurons in this image fired, after analysis of timelapse images.

#### *SKPM and Mechanical AFM detection of action potentials*

Time lapse images were acquired to observe action potentials fluorescently, while the AFM was ready to perform an SKPM scan over a firing

neurite or hillock. After fluorescent imaging, the time lapse images were quickly scanned through to identify firing neurons, since the change in fluorescence over the course of imaging was too slow to be visually detected. Neurons that did fire did not repeat firing within the 5-10 minute window, or after the AFM was positioned next to a firing neuron. It appears that the neurons used would only fire once, and not again. This makes finding active neurons to measure with SKPM very difficult since it takes a few minutes to move the AFM tip and position it over a neurite or axon hillock.

### *Electrical Stimulus of Action Potentials*

The AFM was used to initiate action potentials in inactive neurons by shocking the soma, axon hillock, and neurites. This was done by holding the AFM probe at a  $\sim 0\text{mV}$  potential relative to the cell media, then changing it to  $-200\text{mV} < V < 0\text{mV}$  (to change transmembrane voltage to be more positive, to induce depolarization of the membrane) after making contact with the target. This should change the transmembrane potential to be  $< -70\text{mV}$  and surpass the threshold voltage of  $-55\text{mV}$  and induce firing. Unfortunately, this also failed to initiate a fluorescently detectable action potential during all trials.

### *Mechanical Detection and Stimulus of Action Potentials*

As suggested by research on the mammalian neurohypophysis and giant lobster axons [74, 75], we attempted to mechanically detect and probe, push, and pull the soma, axon hillock, and neurites at different forces. Mechanical detection of action potentials had the same problems encountered with SKPM detection of action potentials, where no neurons fired or fired before alignment with the probe and target was possible. Attempts to perturb neurons mechanically with the probe to induce firing failed at all forces until the neuron or neurite was dislodged from its substrate and floated away.

### *Conclusions*

We have attempted to preform SKPM measurements on live cortical neurons. We were unable to measure the action potential of a live cortical neuron. The first challenge we addressed was if our AFM had the resolution to detect the voltage change of the action potential. We used a gold electrode and systematically changed the voltage instantaneously between the cantilever tip and gold electrode in varying steps in ambient air and 1x DPBS. We were able to detect a small ~6mV signal from a 100mV voltage change. In 1x DPBS, we were unable to detect a signal most likely due to ion screening, even though the probe

was within 10nm of the electrode. Additionally, at higher voltages, the conductivity of the 1x DPBS resulted in hydrolysis of the solution and produced a light film of corrosion on the cantilever holder and produced bubbles that would affect measurement. More work must be done to determine the electrical noise in polar fluids using SKPM. However, the current results from 1xDPBS indicate an action potential could be detected based on the measured noise of  $<1\text{mV}$ . However, no signal was detected with any tip-sample potential change. This could be due to the AFM cantilever geometry holder grounding through the gold substrate when the cantilever holder is very close to the gold substrate, which would not be a problem with neurons grown on glass.

Despite these issues, we also attempted to detect mechanical deformations of the axonal membrane during a firing event (and electrical measurements simultaneously). To do this, we acquired fluorescent time lapse of an area for 5-10 minutes. After the time lapse was completed, we would search the images for an increase in fluorescent intensity in a neuron (An increase then decrease in fluorescence is a firing event) then immediately move the cantilever to that neuron and engage on part of it. We were able to easily position the cantilever over neurites, hillocks, and somas. However, we could either not get the probe over a firing neuron in time, or during the time we checked the time lapse and moved the cantilever, the neuron would no longer fire. We did see a few very active neurites firing at relatively high frequencies after fluorescent imaging was completed, but the neurites stopped firing by the time we were able to engage upon them. More work would be required determine the best DIV to measure our

neurons, and to find a better method to quickly identify active neurites and move the cantilever into position. These will be discussed in chapter 7.

## **CHAPTER 6**

### **AFM measurements of silk based biomaterials, polymer films, and hydrogels**

#### **6.1 Overview**

The atomic force microscopy is a highly versatile tool capable of many types of measurements simultaneously on biomaterials, such as silk based materials, hydrogels, and polymer films. Dynamic mechanical analysis (DMA) is a common instrument used to determine the bulk mechanical properties of materials and lacks spatial resolution. AFM is a better choice since cells only sense surface properties and will yield more relevant material properties.

Additionally, AFM can be used in biologically relevant liquid environments and does not require special sample preparation, such as desiccating and sputter coating, as with scanning electron microscopy (SEM). As shown in previous chapters, the topographic and mechanical properties of the cellular environment can have profound effects on the cells mechanical properties and behaviors.

Mechanical properties influence the rate of growth, adhesion, and cytoskeletal arrangements of cells. The electrical properties of the cells environment also play a significant role in processes such as guidance, signaling, and biomineralization.

We use AFM to characterize these biomaterials with force spectroscopy, AC



topography, and SKPM to determine material stiffness, protein structures, and surface potential.

## **6.2 Electrical AFM on Biomaterials**

### *SKPM on Silk Biomaterials for Biomineralization*

Biomaterialization is observed in a wide range of species, where calcium salts and silicas are aggregated into structures for protection and support (such as shells and bones) [173]. Here, the biosilica mineralization process is mediated by a short silica-binding peptide, R5, derived from the silaffin protein of *Cylindrotheca fusiformis* [173]. Solutions of Glucose Oxidase bound R5 and protein polymers have been shown to precipitate silica [173-176]. Silk-Silica biomaterials have been shown to promote osteogenic differentiation of human mesenchymal stem cells (hMSCs) [177]. This implies a Silk-R5 chimera (a fusion protein is produced by joining two genes that code for two different proteins to produce a hybrid protein) may be used for osteogenic tissue engineering [177]. By binding hydroxyapatite binding sequences (VTK64) to Silk, calcification can be promoted [173-177]. Biosilification is driven by negative charges and biocalcification is driven by positive charges, so by changing the charge of the

Silk-R5 or Silk-VTK64 chimeras, tunable biomaterials can be made for osteogenesis [178]. Here, we use SKPM to characterize the surface potentials of these biomaterials to test if these silk biomaterials can be engineered to produce varying degrees of biomineralization based on surface potential.

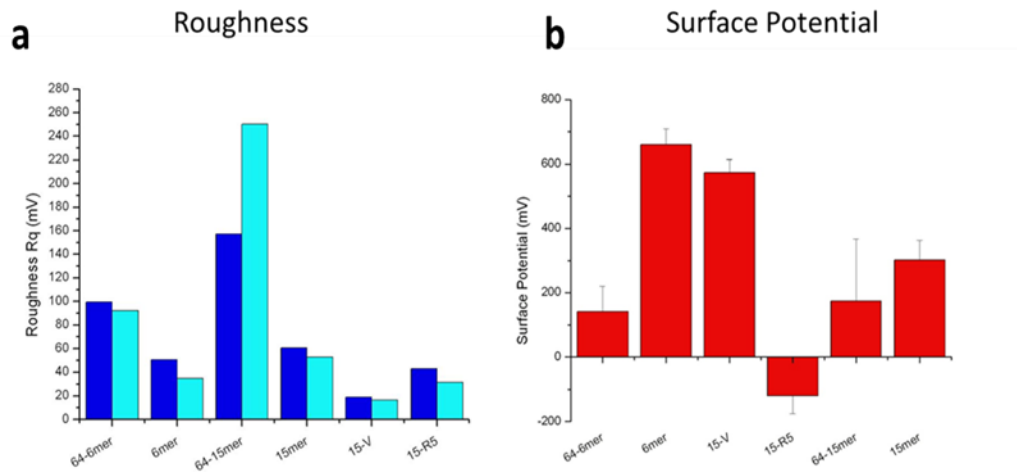


**Figure 6.1.** Roughness and surface potential comparison of silk chimeras.

*a. Roughness of each chimera. Adjacent dark blue and light blue bars are different roughnesses for different areas of the same sample for each type. b. Average surface potential profiles for each chimera. Each bar represents the combination of two SKPM scans, with error bars representing standard error.*

The Silk Biomaterials were made from dissolving the lyophilized chimeras in distilled water to 2.5% wt/vol. 30 $\mu$ l of the solutions were cast into 6mm diameter PDMS molds and allowed to air dry. The dried chimeras were then

vapor annealed to promote  $\beta$ -sheet formation. There are six samples: 6mer, 64-6mer, 15mer, 64-15mer, 15-V, and 15-R5. 6mer and 15 mer are control samples, 64 denotes the protein has a hydroxyapatite binding sequence. 15-R5 is the control for silification. The results shown in Figure 6.1 are from a single sample of each type.

An MFP3D-BIO AFM was used to scan the biomaterial surfaces in AC Topography and SKPM mode simultaneously, with Electrilever cantilevers driven at resonance, to characterize the surfaces' topographically and electrically. Each sample was super-glued to the center of a glass slide. The AFM probe was electrically then calibrated at a 300nm height over each sample with a 700-800mV set point before measurements. Since SKPM measurements are difficult to obtain, parameters were very strictly maintained between samples. Each sample was scanned at least twice with a  $5 \times 5 \mu\text{m}^2$  area, with a scan rate of 0.3hz, tip bias of 3V, no sample bias, Potential I Gain and Potential P Gains each set to 6, and a start-delta-height and delta-height of 0 to -50nm. Roughnesses and surface potentials were determined from Igor Pro 6.36 (WaveMetrics Inc, Portland Oregon, USA).

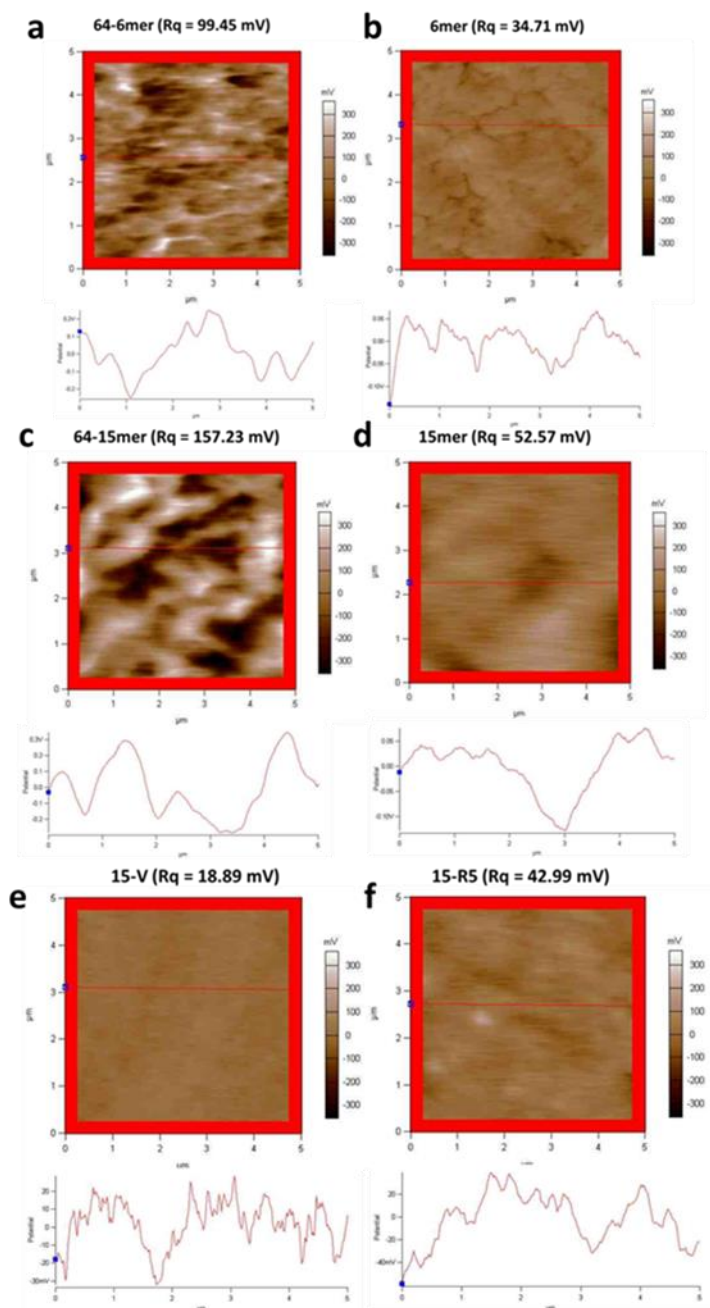


**Figure 6.2.** Surface potential SKPM scans and accompanying potential profile (below scan). The potential profile is the red line on each scan. 64-6mer, 6mer, 64-15mer, 15mer, 15-V, 15-R5, as a,b,c,d,e,f, respectively.

Results showed a difference in surface potentials and potential roughnesses across the samples, with the 64 series of chimeras being the roughest (figure 6.2). Higher potential roughness indicates a more varied surface potential. The SKPM scans (Figure 6.2.) show the most varied protein domains for the 64 series chimeras, where the largest potential changes occur at the surface. For 6mer, 15mer, 15-V, and 15-R5, we did not see as distinct domains. More interestingly, the average surface potentials show only 15-R5 has a negative surface potential (Figure 6.1.), where all others are positive. This suggests 15-R5 will promote silification, and the other proteins will promote calcification to varying degrees based on surface potential magnitude. Currently, further analysis is pending on theoretical interpretations/calculations from the data. Though, the research is promising since it shows SKPM can be used to detect the surface potential variations in these samples.

### **6.3 Force Spectroscopy of Silk Films and Hydrogels**

#### **Tunable Fibroin/Collagen Films**

Creating tunable silk films is of interest for controlling cell function and behavior. This can be done by manipulating the mechanical and biochemical characteristics of silk materials; mainly their stiffness. Fine tuning the mechanical

properties of these biomaterials is crucial to later vary biochemical properties. To alter the material stiffnesses, three sample types were used; pure silk, silk with Collagen I, and Silk with Collagen IV. Each sample type was then water annealed or methanol annealed to render the samples as low stiffness or high stiffness, respectively.

The silk solutions were spin coated onto glass coverslips with 120 $\mu$ l of 1% and 3% wt/vol silk solution, with either 100 $\mu$ l/ml of Silk, Collagen I, or Collagen IV and air dried overnight to make  $\sim$ 20 $\mu$ m thick films. Samples were then water or methanol annealed to induce different degrees of  $\beta$ -sheet formation. The low stiffness samples were water annealed for 16 hours at room temperature. The High stiffness samples were annealed with 100% methanol for 30 minutes at room temperature.

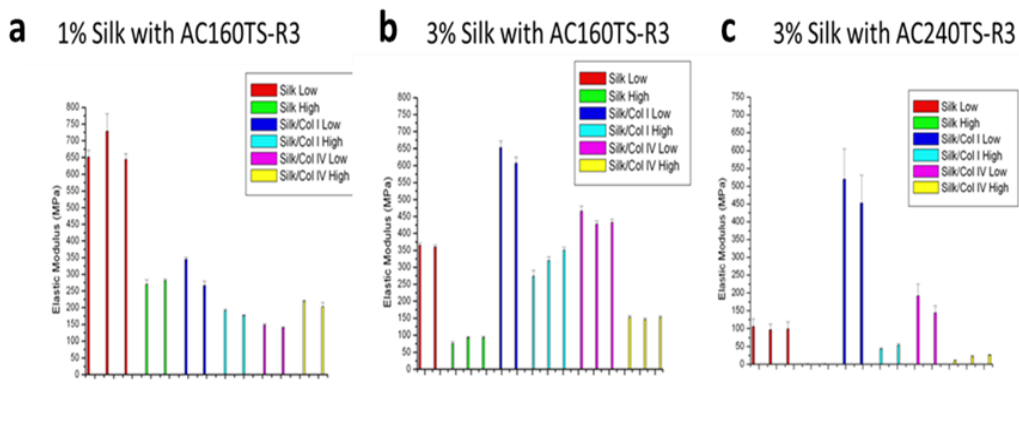


**Figure 6.3.** Histograms of sample elastic modulus in MPa. Error bars are standard error of the mean. Silk Low, Silk high, Silk/Collagen I Low,

*Silk/Collagen I High, Silk/Collagen IV Low, Silk/Collagen IV High, as red, green, blue, teal, magenta, and yellow, respectively. a. 1% silk solution measured with AC160TS-R3. b. 3% Silk solution measured with AC160TS-R3. c. 3% Silk solution measured with AC240TS-R3 Silk high is not visible.*

AFM was used to measure the elastic modulus of each sample, hydrated in 20 $\mu$ l of 1x DPBS at room temperature. Force Spectroscopy (FS) AFM was used to map a 20x20 $\mu$ m<sup>2</sup> with a 20x20 point grid in fluid immediately after the addition of 1xDPBS. Force mapping was done using AC160TS-R3 or a AC240TS-R3 cantilevers calibrated on clean glass microscope slides with a 2  $\mu$ m/s indentation rate. The later cantilever was used to match the previous measuring protocol, though the only difference was cantilever stiffness (the cantilevers have the same geometry). AC240TS-R3 cantilevers were chosen at the end to stay consistent with previous measurements.

Interestingly, Force Spectroscopy AFM yielded the opposite of the expected results for the 3% silk (Figure 6.3 b and c) measured with AC160TS-R3 Cantilevers, showing “High Stiffness” samples having a much lower elastic modulus than “Low Stiffness” samples. Unfortunately, the water annealed silk sample showed the film as having an elastic modulus as about 3x higher than previous experiments, which put the results in question. This is what prompted the change in cantilever to a AC240TS-R3 to match the previous protocol. This change yielded the expected modulus for water annealed silk at ~100MPa. Even with the change in cantilever and the better result for water annealed silk, the

trend held and was further exaggerated showing a more extreme difference between water annealed and methanol annealed films. For the 1% films (Figure 6.3 a), only Silk/Collagen IV followed the expected stiffness trend, and the methanol treated films were only slightly stiffer than the water annealed one.

This opposite trend in expected stiffness indicates methanol annealing resulted in softer films than water annealing, indicating methanol might denature the proteins by disrupting the secondary and tertiary protein structures. The dry elastic modulus of the samples, other than the silk/collagen I series, was mostly unaltered between high and low samples. This suggests a methanol annealing increases the amount of water absorbed into the films. Further study is required to determine the cause of the opposite stiffness trends.

#### *Tunable Silk/Tropoelastin and Silk/Ionomer Hydrogels [178]*

Silk Fibroin hydrogels with tunable mechanical properties are ideal for the construction of new biomaterials for tissue replacement/ regeneration and therapy. They provide a 3D environment that mimics the extracellular matrix. Biophysical and biochemical properties can be altered in these materials to change the cell's microenvironment, and therefore affect cell differentiation and proliferation. Silk Fibroin with human tropoelastin (SE) or Silk-Ionomer (SF(S)-CO(L-glu)<sub>50</sub>) (SPG) was used to create the hydrogels. Varying the % wt/vol ratios of Silk



Fibroin to Tropoelastin or Silk Fibroin to Ionomer can change the stiffnesses of the hydrogels. Here, these hydrogels are used to grow and study the microenvironmental effects on human bone marrow derived hMSCs. Hydrogels were made from a 2% wt/vol solution silk fibroin derived from the cocoons of *Bombyx Mori*. Tropoelastin was added to the silk solution in varying % wt/vol ratios, from 50:50, 75:25, 90:10, and 100:0 (SE50, SE75, SE90, and SE100, respectively). Ionomer was added to the silk solution in varying %wt/vol ratios of 50:50 and 90:10 (SPG50 and SPG90, respectively). Gels were refrigerated and measured between 1 and 3 weeks after they were made.

AFM Force-Volume maps were obtained with TR800PSA cantilevers in 1xDPBS and calibrated on a glass microscope slide in 1xDPBS. All measurements used a 0.5V set point, 3-5  $\mu\text{m}$  start height and a with a 2  $\mu\text{m/s}$  indentation rate. Four force maps were taken over random  $10 \times 10 \mu\text{m}^2$  areas with 100 to 400 force points per map. The samples were prepared in 6mm diameter, 2mm deep, PDMS molds that were plasma treated onto standard glass microscope

slides.

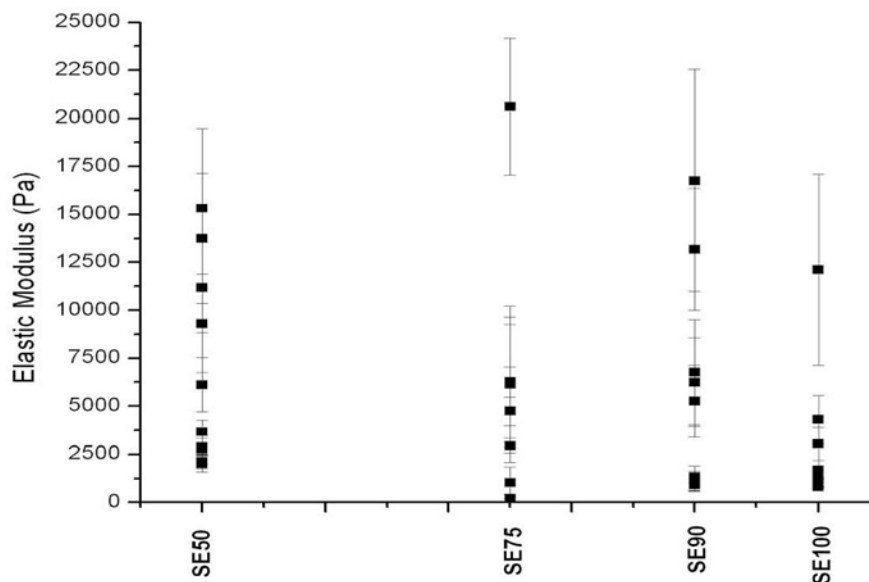


**Figure 6.4.** Elastic modulus vs tropoelastin content. Each point is a force map of the hydrogel. Error bars are standard error.

Characterizing silk hydrogels with different ratios of silk to tropoelastin called SE50 (50:50), SE75 (75:25), SE90 (90:10), SE100 (100:0) and silk to ionomer SPG50 (50:50) and SPG90 (90:10) was carried out by Force Spectroscopy on AFM. Initially, gels were cast in a specially made fluid with 2mm diameter holes 2mm deep. This proved difficult to measure and yielded varied results between a few pascals to 20 kPa and was not repeatable. The gels appeared to be locally homogenous, but globally inhomogeneous as seen by figure 6.4.

So a larger cell was made using a piece of 3mm thick PDMS with a 6mm diameter hole that was adhered to a glass slide. Measurements were repeatable, although the force curve quality varied.

These results (above) with AFM do not agree with previous results or with Dynamic Mechanical Analysis by 3 orders of magnitude. This could be due to hydration of the gel at the PBS/gel interface, or a “polymer brush” interface. Results between Silk-Tropoelastin and Silk-Ionomer hydrogels were not consistent. Multiple hydrogel batches were measured yielding the same inconsistencies. Sometimes, the elastic modulus varied by a factor of 10, such as SE90 sample yielding ~8KPa, and then yielding ~120kPa in the same sample. This suggests the hydrogels did not homogeneously gel and are highly sensitive to some condition that was not controlled. For AFM force measurements, it seems that gel surface quality was highly varied. Sometimes, contact with the gel surface was easy, other times, it was impossible. This is likely due to a poorly defined surface-fluid interface. Dynamic Mechanical Analysis yielded consistent results between hydrogels from different batches, and showed a trend of increasing elastic modulus with increasing tropoelastin concentration and a decrease in elastic modulus by increasing ionomer concentration [178]. These data suggest structural differences in the gels due to electrostatic and hydrophobic interactions between the polymers at different silk concentrations [178].

## 6.4 Topographic and Mechanical Characterization of Silk based Fibers

### *Silk Nanofibrils Measured by Atomic Force Microscopy*

Silk Nanofibrils are self-assembled silk structures a few microns long (contour length) and 80-100 microns wide. The assembly of natural silk nanofibrils allows for the study of silk's structure-process-function relationship. Atomic Force Microscopy (AFM) is well suited to probe the structural and mechanical properties of these nanofibrils. A major question is what protein structures form these nanofibrils, and how these structures are organized in the nanofibril. Preliminary AFM data shows they are composed of segments, generally alternating between 1 and 2 nm tall (Figure 6.5 e). This, with FTIR data showing high  $\beta$ -sheet composition, suggests the nanofibrils are composed of  $\beta$ -sheets stacked 2-4 sheets tall and connected end to end. This is seen in Figure 6.5 d and e, where the red line in figure 6.5 d traversing the fibril is the height profile shown in figure 6.5 e.

Nanofibrils were made from a solution of 0.1% wt/vol silk, from *Bombyx Mori* cocoons, and incubated at 60°C in 7% ethanol/water at 9.5 pH. The solution was diluted 100x-1000x with water and allowed to air dry on glass slides,

resulting in the aggregation of nanofibrils.

AC AFM, using OTESPA cantilevers, was used to topographically scan  $200 \times 200 \text{ nm}^2$ - $10 \times 10 \mu\text{m}^2$  sample areas. At 1000x dilution (Figure 6.5 a, b, c, d), elongated nanofibrils were observed displaying a segmented structure. At 100x dilution, only a film of these segments was observed. 500x dilution yielded dense clusters of tangled fibrils, and further dilution lowered the population density of fibers. AFM showed three main nanofibril morphologies; long single strand nanofibrils (Figure 6.5 a and 6.5 b), Nanofibrils that branch into two new strands (Figure 6.5 c), and rings (faintly seen middle of left upper quadrant in Figure 6.5 a and 6.5 b). The uniform structure suggest the fibrils have high  $\beta$ -sheet content, considering the source of the silk has high  $\beta$ -sheet content, though the fibrils have not been tested for  $\beta$ -sheet content to date.

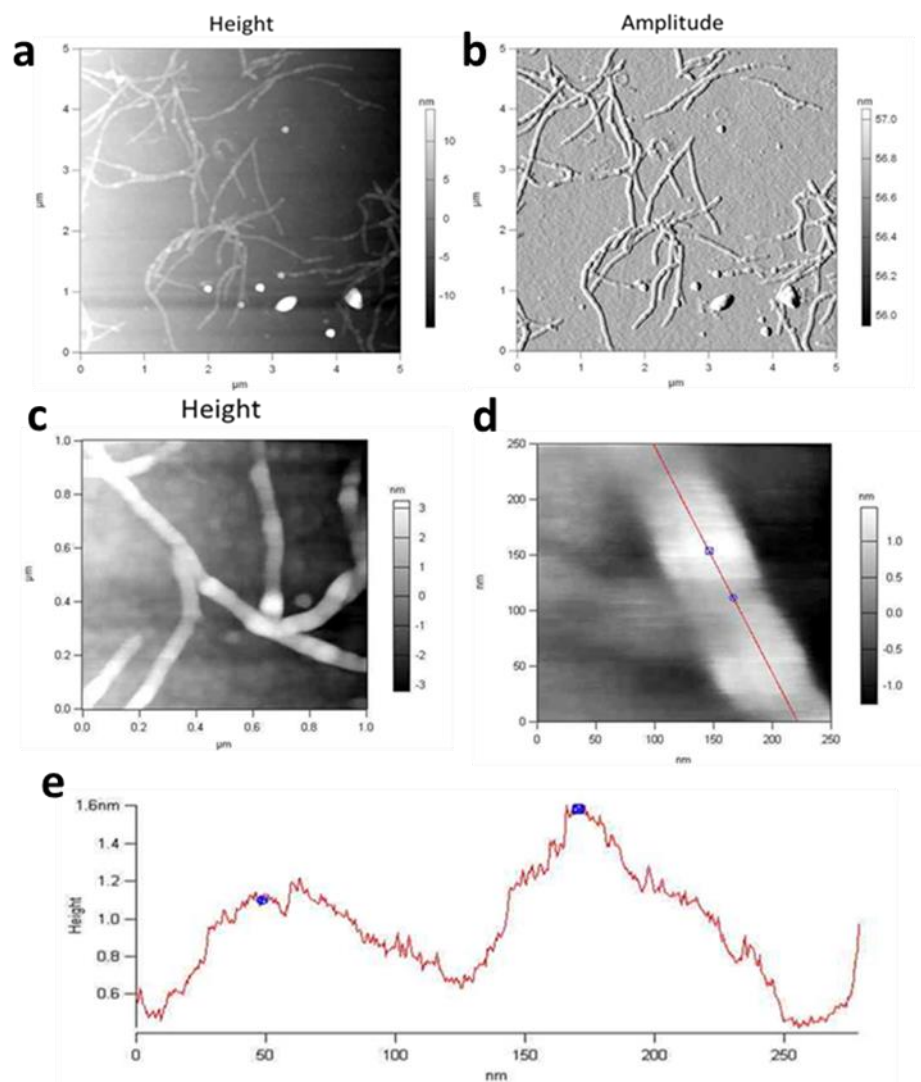


**Figure 6.5.** AFM images of silk nanofibrils. *a.* 5x5μm<sup>2</sup> AC AFM height scan of nanofibrils dried at 1000x dilution. *b.* 5x5μm<sup>2</sup> AC AFM amplitude scan of *a.* *c.* 1x1μm<sup>2</sup> AC AFM height scan of nanofibrils. *d.* 250x250nm<sup>2</sup> AC AFM height scan of two nanofibril segments. *e.* Height profile of nanofibril in *d.*

More data and further analysis is required to better understand the process of fiber formation and structure. Further research aims to provide mechanical stiffness data and charge distribution to determine  $\beta$ -sheet content and orientation in the nanofibrils.

*Effects of sequence features on assembly of spider silk block copolymers*  
[179]

Spider silk is an interesting natural polymer due to mechanical strength (tensile strengths comparable to Kevlar) and biocompatibility (can be used as implants that are not rejected by the body) [179]. Spider silk proteins can be spun in aqueous solutions at ambient conditions to produce high quality fibers. The number of polymer block repeats within the sequence affects the silk fiber mechanical properties and morphology. We use a block design to describe how hydrophilic polymer blocks and hydrophobic polymer blocks sequence affects the self-assembly of these proteins.

Here, two polymer blocks derived from major ampullate dragline silk of the *Nephila Clavipes* were created by cloning their genetic sequences through the pET30a(+) vector before being transformed into a bacterial host for protein expression prior to protein purification [179]. The cloned proteins are composed of hydrophobic and hydrophilic blocks: The hydrophobic A block, composed of

one GAGAAAAGGAG sequence, and the hydrophilic B block, composed of four GGX repeats separated by a GSQGSRG sequence [179]. When the proteins are assembled in an aqueous environment, the A blocks pack together, while the B blocks shield the A blocks from water, to fold into an entropically favorable configuration. Altering the number of A and B blocks, and their sequence, results in different folded configurations, such as lamellae and spheres [179]. Two cloned protein constructs were used,  $H(AB)_2$  and  $H(AB)_{12}$ , to investigate the effect of block sequence on protein microstructures.

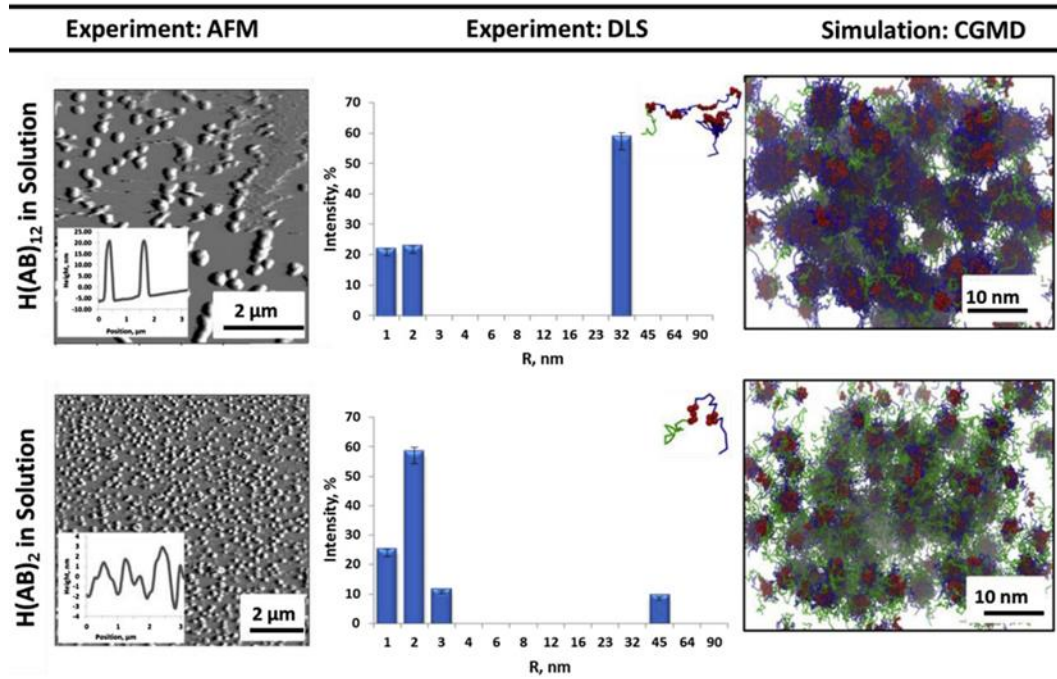


**Figure 6.6.** AFM scans of micelles ( left top and bottom) with % of micelles vs average micelle radius (center top and bottom) and simulated micelles (right top and bottom) [179].



Under ambient conditions with a 0.25 mg/ml aqueous protein solution, both protein constructs aggregated into micelles. AFM contact mode topography revealed that H(AB)<sub>12</sub> formed larger spherical aggregates ( $32 \pm 5\text{nm}$ ) and H(AB)<sub>2</sub> formed smaller spherical aggregates ( $2 \pm 0.5\text{nm}$ ). This was qualitatively supported by coarse grain simulation, which showed the same trend (Figure 6.6) [179]. However, upon drying, both constructs failed to maintain this morphology. At a silk/water concentration of 1mg/ml, H(AB)<sub>12</sub> formed thin fibrils while H(AB)<sub>2</sub> formed a film. With an increase in concentration to 2.5mg/ml, H(AB)<sub>12</sub> formed much thicker fibril, while H(AB)<sub>2</sub> formed an apparently thicker film (figure 6.7).

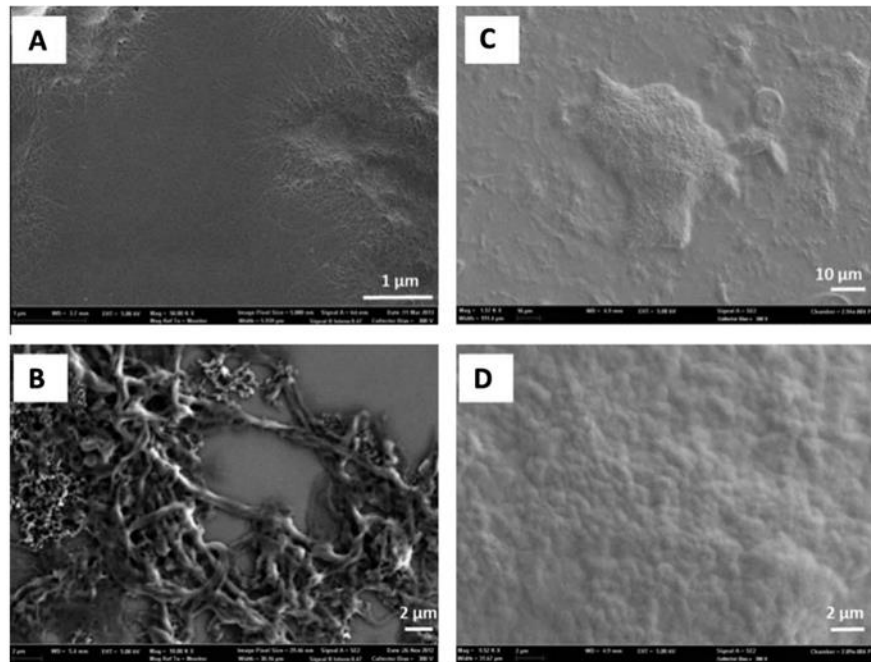


**Figure 6.7.** SEM images of dried H(AB)<sub>12</sub> (A and B) and H(AB)<sub>2</sub> (C and D). A and C are dried proteins at 1mg/ml, and B and D are at 2.5mg/ml [179].

After drying at 100mg/ml,  $H(AB)_{12}$  began forming organized structures. At 200mg/ml,  $H(AB)_{12}$  a protein rich and protein poor phase separation occurred, resulting in  $5 \pm 1 \mu\text{m}$  wide periodic structures composed of aligned lamellar structures perpendicular to the larger structures (figure 6.8). This shows block sequence plays a crucial role in structure formation. We see that increasing the number of (AB) repeats causes the constructs to form more ordered structures. This demonstrates the influence of chain length in forming microstructures.

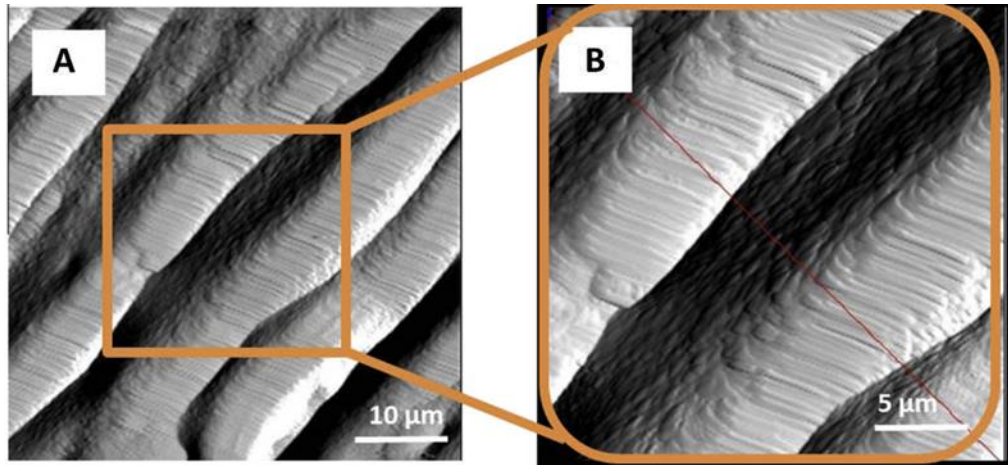


**Figure 6.8.** AFM amplitude scan of dried  $H(AB)_{12}$  fibers. AFM scans reveal fibers are comprised of highly organized lamellar structures [179].

#### *Effect of Treatment on Spun Silk Fibers*

Silk fiber structural and mechanical properties are highly dependent on the method in which they were spun and treated. Spinning induces shear forces upon

the forming fibers and results in the formation of beta sheet conformations in the proteins via fluid shear forces [179]. The fluid in which they are spun or stored also affects the beta sheet content and chemistry of the proteins from chemical and entropic forces. AFM is one of the best tool for studying individual fibers due to its high spatial resolution and sensitivity. Here, variations of the spider dragline silk H(AB)<sub>12</sub> NtSp (unless otherwise specified at H(AB)<sub>12</sub> 2-2 or H(AB)<sub>12</sub> 2), is treated, with different alcohols (isopropyl alcohol and methanol), and probed with AFM force spectroscopy to determine fiber elastic modulus. The fibers were also scanned in AC AFM mode to observe surface microstructures.

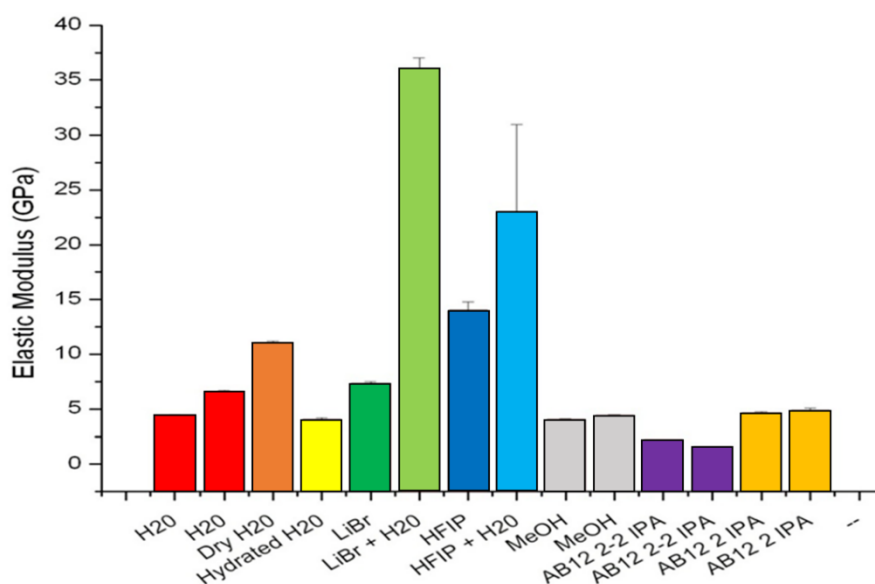


**Figure 6.9.** Graph of fiber elastic modulus (GPa) versus treatment chemical. Proteins are H(AB)<sub>12</sub> NtSp unless otherwise specified in the horizontal axis. Error bars are standard error of the mean. Repeated treatments denote

*different fibers. Each bar represents at least 400 force points. Like colors indicate a repeated sample.*

H(AB)<sub>12</sub> constructs were cloned from spider dragline silk and expressed by E. Coli. H(AB)<sub>12</sub> solutions of 20% wt/vol in water at pH 7.4. The proteins were then dissolved in 9 M LiBr before water dialysis. The proteins were spun through a PDMS microfluidic device and collected in a reservoir of methanol (MeOH), isopropyl alcohol (IPA), HFIP, HFIP and water, LiBr, LiBr and water, or water. Some water samples were also allowed to air dry for a few days before measurement, and are denoted as “dry”. Other water samples were dried for ~10 minutes just before FS AFM measurements, and are denoted as “hydrated”. HFIP, HFIP and water, LiBr, and LiBr and water samples were stored in water prior to measurements and dried for 10 minutes in air before measurements. All samples were placed on glass microscope slides and dried on those slides before measurements, and fibers were carefully chosen as not to deform under measurement.

The fibers were studied with an MFP3D Bio AFM in AC AFM and FS AFM. AC AFM was performed with OTESPA cantilevers over large fibers. Scans varied between 250x250nm<sup>2</sup> and 20x20um<sup>2</sup>. FS AFM used the same OTESPA cantilevers calibrated on a glass slide. Force maps were acquired over the AC AFM scan region with 100 - 400 points. The majority of data taken was FS AFM without AC AFM, over random areas of the fibers.

FS AFM revealed different elastic moduli between fiber treatments (Figure 6.9). Protein in LiBr in water and HFIP in water yield the highest elastic moduli, followed by HFIP, and dry. Dry protein is stiffer than wet protein because water acts as a solvent and bonds to hydrophilic protein domains, loosening the Van der Waals bonds between  $\beta$ -sheets. Methanol treated H(AB)<sub>12</sub> NtSp and IPA treated H(AB)<sub>12</sub> 2-2 and H(AB)<sub>12</sub> 2 are less stiff than the pure water samples, showing alcohol treatments denature the proteins in the fibers.

*Combined modelling-experimentation analysis of the spider silk N-terminal  
Consequences on fiber properties [180]*

Spider silk terminal domains are believed to play an important role in fiber formation and properties. Adding a N-terminal domain to H(AB)<sub>12</sub> (making NtSP H(AB)<sub>12</sub>) has the ability to change the fiber properties, and allows for the study of the role of terminal domains in fiber mechanical properties. The effects of the addition of N terminal to addition to H(AB)<sub>12</sub> is investigated here. We find the N terminal contributes to a change in fiber physical properties, such as average diameter and toughness [181]. Interestingly, the N terminal does not seem to change the Young's modulus of the fibers.

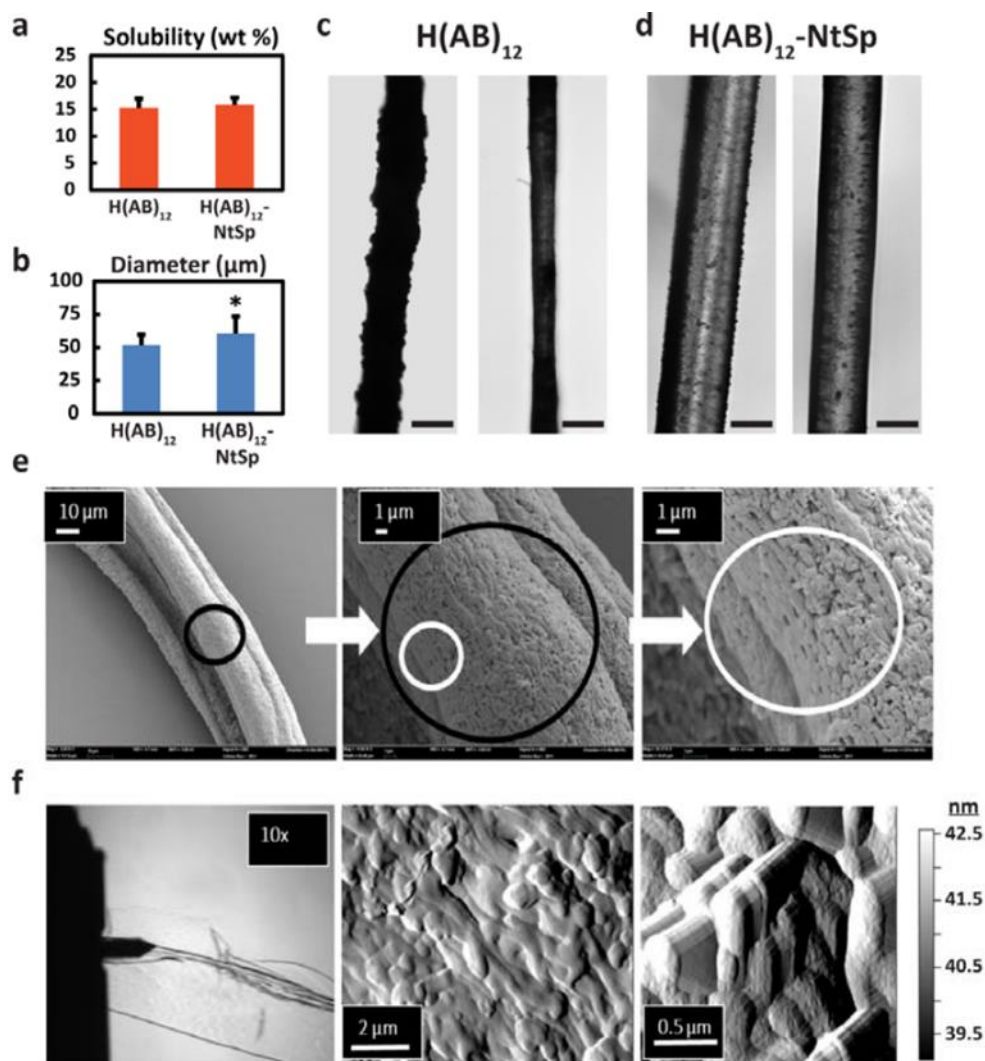


**Figure 6.10.** Images of H(AB)<sub>12</sub> silk fibers. *a* and *b*. Comparison of fiber solubility in water and diameter, respectively. *c* and *d*. Optical images of H(AB)<sub>12</sub> and NtSP H(AB)<sub>12</sub> fibers, respectively. *e*. SEM images of NtSP H(AB)<sub>12</sub> fiber with increasing magnification. *f*. left. Optical image of AFM cantilever and fiber (10x). *f*. middle and right. AFM topography scans of micelle micro structures [180].

The N terminal significantly changes average fiber diameter as measured by optical microscopy (figure 6.10 c and d), with the N terminal addition causing larger fiber diameters. This is most likely due to larger aggregate size of NtSP H(AB)<sub>12</sub>. AFM and SEM scans of wet spun 15% wt/vol NtSP (N terminal) H(AB)<sub>12</sub> and H(AB)<sub>12</sub> shows smooth and rough fibers, respectively. This implies the NtSP fibers are formed through micelle aggregation as seen in figure 6.10 e and f.

Uniaxial tensile strength tests show a difference in tensile strength, however this is accounted for by the differences in fiber diameter, which indicates the silk constructs have similar strength and does not affect Young's modulus. The N terminal contributes to a 40% decrease in toughness (50% to 10%, between H(AB)<sub>12</sub> and NtSP H(AB)<sub>12</sub>), which is similar to native dragline silks (15%). However, the toughness properties between the two silks are almost identical before failure. This implies NtSP H(AB)<sub>12</sub> has a higher crystalline content than H(AB)<sub>12</sub>. Also, NtSP H(AB)<sub>12</sub> has half the  $\beta$ -sheet content as H(AB)<sub>12</sub> and double the  $\alpha$ -helix content (determined by Fourier transform infrared spectroscopy), which is counter intuitive to the mechanical results [180]. Usually, a decrease in  $\beta$ -sheet content would decrease the strength of the material, however it has little effect here. This implies  $\alpha$ -helix interactions must account for lack of change in mechanical properties.

## 6.5 AFM on Polymer Films

### *Thiophene-Based Conjugated Polymers with Photolabile Side Chains [181]*

Conjugated polymers (CP) are used in many organic solid state optoelectric technologies. These polymers generally have Alkyl side chains, which make the polymers soluble under certain conditions. Solubility is crucial to the preparation and processing of these polymers into thin films, which gives them advantages of inorganic soluble polymers [181]. Though, this property restricts the deposition substrate to one that has soluble orthogonal side-groups [181]. Additionally, CPs are generally made with other optoelectronic materials and they contribute to conjugated polymer degradation processes [181]. These problems are addressed by using a polythiophene derivative comprising n-octyloxy chains connected to the conjugated thiophene backbone using photolabile ONB esters, which are cleaved by 365nm UV radiation and rendered insoluble to  $\text{CHCl}_3$  [181]. Another advantage of using these esters is high spatial control over solubility using photomasking techniques.

AFM was used to test the film thickness of the polymer with 5 different ONB ester or ether side chains before and after rinsing with  $\text{CHCl}_3$  for 30s. Films prior to irradiation and rinsing are denoted in figure 6.11 as “thick”, while irradiated and rinsed films are “thin” [181].



Film thicknesses of UV irradiated PTBNB Ester, MNB Ester, PTNM Ether, PTMNB Ether, and DAMNB Ether spin coated onto glass coverslips in a thick or thin film and imaged them using AC mode on the AFM. To find the thickness, the films were scratched with a razor to expose the coverslip and immediately followed by a  $5 \times 5 \mu\text{m}^2$  scan of the scratch. AFM topography scans were repeated multiple times over different scratches on the same sample to show consistency, then the vertical distance between the scratch bottom and film surface was measured in 10 different locations for each film to find the thickness distributions. Only one sample was used for each type due to the uniformity of sample thicknesses determined by monitoring absorbance with UV/vis spectroscopy [181]. Mean film thickness is seen in figure 6.11 with standard deviation as error bars.

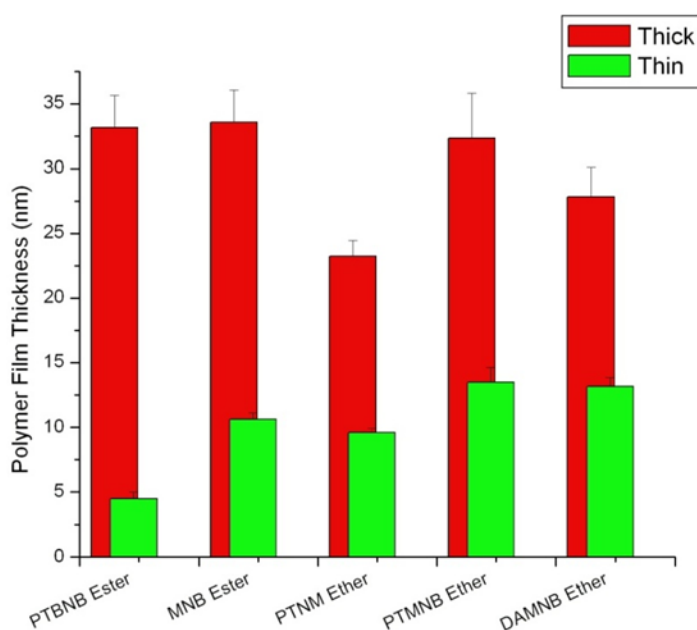


**Figure 6.11.** *Film thickness vs side chain type measured via AFM. Green bars are thin samples, red bars are thick samples used [181].*

These results show that polymer film retention reduced significantly upon irradiation and rinsing. Film thicknesses were compared to UV/vis absorbance spectra before and after to determine the degree of decrease in absorbance spectra of the thiophene backbone. AFM showed film thicknesses after irradiation and rinsing decreased over ~50% for all films, while the absorbance spectra only decreased by ~ 10%. This result is attributed to UV induced close packing of the polymer chains.

#### *Stimuli-Responsive Free-Standing Layer-By-Layer Films [182]*

Layer by layer films have a variety of applications from antifouling surfaces to therapeutic delivery systems. They can be specially tuned to be responsive to external stimuli, by disrupting interactions between the layers. Here, a triple-responsive layer-by-layer (LbL) film is used that delaminates with UV radiation, releases a dye by chemical reduction, and dissolves upon increase in pH. The first stratum (composed of a poly(styrene sulfonate) (PSS) with photodegradable polycation P1 bilayers) is deposited on a plasma cleaned quartz

substrate. A second stratum of bilayers (PSS and the redox/pH responsive polycation P2) is deposited on top of the first [182].

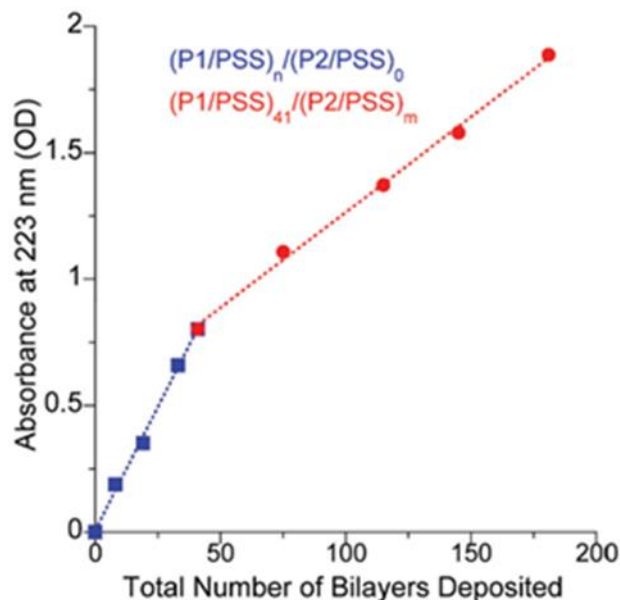


**Figure 6.12.** 223nm absorbance dependence on number of deposited bilayers per stratum. Blue points are from the P1 bilayers. Red points are from a P1 layer plus multiple P2 bilayers [182].

AFM was used (in AC mode with cantilevers of  $k = 2\text{N/m}$ ) to measure the thickness of the films to determine the number of bilayers ( $\sim 2\text{-}3\text{nm}$  per bilayer) per stratum deposited onto the substrate, and the absorbance spectra as a function of number of bilayers (figure 6.12). Measurements were performed by optically identifying a boundary between the film and the substrate, and scanning over a  $10 \times 10 \mu\text{m}^2$  area. Film thickness was used to calculate the number of bilayers

composing the film, and compare it to UV absorbance spectra at 223nm. Results show a linear dependence of 223nm absorbance with number of bilayers.

## **6.6 Neurons Grown on Soft Gels and Fibers**

### *Axon Guidance with Functionalized AFM Probe*

AFM was used to guide 4 to 5 day post culture rat cortical neuron axon extension using functionalized sphere tipped cantilevers by haptotaxis and chemotaxis. I performed the experiments with cantilevers functionalized with Laminin, NGF doped Silk Beads, riboflavin gel, and Silk Gels. Time-lapse images of the neurons were taken for 30-60 minutes at 5 minute intervals.

Initially, a chemotactic approach was tried. A 10  $\mu\text{m}$  glass bead was epoxied onto a broken (tip missing) AC160TS cantilever and doping the entire cantilever in 1mg/ml laminin for 2 hours at 37°C. The neurons were cultured on PDL coated glass slides (1mg/ml for 2 hours at ambient temperature). The prepared cantilever was brought into contact with a clear region on the glass surface about 30  $\mu\text{m}$  away from a growth cone at a position different than the axon's current growth direction. If no direction change was observed within 30 minutes, the cantilever was moved about 10  $\mu\text{m}$  closer to the growth cone. I only

saw a direction change once with the cantilever sphere center about 20  $\mu\text{m}$  from the growth cone. The axon extended directly towards the bead before dying and retracting.

Another chemotactic approach was attempted with NGF (neuron growth factor) doped silk beads. The beads were prepared with 1:5 ratio of 5% Silk and 5% PVA with 200  $\mu\text{g/ml}$  NGF, stirred for 4 hours, and air dried into a film for 3 days. The film was dissolved in DI water, and centrifuged to separate beads from the PVA/DI water solution. After beads were separated and dried, a bead around 25  $\mu\text{m}$  diameter was glued to a MLCT O10 silicon cantilever with epoxy and allowed to dry at 8°C overnight. The experiment was performed the same as the laminin coated bead experiment. After multiple attempts, no growth was observed, or the neurons died. The death was most likely due to uncured epoxy that diffused from the porous silk bead.

A haptotactic approach was also tried by coating a sphere tipped cantilever with silk gel and riboflavin gel with the idea of scraping the gel off onto a PDL coated surface like a paintbrush to guide the axons. Riboflavin failed to polymerize onto the cantilever tip using the fluorescent microscopes blue light source. Silk gel, made from 2% silk solution sonicated for 10 seconds at 20% amplitude, successfully adhered to the cantilever. However, the gel adhered too well and could not be removed with friction between the PDL coated slide.

### *Neuron Mechanics on Polyacrylamide Hydrogels*

Fetal rat cortical neurons were grown on PDL coated soft polyacrylamide gels (pAG) of about 160 Pa and glass to measure the effect of substrate stiffness on neuron elastic modulus. Soft pAGs were made by altering the standard protocol (Gels of ~25KPa) by lowering the amount of Bis/Acrylamide by 33% and raising the amount of 1x PBS to maintain volume. pAG and glass surfaces were coated with 0.1 mg/ml PDL and water solution for 2 hours before plating neurons at a density of about 180 cells/mm<sup>2</sup> and incubating at 37°C for 3-4 days. Neurons were measured with a BL-RC-150VB cantilever over a 256 µm<sup>2</sup> area at an indentation velocity of 1 µm/s.

Force Spectroscopy showed the 5 neurons grown on pAG and the 6 neurons grown on glass did not show an important difference in elastic modulus (figure 6.13). Neurons grown on pAG were also poorly adhered to the surface, and moved during force mapping, which could have contributed to the relatively wide standard deviations.

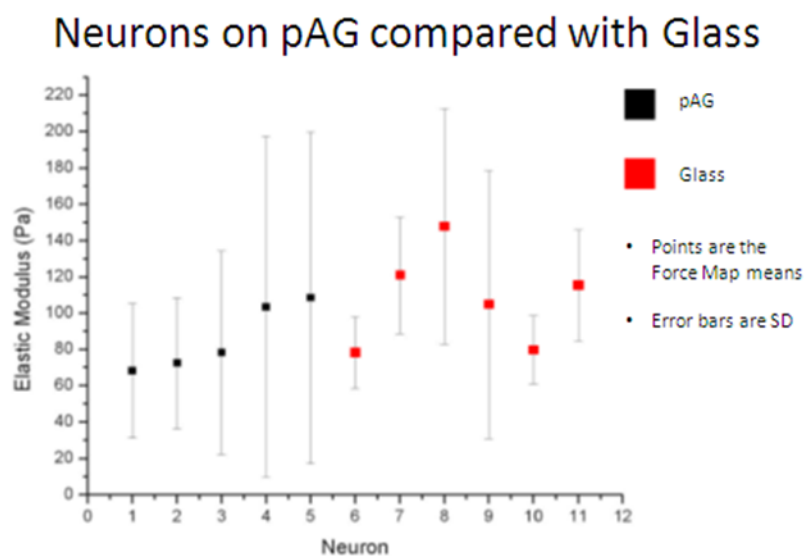


**Figure 6.13.** Average Elastic Modulus vs individual cell grown on PDL coated glass slides (red) or polyacrylamide gel (pAG). Error bars are standard deviation.

#### *Direction Growth of neurons on PLLA and PLGA Fibers*

Fetal rat cortical neurons were grown on PDL coated electrospun PLGA and PLLA fibers with and without (neat) carbon nanotubes (CNTs) to show a directional bias to axon extension relative to the fiber orientation, and if CNTs affected guidance. Neurons were fluorescently stained with a 0.02 mg/ml of Fluorescein Diacetate (FDA) in 1x PBS to show contrast to the fibers and viewed through the 10x objective. An associated optical transmission image (using a LED

flashlight) for each fluorescent image of the fibers was taken to determine axon growth direction relative to the fiber orientation. The fibers with CNTs had 1% CNTs 15% polymer in HFIP and spun at 25 kV, where the neat fibers 15% polymer in HFIP and spun at 25 kV. The neurons were plated on the fibers and incubated at 37°C for 2-3 days. The fibers were held down by rubber rings to prevent floating. Before imaging, the media was aspirated and replaced with the FDA working solution, and the fibers were flipped in a well plate neuron-side-down (for our bottom up optical microscope). Fluorescent images (3 second exposure, averaged 8 times) were taken of the neurons at ambient temperature. Angular distributions were calculated by breaking axons into 20  $\mu\text{m}$  segments in Image J and making histograms.

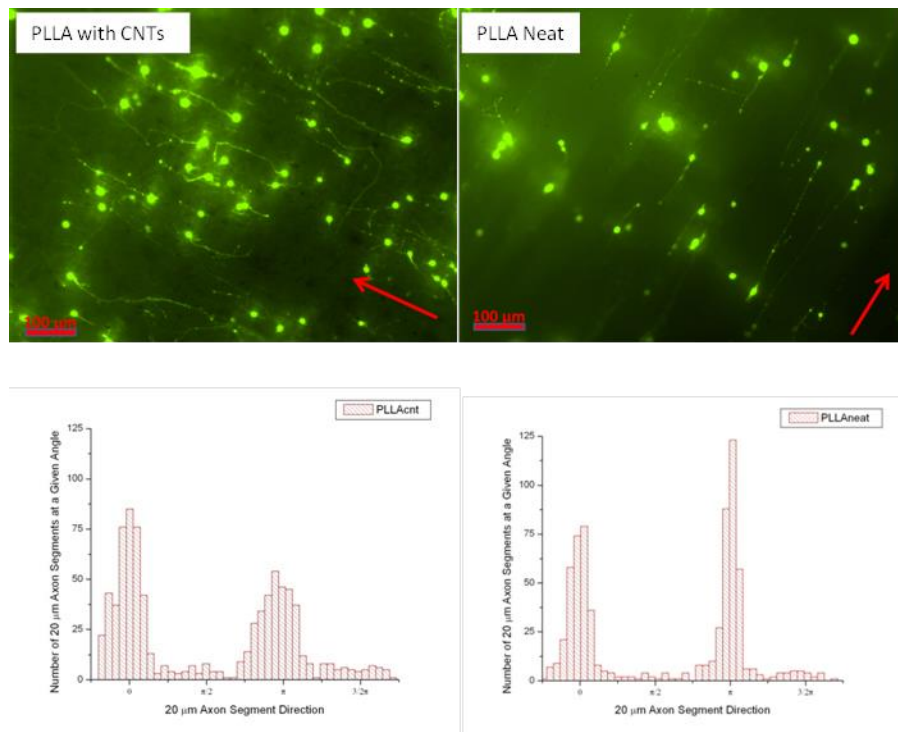


**Figure 6.14.** Fluorescent images of neurons on PLLA fibers (top) with



*corresponding angular distributions (below Left. PLLA with imbedded CNTs. Right. PLLA with no CNTs. Red arrow indicates average parallel fiber direction.*

PLGA and PLLA fibers chemically degraded killed the cells. This was attributed to residual HFIP as shown from Thermogravimetric Analysis. To remedy this, the PLLA and PLGA fibers were sandwiched between two glass slides and heated to just above their glass transition temperature for 30 seconds in an effort to evaporate off any residual HFIP. This helped for the PLLA neat and PLLA with CNTs, but not for any PLGA. Results for PLLA neat (figure 6.14) and PLLA with CNTs (figure 6.14) showed highly direction growth along the fiber orientation (red arrows). Neuron viability on PLLA with CNTs seemed higher than that on PLLA neat, but cell viability between successive experiments was unpredictable.

### *Conclusions*

AFM is a unique and versatile tool for exploring the properties of biomaterials, polymers, and hydrogels, and their effects on living cells. We use electrical AFM to measure different silk chimeras to identify the best candidates to promote biomineralization. We found 15-R5 should promote silification, and all others will promote calcification to varying degrees, which can be useful for

regeneration of bone material. We used mechanical AFM methods to determine the effect of different collagens and their concentrations on the stiffnesses of silk films. This showed an opposite stiffness trend than expected, with methanol treated films being less stiff than water annealed films. We showed the effect of human tropoelastin and silk ionomers on silk based hydrogels, and found them difficult to measure. Topographic and mechanical AFM was used to extensively study the structure and stiffnesses of genetically engineered spider silk fibers and study the structure of polymer films [179, 180]. We found  $H(AB)_{12}$  silk fibers were composed of lamellar  $\beta$ -sheet structures [179], and micelle aggregation plays a crucial role in fiber formation for NtSP  $H(AB)_{12}$  [180]. We also tested the effect of different treatments of fiber quality/stiffness. We found LiBr and water treated fibers were the strongest. We also found methanol treated fibers were less stiff than water annealed fibers, which is a similar result shown on our collagen films. This result indicated methanol denatures both spider silk and silk worm silk proteins. Additionally, we grew neurons on soft gels to study cytoskeletal effects of substrate stiffness and PLLA fibers pathfinding on fibers. We found neurons grown on glass substrates were slightly stiffer than those on soft polyacrylamide gels. However, this result must be studied further to determine whether this effect is due to cytoskeletal arrangements, a change in pericellular brush, or substrate interference with measurement. We also found neurons are highly likely to grow parallel to PLLA fibers both with and without CNTs, however the presence of CNTs results in wider peak distributions.

## **CHAPTER 7**

### **Future Directions and Conclusions**

#### **7.1 Overview**

We have measured the mechanical properties of the neuronal pericellular brush, contact guidance behaviors of cortical neurons, and made attempts at using AFM to measure neuronal action potentials. Interesting continuations of this research can include combining AFM measurement with confocal microscopy or single molecule fluorescence to directly observe bioproteins within the cell under AFM measurement. This method can be used to measure integrin densities and diffusion as a function of membrane curvature on growing growth cones and fluorescently observe molecular rearrangements of the pericellular brush while under load (by AFM). Additionally, electron beam lithography can be implemented to manufacture a wide range of surface topographies to study contact guidance mechanics of neurons and other cell types. We also explore alternative experiments to measure action potentials via AFM. Here, we discuss possible future directions of the research in this thesis.

## 7.2 Future Directions

### *Combined AFM and confocal microscopy on pericellular brush*

Confocal microscopy is a form of fluorescent microscopy that uses focused lasers to XY raster over a sample at different Z depths. It has the capability to spatially resolve 3D cellular structures tagged for specific biomolecules. We have shown the properties of the pericellular brush using atomic force microscopy, and indicated its components using digestion enzymes. Confocal microscopy would allow for fluorescent tagging of specific biomolecules to identify the components of the brush, rather than suggest what the components are. A reasonable extension for this experiment would be to use combined AFM and confocal microscopy to take force curves of the brush layer and 3D images of the brush components as they rearrange. This would reveal how the brush's molecular components respond to mechanical stresses in time. Additionally, one could use this method to track cytoskeletal components in 3D while the cell is compressed.

Electron beam lithography (EBL) is the main method for nanolithography, which uses electron beams to etch silicon. We used commercial diffraction gratings with saw tooth cross-sections to micropattern our PDMS substrates. This limited us to ratchet (saw tooth) cross-section ridged, and did not give us control over ridge geometry. A wider variety of micropatterns would allow for a much broader geometric space to explore, and allow us to systematically test for other parameters we could not have done with diffraction gratings, such as feature curvature, heights, widths, cross section shapes, or even different geometries, such as arrays of pillars, spikes, trenches, etc. Electron beam lithography is the ideal tool for this, and can be used to make custom silicon molds to cast PDMS over. It would be interesting to use EBL to make parallel ridges with a triangular cross section (and constant spacing and approximately constant height, or by beginning with a square cross section and evolving towards a sinusoidal one), with varying apex radii, and see how probability densities are dependent on the apex curvature. This could also be used in conjunction with confocal microscopy to fluorescently tag integrins in the growth cone, to see how growth cone integrin density is related to curvature (in addition to growth cone shape). Additionally, one could use confocal timelapse imaging to fluorescently tag cytoskeletal components like tubulin and actin to see how these are interacting with the integrins during growth.

### *Develop a curvature sensing model of neuronal pathfinding*

We are currently looking into how growth cone curvature sensing affects growth cone guidance. We have shown the topographic dependence of cortical neurons with micropatterned PDMS surfaces. We theorize that higher curvatures (approaching sharp angles, compared to radii) will induce defects in the lipid bilayer that could encourage diffusion of integrins and focal adhesions to those sites to relieve membrane stresses. This would reinforce adhesion at the sites of high curvature, causing increased traction forces from cytoskeletal/integrin coupling. Using AFM to measure the curvature, and confocal microscopy to observe the growth cone in 3D on the surfaces, and the integrin surface densities would allow us develop a model of curvature sensing for neurons, and could lead to new insights on the mechanisms of neuronal fasciculation.

### *Neurite branching mechanics*

Considering the amount of data gathered exploring neurite contact mechanics, branching (e.g. when a solitary neurite splits into multiple neurites at the growth cone, or when a long neurite sprouts smaller neurites from its length) would be an

interesting next step to explore. To our knowledge, no one has investigated the differences of main neurite alignment vs branched neurites on micropatterned surfaces. By performing the same type of experiment as in chapter 3, we could learn if branched neurites display different contact guidance mechanics than main neurites.

#### *Electrical AFM to measure neuronal action potentials*

We attempted to detect and measure the action potential of embryonic cortical neurons in vitro with little success. One of the largest hurdles to overcome was timely detection of action potentials fluorescently and accurately positioning the ~60nm diameter cantilever tip on top of an active neurite to measure them directly. We attempted to increase the degree of firing with drugs such as KCl, L-Glutamate, or caffeine while simultaneously staining them with the NW “no wash” calcium indicator on the AFM stage. The difficulty in this lies with keeping the neurons healthy for the required time in the AFM bioheater. Additionally, simultaneous application of the calcium indicator, drug, and AFM calibration did not work. Previously, we would stain the neurons with a calcium indicator then add either KCl or L-Glutamate at 37°C, then wait and observe for around 30 minutes for uptake of the drugs and stain. Since the neurons die from excitotoxicity soon after uptake (~ 30 minutes after), we cannot drug them first in an incubator prior to staining, since the stain takes ~20-30 minutes to be absorbed.

All though this is the normal protocol for stimulating electrical activity fluorescently, it does not allow for the time required for AFM cantilever tuning or electric/force calibration in fluid, let alone the time required to run the experiment. Additionally, neurons fire so infrequently and for such a short time once an action potential is initiated, we are unlikely to detect firing with AFM once we are able to position the cantilever.

A proposed solution would be to culture neurons on a grounded conductive substrate (such as gold) and position the AFM cantilever over a particular neuron's axon. That neuron would then be electrically stimulated by an electrode, which would send a small current through the neuron and ground onto the conductive substrate. With luck, the stimulation would induce an action potential. This method could be further refined by patterning proteins on the conductive substrate, similar to Staii's work [13, 14] with gold substrates, to allow for very long and straight axons. This could allow us to easily stimulate an axon away from the soma, and measure the action potential propagation far away from the electrode electrically or mechanically. Additionally, we could employ MEAs as electrodes to stimulate the neurons. Unfortunately, this would eliminate our ability to fluorescently detect action potentials, considering our AFM's fluorescent microscope is inverted and cannot see through gold. However, we can perform a proof of concept without AFM on a top-down fluorescent microscope with calcium ion staining. Despite this drawback, it would be ideal not to rely on chemical stimulation and detection of action potentials, and instead to directly stimulate them with electrodes on protein nanopatterned gold substrates.



Additionally, this would allow us to explore different AFM modes for action potential detection in polar fluids if reliable and successful.

### *Conclusions*

In this thesis, we used atomic force microscopy and fluorescent microscopy to explore the mechanical, electrical, and behavioral properties of embryonic rat cortical neurons. We perform the first mechanical measurements of the pericellular brush and delineate neuron elastic properties into an elastic contribution from the soma, and a contribution from the viscoelastic precellular brush. We show that if this layer is not taken into account when reporting cell soma elastic values, the reported value will be artificially low. We also show that substrate topography has a profound effect on the effective potential and probability densities biasing neuronal pathfinding. Neurons respond to feature frequency and have a tendency to preferentially align parallel to ridges with a spacing of  $3.27 \pm 0.05\mu\text{m}$ , and also show time dependent behavior. At a spacing of  $1.59 \pm 0.03\mu\text{m}$ , neurons show less parallel/perpendicular preference, but show distinct peaks in the parallel and perpendicular directions. At a spacing of  $0.821 \pm 0.024\mu\text{m}$  spaced parallel ridges with ratchet-like cross sections, growth approaches a random distribution, with preferential growth in the perpendicular directions. As spacing between ridges decreases, there is a decrease in parallel growth and an increase in perpendicular growth. This work highlights the geometric sensing ability of the growth cone by

determining topography and time dependent angular probability densities and potentials. Additionally, we began work on detecting the electrical properties of action potentials measured via AFM and fluorescent imaging. Thus far, we have shown there are many obstacles to overcome when measuring electrical signals via electrical AFM in biologically compatible polar fluids. The highest degree of difficulty was faced when identifying electrically active neurons fluorescently, and engaging the AFM probe over the soma, neurite, or hillock in a timely manner.

The most promising future direction of this research lies with determining the mechanism of pathfinding in neurons, and how the integrins and other focal adhesion molecules interact with our ridges. This could be performed using fluorescent staging of the integrins and observing integrin concentrations over the growth cone as it interacts with the ridges with confocal microscopy. This could be combined with staining for vinculin and talin to determine their interactions with the integrins and cytoskeleton during contact guidance. Additionally, it would be interesting to investigate and compare growth cone morphologies on the three different PDMS surfaces and a control. This would allow us to learn the underlying mechanisms of growth cone topography detection, which is currently not known.

## **References**

1. Georges, P.C., et al., Matrices with compliance comparable to that of brain tissue select neuronal over glial growth in mixed cortical cultures. *Biophys J*, 2006. 90(8): p. 3012-3018.
2. Franze, K., The mechanical control of nervous system development. *Development*, 2013. 140(15): p. 3069-77.
3. Lu, Y.B., et al., Viscoelastic properties of individual glial cells and neurons in the CNS. *Proc Natl Acad Sci U S A*, 2006. 103(47): p. 17759-64.
4. Koch, D., et al., Strength in the Periphery: Growth Cone Biomechanics and Substrate Rigidity Response in Peripheral and Central Nervous System Neurons. *Biophysical Journal*, 2012. 102(3): p. 452-460.
5. Norman, L. and H. Aranda-Espinoza, Cortical Neuron Outgrowth is Insensitive to Substrate Stiffness. *Cellular and Molecular Bioengineering*, 2010. 3(4): p. 398-414.
6. Betz, T., D. Lim., J.A. Kas, Neuronal growth: a bistable stochastic process. *Phys Rev Lett*, 2006. 96(9): p. 098103.
7. Spedden, E., et al., Effects of Surface Asymmetry on Neuronal Growth. *PLoS ONE*, 2014. 9(9): p. e106709.
8. Franze, K. and J. Guck, The biophysics of neuronal growth. *Reports on Progress in Physics*, 2010. 73(9): p. 094601.
9. Lowery, L.A. and D.v. Vactor, The trip of the tip: understanding the growth cone machinery. *Nature Rev. Mol. Cell Biology*, 2009. 10: p. 332-343.
10. Xiong, Y., et al., Topography and Nanomechanics of Live Neuronal Growth Cones Analyzed by Atomic Force Microscopy. *Biophysical Journal*, 2009. 96(12): p. 5060-5072.
11. Wen, Z. and J.Q. Zheng, Directional guidance of nerve growth cones. *Current Opinion in Neurobiology*, 2006. 16(1): p. 52-58.
12. Huber, A.B., et al., Signaling at the growth cone: ligand-receptor complexes and the control of axon growth and guidance. *Annu Rev Neurosci*, 2003. 26: p. 509-63.

13. Staii, C., et al., Distance Dependence of Neuronal Growth on Nanopatterned Gold Surfaces. *Langmuir*, 2011. 27: p. 233-239.
14. Staii, C., et al., Positioning and guidance of neurons on gold surfaces by directed assembly of proteins using Atomic Force Microscopy. *Biomaterials*, 2009. 30(20): p. 3397-404.
15. Rosoff, W.J., et al., A new chemotaxis assay shows the extreme sensitivity of axons to molecular gradients. *Nature Neuroscience*, 2004. 7(6): p. 678-82.
16. Dent, E.W. and F.B. Gertler, Cytoskeletal dynamics and transport in growth cone motility and axon guidance. *Neuron*, 2003. 40(2): p. 209-27.
17. Gruler, H. and K. Franke, Automatic control and directed cell movement. Novel approach for understanding chemotaxis, galvanotaxis, galvanotropism. *Z Naturforsch C*, 1990. 45(11-12): p. 1241-9.
18. Kerstein, P.C., R.H. Nichol, and T.M. Gomez., Mechanochemical regulation of growth cone motility. *Frontiers in Cellular Neuroscience*, 2015. 9.
19. Hancock, M.J., K. Sekeroglu, and M.C. Demirel, Bioinspired Directional Surfaces for Adhesion, Wetting and Transport. *Adv Funct Mater*, 2012. 22(11): p. 2223-2234.
20. Wen, Z. and J.Q. Zheng, of nerve growth cones. *Current Opinion in Neurobiology*, 2006. 16(1): p. 52-8.
21. Kuznetsova, T.G., et al., Atomic force microscopy probing of cell elasticity. *Micron*, 2007. 38(8): p. 824-833.
22. Beighley, R., et al., Neuronal alignment on asymmetric textured surfaces. *Appl Phys Lett*, 2012. 101(14): p. 143701.
23. Zheng, J.Q., et al., Turning of nerve growth cones induced by neurotransmitters. *Nature*, 1994. 368(6467): p. 140-144.
24. Fan, Y.W., et al., Culture of neural cells on silicon wafers with nano-scale surface topography. *J Neurosci Methods*, 2002. 120(1): p. 17-23.
25. Fozdar, D.Y., et al., Selective axonal growth of embryonic hippocampal neurons according to topographic features of various sizes and shapes. *Int J Nanomedicine*, 2011. 6: p. 45-57.
26. Johansson, F., et al., Axonal outgrowth on nano-imprinted patterns. *Biomaterials*, 2006. 27(8): p. 1251-8.

27. Rajnicek, A., S. Britland, and C. McCaig, Contact guidance of CNS neurites on grooved quartz: influence of groove dimensions, neuronal age and cell type. *J Cell Sci*, 1997. 110 ( Pt 23): p. 2905-13.
28. Hart, S.R., et al., Adhesive micro-line periodicity determines guidance of axonal outgrowth. *Lab Chip*, 2013. 13(4): p. 562-9.
29. Song, M. and K.E. Uhrich, Optimal micropattern dimensions enhance neurite outgrowth rates, lengths, and orientations. *Ann Biomed Eng*, 2007. 35(10): p. 1812-20.
30. Kam, L., et al., Axonal outgrowth of hippocampal neurons on micro-scale networks of polylysine-conjugated laminin. *Biomaterials*, 2001. 22(10): p. 1049-54.
31. Tessier-Lavigne, M. and C.S. Goodman, *The Molecular Biology of Axon Guidance*. Science, 1996. 274(5290): p. 1123-1133.
32. Peskin, C S, G M Odell, and G F Oster. *Cellular Motions and Thermal Fluctuations: The Brownian Ratchet*. *Biophysical Journal* 65.1 1993. 316–324.
33. Segev, R. and E. Ben-Jacob, Generic modeling of chemotactic based self-wiring of neural networks. *Neural Networks*, 2000. 13(2): p. 185-199.
34. Pearson, Y.E., et al., Mathematical Modeling of Axonal Formation Part I: Geometry. *Bull Math Biol*, 2011. 73(12): p. 2837-2864.
35. Spedden, E., et al., Young's Modulus of Cortical and P19 Derived Neurons Measured by Atomic Force Microscopy. *MRS Online Proceedings Library*, 2012. 1420: p. null
36. Lodish H., Berk A., Zipursky S.L., *Molecular Cell Biology*. 4th edition. 2000, W.H. Freeman.
37. Partridge, M.A., E.E., Marcantonio, Initiation of Attachment and Generation of Mature Focal Adhesions by Integrin-containing Filopodia in Cell Spreading. *Molecular Biology of the Cell*, 2006. 17(10): p. 4237-4248.
38. Cox, E.A., S.K. Sastry, and A. Huttenlocher, Integrin-mediated Adhesion Regulates Cell Polarity and Membrane Protrusion through the Rho Family of GTPases. *Molecular Biology of the Cell*, 2001. 12(2): p. 265-277.
39. O'Toole, M., P. Lamoureux, and K.E. Miller, A physical model of axonal elongation: force, viscosity, and adhesions govern the mode of outgrowth. *Biophys J*, 2008. 94(7): p. 2610-20.

40. M. Simon, M. Dokukin, V. Kalaparthy, E. Spedden, I. Sokolov, and C. Staii, Load Rate and Temperature Dependent Mechanical Properties of the Cortical Neuron and Its Pericellular Layer Measured by Atomic Force Microscopy, *Langmuir*. 2016. 1111-1119
41. Lu, Y.B., et al., Reactive glial cells: increased stiffness correlates with increased intermediate filament expression. *Faseb J*, 2011. 25(2): p. 624-631.
42. Sokolov, I., et al., Detection of surface brush on biological cells in vitro with atomic force microscopy. *Applied Physics Letters*, 2007. 91: p. 023902-1-3.
43. GM, Cooper., *The Cell: A Molecular Approach*. 2nd edition. 2000, Sinauer Associates.
44. Spedden, E., et al., Elasticity Maps of Living Neurons Measured by Combined Fluorescence and Atomic Force Microscopy. *Biophysical Journal*, 2012. 103(5): p. 868-877.
45. Spedden, E., D.L. Kaplan, and C. Staii, Temperature response of the neuronal cytoskeleton mapped via atomic force and fluorescence microscopy. *Physical Biology*, 2013. 10(5): p. 056002.
46. Philip Nelson., *Biological Physics: Energy, Information, Life*. Updated first edition. 2004. W.H. Freeman.
47. F. C. MacKintosh, J. Käs, and P. A. Janmey., Elasticity of Semiflexible Biopolymer Networks. *Phys. Rev. Lett.* 75, 4425. 1995
48. Frey, M.T., et al., Cellular responses to substrate topography: role of myosin II and focal adhesion kinase. *Biophys J*, 2006. 90(10): p. 3774-82.
49. Kolomeinsky. AB., Fisher. ME. Molecular motors: A theorist's perspective. *Annu. Rev. Chem.* 2007. 58:675-95.
50. Mullins, R.D., J.A. Heuser., T.D. Pollard, The interaction of Arp2/3 complex with actin: Nucleation, high affinity pointed end capping, and formation of branching networks of filaments. *Proceedings of the National Academy of Sciences of the United States of America*, 1998. 95(11): p. 6181-6186.
51. Moore, S.W., M.P. Sheetz, Biophysics of substrate interaction: influence on neural motility, differentiation, and repair. *Dev Neurobiol*, 2011. 71(11): p. 1090-101.

52. Micholt, L., et al., Substrate topography determines neuronal polarization and growth in vitro. PLoS One, 2013. 8(6): p. e66170.
53. Grzywa, E.L., et al., High-resolution analysis of neuronal growth cone morphology by comparative atomic force and optical microscopy. Journal of Neurobiology, 2006. 66(14): p. 1529-1543.
54. Jang, MJ., Nam, Y. Geometric Effect of Cell Adhesive Polygonal Micropatterns on Neuritogenesis and Axon Guidance. J. Neural. Eng. 2012. doi: 10.1088/1741-2560/9/4/046019
55. Smith, C.L., Cytoskeletal movements and substrate interactions during initiation of neurite outgrowth by sympathetic neurons in vitro. J Neurosci, 1994. 14(1): p. 384-98.
56. Etienne-Manneville, S. and A. Hall, Rho GTPases in cell biology. Nature, 2002. 420(6916): p. 629-635.
57. Hytönen, V.P. and V. Vogel, How Force Might Activate Talin's Vinculin Binding Sites: SMD Reveals a Structural Mechanism. PLoS Computational Biology, 2008. 4(2): p. e24.
58. Martens, J.C., M. Radmacher,. Softening of the actin cytoskeleton by inhibition of myosin II, Pflugers Arch, 2008. 456(1): p. 95-100.
59. Svoboda, K.K., et al., ROCK inhibitor (Y27632) increases apoptosis and disrupts the actin cortical mat in embryonic avian corneal epithelium. Developmental Dynamics, 2004. 229(3): p. 579-90.
60. Bogatcheva, N.V., et al., The suppression of myosin light chain (MLC) phosphorylation during the response to lipopolysaccharide (LPS): beneficial or detrimental to endothelial barrier? J Cell Physiol, 2011. 226(12): p. 3132-46.
61. Ishizaki, T., et al., Pharmacological properties of Y-27632, a specific inhibitor of rho-associated kinases. Mol Pharmacol, 2000. 57(5): p. 976-83.
62. Sabass, B., et al., High Resolution Traction Force Microscopy Based on Experimental and Computational Advances. Biophysical Journal, 2008. 94(1): p. 207-220.
63. Goodhill, G.J. and J.S. Urbach, Theoretical analysis of gradient detection by growth cones. Journal of Neurobiology, 1999. 41(2): p. 230-241.
64. Goodhill, G.J. and H. Baier, Axon guidance: Stretching gradients to the limit. Neural Computation, 1998. 10(3): p. 521-527.

65. Goodhill, G.J., Mathematical guidance for axons. Trends in Neurosciences, 1998. 21(6): p. 226-231.
66. Hentschel, H.G. and A. van Ooyen, Models of axon guidance and bundling during development. Proc Biol Sci, 1999. 266(1434): p. 2231-8.
67. Rizzo, D.J., et al., Neuronal growth as diffusion in an effective potential. Physical Review E, 2013. 88(4): p. 042707.
68. Buettner, H.M., Computer simulation of nerve growth cone filopodial dynamics for visualization and analysis. Cell Motil Cytoskeleton, 1995. 32(3): p. 187-204.
69. Odde, D.J., et al., Stochastic dynamics of the nerve growth cone and its microtubules during neurite outgrowth. Biotechnol Bioeng, 1996. 50(4): p. 452-61.
70. Robert, M.E. and J.D. Sweeney, Computer model: Investigating role of filopodia-based steering in experimental neurite galvanotropism. J Theor Biol, 1997. 188(3): p. 277-288.
71. Vanveen, M. and J. Vanpelt, A Model for Outgrowth of Branching Neurites. J Theor Biol, 1992. 159(1): p. 1-23.
72. Franze, K., et al., Neurite branch retraction is caused by a threshold-dependent mechanical impact. Biophys J, 2009. 97(7): p. 1883-90.
73. Fricker, Desdemona, Jos A H Verheugen, and Richard Miles. Cell-Attached Measurements of the Firing Threshold of Rat Hippocampal Neurones. The Journal of Physiology 517.Pt 3. 1999.
74. Kim, G.H., Kosterin, P., Obaid, A.L., Salzberg, B.M. (2007) A Mechanical Spike Accompanies the Action Potential in Mammalian Nerve Terminals. Biophys. J. 92, 3122-3129.
75. Gonzalez-Perez, Alfredo., D. Mosgaard, Lars., Budvytyte, Rima., Villagran-Vargas, Edgar., Jackson, Andrew., Heimburg, Thomas. (2015) Solitary electromechanical pulses in lobster neurons. ArXiv. 1502.07166v1
76. Granato, A. and J. Van Pelt, Effects of early ethanol exposure on dendrite growth of cortical pyramidal neurons: inferences from a computational model. Developmental Brain Research, 2003. 142(2): p. 223-227.
77. Elkin B S, A.E.U., Costa K D and Morrison B III, Mechanical heterogeneity of the rat hippocampus measured by atomic force microscope indentation. Neurotrauma, 2007(24).



78. Dickson, B.J., Molecular mechanisms of axon guidance. *Science*, 2002. 298(5600): p. 1959-64.
79. Geraldo, S. and P.R. Gordon-Weeks, Cytoskeletal dynamics in growth-cone steering. *Journal of Cell Science*, 2009. 122(Pt 20): p. 3595-604.
80. Sunyer, R., et al., The temperature dependence of cell mechanics measured by atomic force microscopy. *Physical Biology*, 2009. 6(2): p. 025009.
81. Petersen, N.O., W.B. McConnaughey, and E.L. Elson, Dependence of locally measured cellular deformability on position on the cell, temperature, and cytochalasin B. *Proceedings of the National Academy of Sciences of the United States of America*, 1982. 79(17): p. 5327-31.
82. Li, Q.S., et al., Probing the Elasticity of Breast Cancer Cells Using AFM, in 13th International Conference on Biomedical Engineering, C. Lim and J.H. Goh, Editors. 2009, Springer Berlin Heidelberg. p. 2122-2125.
83. Tan, S.C., et al., Viscoelastic behaviour of human mesenchymal stem cells. *BMC Cell Biology*, 2008. 9: p. 40.
84. Berdyeva, T., C.D. Woodworth, and I. Sokolov, Visualization of cytoskeletal elements by the atomic force microscope. *Ultramicroscopy*, 2005. 102: p. 189-98.
85. Franze, K., Atomic force microscopy and its contribution to understanding the development of the nervous system. *Curr Opin Genet Dev*, 2011. 21(5): p. 530-7.
86. Mustata, M., K. Ritchie, and H.A. McNally, Neuronal elasticity as measured by atomic force microscopy. *J Neurosci Methods*, 2010. 186(1): p. 35-41.
87. Moore, S.W., P. Roca-Cusachs, and M.P. Sheetz, Stretchy proteins on stretchy substrates: the important elements of integrin-mediated rigidity sensing. *Dev Cell*, 2010. 19(2): p. 194-206.
88. Kawaguchi, K. and A. Yamaguchi, Temperature dependence rigidity of non-taxol stabilized single microtubules. *Biochemical and Biophysical Research Communications*, 2010. 402(1): p. 66-9.
89. Trickey, W.R., et al., Determination of the Poisson's ratio of the cell: recovery properties of chondrocytes after release from complete micropipette aspiration. *J Biomech*, 2006. 39(1): p. 78-87.
90. Brown, A., Slow axonal transport: stop and go traffic in the axon. *Nat Rev Mol Cell Biol*, 2000. 1(2): p. 153-6.

91. Spedden, E. and C. Staii, Neuron Biomechanics Probed by Atomic Force Microscopy. *International Journal of Molecular Sciences*, 2013. 14(8): p. 16124-16140.
92. Malara, A., et al., Brief report Extracellular matrix structure and nano-mechanics determine megakaryocyte function. *Blood*, 2011. 118(16): p. 4449-4453.
93. Fass, J.N. and D.J. Odde, Tensile force-dependent neurite elicitation via anti-beta1 integrin antibody-coated magnetic beads. *Biophys J*, 2003. 85(1): p. 623-36.
94. Kundu, A., et al., Superimposed topographic and chemical cues synergistically guide neurite outgrowth. *Lab on a chip*, 2013. 13(15): p. 10.1039/c3lc50174d.
95. Cetinkaya, M., N. Malvadkar, and M.C. Demirel, Power-law scaling of structured poly(p-xylylene) deposited by oblique angle. *Journal of Polymer Science Part B-Polymer Physics*, 2008. 46(6): p. 640-648.
96. Cetinkaya, M., S. Boduroglu, and M.C. Demirel, Growth of nanostructured thin films of poly (p-xytylene) derivatives by vapor deposition. *Polymer*, 2007. 48(14): p. 4130-4134.
97. Malvadkar, N.A., et al., An engineered anisotropic nanofilm with unidirectional wetting properties. *Nat Mater*, 2010. 9(12): p. 1023-8.
98. Lowery, L.A. and D.v. Vactor, The trip of the tip: understanding the growth cone machinery. *Nature Rev. Mol. Cell Biology*, 2009. 10: p. 332-343.
99. Witte, H., D. Neukirchen, and F. Bradke, Microtubule stabilization specifies initial neuronal polarization. *The Journal of Cell Biology*, 2008. 180(3): p. 619-632.
100. Dowell-Mesfin, N.M., et al., Topographically modified surfaces affect orientation and growth of hippocampal neurons. *J Neural Eng*, 2004. 1(2): p. 78-90.
101. Asylum Research., MFP3D Manual, 2008. Asylum Research: An Oxford Instruments Company.
102. SecretDisk, WikiCommons, 2008. Permission: GFDL, CC-BY-SA-3.0
103. Butt, Hans-Jurgen., Cappella, Hans-Jurgen., Kappl, Michael., Force measurements with the atomic force microscope: Technique, interpretation and applications. *Surface Science Reports*, 2005. 59: p. 1-152.

104. Kawaguchi, K. and A. Yamaguchi, Temperature dependence rigidity of non-taxol stabilized single microtubules. *Biochemical and Biophysical Research Communications*, 2010. 402(1): p. 66-9.
105. H. Wang. Several Issues in Modeling Molecular Motors. *J. of Comp. and Theor. Nanosci.* 2008. 5. 1-35.
106. Koch, D., et al., Strength in the Periphery: Growth Cone Biomechanics and Substrate Rigidity Response in Peripheral and Central Nervous System Neurons. *Biophysical Journal*, 2012. 102(3): p. 452-460.
107. Lamoureux, P., et al., Mechanical tension can specify axonal fate in hippocampal neurons. *J Cell Biol*, 2002. 159: p. 499-508.
108. Streitberger, K.J., et al., Brain Viscoelasticity Alteration in Chronic-Progressive Multiple Sclerosis. *PLoS One*, 2012. 7(1): p. e29888.
109. da Silva, J., et al., The cavity-to-cavity migration of leukaemic cells through 3D honey-combed hydrogels with adjustable internal dimension and stiffness. *Biomaterials*, 2010. 31(8): p. 2201-2208.
110. Iyer, S., et al., Atomic force microscopy detects differences in the surface brush of normal and cancerous cells. *Nat Nanotechnol*, 2009. 4(6): p. 389-393.
111. Berdyeva, T.K., C.D. Woodworth, and I. Sokolov, Human epithelial cells increase their rigidity with ageing in vitro: direct measurements. *Phys Med Biol*, 2005. 50(1): p. 81-92.
112. Sokolov, I., Atomic Force Microscopy in Cancer Cell Research, in *Cancer Nanotechnology – Nanomaterials for Cancer Diagnosis and Therapy*, H.S.N.a.T. Webster, Editor. 2007, APS: Los Angeles. p. 43-59.
113. Sokolov, I., S. Iyer, and C.D. Woodworth, Recover of Elasticity of Aged Human Epithelial Cells In-Vitro. *Nanomed-Nanotechnol*, 2006. 2: p. 31–36.
114. Caille, N., et al., Contribution of the nucleus to the mechanical properties of endothelial cells. *J Biomech*, 2002. 35(2): p. 177-187.
115. Sokolov, I., M.E. Dokukin, and N.V. Guz, Method for quantitative measurements of the elastic modulus of biological cells in AFM indentation experiments. *Methods*, 2013. 60(2): p. 202-213.
116. Evanko, S.P., et al., Hyaluronan-dependent pericellular matrix. *Adv Drug Deliver Rev*, 2007. 59(13): p. 1351-1365.

117. Iyer, S., et al., AFM Detects Differences in the Surface Brush on Normal and Cancerous Cervical Cells. *Nature Nanotechnology*, 2009. 4: p. 389-393.
118. Zimmerman, E., B. Geiger, and L. Addadi, Initial stages of cell-matrix adhesion can be mediated and modulated by cell-surface hyaluronan. *Biophys J*, 2002. 82(4): p. 1848-57.
119. Cohen, M., et al., Hyaluronan in the pericellular coat: an additional layer of complexity in early cell adhesion events. *Soft Matter*, 2007. 3(3): p. 327-332.
120. Dokukin, M.E., N.V. Guz, and I. Sokolov, Quantitative Study of the Elastic Modulus of Loosely Attached Cells in AFM Indentation Experiments. *Biophys J*, 2013. 104(10): p. 2123-31.
121. Iyer, K.S., et al., Physical Labeling of Papillomavirus-Infected, Immortal, and Cancerous Cervical Epithelial Cells Reveal Surface Changes at Immortal Stage. *Cell Biochem Biophys*, 2012. 63(2): p. 109-116.
122. Iyer, S., et al., Towards nonspecific detection of malignant cervical cells with fluorescent silica beads. *Small*, 2009. 5(20): p. 2277 - 2284.
123. Vincent, T.L., et al., FGF-2 is bound to perlecan in the pericellular matrix of articular cartilage, where it acts as a chondrocyte mechanotransducer. *Osteoarthritis Cartil*, 2007. 15(7): p. 752-763.
124. Itano, N., et al., Abnormal accumulation of hyaluronan matrix diminishes contact inhibition of cell growth and promotes cell migration. *Proc Natl Acad Sci U S A*, 2002. 99(6): p. 3609-3614.
125. Jiang, D., et al., Regulation of lung injury and repair by Toll-like receptors and hyaluronan. *Nat Med*, 2005. 11(11): p. 1173-9.
126. Hedman, K., et al., Isolation of the Pericellular Matrix of Human Fibroblast-Cultures. *J Cell Biol*, 1979. 81(1): p. 83-91.
127. Nijenhuis, N., et al., High-resolution microrheology in the pericellular matrix of prostate cancer cells. *J R Soc Interface*, 2012. 9(73): p. 1733-1744.
128. Cohen, M., et al., Organization and adhesive properties of the hyaluronan pericellular coat of chondrocytes and epithelial cells. *Biophys J*, 2003. 85(3): p. 1996-2005.
129. McLane, L.T., et al., Spatial organization and mechanical properties of the pericellular matrix on chondrocytes. *Biophys J*, 2013. 104(5): p. 986-96.

130. Ng, L., et al., Nanomechanical properties of individual chondrocytes and their developing growth factor-stimulated pericellular matrix. *J Biomech*, 2007. 40(5): p. 1011-23.
131. Sokolov, I., et al., On averaging force curves over heterogeneous surfaces in atomic force microscopy. *Ultramicroscopy*, 2012. 121: p. 16-24.
132. Bernick, K.B., et al., Biomechanics of single cortical neurons. *Acta Biomater*, 2011. 7(3): p. 1210-9.
133. Radmacher, M., Measuring the elastic properties of biological samples with the AFM. *IEEE Eng Med Biol Mag*, 1997. 16(2): p. 47-57.
134. Guz, N., et al., If cell mechanics can be described by elastic modulus: study of different models and probes used in indentation experiments. *Biophys J*, 2014. 107(3): p. 564-75.
135. Nawaz, S., et al., Cell visco-elasticity measured with AFM and optical trapping at sub-micrometer deformations. *PLoS One*, 2012. 7(9): p. e45297.
136. Ren, J., et al., Indentation quantification for in-liquid nanomechanical measurement of soft material using an atomic force microscope: rate-dependent elastic modulus of live cells. *Phys Rev E Stat Nonlin Soft Matter Phys*, 2013. 88(5): p. 052711.
137. Wilusz, R.E. and F. Guilak, High resistance of the mechanical properties of the chondrocyte pericellular matrix to proteoglycan digestion by chondroitinase, aggrecanase, or hyaluronidase. *J Mech Behav Biomed Mater*, 2013. 10.1016
138. Attili, S. and R.P. Richter, Combining Colloidal Probe Atomic Force and Reflection Interference Contrast Microscopy to Study the Compressive Mechanics of Hyaluronan Brushes. *Langmuir*, 2012. 28(6): p. 3206-3216.
139. Chen, R.J., C.C.K. Lin, and M.S. Ju, Quasi-linear viscoelastic properties of PC-12 neuron-like cells measured using atomic force microscopy. *J Chin Inst Eng*, 2011. 34(3): p. 325-335.
140. Boehm, H., et al., Mapping the mechanics and macromolecular organization of hyaluronan-rich cell coats. *Soft Matter*, 2009. 5(21): p. 4331-4337.
141. Carl, P. and H. Schillers, Elasticity measurement of living cells with an atomic force microscope: data acquisition and processing. *Pflug Arch Eur J Phy*, 2008. 457(2): p. 551-559.

142. Cross, S.E., et al., AFM-based analysis of human metastatic cancer cells. *Nanotechnology*, 2008. 19(38): p. 384003.
143. Fuhrmann, A., et al., AFM stiffness nanotomography of normal, metaplastic and dysplastic human esophageal cells. *Phys Biol*, 2011. 8(1): p. 015007.
144. Johnson, A.S., Nehl, C.L., Mason, M.G., Hafner, J.H. *Fluid Electric Force Microscopy for Charge Density Mapping in Biological Systems*. *Langmuir*. 19. 10007-10010,
145. Butt, H.-J. and M. Kappl, *Introduction*, in *Surface and Interfacial Forces*. 2010, Weinheim, Germany: Wiley-VCH Verlag GmbH & Co. KGaA.
146. Rotsch, C., et al., AFM imaging and elasticity measurements on living rat liver macrophages. *Cell Biol Int*, 1997. 21(11): p. 685-696.
147. Matzke, R., K. Jacobson, and M. Radmacher, Direct, high-resolution measurement of furrow stiffening during division of adherent cells. *Nat Cell Biol*, 2001. 3(6): p. 607-10.
148. Li, H. and J.J. Vlassak, Determining the elastic modulus and hardness of an ultra-thin film on a substrate using nanoindentation. *J Mater Res*, 2009. 24(3): p. 1114-1126.
149. King, R.B., *Elastic Analysis of Some Punch Problems for a Layered Medium*. *Int J Solids Struct*, 1987. 23(12): p. 1657-1664.
150. Lieleg, O., et al., Cytoskeletal Polymer Networks: Viscoelastic Properties are Determined by the Microscopic Interaction Potential of Cross-links. *Biophys J*, 2009. 96(11): p. 4725-4732.
151. Tharmann, R., M.M.A.E. Claessens, and A.R. Bausch, Viscoelasticity of isotropically cross-linked actin networks. *Phys Rev Lett*, 2007. 98(8): p. 088103.
152. Wagner, O., et al., Viscoelastic properties of f-actin, microtubules, f-actin/alpha-actinin, and f-actin/hexokinase determined in microliter volumes with a novel nondestructive method. *Biophys J*, 1999. 76(5): p. 2784-2796.
153. Cross, S.E., et al., Nanomechanical analysis of cells from cancer patients. *Nat. Nanotechnol.*, 2007. 2(12): p. 780-783.
154. Jerusalem, A. and M. Dao, Continuum modeling of a neuronal cell under blast loading. *Acta Biomater*, 2012. 8(9): p. 3360-71.
155. Rashid, B., M. Destrade, and M.D. Gilchrist, Temperature effects on brain tissue in compression. *J Mech Behav Biomed Mater*, 2012. 14: p. 113-8.

156. Young, R.J. and P.A. Lovell, Introduction to polymers. 3rd ed. 2011, Boca Raton: CRC Press., 668.
157. Baker BJ, Kosmidis EK, Vucinic D, Falk CX, Cohen LB, Djuricic M, et al. Imaging brain activity with voltage- and calcium-sensitive dyes. *Cell Mol Neurobiol.* 2005;25:245-82.
158. Ebner TJ, Chen G. Use of voltage-sensitive dyes and optical recordings in the central nervous system. *Prog Neurobiol.* 1995;46:463-506.
159. Zochowski M, Wachowiak M, Falk CX, Cohen LB, Lam YW, Antic S, et al. Imaging membrane potential with voltage-sensitive dyes. *Biol Bull.* 2000;198:1-21.
160. Rutten WL. Selective electrical interfaces with the nervous system. *Annu Rev Biomed Eng.* 2002;4:407-52.
161. Dwarak, B.J., Wheeler, B.C., Novel MEA platform with PDMS microtunnels enables the detection of action potential propagation from isolated axons in culture. *Lab Chip.* 2009;9:404-10
162. Johnson, A.S., Nehl, C.L., Mason, M.G., Hafner, J.H. (2003) Fluid Electric Force Microscopy for Charge Density Mapping in Biological Systems. *Langmuir.* 19. 10007-10010.
163. Yang, Y., Mayer, K.M., Hafner, J.H. (2007) Quantitative Membrane Electrostatics with Atomic Force Microscope. *Biophysical. J.* 92. 1966-1974.
164. Staii C, Johnson AT, Pinto NJ. Quantitative analysis of scanning conductance microscopy. *Nano Letters.* 2004;4:859-62.
165. Zhou YX, Freitag M, Hone J, Staii C, Johnson AT, Pinto NJ, et al. Fabrication and electrical characterization of polyaniline-based nanofibers with diameter below 30 nm. *Appl Phys Lett.* 2003;83:3800-2.
166. Collins, L., Jesse, S., Kilpatrick, J.I., Tselev, A., Varenky, O., Okatan, M.B., Weber, S.A.L., Aumar, A., Balke, N., Kalinin, S.V., Rodriguez, B.J. (2014) Probing charge screening dynamics and electromechanical processes at the solid-liquid interface with electrochemical force microscopy. *Nature Communications.* 5:3871 10.1038
167. Marliere, Christian., Dhahri, S. (2015) An in vivo study of electrical charge distribution on the bacterial cell wall by atomic force microscopy in vibrating force mode. *Nanoscale.* 7. 8843-8857.

168. Rodriguez, B.J., Kalinin, S.V., Shin, J., Jesse, S., Grichko, V., Thundat, T., Baddorf, A.P., Gruverman, A. (2006) Electromechanical imaging of biomaterials by scanning probe microscopy. *J. of Stuct. Bio.*153. 151-159.
169. Thompson, G.L., Reukov, V.V., Nikiforov, M.P., Kalinin, S.V., Vertegel, A.A. (2012) Electromechanical and Elastic Probing of Bacteria in Cell Culture Medium. *Nanotechnology.* 23. 245705
170. Upadye, K.V., Candiella, J.E., Davidson, L.A., Lin, H. (2012) Whole Cell Electrical Activity Under Direct Mechanical Stimulus by AFM Cantilever Using Planar Patch Clamp Chip Approach. *Cell. Mol. Bioeng.* 4(2). 270-280.
171. Hady, A.E., Machta, B.B. Mechanical surface waves accompany action potential propagation. *Nature Communications.* 2015. DOI: 6:6697 10.1038
172. Belton DJ, Mieszawska AJ, Currie HA, Kaplan DL, Perry CC. Silk-silica composites from genetically engineered chimeric proteins: materials properties correlate with silica condensation rate and colloidal stability of the proteins in aqueous solution. *Langmuir.* 2012;28(9):4373-4381. doi:10.1021/la205084z.
173. Canabady-Rochelle LLS, Belton DJ, Deschaume O, Currie HA, Kaplan DL, Perry CC. Bio-inspired Silicification of Silica-binding Peptide-Silk Protein Chimeras: Comparison of Chemically and Genetically Produced Proteins. *Biomacromolecules.* 2012;13(3):683-690. doi:10.1021/bm201555c.
174. Zhou S, Huang W, Belton DJ, et al. Control of silicification by genetically engineered fusion proteins: Silk–silica binding peptides. *Acta biomaterialia.* 2015;15:173-180. doi:10.1016/j.actbio.2014.10.040.
175. Plowright R, Dinjaski N, Zhou S, Belton DJ, Kaplan DL, Perry CC. Influence of silk-silica fusion protein design on silica condensation in vitro and cellular calcification. *RSC advances.* 2016;6(26):21776-21788.
176. Mieszawska AJ, Furligas N, Georgakoudi I, et al. Osteoinductive silk-silica composite biomaterials for bone regeneration. *Biomaterials.* 2010;31(34):8902-8910.
177. Belton DJ, Patwardhan SV, Annenkov VV, Danilovtseva EN, Perry CC. From biosilicification to tailored materials: Optimizing hydrophobic domains and resistance to protonation of polyamines. *Proceedings of the National Academy of Sciences of the United States of America.* 2008;105(16):5963-5968.
178. Calabrese, R.J., Raia N., Huang, W., Ghezzi, C.E., Simon, M., Staii, C., Weiss, A.S., Kaplan, D.L. Silkionomer and silk tropoelastin hydrogels as



charged three-dimensional culture platforms for the regulation of hMSC response. (in review). *Journal of Tissue Engineering and Regenerative Medicine*.

179. O. Tokareva., S. Lin., M. Jacobsen., W. Huang., D. Rizzo., D. Li., M. Simon., C. Staii., P. Cebe., J. Wong., M. Buehler., D. Kaplan. Effect of sequence features on assembly of spider silk block copolymers. *J Struct Bio*. 2014. p. 412-419.

180. M. Jacobsen., O. Torakeva., D. Ebrahimi., W. Huang., S. Ling., N. Dijanski., D. Li., M. Simon., C. Staii., K. Quinn., I. Georgakoudi., M. Buehler., D. Kaplan., J. Wong. Combined modeling-experimentation analysis of the spider silk N-terminal: Consequences on fibre properties. (in review). *Nature Materials*.

181. Z. Smith, D. Meyer, M. Simon, C. Staii, D. Shukla, and S.W. Thomas, Thiophene-Based Conjugated Polymers with Photolabile Solubilizing Side Chains, *Macromolecules*, 2015 48 (4), pp 959–966

182. X. Hu, E. McIntosh, M. Simon, C. Staii, and S.W. Thomas, Stimuli-Responsive Free-Standing Layer-By-Layer Films, *Advanced Materials*, 2016. 28, 715-721

